

DAMAGE PROGRESSION QUANTIFICATION AND DATA ROBUSTNESS
EVALUATION IN SELF-POWERED SENSORS NETWORKS

By

Hassene Hasni

A DISSERTATION

Submitted to
Michigan State University
in partial fulfillment of the requirements
for the degree of

Civil Engineering - Doctor of Philosophy

2018

ABSTRACT

DAMAGE PROGRESSION QUANTIFICATION AND DATA ROBUSTNESS EVALUATION IN SELF-POWERED SENSORS NETWORKS

By

Hassene Hasni

This research proposes novel damage progression quantification and data robustness evaluation approaches, for structural health monitoring (SHM), using a new class of self-powered piezo-floating-gate (PFG) sensors. This system relies on harvesting the mechanical energy from structures through the direct effect of piezoelectricity. The operating power of the smart sensor and the data used for damage identification is harvested directly from the sensing signal induced by a piezoelectric transducer under dynamic loading.

The developed models integrate structural simulations using finite element method (FEM) techniques, experimental studies, and statistical and artificial intelligence (AI) methods. In this work, the performance of the sensing system in identifying damage is investigated for various damage scenarios based on numerical and experimental studies. Both steel and pavement structures are studied. A new surface sensing approach for detecting bottom-up cracks in asphalt concrete (AC) pavement is proposed.

Two types of self-powered wireless sensors are investigated in this research. Different data interpretation techniques are developed for each type of sensor. The data are obtained from finite element simulations, or experimental measurement, and are fitted to probability distributions to define initial damage indicators. Sensor fusion models are developed based on the concept of group-effect of sensors, in order to increase the damage detection resolution of individual sensors. Probabilistic neural network (PNN) and support vector machine (SVM) methods are used to improve the accuracy of the proposed damage identification methods for the case of

multi-class damage progression. The proposed work is divided into four main parts: (i) Damage identification in steel structures using data from a uniform PFG sensor, (ii) Damage detection in steel and pavement structures using a non-uniform PFG sensor, (iii) Damage detection and localization in steel frame structures using hybrid network of self-powered strain and vibration sensors, and, (iv) a field demonstration of the new technology on the Mackinac Bridge in Michigan. The cases of the U10W gusset plate of the I-35W bridge in Minneapolis, MN, a steel girder, a steel plate under compaction tension mode, and an AC beam under three-point bending configuration are investigated. A surface sensing approach to detect bottom-up cracking in AC pavement under dynamic moving load is also proposed. This approach is based on interpreting the data of a surface-mounted network of sensors. Moreover, a hybrid network of strain and vibration-based sensors is used to detect damage in bolted steel frames. The objective is to establish a local-to-global strategy for damage identification in frames. Data fusion models combined with AI classifiers are developed. Uncertainty analysis is performed to verify the performance of the sensors under different noise levels.

Copyright by
HASSENE HASNI
2018

To my parents, for their devotion and sacrifice,
To my siblings, for their help and encouragement,
To my friends, with whom I spent so many precious moments.
I dedicate my work,
Symbol of gratitude and love.

ACKNOWLEDGMENTS

I would like to express my deepest gratitude to Dr. Nizar Lajnef and Dr. Karim Chatti for their excellent guidance, valuable knowledge, and encouragement that helped me to conduct this research.

I am also grateful to Dr. Shantanu Chakrabartty for his contribution in developing the sensor, and Dr. Sami F. Masri for his valuable advices.

I would like to thank Dr. Roozbeh Dargazany, Dr. Mahmoodul Haq, and Dr. Arun Ross for being my committee members, for their helpful advices, guidance and for reading my thesis.

My special appreciation should go to my colleagues, Dr. Amir H. Alavi, Dr. Wassim Borchani, and Dr. Pengcheng Jiao for their friendship, and for sharing with me valuable and precious advices.

Last, but not least, I would like to thank my parents, Mouldi and Wassila, and my siblings, Wissem, Mohammed, and Iheb, for their endless support and encouragement, and for the many years of support during my undergraduate studies that provided the foundation for this work.

This work is supported in part by the FHWA grants DTFH61-13-C-00015 and DTFH61-13-H-00009.

TABLE OF CONTENTS

LIST OF TABLES	x
LIST OF FIGURES	xii
CHAPTER 1. INTRODUCTION	1
1.1. Motivation and vision.....	1
1.2. Background and state of knowledge	3
1.3. Research hypothesis and objectives	10
1.3.1. Hypothesis	10
1.3.2. Objectives	10
1.4. Outline.....	11
CHAPTER 2. DAMAGE IDENTIFICATION AND QUANTIFICATION IN STRUCTURES USING UNIFORM PFG SENSORS	15
2.1. Overview	15
2.2. Working principles of the uniform PFG sensor	16
2.3. Health monitoring of steel structures	20
2.3.1. Crack growth detection and quantification in gusset plates	20
2.3.1.1. Crack detection	20
2.3.1.2. Damage quantification	35
2.3.2. Detection of fatigue cracking in steel bridge girders: a support vector machine approach	40
2.3.2.1. Numerical analysis of out-of-plane distortion-induced fatigue cracking	43
2.3.2.1.1. Geometry, loading and boundary conditions of the steel girder.....	43
2.3.2.1.2. Numerical model	44
2.3.2.1.2.1. Shell element-based FE model.....	44
2.3.2.1.2.2. Comparison between shell and 3D solid element-based FE model	49
2.3.2.1.2.3. Fatigue analysis of the steel girder	51
2.3.2.2. Information fusion.....	56
2.3.2.3. Damage detection using support vector machine approach.....	57
2.4. Summary	69
CHAPTER 3. DAMAGE IDENTIFICATION IN STRUCTURES USING NON- UNIFORM PFG SENSORS.....	71
3.1. Overview	71
3.2. Working mechanism of nonuniform PFG sensors	72
3.3. Evaluation of the performance of the nonuniform PFG sensor.....	73
3.3.1. Health monitoring of steel plates.....	73
3.3.1.1. Detection of damage progression using individual self-powered PFG sensors...	74
3.3.1.2. Data fusion in a network of PFG sensors.....	84
3.3.1.3. Uncertainty analysis	95
3.3.2. Pavements health monitoring	97
3.3.2.1. Damage growth detection in AC slabs	98

3.3.2.1.1. FE modeling and damage detection approach	99
3.3.2.1.1.1. Description of the FE model.....	99
3.3.2.1.1.2. FE results.....	106
3.3.2.1.1.3. Damage detection results based on FE model	108
3.3.2.1.2. Experimental investigation.....	113
3.3.2.1.2.1. Test setup.....	113
3.3.2.1.2.2. Damage detection based on experimental results	117
3.3.2.2. Surface sensing of bottom-up cracking in pavements.....	121
3.3.2.2.1. Finite element modeling of pavement structure subjected to a moving load.....	122
3.3.2.2.1.1. Dynamic analysis.....	125
3.3.2.2.1.2. Material characterization.....	127
3.3.2.2.1.3. Loading.....	128
3.3.2.2.1.4. Crack modeling.....	132
3.3.2.2.2. Sensors location	135
3.3.2.2.3. FE results	136
3.3.2.2.4. Proposed damage detection approach.....	140
3.3.2.2.5. Damage classification.....	148
3.3.2.2.5.1. Probabilistic neural network.....	148
3.3.2.2.5.2. Performance of the initial features.....	153
3.3.2.2.5.3. Sensor fusion model.....	156
3.3.2.2.5.4. Uncertainty analysis	164
3.4. Summary	166

CHAPTER 4. LOCAL-GLOBAL DAMAGE IDENTIFICATION APPROACH USING HYBRID NETWORK OF STRAIN AND ACCELERATION PFG SENSORS ... 170

4.1. Overview	170
4.2. Sensing mechanism	171
4.3. Numerical simulation of steel frames with bolted connections	172
4.3.1. Finite element description of the model	172
4.3.2. FE results	178
4.3.2.1. Bolt loosening effect on the mechanical response of the frame.....	178
4.3.2.2. Crack effect on the frame response.....	184
4.4. Energy harvesting from the frame structure.....	186
4.5. Damage detection results.....	193
4.5.1. Bolt loosening detection results.....	193
4.5.2. Crack detection results	200
4.6. Summary	204

CHAPTER 5. FIELD DEPLOYMENT OF THE SELF-POWERED PFG SENSOR: THE MACKINAC BRIDGE CASE STUDY 205

5.1. Overview	205
5.2. Experimental study of strain-sensors	206
5.2.1. Preliminary testing of the transducers	206
5.2.2. Analysis at low frequencies.....	211
5.2.3. Analysis at low temperatures.....	213
5.2.4. Wiring effect on the sensor response.....	215
5.3. Preliminary testing of the sensor: Mackinac Bridge	218

5.4. Final sensing system deployed in the Mackinac Bridge	228
5.5. Summary	235
CHAPTER 6. CONCLUSIONS.....	236
6.1. Research contributions	236
6.2. Conducted work	236
6.3. Future research	240
APPENDIX.....	242
BIBLIOGRAPHY.....	245

LIST OF TABLES

Table 2-1: Material properties, loading and dimensions.	24
Table 2-2: Preselected strain levels for the gusset plate.	27
Table 2-3: Preselected strain levels for the gusset plate.	40
Table 2-4: Geometry and material properties of the girder.	47
Table 2-5: Results of the numerical convergence analysis.	49
Table 2-6: Comparison between the shell and 3D FE models.	51
Table 3-1: Properties of PZT-5A.	75
Table 3-2: Preselected strain levels and gate injection rates considered for the analysis.	100
Table 3-3: Constant values, c_i , used in this study.	104
Table 3-4: PVDF dimensions and properties.	115
Table 3-5: Voltage threshold levels of each gate.	117
Table 3-6: Material properties.	127
Table 3-7: Damage scenarios.	134
Table 3-8: Preselected strain levels and gate injection rates considered for the analysis.	142
Table 3-9: Features selected by SFS and their corresponding detection rates.	160
Table 3-10: Features selected by SBS and their corresponding detection rates.	161
Table 3-11: Model sensitivity to sampling error.	164
Table 3-12: The damage detection performance for various noise levels using the optimal set of features.	165
Table 4-1: Geometry, material properties and loading conditions of the steel frame.	175
Table 4-2: Parameters and bolts pretension values.	177
Table 4-3: Variation of the peak acceleration between damage states.	180
Table 4-4: Peak acceleration for different torque levels.	182

Table 4-5: Properties of the bimorph PZT beam.	191
Table 4-6: Voltage threshold levels of each gate.	195
Table 5-1: Sensor voltage for PZT1.	209
Table 5-2: Sensor voltage for PZT2.	209
Table 5-3: Sensor voltage for PZT3.	210
Table 5-4: Sensor voltage for PZT2 at 0.4 Hz.	212
Table 5-5: Sensor voltage for PZT2 at 0.5 Hz.	212
Table 5-6: Sensor voltage for PZT2 at 20 °C.	214
Table 5-7: Sensor voltage for PZT2 at -20 °C.	214
Table 5-8: Sensor voltage threshold vs strain threshold for sensor 1 (1 st model).	216
Table 5-9: Sensor voltage threshold vs strain threshold for sensor 2 (2 nd model).	217
Table 5-10: Average readings values.	226
Table A-1: Prony series coefficients.	243
Table A-2: Piezoelectric properties.	244

LIST OF FIGURES

Figure 1-1: Prototype of the self-powered wireless sensing system.....	9
Figure 2-1: Working principle of the PFG technology.....	17
Figure 2-2: Level crossing cumulative time counting implemented by the PFG sensor.	19
Figure 2-3: Sensor output distribution (a) CDF fit, and (b) Transformed PDF.....	20
Figure 2-4: U10W gusset plate (Liao, 2009).	22
Figure 2-5: Detection of damage progression using a self-powered wireless sensor.	22
Figure 2-6: 3D perspective of the studied gusset plate with mesh details of the propagated crack.	24
Figure 2-7: (a) Loading conditions and (b) deformed configuration of the gusset plate with a propagated crack.	25
Figure 2-8: Locations of the distributed sensors and propagated crack.....	26
Figure 2-9: Change of the PDFs between damage states.....	28
Figure 2-10: Variation of the STD of (a) μ and (b) σ for sensors S214 to S220 and S242 to S248.	34
Figure 2-11: Damage localization algorithm.	36
Figure 2-12: (a) Results of step 1, (a) results of step 2.	37
Figure 2-13: Crack localization results.	38
Figure 2-14: Prediction of the crack length.	39
Figure 2-15: Schematic illustration of distortion-induced fatigue cracking: (a) bridge before deformation in a perspective view, (b) side view of the bridge in the initial stage, and (c) different types of fatigue cracks caused by out-of-plane distortion (Δ).	42
Figure 2-16: Selected steel structure: (a) technical drawings of the structure, including (a1) a perspective view (a2) an end view, (a3) a top view, and (a4) a side view, and (b) assembly of the structure in Abaqus with loading and boundary conditions.....	46
Figure 2-17: Mesh details: (a) Meshed structure, (b) S4R element.....	47
Figure 2-18: Maximum principal strain around the area stiffener to web connection.....	48

Figure 2-19: Variation of the maximum principal strain as a function of the element size.	48
Figure 2-20: 3D finite element model (a) Assembly and refined mesh portion, (b) maximum ...	50
Figure 2-21: Mesh around the crack tip.....	53
Figure 2-22: The FE results for (a) a=20 mm (maximum principal strain=2753 $\mu\epsilon$); (b) a=70 mm (maximum principal strain=3192 $\mu\epsilon$).	54
Figure 2-23: Number of cycles vs. crack length.	55
Figure 2-24: Locations of the sensing nodes.	55
Figure 2-25: Strain threshold levels.....	56
Figure 2-26: Data fusion flowchart.....	59
Figure 2-27: Schematic illustration of the optimal separating hyperplane and margins for SVM with samples from two classes.....	61
Figure 2-28: SVM performance on the testing data.....	66
Figure 2-29: Set of sensors with the highest detection rate.	67
Figure 2-30: Confusion matrixes for the best sensor configuration.	68
Figure 3-1: Working principle of nonuniform PFG sensor.	73
Figure 3-2: A schematic representation of test setup.....	75
Figure 3-3: Layout of PZTs and strain gages.....	76
Figure 3-4: A comparison of maximum voltage and strain for 0.16 mm displacement and 2 Hz loading frequency.....	77
Figure 3-5: Strain and voltage variation for: (a) PZT 4 and Strain Gage 4, and (b) PZT 7 and Strain Gage 7.....	78
Figure 3-6: The injection thresholds for the PFG sensor.....	79
Figure 3-7: Voltage changes across the floating-gates of the PFG sensor for location 4.....	81
Figure 3-8: Voltage changes across the floating-gates of the PFG sensor for location 7.....	82
Figure 3-9: Projection of the original voltage droppage data onto the first two principal components.	86
Figure 3-10: Projection of the featured data onto the first two principal components.	86

Figure 3-11: Optimization of the polynomial degree in the SVM algorithm.	88
Figure 3-12: Optimization of the box constraint parameter in the SVM algorithm.	89
Figure 3-13: Damage detection performance of the SVM models for different number of gates.	89
Figure 3-14: Confusion matrixes for the training data.	90
Figure 3-15: Confusion matrixes for the testing data.	92
Figure 3-16: Confusion matrixes for the validation data.	94
Figure 3-17: Performance of the SVM models for various noise levels.	96
Figure 3-18: Schematic of the notched asphalt concrete specimen under three-point bending test.	98
Figure 3-19: Flowchart of the proposed method.	99
Figure 3-20: Generalized Maxwell model consisting of n Maxwell elements connected in parallel.	102
Figure 3-21: Prony series fit to the relaxation modulus of the sigmoid function.	105
Figure 3-22: FE model mesh.	105
Figure 3-23: Strain distribution for different damage states.	107
Figure 3-24: Histograms representing the output of the sensor.	108
Figure 3-25: Strain changes across the floating-gates of the PFG sensor.	109
Figure 3-26: Percentage of strain droppage for different sensor gates.	111
Figure 3-27: (a) Three-point bending experimental setup, (b) notch at the initial stage, and (c) crack propagation phase.	114
Figure 3-28: Sensor packaging design to protect the piezoelectric and electronics.	115
Figure 3-29: LDT2-28K PVDF Sensor.	116
Figure 3-30: Voltage changes across the floating-gates of the sensor.	118
Figure 3-31: Percentage of voltage droppage for different gates.	120
Figure 3-32: (a) The 3D FE model of the pavement structure, (b) Meshed cross section of the AC layer.	124
Figure 3-33: Structure of CIN3D8 element.	125

Figure 3-34: Tire contact area.....	129
Figure 3-35: Approximated rectangular loading.....	130
Figure 3-36: Loaded strip of the AC pavement section.....	131
Figure 3-37: (a) Cross section of the damage (b) Crack zone and measurement location.	135
Figure 3-38: Sensors locations.....	136
Figure 3-39: Strain history of sensor S1 for different damage states.	137
Figure 3-40: Strain history of sensor S2 for different damage states.	138
Figure 3-41: Strain history of sensor S17 for different damage states.	138
Figure 3-42: Zooming around the peak values of sensor S18.	139
Figure 3-43: Variation of the Maximum principal strain with the damage state.....	140
Figure 3-44: Strain change across sensor S1 gates.	143
Figure 3-45: GMM fit to the sensor data.	145
Figure 3-46: GMM distributions for different sensors.	146
Figure 3-47: A typical architecture of PNN.....	152
Figure 3-48: Accuracy versus smoothing parameter for the validation set.	155
Figure 3-49: Projection of the featured data onto the first two principal components.	155
Figure 3-50: Data fusion model.....	156
Figure 3-51: Confusion matrixes for the best features selected by the exhaustive search method.	162
Figure 3-52: Accuracy versus smoothing parameter for the validation set using the exhaustive search method.	163
Figure 3-53: Distribution of the optimal set patterns.....	164
Figure 3-54: Damage detection accuracy for different noise levels.	166
Figure 4-1: Sensing mechanism.....	171
Figure 4-2: Mesh details of the steel frame.	173
Figure 4-3: Bolt displacement response of the steel frame.....	177

Figure 4-4: Sensing locations.....	178
Figure 4-5: (a) 1 st floor displacement vs. time, (b) 2 nd floor acceleration vs. time, (c) 3 rd floor acceleration vs. time, and (d) 4 th floor acceleration vs. time.	179
Figure 4-6: Percentage variations of the peak acceleration between damage states.....	181
Figure 4-7: Variation of the acceleration at a node located close to the bolt connection of the second floor as a function time for different torque levels.	181
Figure 4-8: Percentage variation of the acceleration vs damage growth.	182
Figure 4-9: Variation of the strain between damage states, (a) first floor, (b) second floor, (c) third floor and (d) fourth floor.	183
Figure 4-10: Percentage variation of the peak strain between damage states.....	184
Figure 4-11: Crack location.	185
Figure 4-12: Variation of (a) strain and (b) acceleration behavior due to cracking and bolt loosening.	186
Figure 4-13: Schematic description of the cantilever piezoelectric beam.	187
Figure 4-14: Voltage outputted by the bimorph PZT beam on the second floor.....	192
Figure 4-15: Voltage outputted by the strain transducer disc on the third floor.....	192
Figure 4-16: Sensor output histogram for different damage states for: (a) Second floor, (b) Third floor, (c) Fourth floor.....	194
Figure 4-17: The GMM fit to the sensor data on the third floor for the intact structure.	197
Figure 4-18: GMM fit to the sensor data at all sensing locations and for the Healthy, D1bo and D2bo damage states at (a) second floor, (b) third floor, and (c) fourth floor.	198
Figure 4-19: STDs of sensor groups: I (μ_1), II (μ_2), and III (σ_{22}) with respect to the scenarios of (a) sensing nodes 2 and 3 (G1) (b) sensing nodes 3 and 4 (G2), (c) sensing nodes 2 and 4 (G3), and (d) sensing nodes 2, 3 and 4 (G4).	199
Figure 4-20: Sensor output histogram of different damage states for: (a) Second floor, (b) Third floor, and (c) Fourth floor.	201
Figure 4-21: GMM fit to the sensor data at all sensing locations and for the Healthy and CR damage states at (a) second floor, (b) third floor, and (c) fourth floor.	202
Figure 4-22: STDS of sensor groups: I (1), II (G2), III (G3), and IV (G4) for (a) μ_1 and (b) μ_2	203

Figure 5-1: Piezo discs mounted on the aluminum beam.	207
Figure 5-2: Test setup.	207
Figure 5-3: Sensor voltage vs strain.....	208
Figure 5-4: Sensor voltage vs strain for 0.4 and 0.5 Hz.	211
Figure 5-5: Sensor voltage vs strain at 20 °C and -20 °C.....	213
Figure 5-6: Sensor wiring, (a) 1 st model, (b) 2 nd model.....	216
Figure 5-7: Photo of the Mackinac Bridge (Mackinac Bridge Authority, 2018).....	221
Figure 5-8: PFG board (Aono et al., 2018).....	221
Figure 5-9: Preliminary sensor box.....	222
Figure 5-10: September Readings.....	223
Figure 5-11: November Readings.....	224
Figure 5-12: Readings of: (a) Sensors 1, (b) Sensor 3.....	227
Figure 5-13: GMM fit to: (a) Sensor 1, (b) Sensor 3 data.	228
Figure 5-14: New box.	229
Figure 5-15: Sensor installation.....	229
Figure 5-16: Readings.....	230
Figure 5-17: Analog-to-digital converter output as a function of temperature (nominally ~1 kHz at 20 °C) (Aono et al., 2018).....	234
Figure 5-18: Results showing ADC output as function of voltage (i.e. floating gate charge) (Aono et al., 2018).	234

CHAPTER 1. INTRODUCTION

The presented work in this thesis builds upon the novel idea of monitoring civil infrastructures using a newly developed sensor that is self-powered from the signals being sensed (Lajnef et al., 2013; Chakrabarty et al., 2011; Alavi et al., 2016a,b,c,d). The development of data interpretation models for non-uniform sensors and the deployment of the sensor in a real-field structure constitute the major contributions of this thesis.

1.1. Motivation and vision

The field of structural health monitoring (SHM) is of great interest because of its capabilities to provide cost effective and reliable solutions for condition assessment and damage detection in civil infrastructures. The objective of SHM is to provide a monitoring system that alerts bridge owners and engineers about potential damages and prepare maintenance plans at early stages.

Over the last decades, different sensors have been developed to monitor the health status of structures and estimate the remaining life. Deployment of wireless sensors networks in structures allows the detection of changes in the structure response resulting from cracking events or changes in the boundary conditions of the structure. However, there are still major issues that need further development in order to achieve full potential of SHM. Nearly all of the commercial viable wireless sensors require an external power supply (either batteries or solar power). In addition, among the most serious challenges that hampered the practical application of the field of SHM for damage detection in civil infrastructures is the infeasibility of using a large network of sensors (such as strain gages and accelerometers) to provide a high spatial resolution. In fact, a high-enough spatial resolution is essential to detect small cracks that cause

the initiation of damage and could represent the precursors of structural failure.

The sensing technology presented in this work offers several novel features, which are not available in other classical SHM methods including:

- ***Low power requirement:*** The sensor operates in the Nano-watts scale (80 nW power consumption for the latest prototype).
- ***Self-powered continuous sensing:*** These sensors do not need an external power supply, and they operate using the signal being sensed. In fact, the device uses the energy harvested by a piezoelectric transducer for both powering and sensing damage in structures.
- ***Possibility of deployment in dense networks:*** The small size of sensors and the fact that they do not rely on batteries offer the possibility of installing a large number of sensors around the damage sensitive areas.
- ***Autonomous computation and non-volatile storage of sensing variables:*** The data could be stored on board the sensor and retrieved without the need of an external power to activate the system.
- ***Wireless communication:*** The sensor can be integrated with radio frequency identification (RFID) to collect the data stored on board the device.

In order to achieve all the described capabilities, the data is compressed on board the sensor in the form of a histogram of cumulative loading events. Therefore, there would be a considerable loss of information, which results in notable difficulties in interpreting the data generated by the sensor. In addition, due to manufacturing mismatches, the sensors present several behavior variabilities. Due to these variations, two types of analysis assumptions are referred to as uniform and nonuniform piezo-floating-gate (PFG) sensors. Alavi et al. (2016a,b,c,d) have developed a

data interpretation framework for the case of uniform sensors.

This research proposes innovative data interpretation techniques for damage detection, localization and quantification in civil infrastructures using the cost effective and reliable technology. Advanced data interpretation techniques are developed to identify damage in structures based on the limited information provided by the sensor. The proposed work significantly contributes in the efforts to advance the self-powered sensors technology toward an integrated implementable in the context of future Smart Cities.

1.2. Background and state of knowledge

In general, the term ‘damage’ can be defined as the deviation and change of the system’s current and future performance with respect to an established reference. The damage can occur due to changes of the material’s geometrical properties or change in the boundary conditions of a system. It usually grows progressively in structures until it reaches the point that heavily affects the system functionality and performance. This is the so-called ‘failure’ (Farrar and Worden, 2007). Structural health monitoring is the process of implementing a damage identification strategy for civil, mechanical, and aerospace engineering structures. Damage identification technologies have been drawing great research and practical interests for SHM in recent years. Damage identification can be categorized into five related disciplines:

- SHM
- Non-destructive testing and evaluation (NDT&E)
- Condition monitoring (CM)
- Statistical process control (SPC)
- Damage prognosis (DP)

SHM is usually associated with online-global damage identification in structures. The main objective of SHM is to evaluate the long-term sustainability and detect potential damages at early stages. SHM can be categorized into questions in the following five aspects (Maia et al., 2011):

- Detection – Do damages exist?
- Localization – Where are the damages located in the structure?
- Quantification – How severe are the damages effects on the sustainability of a structure?
- Classification – What type of damages? and
- Prediction – How long will the structure remains functional?

To sufficiently answer these questions, a variety of sensing techniques and mechanisms has been developed. SHM methods are generally divided into global and local methods. Global health monitoring methods are used to determine whether the damage is present in the structure. They do not give information of the damage severity and location. Most of these global damage assessment methods rely on finding shifts in the resonant frequencies of a system or on detecting changes in the structural mode shapes. The change of the structure dynamic characteristics indicates that the deviation of the structure response is due to damage. However, other factors, such as, temperature, moisture, and other environmental conditions may affect the interpretation of the results. Therefore, in order for this technique to work, the effect of other factors must be significantly smaller than the damage effect on the structural response (Chang et al., 2003). In addition, due to the low sensitivity of the system's natural frequencies, high levels of damage and high measurement accuracy are essential to detect the damage.

On the other hand, non-destructive evaluation (NDE) methods are used to find the damage. These methods are classified as local health monitoring techniques and can be used to assess structural conditions without removing the individual structural components. Pressure cell,

deflectometer, fiber-optic sensors, strain gages, etc, are examples of commonly used devices for NDE.

Many sensing techniques and mechanisms have been developed to monitor civil infrastructures, e.g., vibration-based sensing, vision-based sensing, sensing skin techniques, and various wireless sensing devices. Vibration-based damage assessment is one of the most widely used technique in SHM. The main classes of the vibration-based technique are the signal and model-based techniques. The signal-based methods are based on defining damage indices by comparing the response of the structure before and after damage occurrence. Model-based techniques require accurate computational model, which is usually achieved through model-updating technique to improve the quality of the final model to be used for damage detection. This technique is computationally expensive and often includes too many parameters.

Zou et al. showed that the vibration-based model-dependent methods provide local-global information about the structure health conditions and they are cost-effective (Zou et al., 2000). Signal-based approaches have been developed. Lee et al. developed a neural networks-based method to detect the damage in structures (Lee et al., 2005). In their study, they have used the mode shape differences or the mode shape ratios between damage states as an input for the neural networks (NN) to reduce the finite element (FE) modeling errors. More recently, Li and Hao investigated the joint conditions of steel truss bridges using relative displacement sensors (Li and Hao, 2016). The authors carried out a signal processing technique to identify damages caused by loosening of bolts based on a time-frequency analysis.

Vision-based sensing technology has received more attention from the SHM community. Fukuda et al. developed a vision-based displacement system for real-time monitoring of the dynamic response of large scale structures with low natural frequencies (Fukuda et al., 2010). The

efficacy of their method was validated on a frame model under seismic loading. Yeum and Dyke developed a vision-based visual inspection technique by processing and analyzing huge amount of collected images (Yeum and Dyke, 2015). The authors used the technique to capture and identify structural damages without controlling angles and positions of the cameras. Shahidi et al. presented two image-based compressive sensing approaches to detect and localize multiple structural damages (Shahidi et al., 2016). Dynamic vision sensors were also developed to detect damage using full-field, high spatial resolution mode shape extracted from videos of the operating structures (Yang et al., 2017; Roeder et al., 2017). The authors conducted spatial fractal dimension analysis on the full-field mode shape of damaged structures to detect damage-induced irregularity. Arguably, vision-based sensing technology is essentially based on processing and analyzing huge amount of collected images captured by cameras. The issue of dealing with large data size is more severe when considering the number of pixels that must be processed and analyze, especially for the images with relatively high resolution.

In recent years, sensing skin techniques, e.g., graphene, carbon nanotubes (CNTs), etc., have been deployed for damage detection. Studies indicated that these materials possess excellent electrical conductivity and piezoresistivity with multifunctional capability (Raghavan et al., 2009). Loh et al. proposed a CNT polyelectrolyte skin to monitor strain and impact damage over spatial areas (Loh et al., 2009). Saafi used CNT sensors to detect damage progression in concrete structures by measuring the electrical resistance of carbon nanotubes (Saafi, 2009). Zha et al. developed strain sensors for damage monitoring using functionalized graphene nanoplates (Zha et al., 2016).

Recent development in SHM was focused on the utilization of new sensing technologies. Wireless sensors are widely used as alternatives to the traditional wired sensors for SHM (Lynch

and Loh, 2006). Chen et al. developed a compact wireless ultrasonic device for localized damage detection (Chen et al., 2016). The authors proposed a signal processing procedure to find key indicators that can be used for crack identification. The damage identification method was validated for a notch and fatigue tests of a dog-bone specimen. Kurata et al. studied the performance of a wireless smart sensor based on the ‘Berkeley Mote’ platform (MICA and MICA2) (Kurata et al., 2004). The performance of their system was investigated on a two-story structure under an earthquake excitation. The results demonstrated that MICA2 was able to measure the response wirelessly with minimal data loss and detected damage. Cho et al. presented an approach for system identification using wireless sensors (Cho et al., 2015). The proposed system was evaluated on a historic swing bridge. A sensor orientation correction technique was introduced to improve the accuracy of the system in identifying the modal parameters. Lynch et al. designed a proof of concept wireless sensing unit for SHM (Lynch et al., 2001). The prototype sensing system acquired data and transmitted directly to the base station over a single hop.

While the development of wireless technology has eliminated the need of performing the arduous task of stringing lots of connecting cables on extended structures such as bridges, there is still the challenge of ensuring an adequate energy source to power the sensor network for long-term, autonomous, and continuous monitoring. Embedment and long-term operational requirements preclude the use of batteries, whereas the small volume of the sensor severely limits the energy storage capacity of energy harvesting devices. On the other hand, the prohibitive cost and maintenance of solar panels seems to be another drawback of conventional SHM wireless sensors. A viable solution to this power dilemma is to harvest energy from the ambient excitations (Sirohi and Chopra, 2000; Borchani et al., 2016). In this context,

piezoelectric transducers are widely used to convert environmental mechanical energy into an electrical energy (Elvin et al., 2003; Lajnef et al., 2011). In general, piezo-based self-powering can be categorized as: 1) harvesting electrical energy from the signals that are different from the signal being monitored, or: 2) from the signal being monitored (Huang et al., 2010). Nearly all the existing energy harvesting studies were focused on the first approach (Alippi and Galperti, 2008; Yen and Lang, 2006). Based on the second approach, a new class of PFG self-powered sensor has been recently developed and tested at Michigan State University (MSU) (Lajnef et al., 2013; Chakrabarty et al., 2011; Alavi et al., 2016a,b,c). A prototype of the sensor is shown in Figure 1-1. This type of sensor uses piezoelectric transducers to empower an array of ultra-low power floating gate computational circuits. The PFG sensor has a series of memory cells, referred as memory gates or channels, that cumulatively store the duration of strain/voltage events when the amplitude of the input signal, coming from the piezoelectric material, exceeds different thresholds. In addition, the sensor acts as a non-volatile memory for data storage, which optimizes the need of the sensor for power. The data could be retrieved offline without the need to power the sensor. An RFID scanner can be used to periodically read the data stored on-board the sensor (Lajnef et al., 2011; Lajnef et al., 2013; Alavi et al., 2016a,b,c).

One of the main advantages of this sensing system is the fact that it is “response-based”. All the effects due to variations in load location, load magnitude, traffic wander, environmental effects such as temperature and moisture, material aging and degradation are aggregated in the strain response recorded by the sensor over time. This feature makes the sensor suitable for long-term SHM. Most of the other existing solutions evaluate the conditions of the system at a given instant. These methods present only a snapshot at the time where the measurements are taken. Thus, the obtained results are highly influenced by the environmental conditions. Since the

developed PFG sensor records each and every event at all time, it will aggregate all these short-term fluctuations. Thus, if long-term shifts are observed in the results, they are most probably correlated with condition degradation. Illustrative examples of the level crossing cumulative time counting implemented by the sensor gates can be found in (Alavi et al., 2016a,b). Despite several advantages offered by this self-powered sensing technology, the interpretation of the compressed data generated by such system is a challenging task.

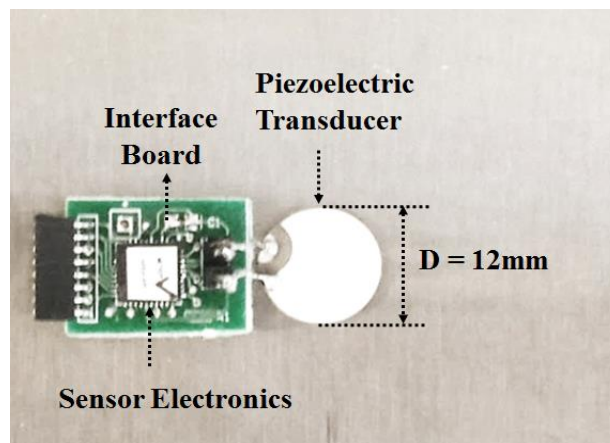


Figure 1-1: Prototype of the self-powered wireless sensing system.

The information that can be extracted from the sensor gates is compressed as a function of the cumulative loading at each memory gate. Therefore, there is a considerable loss of information about the strain distribution.

On the other hand, there are two types of PFG sensors: uniform and nonuniform PFG sensors. The difference between these two classes is in the form of data outputted from the sensors. The task of interpreting the sensor output becomes more challenging for the case of nonuniform distributions. Previous studies were focused on detecting damage by comparing the responses from a single loading cycle and did not take into account the number of cycles to failure, which is crucial in the case of fatigue failure (Alavi et al., 2016a,b,c,d). Moreover, the interpretation

and robustness of the data of nonuniform sensors are yet to be studied. Accordingly, this research aims to develop a robust damage detection methodology and an innovative data interpretation technique for both type of PFG sensors, with more focus on the nonuniform type. In addition, one the main goals of this research is to implement a network of PFG sensors in real-life structure to test their performance under real operating conditions.

1.3. Research hypothesis and objectives

1.3.1. Hypothesis

The main hypothesis behind this research is that the compressed data on board the sensor is reliable in detecting, localizing, and quantifying damages in civil infrastructures. The detection accuracy can be enhanced by fusing the information from a network of PFG sensors and by using artificial intelligence (AI) approaches.

1.3.2. Objectives

The objective of this research is to develop a robust self-powered sensing mechanism to detect damage in civil infrastructures. The proposed SHM system uses the energy harvested by a piezoelectric transducer for both powering the sensor and monitoring the health status of structures. In other words, the operating power of the sensor is harvested directly from the signal being sensed.

This work is divided into two major parts. In the first part, the performance of the sensor is evaluated for both the uniform and nonuniform classes of sensors. Numerical simulations are performed to obtain the structural response and to simulate the sensor output. Strains and accelerations are extracted from FE simulations to calculate the sensor output at different sensing

nodes. To validate the efficiency of the proposed damage detection approach, experiments are conducted on samples with different construction materials. Piezoelectric strain transducers and vibration-based harvesters are used to convert the applied mechanical energy into an electric signal. For each sensor type, data interpretation algorithms were proposed to characterize the sensor output and to identify damage. Furthermore, an algorithm is developed to detect, localize and quantify damage progression in structures.

The second part is focused on the implementation of the sensor on real life structures. The case of the Mackinac bridge in Michigan is studied. In this work, experimental study is performed to select the right type of piezoelectric transducers, to study the effect temperature on the harvester, and to investigate the wiring effect on the sensor response. The temperature effect on the wireless reading is also investigated.

1.4. Outline

This dissertation is organized as follows: Chapter 2 deals with the development of a damage identification technique using the uniform class of sensors. In this chapter, the uniform PFG sensor data is characterized using a cumulative density function (CDF). The performance of the sensor is evaluated for two different structures with complex behavior. The first study is focused on damage quantification in gusset plates using strain-sensors to detect multi-state crack propagation. In this dissertation, multi-state or multi-class damage refer to damage progression in the studied structures. A structure similar to the U10W gusset plate of the I-35W Highway Bridge in Minneapolis, MN, USA, is chosen for the analysis. 3D FE models are developed to simulate the behavior of the structure under loading. An algorithm is proposed to localize and quantify the crack in the gusset plate. Thereafter, a fatigue analysis of steel bridge girder is studied to identify crack propagation in steel bridge girders caused by out-of-plane distortions.

Extensive finite element analyses are performed to obtain the structural response of the girder under fatigue loading. A data fusion model is proposed to increase the damage detection efficiency. The data fusion model incorporates the group effect of a sensors network based on the average and standard deviation (STD) of a group of sensors. An AI approach is used to evaluate the condition of the girder under different damage scenarios. Each damage state (or damage class) is defined based on the damage length.

In Chapter 3, the case of nonuniform sensors is investigated for both steel and pavement structures. Three structures are studied: Steel plate, Asphalt concrete (AC) beam, and Pavement structure. For the steel plate case, a wireless sensors network (WSN) is placed on the surface of the plate to detect the predefined damage states. Features are extracted from the sensor output and fused to improve the damage detection accuracy. A support vector machine approach (SVM) is applied to the featured data to separate damage classes. Furthermore, an uncertainty analysis is carried out to verify the performance of the SHM model under different noise levels. For the second case study, an AC beam under three-point bending configuration is studied. FE simulations and experiments are conducted to verify the damage detection method. An H-shape packaging system is designed and tested to protect the sensor electronics embedded inside the asphalt. Based on the response of the nonuniform sensor, damage indicator features are defined to identify bottom-up cracking in AC pavements. However, a major limitation of embedding the sensor inside AC pavement layer is that the device could be damaged due to excessive stresses at the bottom of the AC layer and their replacement might be expensive. In addition, new pavement construction projects are negligible when compared to the extent of the existing pavement network. It is thus more critical for State Highway Agencies (SHAs) to adopt monitoring techniques that can be adapted to existing pavements. On this basis, the third case study of

Chapter 3 outlines the development details of a self-powered surface sensing approach for pavement health monitoring. A realistic FE model is developed to obtain the behavior the pavement under dynamic moving load. The sensor output is generated for each predefined damage state. Each damage state is defined based on the reduction of the AC modulus and the damage height. Thereafter, a data fitting model is proposed to characterize the sensor response and to define surface indicators of progression of bottom-up cracking in pavements. A detailed sensor fusion model, feature selection algorithm, and AI approach are presented. Probabilistic neural network (PNN) classifier is used to identify damage classes in pavements, and noise verification phase is also presented to verify the robustness of the proposed method under different noise levels.

The limitation of the proposed sensing mechanism presented in chapters 2 and 3 is that they are only useful for identifying local damage using strain-sensors. Therefore, the main goal of Chapter 4 is to develop a local-global damage detection method by combining strain and acceleration PFG sensors. A steel frame under base acceleration is studied. Local damage is defined by cracking the structural members of the frame and global damage is defined by loosening the bolts that are connecting the columns to the beams. Both numerical and theoretical studies are developed to calculate the sensor data. The acceleration time-history of each sensing node is converted into voltage using a Lead Zirconate Titanate (PZT) cantilever bimorph beam. The voltage harvested from the acceleration is more sensitive to global damage rather than local cracks. Strain Transducers are used to detect cracks in the frame. The damage location is also assessed using a sensor fusion model.

Chapter 5 presents the details of a deployment study of the sensor in the Mackinac Bridge in Michigan. Strain-transducers are prepared for installation, and the effect of temperature and

season variability is also addressed in this chapter. Experiments are conducted to estimate the strain threshold level of different PZT transducers to activate the sensors. A detailed procedure of the installation of the sensors on the Mackinac Bridge is presented and the performance of the PFG sensor is reported in this chapter.

Chapter 6 summarizes the performed work in this research, presents the main findings, and proposes future research directions.

CHAPTER 2. DAMAGE IDENTIFICATION AND QUANTIFICATION IN STRUCTURES USING UNIFORM PFG SENSORS¹

2.1. Overview

This chapter presents damage detection and quantification approaches in civil engineering infrastructures using uniform strain PFG sensor. In section 2.2, the working principle of the uniform sensor is presented. Section 3.3 deals with the development of a data interpretation system for damage identification in steel structures. Two different structures with complex behavior are studied. The case of the U10W gusset plate of the I-35W Bridge in Minneapolis, MN, USA and fatigue cracking of steel bridge girders are investigated. The cracking of the gusset plate is numerically investigated using the extended finite element method (XFEM). Six damage states are defined based on the crack length. A network of sensors is placed at the surface of the plate to detect the damage. Features extracted from the sensors distributions are used to define damage indicator features. A sensor fusion scheme is developed to detect, localize and quantify cracks in the gusset plate.

For the girder, extensive finite element simulations are carried out to obtain the structural response of an existing highway steel bridge girder (I-96/M-52) in Webberville, Michigan, USA. Different damage states are defined by extending the lengths of the crack at the web gap from 10 mm to 100 mm. Damage indicator features are extracted at different data acquisition nodes based on the sensor output data. Subsequently, an SVM classifier is developed to fuse the clustered features and identify multiple damage states.

¹ The presented results in this chapter were published in Hasni et al. (2017a,b; 2018a).

2.2. Working principles of the uniform PFG sensor

It is known that piezoelectric materials can convert mechanical applied loading into an electrical charge, using the direct piezoelectricity effect. The open source voltage (V) generated across the piezoelectric PZT ceramic transducer is given by the following equation (Lajnef et al., 2011):

$$V = \frac{S Y d_{31} h}{\varepsilon} \quad (2-1)$$

where S, Y, d_{31}, h and ε , are the applied strain, Young's modulus of the piezoelectric material, piezoelectric constant, thickness, and the electrical permittivity, respectively. The generated energy E_n from a piezoelectric transducer across a load resistance (R) is given by the following equation:

$$E_n = \int_0^{t_f} \frac{V(t)^2}{R} dt \quad (2-2)$$

where t_f is the loading time. In the proposed self-powered PFG sensor, the piezoelectric transducer converts the mechanical energy into high-energy electrons variation (hot electrons). Depending on the frequency and amplitude of the applied load, the kinetic energy of the electrons varies. If the energy of electrons exceeds the energy barrier of the silicon, which is 3.2 eV, the electrons surpass the barrier and get injected into the floating-gate (Huang et al., 2010; Borchani et al., 2016; Chakrabartty et al., 2013). Figure 2-1 illustrates the working principle of the PFG technology.

For a periodic excitation of the piezoelectric transducer, more electrons are injected into the floating-gate. After the electrons have been injected into the floating-gate, they remain trapped for a long period of time due to the high oxide electrical insulation of the gate. The duration and

extent of the mechanical disturbance can be then evaluated by measuring the total amount of charge on the floating gate (Borchani et al., 2016). It has been shown that the sensor can operate at pico-watt ($10^{-12} - 10^{-9}$ W) power dissipation levels (Borchani et al., 2016).

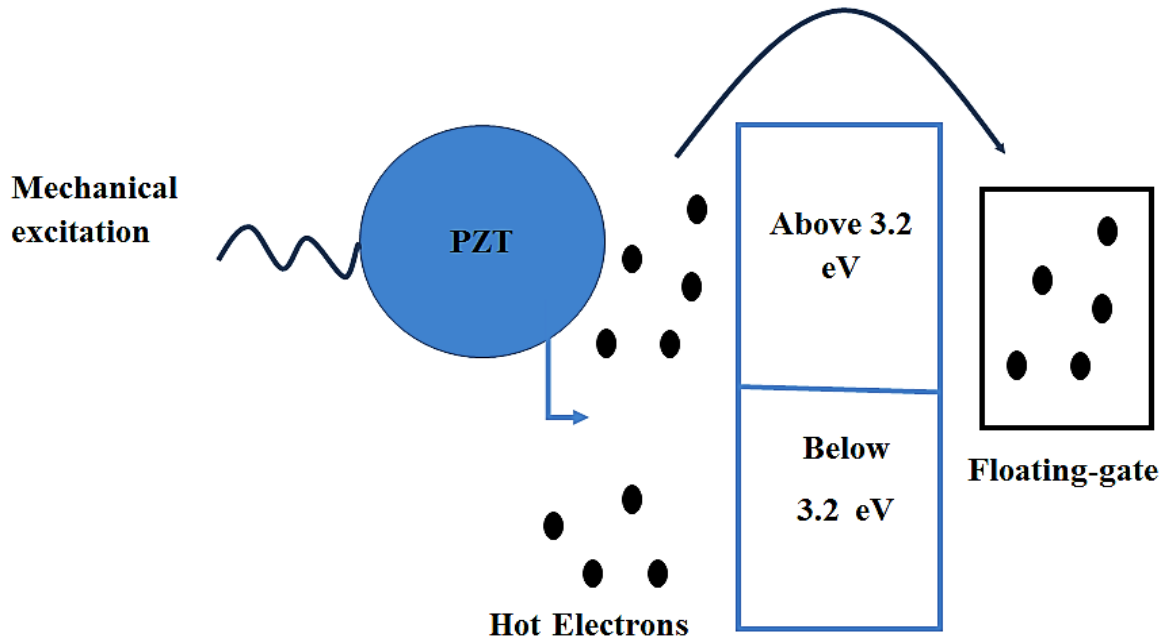


Figure 2-1: Working principle of the PFG technology.

In a recent study, the PFG sensor was used to monitor the post-operative bone healing (Borchani et al., 2016). Under fatigue loading, the sensor was able to record the variation of the strain energy during the healing process. Therefore, the PFG sensor can monitor short loading events as well as fatigue loading events.

Moreover, the beauty of the floating-gate is that it acts as a non-volatile memory for data storage. Thus, data can be stored on-board the sensor and retrieved without a need for an external power source to activate the sensor (Borchani et al., 2016). Each memory gate of this technology has two fundamental properties: activation threshold, and injection rate. The voltage injection rate could be defined as the droppage of voltage in one second. The total droppage of voltage (ΔV) in

a memory gate i can be expressed as follows:

$$\Delta V_i = V_0 - V_{sensor}^i = V_{inj_i} \sum_j \Delta t_j^i \quad (2-3)$$

where,

V_0 : Initial voltage of all the sensor gates, usually set to 1.2 V

V_{sensor}^i : Voltage across memory gate i after applying a number of loading cycles

V_{inj_i} : Voltage droppage rate of memory gate i

$\sum_j \Delta t_j^i$: Cumulative injection time of gate i

Δt_i can be calculated based on the threshold level of each memory gate and the applied loading. Evidently, the sensor output is a function of the gate threshold level, the amplitude of the signal, the V_{inj_i} and V_0 of each gate. According to the relationship voltage to strain for a piezoelectric material (Equation (2-1)), the output of the sensor could be also characterized as a function of the strain. The level crossing cumulative time counting implemented by the proposed uniform PFG sensor is schematically presented in Figure 2-2. The main information that can be extracted from the sensor is the cumulative duration of strain/voltage events. As it seen in this figure, the sensor output is presented in the form of a histogram. For uniform PFG sensors, the V_{inj_i} is constant for all the gates. Therefore, the sensor histograms are proportional to the cumulative time durations as shown in Figure 2-2. In this chapter, the analysis is based on the strain behavior extracted from the finite element models.

Based on previous studies (Hasni et al., 2017a,b; 2018; Alavi et al., 2016a,b,c), the sensor output can be expressed by the following Gaussian Cumulative Density Function:

$$CDF_{Gaussian}(g) = \frac{\alpha}{2} \left[1 - \operatorname{erf} \left(\frac{g - \mu}{\sigma \sqrt{2}} \right) \right] \quad (2-4)$$

in which μ , σ , α and g refer to the mean of the strain distribution, standard deviation with respect to load and frequency, the total cumulative time of the applied strain measured by the entire gates, and the gate number, respectively.

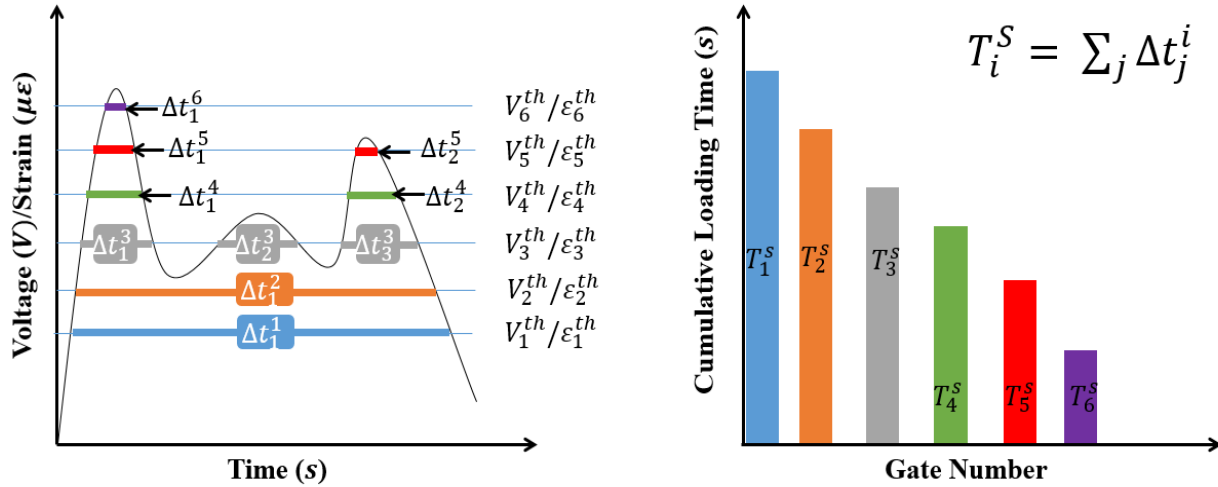


Figure 2-2: Level crossing cumulative time counting implemented by the PFG sensor.

For a better representation, the CDF can be transformed to a Probability Density Function (PDF) as follows:

$$PDF(g) = \frac{1}{\sigma \sqrt{2\pi}} e^{-\frac{(g-\mu)^2}{2\sigma^2}} \quad (2-5)$$

This probability density function is characterized by two parameters, the mean and the standard deviation. The advantage of this fitting method is that the damage can be characterized by the PDF parameters. Figure 2-3 displays the transformation from CDF to PDF.

In previous studies, it was shown that the PDF parameters changes with damage progression in the structure. This means that the damage can be measured based on the relative variation of the strain distribution with respect to damage propagation in the structure. Alavi et al. (Alavi et al., 2016c) show that the PDFs shift to the left and expand at the crack tip of a damaged steel plate.

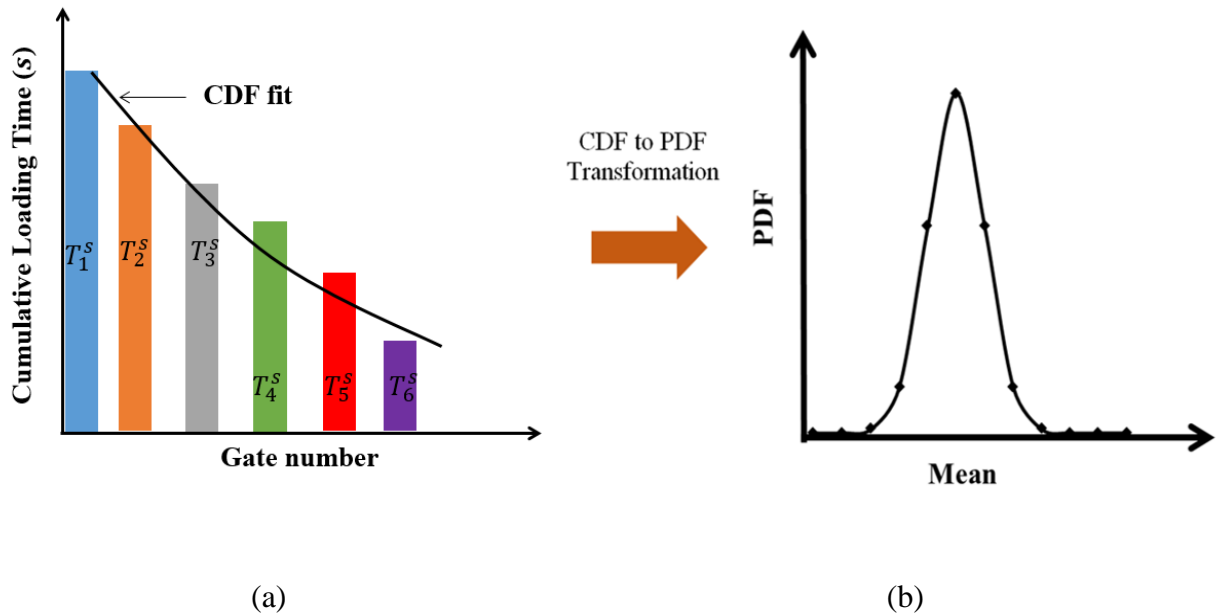


Figure 2-3: Sensor output distribution (a) CDF fit, and (b) Transformed PDF.

2.3. Health monitoring of steel structures

As mentioned before, the objective of this section is to evaluate the performance of uniform PFG sensors in structures with complex geometry. Crack propagation in gusset plates and fatigue cracking in steel bridge girders are investigated.

2.3.1. Crack growth detection and quantification in gusset plates

2.3.1.1. Crack detection

On August 1, 2007, the I-35W Highway Bridge over the Mississippi river in Minneapolis collapsed. This bridge was 1,907 feet long. According to the center for transportation studies (CTS), 111 vehicles were present on the bridge at the time of the collapse. This tragic event resulted on 13 deaths and 145 injuries. This failure was the focus of many studies. An investigation conducted by the national safety board (NTSB) concluded that the collapse was

mainly caused by the mechanical conditions of the U10W gusset plate at the time of the collapse. The CTS found that the U10W gusset plate did not have an appropriate thickness to remain in the elastic range under the traffic loading and the dead load of the structure. In fact, a portion of U10W gusset plate yielded due to the insufficiency of strength. A picture of the U10W gusset plate is displayed in Figure 2-4.

In this section, a structure similar to the U10W gusset plate of the I-35W Bridge is studied to evaluate the performance of the PFG sensor in quantifying damages in gusset plates. Figure 2-5 schematically illustrates the application of the proposed approach to detect damage progression in a bridge. As seen, the sensors are distributed over a part of the structure. Based on the relative variation in the strain response which is represented by PDFs, the condition of the structure can be assessed. The impact of damage can be detected by tracking the shifts of PDFs over time, rather than measuring the damage directly.

The material properties and dimensions of the studied gusset plate are shown in Table 2-1. A finite element model is built under Abaqus/CAE to predict the behavior of the structure, as shown in Figure 2-6. Static analysis is selected and cyclic loading is applied to the gusset plate. The model consists of 50000 C3D4 elements.



Figure 2-4: U10W gusset plate (Liao, 2009).

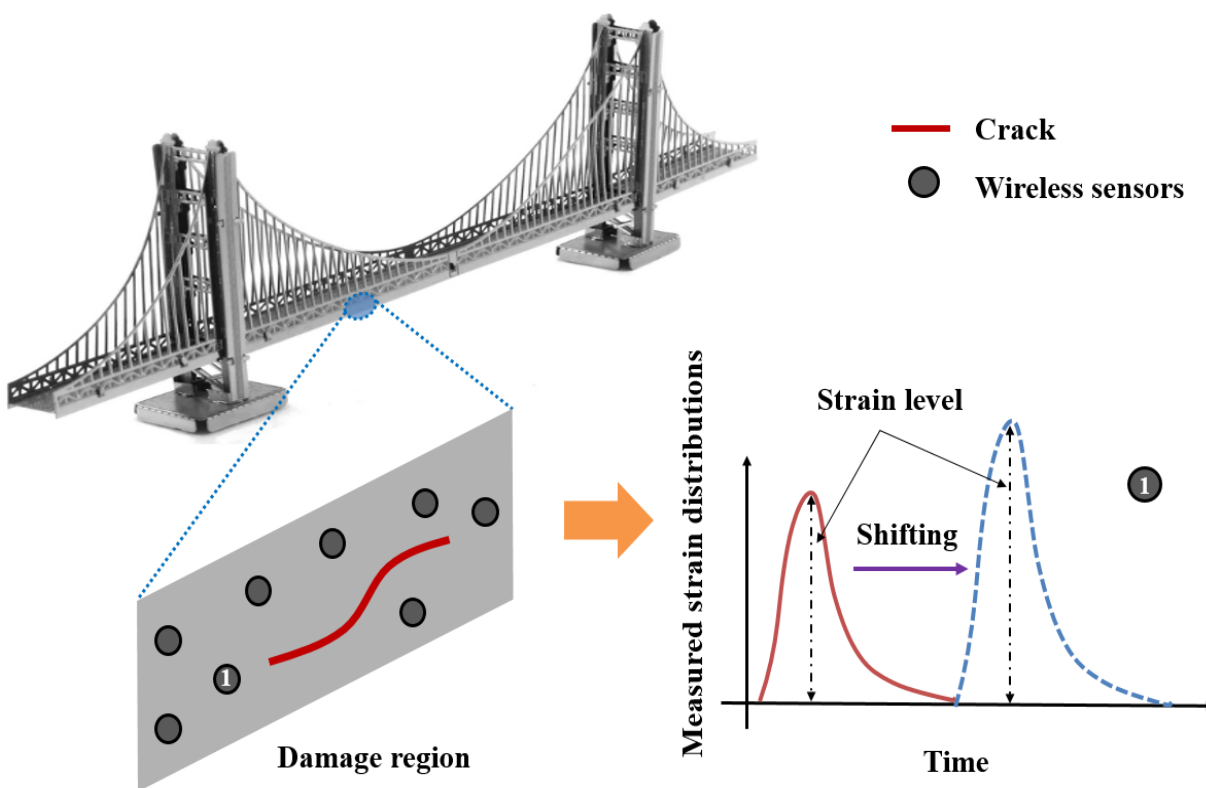


Figure 2-5: Detection of damage progression using a self-powered wireless sensor.

Damage is defined by introducing a crack at the middle of the plate. Six damage states are defined based on the crack length (a) as follows:

- D0: $a = 0$ mm (Healthy plate)

- D1: $a = 10$ mm
- D2: $a = 130$ mm
- D3: $a = 250$ mm
- D4: $a = 370$ mm
- D5: $a = 490$ mm

The direction of the propagation of the crack is estimated using the extended finite element method in Abaqus. This method allows modeling and the simulation of progressive 3-D arbitrary crack growth. Three steps are required to perform a crack propagation analysis: crack initiation, crack propagation and failure. No re-meshing is required during the crack propagation phase. However, a finer mesh should be used in the area located around the crack path. Hence, a mesh refinement technique is adopted around the damage zone in order to capture the high stress concentration at the crack tip and to ensure the convergence the numerical results. A total of 448 data acquisition nodes are defined on the gusset plate to represent the actual strain-transducers. Each data acquisition node has a circular shape of 10 mm diameter. The dots in Figure 2-6 represent the chosen data acquisition nodes. These locations refer to the location of the PFG sensors.

The gusset plate is subjected to six forces as shown in Figure 2-7(a). After obtaining the direction of the propagated crack, the damage states are defined. For the simulations, the applied load magnitude was equal to 10% of the critical loading at the time of the collapse. Figure 2-7(b) displays the results of the numerical simulations.

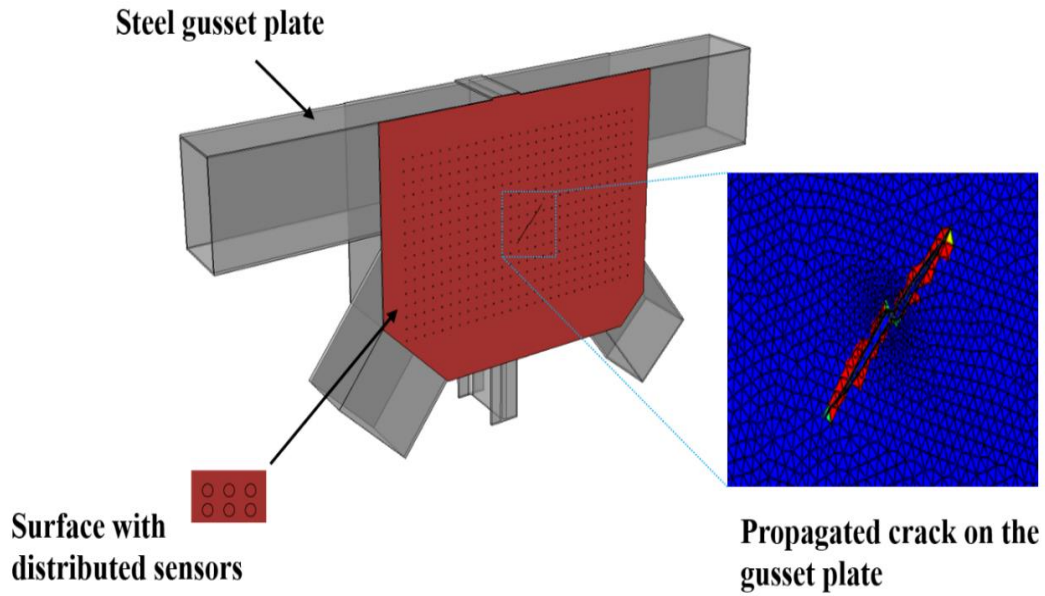


Figure 2-6: 3D perspective of the studied gusset plate with mesh details of the propagated crack.

Table 2-1: Material properties, loading and dimensions.

Property	Symbol	Value
Elastic Modulus (GPa)	E	200
Poisson's Ratio	ν	0.3
Material Density (kg/m^3)	ρ	7800
Load Frequency (Hz)	f	0.5
Plate Thickness (mm)	H	12.7
Plate Length (mm)	L	2540
Plate Width (mm)	b	1828

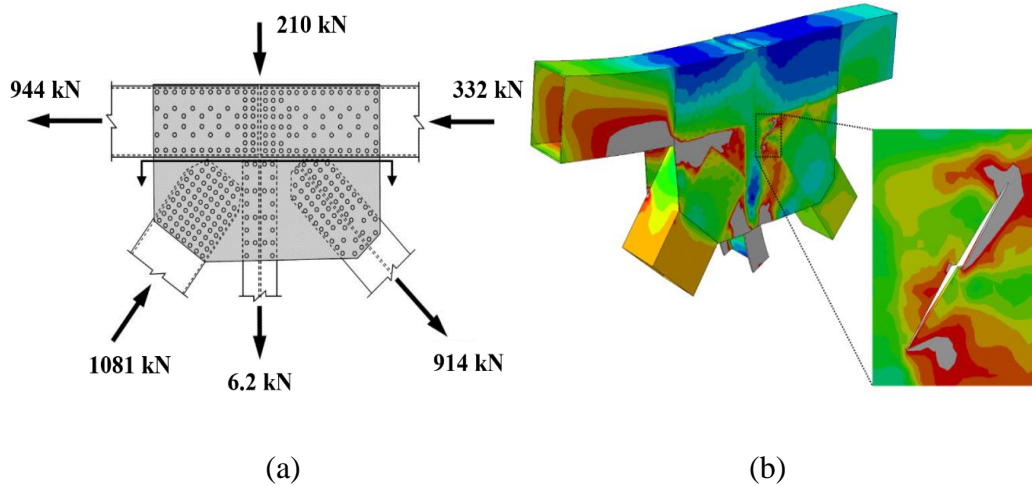


Figure 2-7: (a) Loading conditions and (b) deformed configuration of the gusset plate with a propagated crack.

The average of the maximum principle strains at each sensor location are used in the analysis. The distance between two consecutive sensors is 80 mm. The sensors are placed along the surface of the plate (28×16). Strain threshold levels of a typical piezoelectric transducer are displayed in Table 2-2. The activation strain of the sensor is set to $30 \mu\epsilon$ and the maximum threshold level is $150 \mu\epsilon$ above which all the sensor channels records the cumulative time durations of the applied strain.

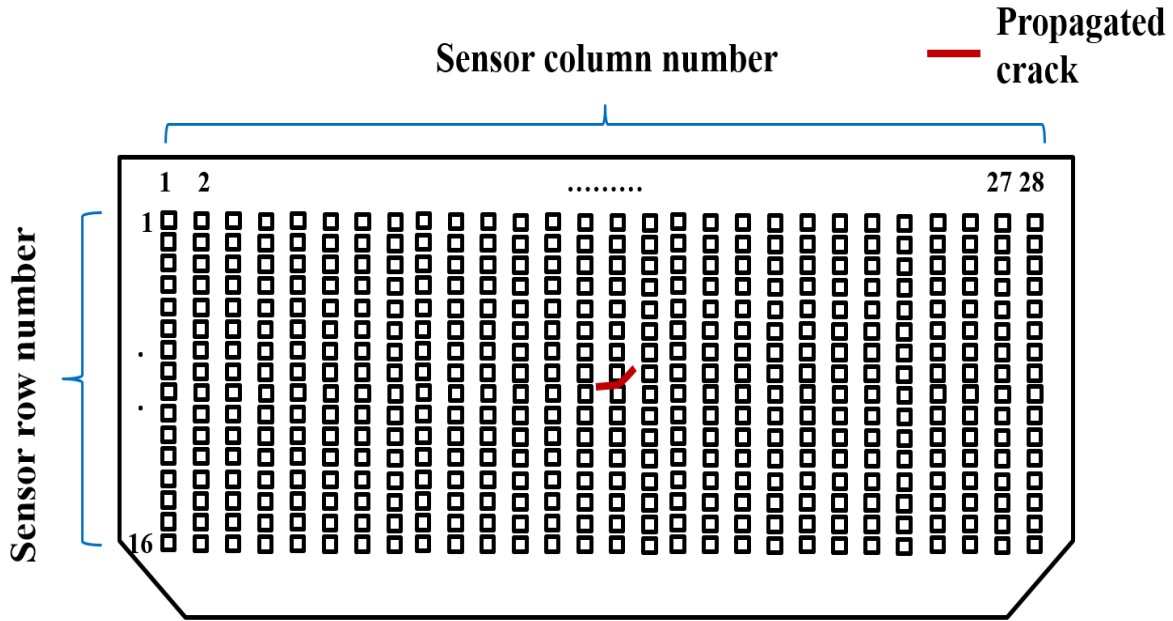


Figure 2-8: Locations of the distributed sensors and propagated crack.

Sensor located at the intersection of row i and column j is denoted by S_{ij} as shown in Figure 2-8.

The initial crack (10 mm) is located at the middle of the plate.

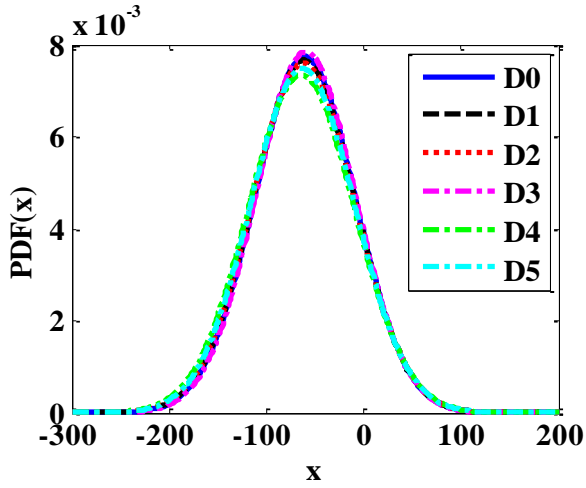
Following the procedure described in section 2.2, the the cumulative time is caculated and the data is fitted to a CDF and then tranformed to a PDF. Figure 2-9 displays the PDFs of some of the selected sensors. As seen in these figures, the PDFs loacted far from the damage zone are fairly identical (S10, S28, S42, S400, S448). In fact, the strain amplitude of these sensors is not affected by the damage progression as they are located outside the stress concentration zone generated by the crack. Threfore, the cumulative time histograms are identical at these locations, which results in almost the same CDF fit. By getting closer to the damage, the PDFs change remarkably with damage progression (S185, S212, S214, S239, S240, S266, S270 and S296).

For sensors S214, S236 and S296, The PDFs shift to the left and they expand with damage progression. The mean of the distribution decreases and the standard deviation increases according to the crack growth. Conversely, as seen in Figure 2-9(o), the PDFs slightly shift to the

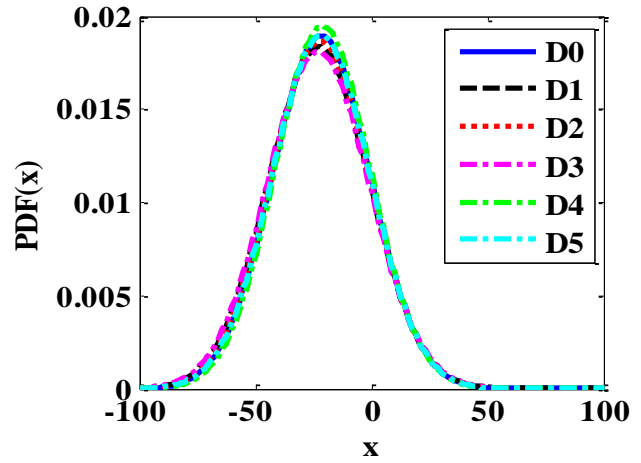
right and they shrink as the damage progresses. Other sensors, such as S212, do not have a clear trend between damage states.

Table 2-2: Preselected strain levels for the gusset plate.

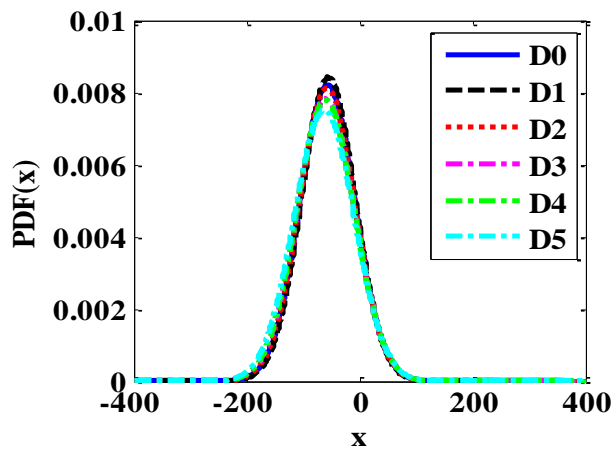
Gate Number	Strain Level ($\mu\epsilon$)
1	30.00
2	43.33
3	56.67
4	70.00
5	83.33
6	96.67
7	110.00
8	123.33
9	136.67
10	150.00



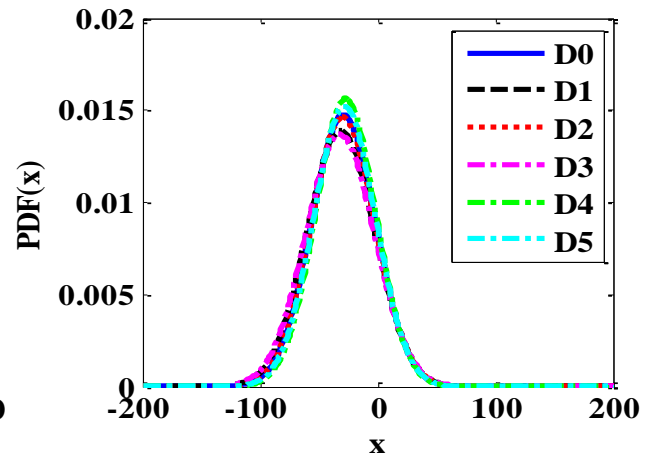
(a) S10



(b) S28



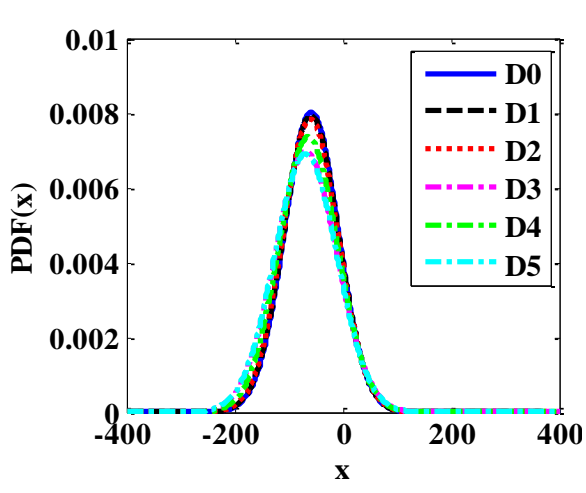
(c) S42



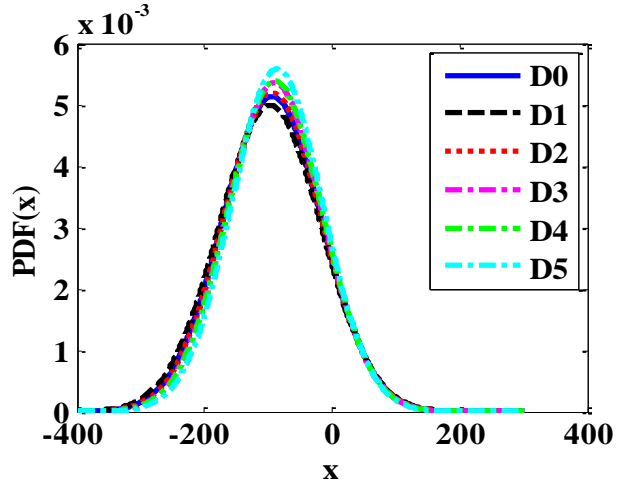
(d) S56

Figure 2-9: Change of the PDFs between damage states.

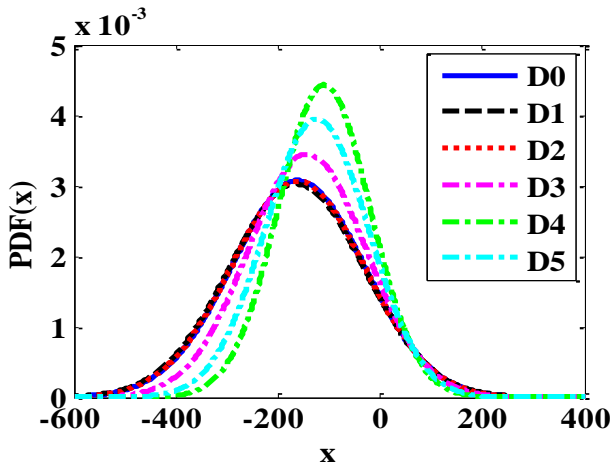
Figure 2-9 (cont'd)



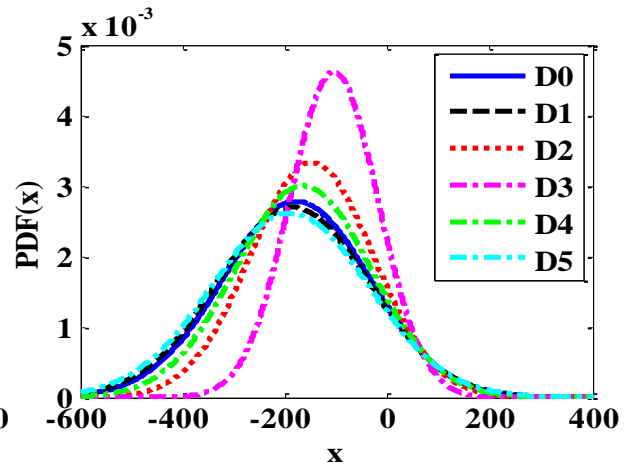
(e) S100



(f) S180

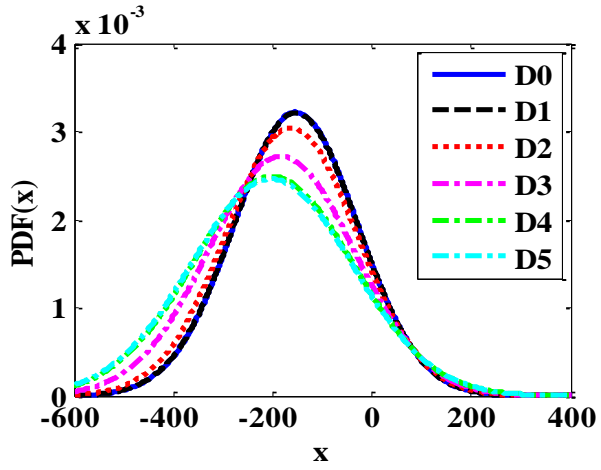


(g) S185

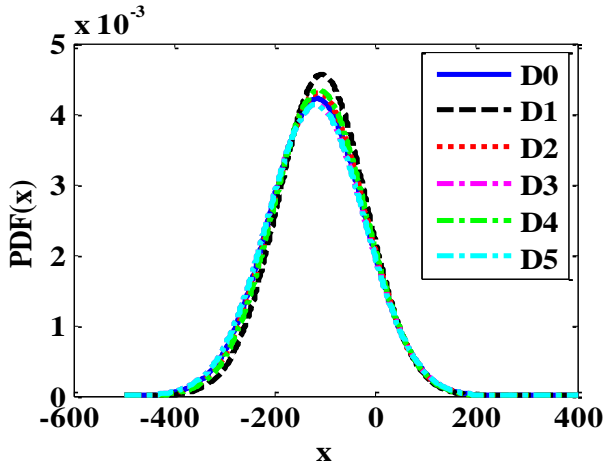


(h) S212

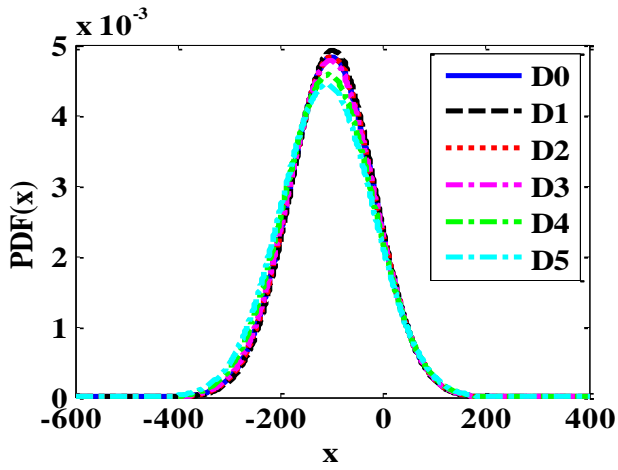
Figure 2-9 (cont'd)



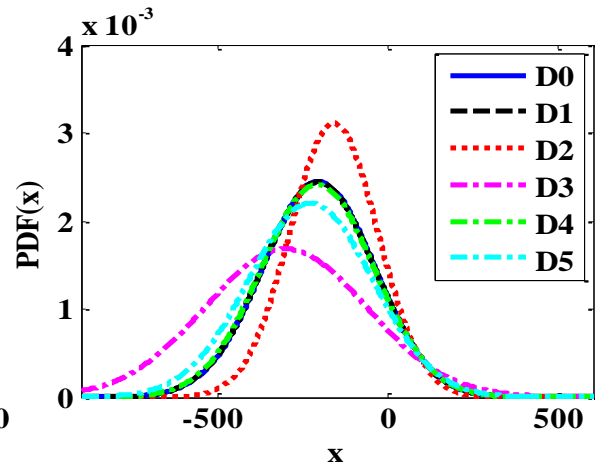
(i) S214



(j) S220

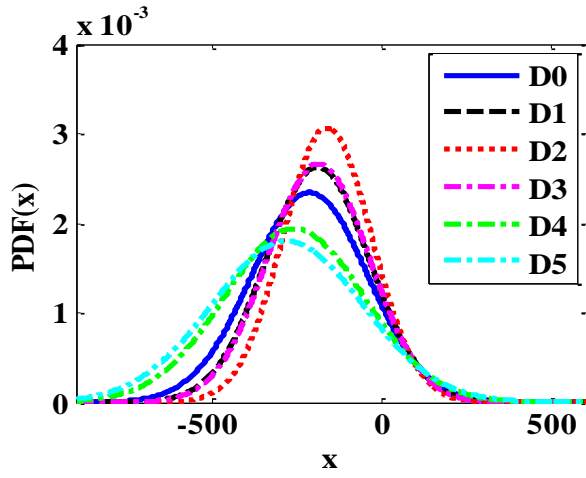


(k) S236

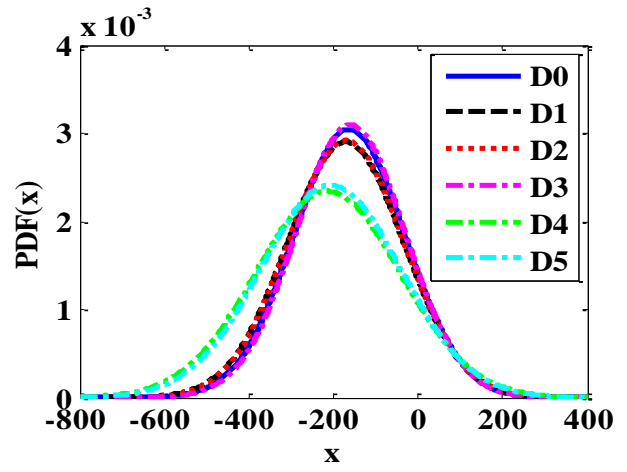


(l) S239

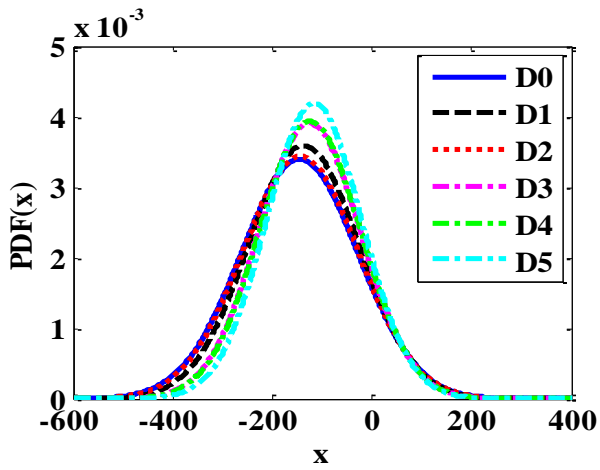
Figure 2-9 (cont'd)



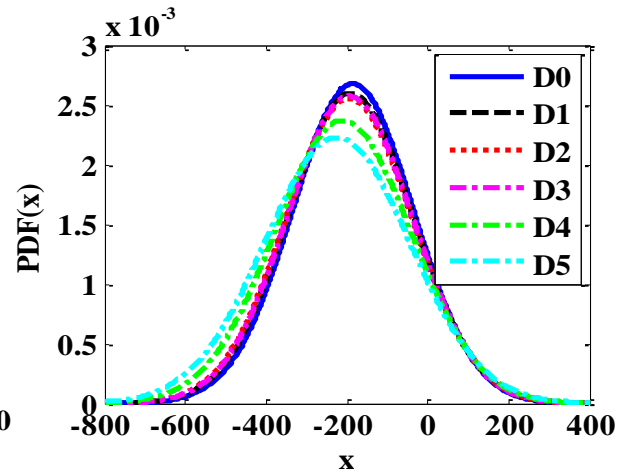
(m) S240



(n) S266

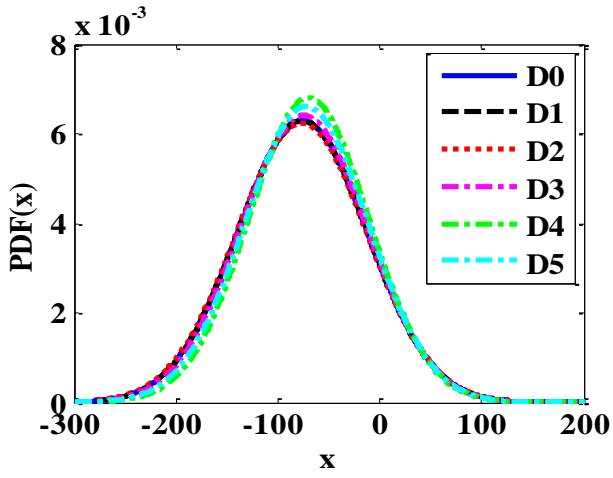


(o) S270

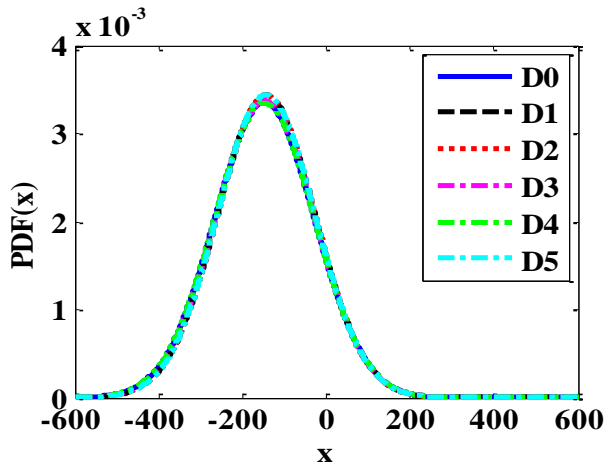


(p) S296

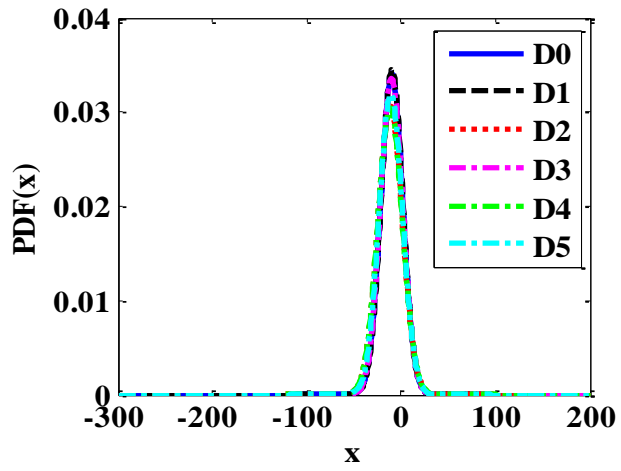
Figure 2-9 (cont'd)



(q) S321



(r) S400



(p) S448

Therefore, depending on the location of the sensor with respect to the damage zone, the PDF parameters have different trends. Hence, the crack propagation can be monitored by the PDF sensor and the damage can be represented by the PDFs' parameters as follows:

$$Damage = f(\mu_{ij}, \sigma_{ij}, \underline{X}_{ij}) \quad (2-6)$$

where μ_{ij}, σ_{ij} are the mean and the standard deviation of the distribution of sensor S_{ij} , and \underline{X}_{ij} is location of the sensor. These parameters are called individual damage predictors.

On the other hand, there are limitations of using the individual sensing predictors. As described above, the PDFs of sensors located far from the damage zone do not sense the crack propagation. Moreover, even if the sensor can detect the damage, the trends of PDF features are not clear as it depend on the relative location of the sensor with respect to the crack. In fact, the strain patterns increase around the crack tip and they decrease in the direction perpendicular to the crack direction (along the crack edge). As a result, the sensors that are subjected to higher strains have a longer duration of the applied strain, and sensors subjected to lower strains record less time duration. Moreover, for this type of complex structures, the distribution of the stress/strain cannot be expected. Therefore, a statistical analysis is performed to find a sound relationship between the PDF parameters and damage progression by combining the effect of a group of sensors. Different statistical indexes are performed in the data ($\mu_{ij}, \sigma_{ij}, i = 1:16, j = 1:28$). Among the average, standard deviation, range, minimum, maximum, skewness, and kurtosis, the STD is found to have a sound relationship with damage progression.

Multiple iterations are performed to obtain the best set of sensors that has a unique trend with damage growth. One of the best configurations is given by the set of sensors {S214...S220 and S242...S248}. As seen in Figure 2-10, the standard deviation continuously increases between

damage states (D1-D5). Each point of the plot represents the STD of a group of sensors for a specific damage state. If G denotes the group of sensors, then each point is defined by:

$$y_k = std(\mu_G \text{ or } \sigma_G) \quad (2-7)$$

where k is the damage state number. This result indicates that the damage could be detected and classified using the standard deviation of a specific set of sensors.

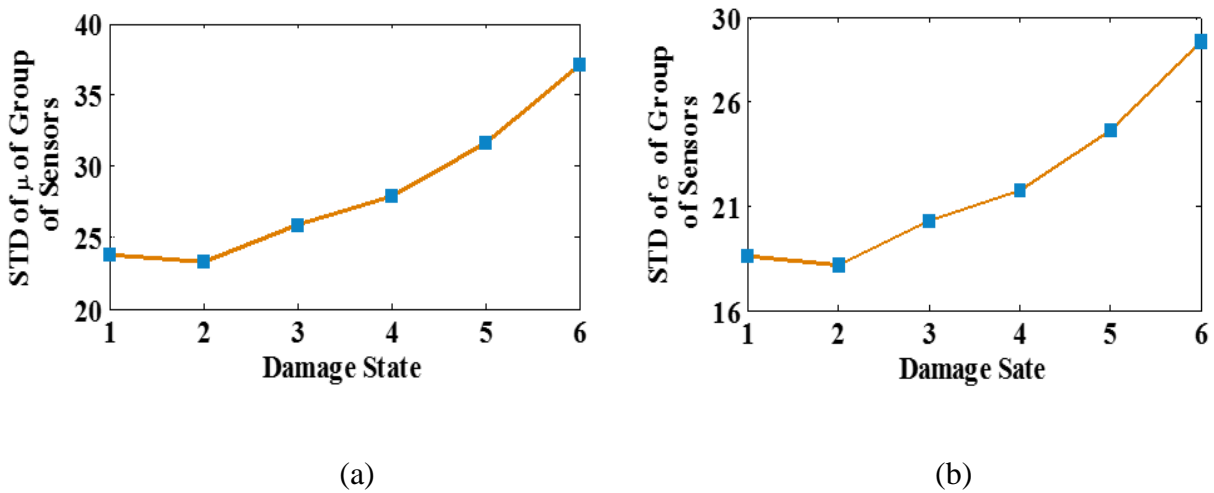


Figure 2-10: Variation of the STD of (a) μ and (b) σ for sensors S214 to S220 and S242 to S248.

An interesting observation from Figure 2-10 is that the slope of the curve is a good indicator of the damage severity. As the initial crack length was only 10 mm, the STD deviation does not show a considerable variation between the intact and D1 damage states. As soon as the crack propagates, the STD increases rapidly. Both the STDs of μ and σ have the same trend. Moreover, the STD increases almost linearly between damage states. This is because the variation of the crack is constant from one damage class to another ($\Delta a = 120$ mm).

2.3.1.2. Damage quantification

In order to identify the crack location, a search algorithm is developed. Figure 2-11 shows a flowchart of the crack localization algorithm. The search process is divided into two different steps:

- Removing rows of sensors during iterations: A row of sensors is removed at each iteration, and the STD of the remaining set is calculated for each damage state. Thereafter, the maximum percentage variation of each damage state is calculated with respect to the intact plate.
- Removing columns of sensors during iterations: The obtained set of sensors from the precedent iterations are used as the initial input in this step. The same procedure is then followed on the columns of sensors.

The algorithm can be written as:

Step 1:

1. Starting with full set of sensors: $\underline{S} = \underline{S}_0 = \{S_1, S_2, \dots, S_n\}$, n is the total number of sensors that can be divided into $n_1 \times n_2$, where n_1 is the number of sensor for each row and n_2 is the number of sensors for each column.
2. Remove the i^{th} row of sensors:
 - $\underline{S} = \underline{S} - \underline{S}_i$
 - and calculate:
 - $m_i = \max_{k=1..ND} (STD(\mu_{\underline{S}}))$, ND is the number of damage states
 - $i = i + 1, i = 1..n_1$
3. Determine the final set of sensors \underline{S}_h based on the STD variation trends.

Step 2:

1. Start from: $\underline{S} = \underline{S}_h$
2. Remove the j^{th} column of sensors:
 - $\underline{S} = \underline{S} - \underline{S}_j$,

and calculate:

- $m_j = \max_{k=1..ND} (STD(\mu_{\underline{S}}))$
- $j = j + 1, j = 1..n_2$

3. The final set (\underline{S}_q) of sensors shows the damage location.

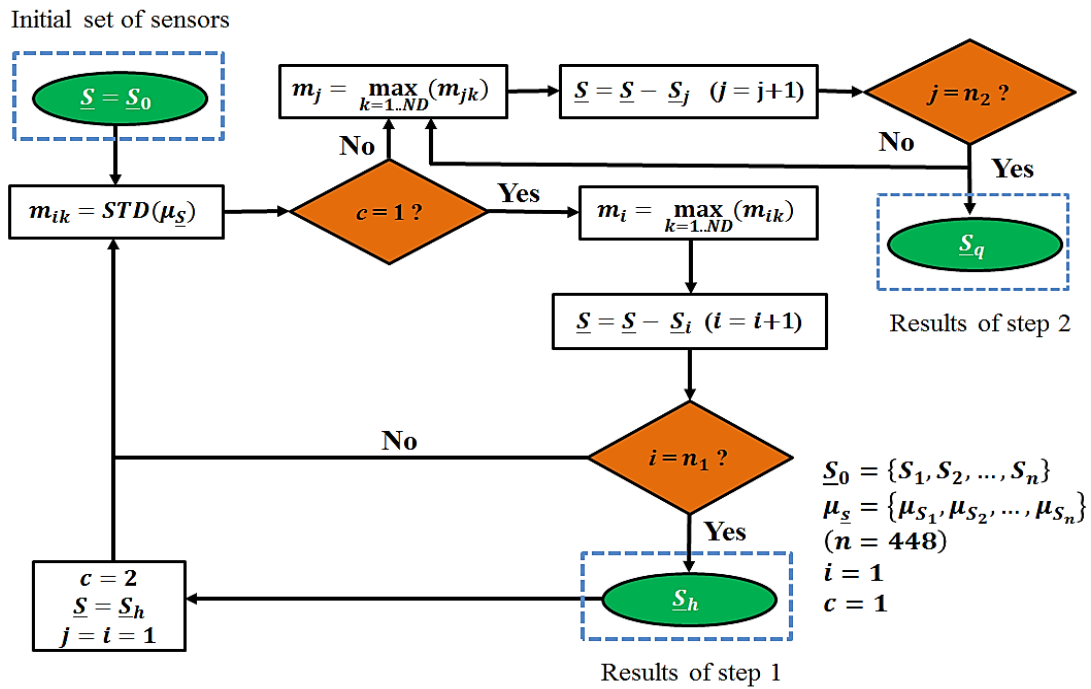


Figure 2-11: Damage localization algorithm.

Figure 2-12 displays the results of the damage localization approach. As seen in Figure 2-12(a) the maximum variation of the STD presents a peak after removing the first 8 rows from the

initial set of sensors (\underline{S}_0). After removing 9 rows the maximum variation of the STD decreases and returns to the low portion of the plot. Therefore, it can be concluded that crack is located between rows 8 and 9. The final set of sensors for the first step is:

$$\underline{S}_h = \{S_{197} \dots S_{252}\} \quad (2-8)$$

Next, after applying the procedure described in step 2, the plot shown in Figure 2-12(b) is obtained. The final set of the procedure is:

$$\underline{S}_q = \{S_{211}, S_{212}, S_{239}, S_{240}\} \quad (2-9)$$

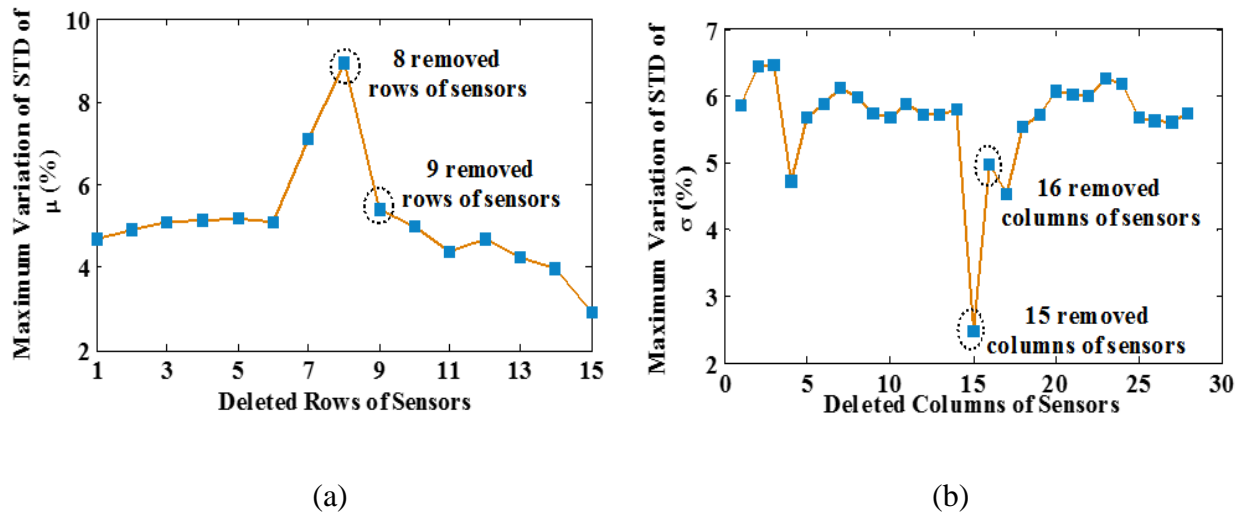


Figure 2-12: (a) Results of step 1, (a) results of step 2.

The obtained set is located around the crack region as indicated in Figure 2-13. Up to this point, the PDF parameters are good predictors of damage occurrence in gusset plate structures. The STD of μ and σ of a group of sensors are good indicators of damage progression and damage severity. The crack could be localized using the proposed search algorithm. After finding crack location, the remaining task is to quantify the damage. Therefore, the curve describing the

standard deviation of each damage state (i.e. crack length) is fitted to a linear function.

The standard deviations are calculated based on the whole network of sensors. As it is seen in Figure 2-14, the data is fitted to:

$$y = 0.0072 x + 67.31 \quad (2-10)$$

where the obtained R-squared is about 94.1%.

In order to verify the accuracy of the proposed approach, five new data points are tested. The procedure described in the first section is followed to obtain the mean and the standard deviation for each sensor and for each introduced damage states.

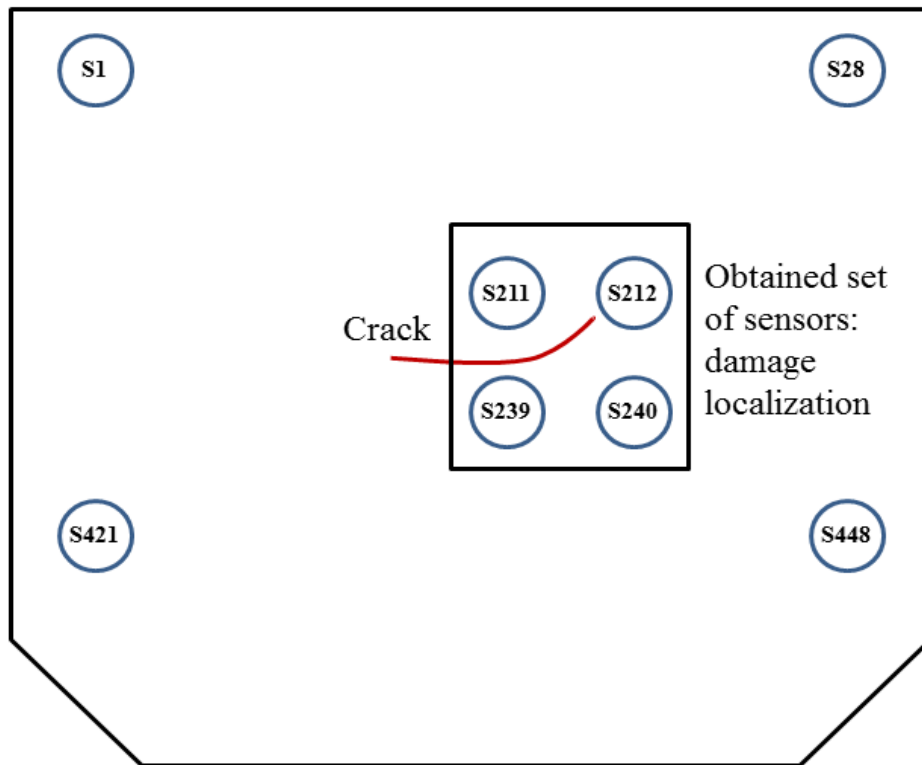


Figure 2-13: Crack localization results.

Thereafter, using Equation (2-10), the predicted crack length is calculated. Table 2-3 shows the

error between the true crack length and the predicted one. The maximum obtained error is 6.09 % which is satisfactory to validate the accuracy of the method.

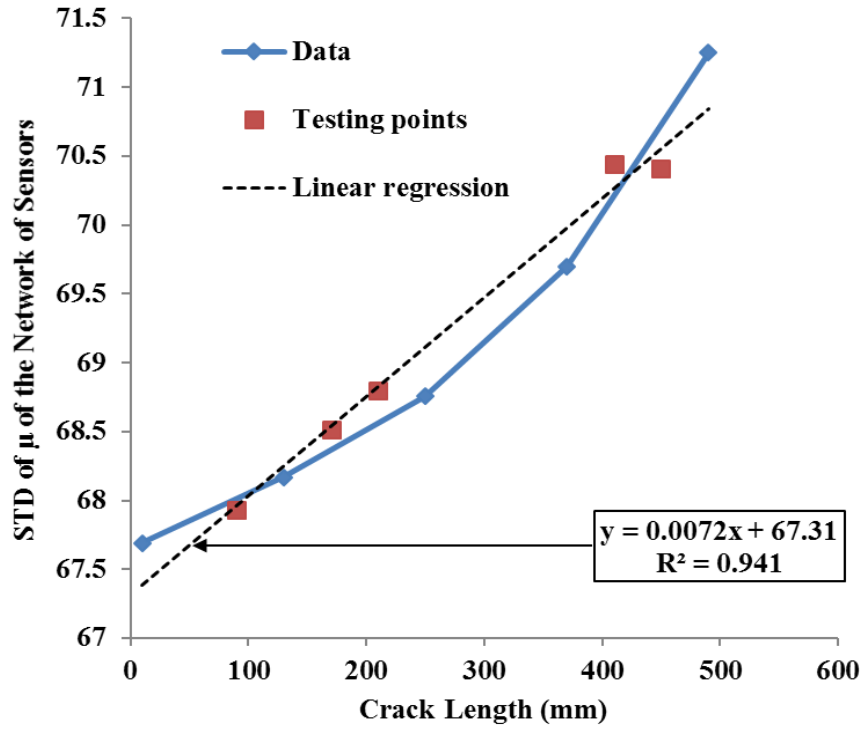


Figure 2-14: Prediction of the crack length.

Table 2-3: Preselected strain levels for the gusset plate.

Measured Crack	Predicted Crack	Error
Size (mm)	Size (mm)	(%)
90	86.32851	-4.08
170	166.8994	-1.82
210	207.193	-1.34
410	434.9739	6.09
450	430.0995	-4.42

2.3.2. Detection of fatigue cracking in steel bridge girders: a support vector machine approach

Multi-girder steel bridges are widely used throughout the highways in the United States. One of the main factors affecting the performance of these structures is the application of the repetitive loading over the steel-girder components. These load-carrying components deform under the live (traffic load) and the dead load of the structure. Typical steel girder bridge is composed by three main parts: girders, diaphragms, and stiffeners. The diaphragms are structural elements that provide resistance to the transverse traffic and wind loading. The stiffeners connect the girder to diaphragm. Over many years, inspections conducted on steel-girder bridges revealed that these structures are suffering from fatigue cracking under cyclic loading (Fisher, 1984). More specifically, low resistance to fatigue has been observed in structural members subjected to out-of-plane distortion. The phenomenon of out-of-plane distortion is impacted by a variety of factors such as thermal forces, traffic flow, differential deflection of the adjacent beams, etc

(Zhao and Roddis, 2004; Juntunen, 1998).

Figure 2-15 displays a schematic illustration of the formation of fatigue cracks in a steel girder caused by out-of-plane distortion. Figure 2-15(a) displays an illustration of a steel bridge before deformation in a perspective view, and Figure 2-15(b) shows the side view of the bridge at the initial stage. Figure 2-15(c) schematically indicates the cracks caused by out-of-plane distortions. It can be seen that the deformations of the girder web are caused by the differential displacement (δ) between the two girders, which leads to the out-of-plane distortion (Δ). Such distortion eventually causes fatigue cracks to the girders, i.e., horseshoe and horizontal cracks. Therefore, fatigue cracks usually occur at the girder web gap due to out-of-plane distortion. The distortion-induced fatigue cracks may occur as horizontal or horseshoe cracks at the top or bottom of the girder to stiffener connections (Figure 2-15(c)).

More details on the forming mechanism of these cracks can be found in (Fisher and Mertz, 1985; Elewa, 2004). Different models have been developed to investigate the behavior of bridges (Dexter and Ocel, 2013), with particular focus on the retrofitting approaches to deal with this common type of structural damage (Elewa, 2004; Stallings et al., 1997). However, the selection of an appropriate repair strategy is complicated and depends on many factors. On the other hand, the significant cost of maintenance and retrofitting of stiffener-girder connections implies the necessity of detecting the damage progression at early stages to prevent severe damage to the bridge structures.

This study proposes an SVM approach for the detection of fatigue cracking of steel bridges using the data provided by the PFG sensor. The emphasis is placed on the out-of-plane distortion-induced fatigue cracks.

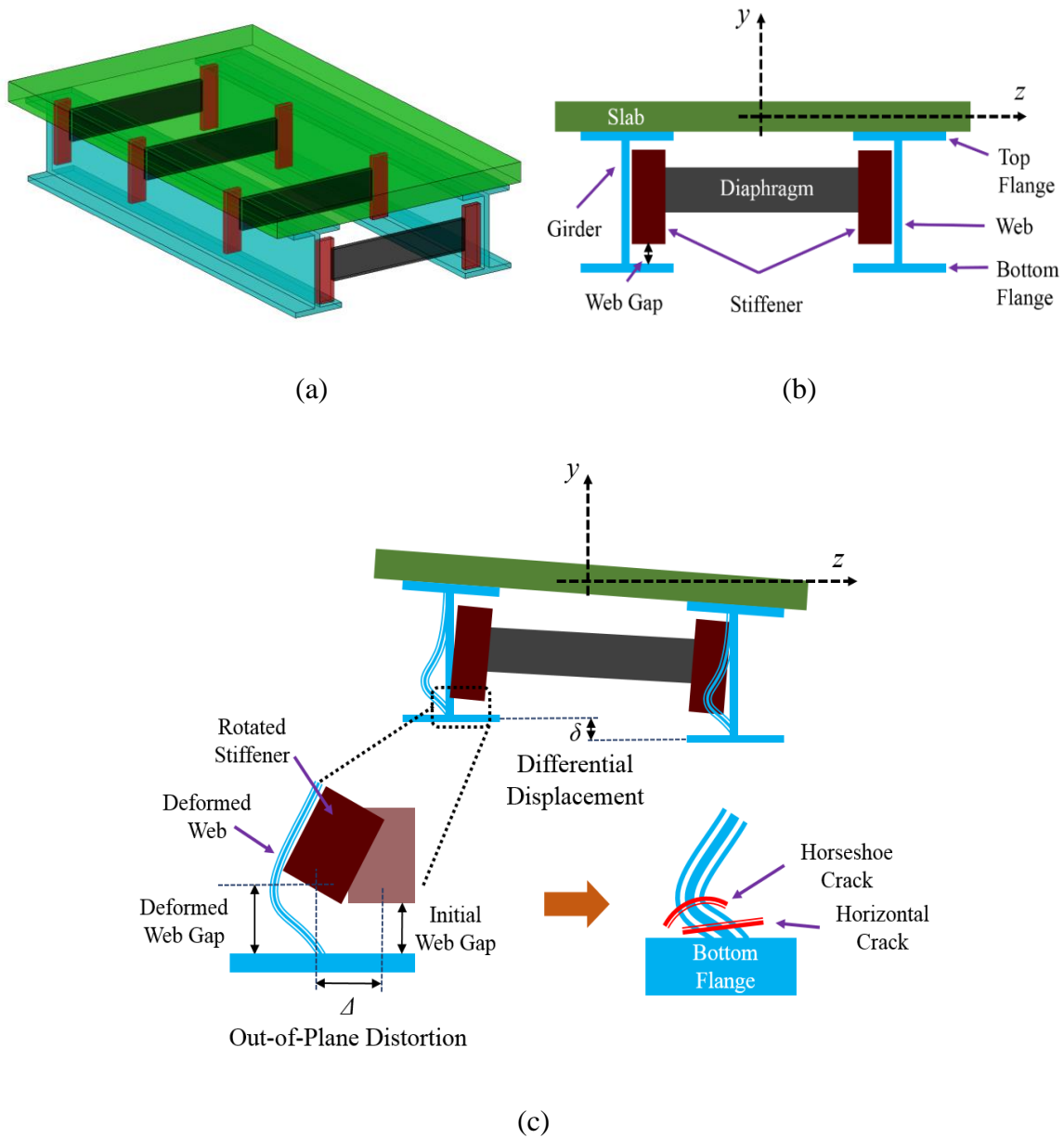


Figure 2-15: Schematic illustration of distortion-induced fatigue cracking: (a) bridge before deformation in a perspective view, (b) side view of the bridge in the initial stage, and (c) different types of fatigue cracks caused by out-of-plane distortion (Δ).

The entire damage detection procedure is divided into the following major phases:

- Numerical simulation of the targeted structure;
- Extraction of strain data and generation of the distribution histograms based on the

sensing mechanism of the PFG sensor;

- Extraction of the preliminary damage indicator features;
- Fusion of the data from a network of sensors to define more informative damage indicators;
- Fatigue damage classification using an SVM approach.

In order to calibrate the AI models, different FE simulations of steel girders with complex geometry components are performed and the structural response of the girder is subsequently obtained. The fatigue life of the girder is determined based on the J-integral concept and Paris Law (El Haddad et al., 1980; Pugona et al., 2006).

Several damage states are defined by extending the crack lengths. Sensing locations are defined to monitor the strain changes due to damage progression. The sensing nodes are placed around the connection between the webs and the stiffeners to determine the optimal sensors configurations that maximize the detection performance of fatigue cracking. Thereafter, features representing the sensor output are extracted from the strain data. The obtained features are then fed into an SVM classifier to identify multiple damage states.

2.3.2.1. Numerical analysis of out-of-plane distortion-induced fatigue cracking

2.3.2.1.1. Geometry, loading and boundary conditions of the steel girder

For the numerical simulation carried out in this study, the highway steel bridge (I-96/M-52) in Webberville, Michigan, U.S. is selected. The steel girder under consideration is modeled using Abaqus Version 6.12. Figure 2-16 shows the geometry, loading and boundary conditions of the selected structure. Figure 2-16(a) presents the geometry of the structure. In Figure 2-16(a1), a 3-D model was created using SolidWorks. Figure 2-16(a2), (a3), and (a4) show the end

view, top view, and side view of the model respectively. It can be seen that the overall length of the girder is 7.62 m and the three beams are spaced by 1.93 m. The steel girders have the same cross section ($W920 \times 233$) as the I-96/M-52 bridge. A web gap length of 25.4 mm is considered for the simulations. Figure 2-16(b) displays the boundary conditions of the model. The steel girders are modeled with a simply supported boundary conditions. The top flanges of the three beams are restrained with respect to translation in the z direction and rotation along x axis.

The loading is applied in the form of vertical displacements to the cut edges of the lower flanges of the two exterior I-beams (Figure 2-16(b)). The imposed displacements are 5 mm vertical displacement at the left outer girder and 15 mm at the right outer girder. More details of the dimensions and material properties of the stiffener and diaphragm plates are listed in Table 2-4. A linear elastic material is selected for the analysis.

2.3.2.1.2. Numerical model

2.3.2.1.2.1. Shell element-based FE model

The structure is modeled using shell elements under Abaqus. Shell elements performs sufficient computation efficiency since they formulate thin structures with much less elements than 3D solid elements. Quadrilateral shell elements with reduced integration (S4R) are used in this study. The total number of elements and nodes of the intact structure are 180320 and 182050, respectively. The meshed structure is shown in Figure 2-17(a) and an isometric drawing of the used S4R element is shown in Figure 2-17(b). A static analysis is selected for the simulations and the analysis is done for small deformations.

At the region of web gap, a finer mesh is used with an element size smaller than 2 mm such that the stress concentration zones can be accurately captured. The maximum stresses in the central

girder are located around the connection stiffener to web. As it seen in Figure 2-18, the maximum obtained principal strain of the intact structure is 1.103×10^{-3} .

The stiffeners and diaphragms are meshed using an element size of $25 \text{ mm} \times 25 \text{ mm}$ and the beams are meshed using $2 \text{ mm} \times 2 \text{ mm}$ element size around the stiffener to web connection. The rest of the central girder is meshed using $2 \text{ mm} \times 76 \text{ mm}$ quadrilateral element. Different simulations are performed to find the optimal mesh size that guarantees the numerical convergence of the solution. The results of the convergence analysis are shown in Figure 2-19 and Table 2-5.

It should be noted that the strain values are obtained for an element of the central girder web at the connection stiffener-web. As mentioned above, this element presents the highest deformation of the central girder. Figure 2-19 shows that the element size of $2 \text{ mm} \times 2 \text{ mm}$ is sufficient to obtain satisfactory results. In particular, the error between element sizes of $1.5 \text{ mm} \times 1.5 \text{ mm}$ and $2 \text{ mm} \times 2 \text{ mm}$ is only 0.18 % ($2 \mu\epsilon$ difference). Therefore, the 2 mm S4R elements provide adequate accuracy of the numerical results.

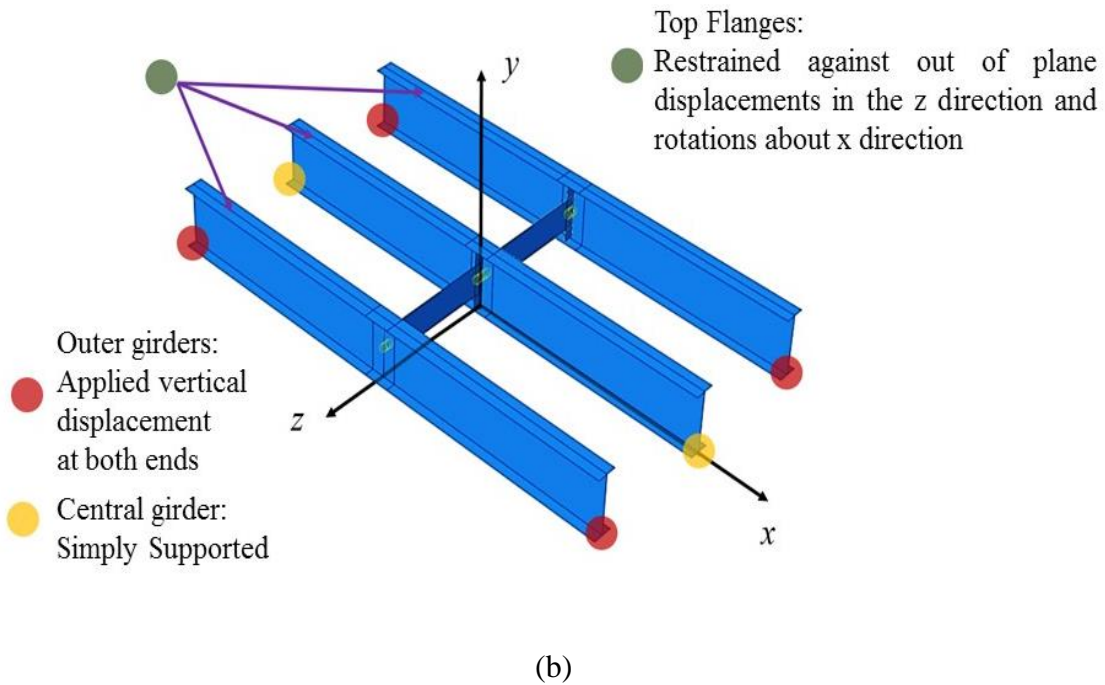
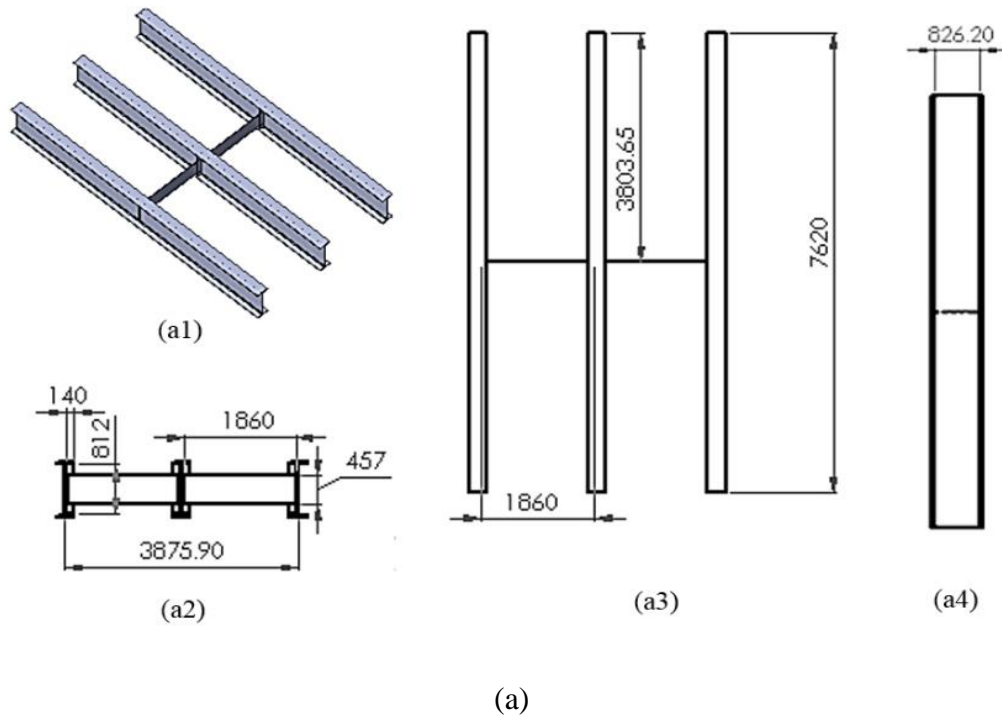


Figure 2-16: Selected steel structure: (a) technical drawings of the structure, including (a1) a perspective view (a2) an end view, (a3) a top view, and (a4) a side view, and (b) assembly of the structure in Abaqus with loading and boundary conditions.

Table 2-4: Geometry and material properties of the girder.

Material	Geometry (mm)						Beam s
	Overall Model		Stiffener		Diaphragm		
Young's Modulus (GPa)	Length	7620	Length	812	Length	1863	W920 ×223
	Spacing	1933	Width	140	Width	457	
Poisson's Ratio	Web Gap	25.4	Thickness	12.7	Thickness	12.7	

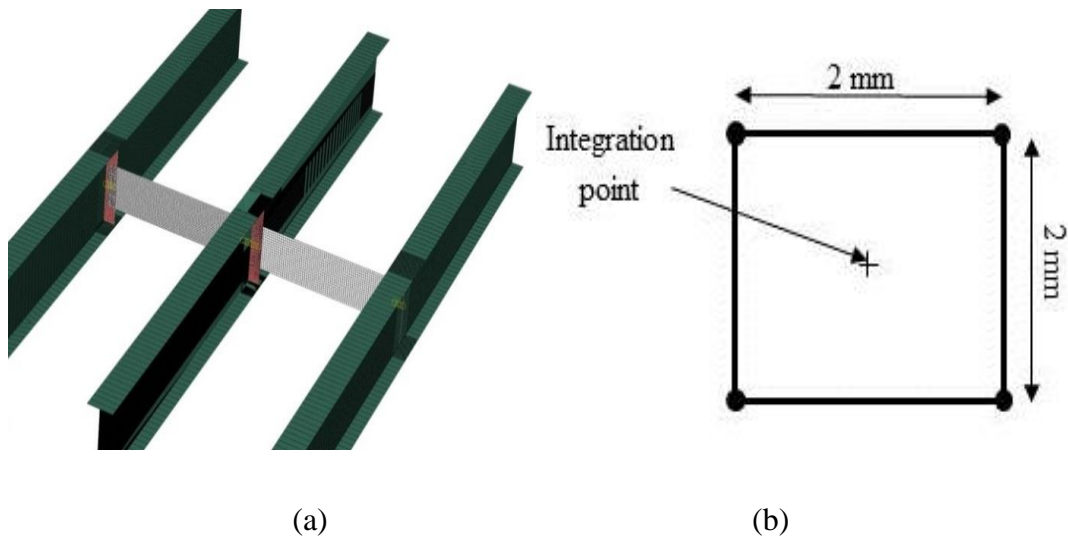


Figure 2-17: Mesh details: (a) Meshed structure, (b) S4R element.

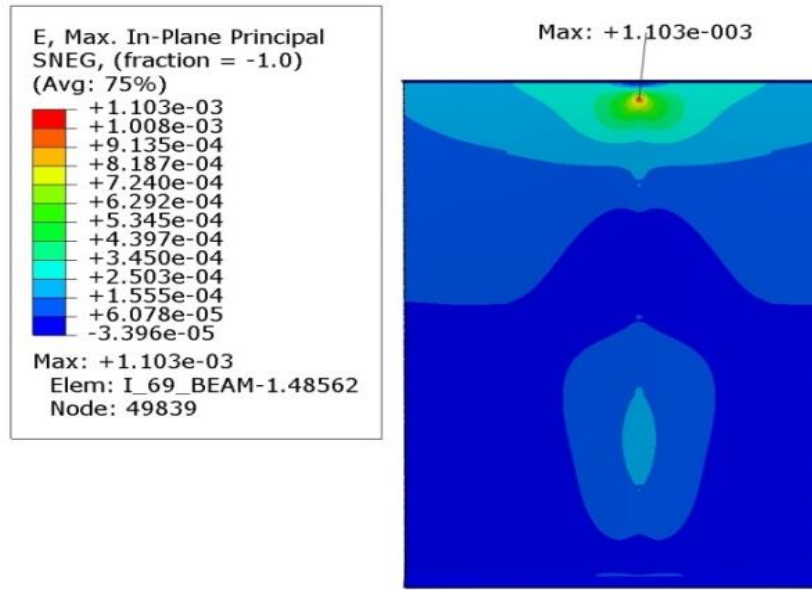


Figure 2-18: Maximum principal strain around the area stiffener to web connection.

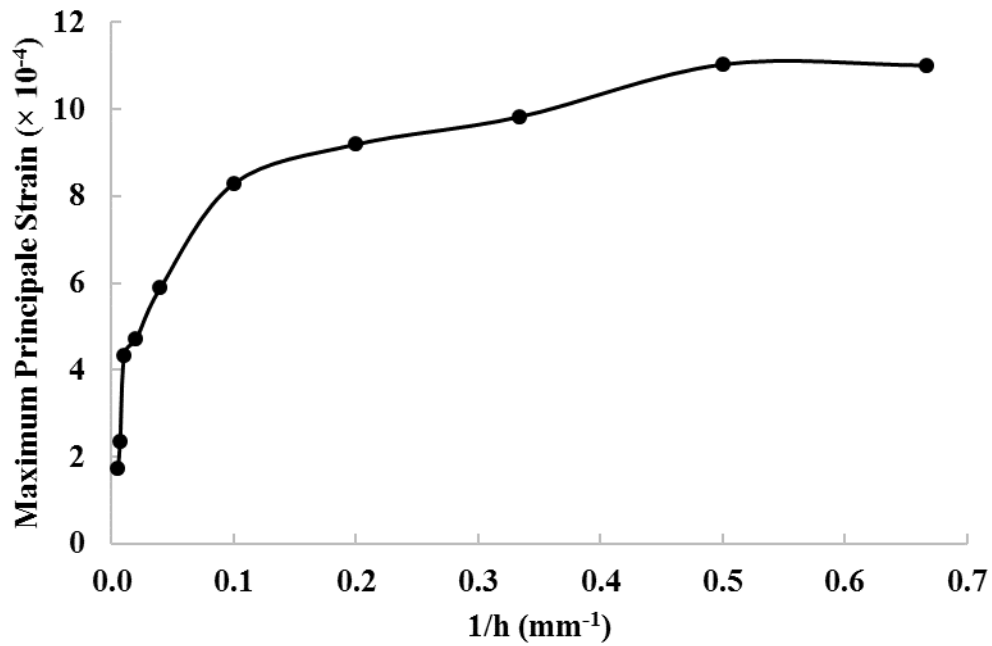


Figure 2-19: Variation of the maximum principal strain as a function of the element size.

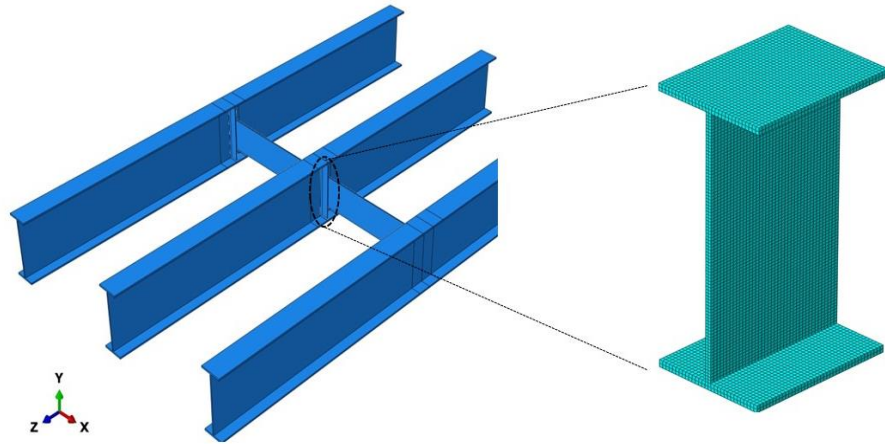
Table 2-5: Results of the numerical convergence analysis.

Element Size	Maximum Principal
h (mm)	Strain ($\times 10^{-4}$)
200	1.74
150	2.37
100	4.34
50	4.71
25	5.9
10	8.29
5	9.19
3	9.82
2	11.03
1.5	11.01

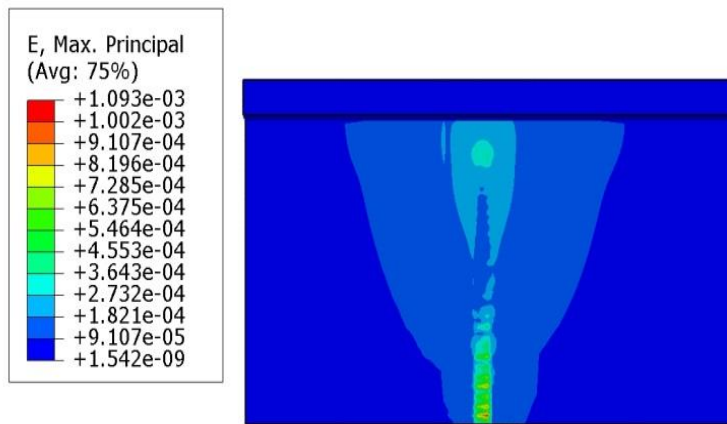
2.3.2.1.2.2. Comparison between shell and 3D solid element-based FE model

In order to validate the accuracy of the shell model developed in the previous, a 3-D solid finite element model is built and simulated using Abaqus. The FE model has the same geometry, loading, and boundary conditions of the shell model. The entire steel girder is meshed using eight-node brick elements with reduced integration (C3D8R).

Figure 2-20 shows the assembly of the structure, the refined portion of the central girder (at connection stiffener to web), and the maximum principal strain at the connection between the stiffener and the web.



(a)



(b)

Figure 2-20: 3D finite element model (a) Assembly and refined mesh portion, (b) maximum principal strain around the connection stiffener to web.

Different simulations are conducted to obtain the optimal element size that guarantees the numerical convergence. The optimum is found to be $2 \text{ mm} \times 2 \text{ mm} \times 2 \text{ mm}$ close to the stiffener to web connection as shown in Figure 2-20(a). The stiffeners are meshed with an element size of $20 \text{ mm} \times 20 \text{ mm} \times 4 \text{ mm}$. The element size of all the other regions varied between 50 mm and

150 mm. A summary of the comparison between the shell model (S4R element-based) and the 3D solid model (C3D8R element-based) is illustrated by Table 2-6.

The error of the maximum principal strain occurred at elements located at the connection stiffener to web is found to be 0.91 %. However, the computational time of the 3D solid finite element model is up to 20.5 times higher than the shell model. Compared to the 3D solid model, the shell model delivered accurate results in much less computational time, and therefore, the shell model is used for the rest of the simulations.

Table 2-6: Comparison between the shell and 3D FE models.

	Shell	3D Solid	Error (%)
Maximum Principal Strain ($\times 10^{-4}$)	11.03	10.93	0.91
Computational Time (min)	2	41	-

2.3.2.1.2.3. Fatigue analysis of the steel girder

The contour integral method is used to calculate the stress intensity factor. A predefined crack is placed at 25.4 mm (1 inch) from the upper flange of the central girder, with an initial length of 10 mm. Damage states are defined by increasing the crack length from 10 mm to 100 mm. For each damage state, the maximum principal strains and the J-integral values are extracted to determine the number of cycles needed to propagate the crack and to compute the sensor output. The optimal element size of the damaged structure is 0.2 mm around the crack tip vicinity and 1.8 mm in the contact area between the stiffener and the web of the central girder.

Triangular elements are used to mesh the crack front. In order to perform a contour integral analysis under Abaqus, three different entities should be defined: the crack front, the crack tip, and the crack extension direction. The crack front is the forward part of the crack and it is useful to evaluate the first contour integral (Figure 2-21). The crack tip is a point (for 2-D parts) to be selected from the assembly where the crack extension direction is defined. Thereafter, the crack extension direction is defined by selecting the points representing the start and the end of the crack.

Triangular elements of type S3 are used to mesh the crack front region and the remaining part is meshed using quadrilateral elements (S4R) as indicated in Figure 2-21. The triangular elements are recommended to mesh the crack front. However, this type of elements should not be used to mesh the contour integral region. Quadrilateral elements should be used instead (Abaqus, 2011). A finer mesh around the crack tip is used to capture the high stress field at the crack front region. The J-integral is calculated based on elements surrounding the crack front. More contours should be requested in the analysis to check the accuracy of the results. In some cases, J-integral estimates might vary from one contour to the other. A strong or gradual variation of these estimates indicates an error in the contour integral definition or the mesh is not small enough to accurately calculate the J-integrals (Abaqus, 2011). In linear elastic problems, the first and second contours are usually inaccurate. In the present study, 8 contours are requested to ensure the accuracy of the J-integral calculations. The percentage variation of J-integral values between the last two contours varied between 1 % to 3 % depending on the damage state. Therefore, the average of the last 2 contours are used for the analysis. In addition, the element dimensions are 14 mm × 14 mm for the stiffeners and 18 mm × 15 mm for the diaphragms. Computational time took about 3 min for each case. The maximum principal strains for two typical crack lengths are

presented in Figure 2-22.

Thereafter, based on the J-integral estimates, the stress intensity factor is calculated with respect to the crack length. Then, Paris Law is used to estimate the number of loading cycles to propagate the crack by Δa based on the following equation (El Haddad et al., 1980; Pugona et al., 2006):

$$\frac{\Delta a}{\Delta N} = c \Delta K^n \quad (2-11)$$

where c and n are material constants, a is the crack length, N is the number of cycles and K is the stress intensity factor. These parameters are taken 2.40×10^{-12} and 3.3, respectively (Schreurs, 2012).

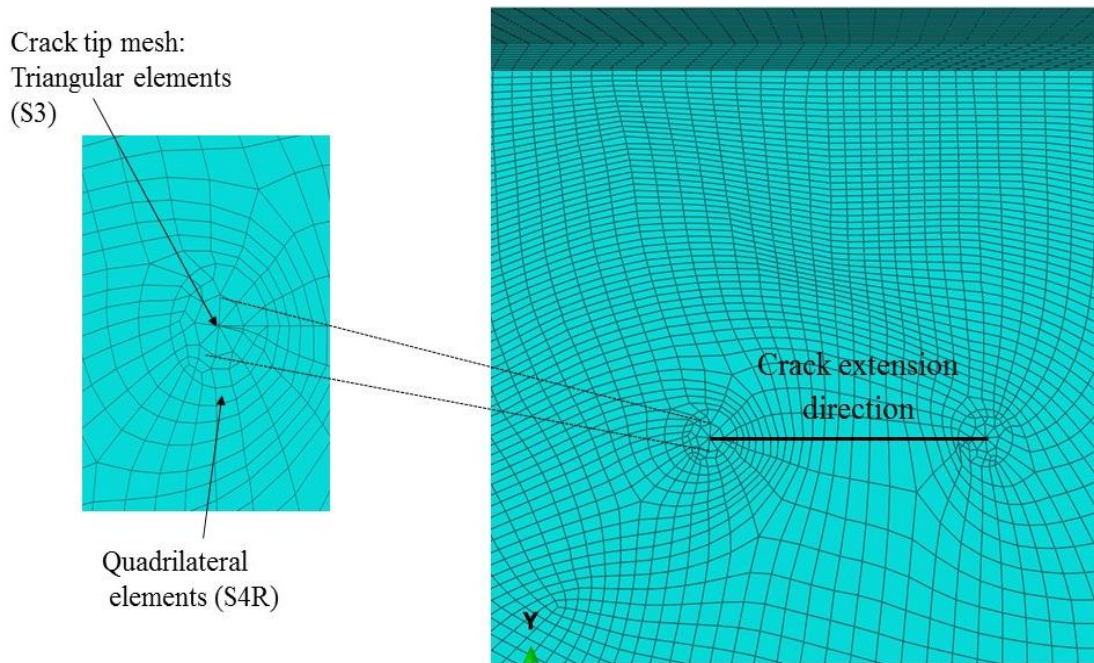


Figure 2-21: Mesh around the crack tip.

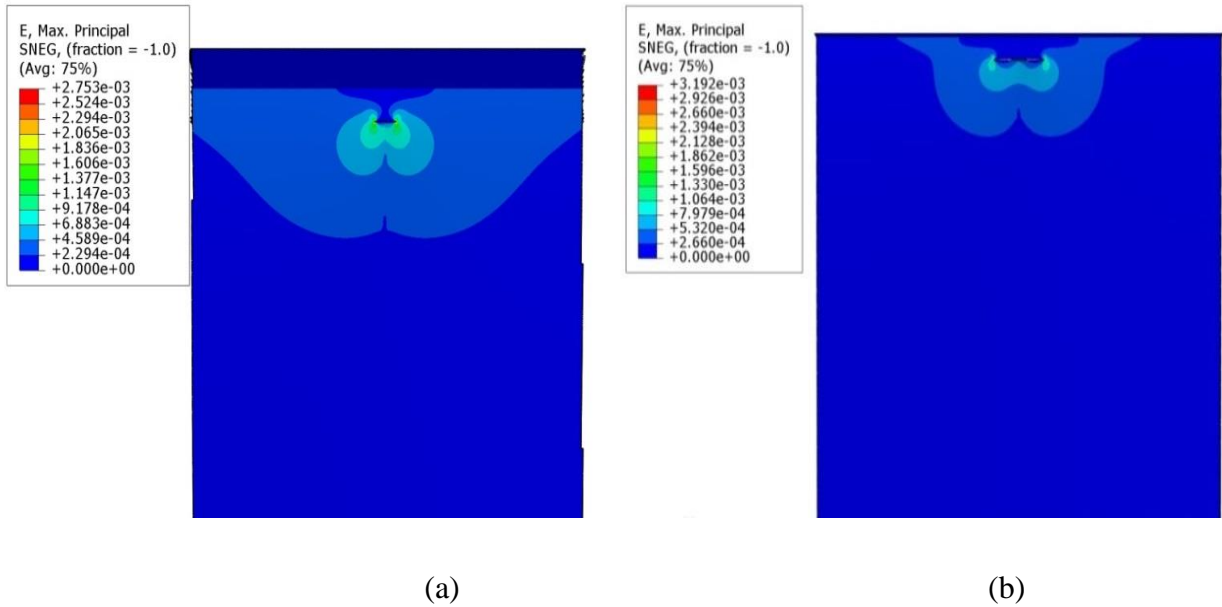


Figure 2-22: The FE results for (a) $a=20$ mm (maximum principal strain= $2753 \mu\epsilon$); (b) $a=70$ mm (maximum principal strain= $3192 \mu\epsilon$).

As seen in Figure 2-23, a 100 mm crack will occur after about six million cycles. Accordingly, the life span of the girder is divided into 6 different stages. These periods represent the date/time of readings of the sensor output for the post-processing. Each stage consists of 1 million loading cycle.

For the analysis, 400 sensing nodes are placed in the horizontal and vertical directions on the upper half of the central girder around the stiffener to web contact area (20×20 with 20 mm spacing). These nodes represent the actual piezoelectric transducers that are attached to the structure. The average strain of elements located inside a 10 mm diameter circle centered at the sensing node locations is used for the analysis. Figure 2-24 displays the locations of the 400 data acquisition nodes on the structure. Ten strain levels are defined for the girder as shown in Figure 2-25.

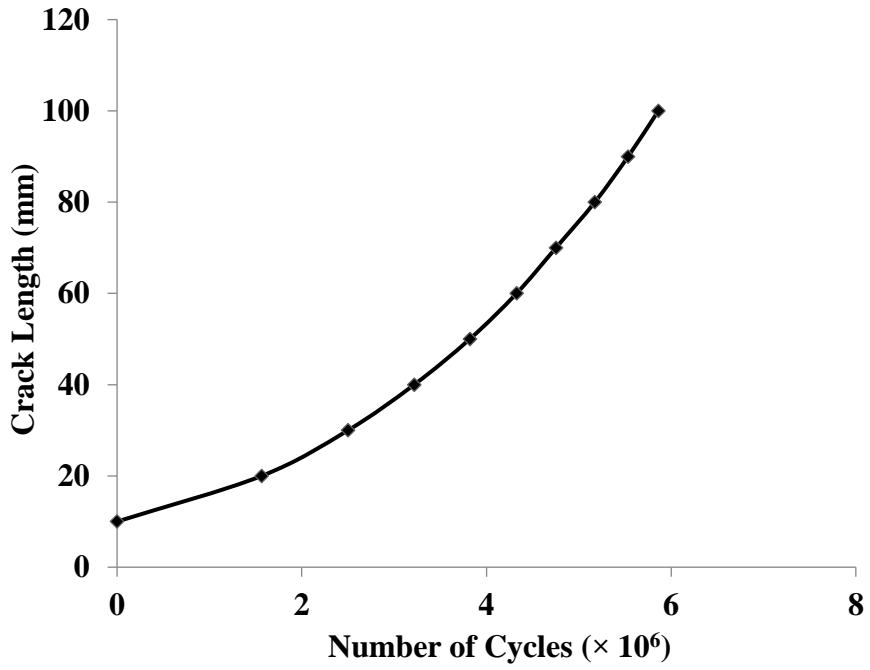


Figure 2-23: Number of cycles vs. crack length.

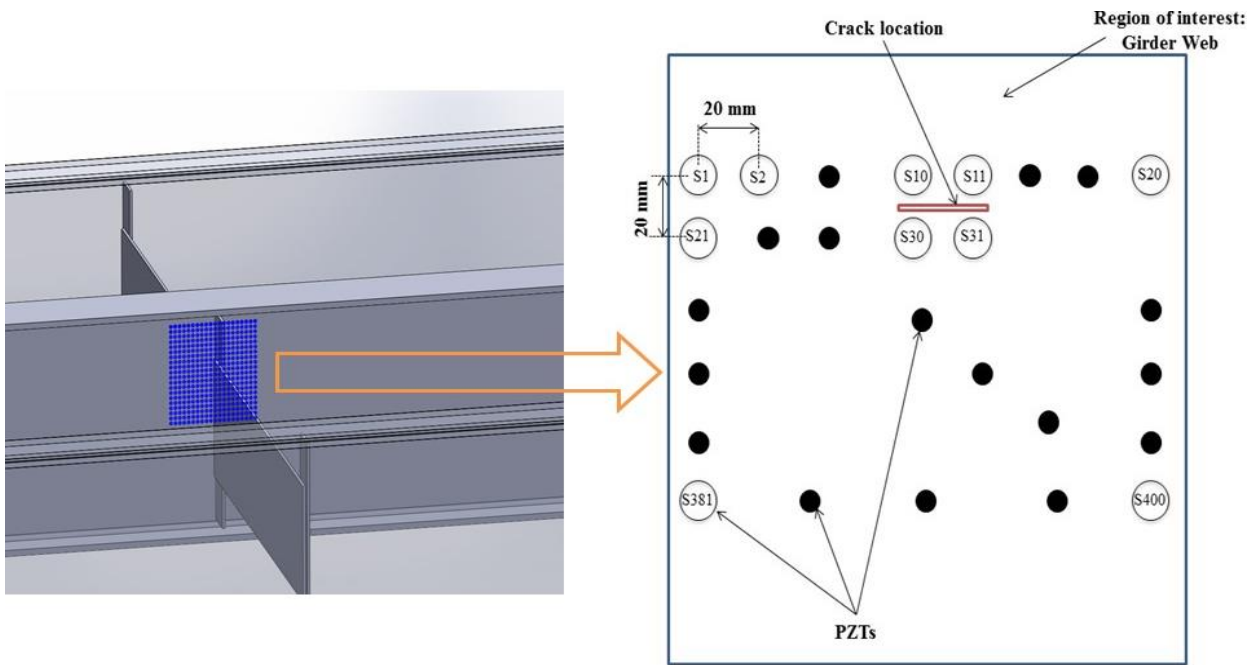


Figure 2-24: Locations of the sensing nodes.

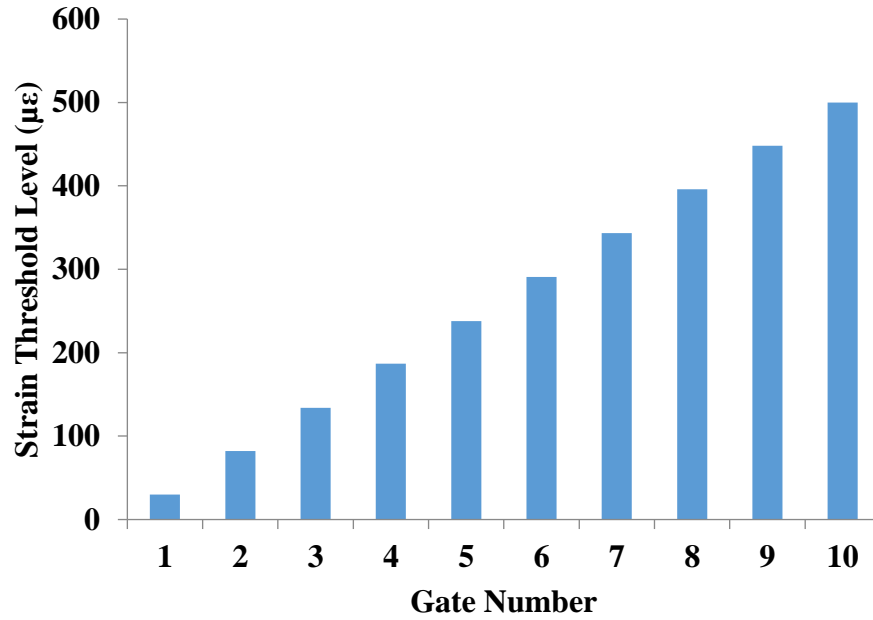


Figure 2-25: Strain threshold levels.

2.3.2.2. Information fusion

In order to evaluate the information provided by the sensing nodes, the μ and σ values for all of the 400 sensors for different damage scenarios are calculated. Then, a data fusion approach is proposed for the detection of damage progression in the girder. The basic idea is to use original parameters from the distribution (μ and σ) and define new features that include the effect of sensors network. The sensor fusion process integrates and extracts useful information from two or more sensors. Fused multi-sensor data can offer significant advantages in comparison with the data from a single sensor (Hall and Llinas, 2001). On this basis, it was decided to fuse the information provided by a group of sensors. Even if the location of damage is not known in advance, the group effect can be checked to assess the damage growth. A set of features Z_i are defined as:

$$\begin{cases} Z_{\sigma_i}^p = \frac{\sigma_i^p - \sigma_{av}^p}{\sigma_{STD}^p} \\ Z_{\mu_i}^p = \frac{\mu_i^p - \mu_{av}^p}{\mu_{STD}^p} \\ Z_{\sigma\mu_i}^p = \frac{\sigma_i^p - \mu_{av}^p}{\sigma_{av}^p} \\ Z_{\mu\sigma_i}^p = \frac{\mu_i^p - \mu_{av}^p}{\sigma_{av}^p} \end{cases} \quad (2-12)$$

where, $\mu_{av}^p, \mu_{STD}^p, \sigma_{av}^p, \sigma_{STD}^p$ are, respectively, the average of μ , standard deviation of μ , average of σ and the standard deviation of σ of all sensors for a specific damage state p. The subscript i is the number of the sensor (the data acquisition node). The new defined features are inspired from the conventional z-score function (Alavi et al, 2016a,b). It should be noted that a z-score is a statistical measurement of a score's relationship to the mean in a group of scores. As indicated by the equations above, the average and standard deviation of μ and σ include the effect of the whole group of sensors at the sensing location i.

2.3.2.3. Damage detection using support vector machine approach

A damage detection process can be treated as a pattern recognition problem (Alavi et al, 2016a). The solution is to use a classifier which can classify structures either as damaged or healthy. To this aim, an AI-based data fusion system is proposed for damage detection (Figure 2-26). The AI techniques are considered as alternatives to existing traditional methods for tackling real world problems. They determine the model structure by automatically learning from data. AI has different well-known branches such as artificial neural network (ANN), fuzzy inference system (FIS), adaptive neuro-fuzzy system (ANFIS), and support vector machines. In the last two decades, the AI methods have been widely used for tackling problems in civil engineering domains such as structural engineering, hydraulic engineering, geotechnical engineering, earthquake engineering, etc. In this context, some well-established studies are:

calculation tensile strength and yield strength of dual phase steels (Krajewski and Nowacki, 2014), modelling true stress of dynamic strain aging regime of austenitic stainless steel (Garg et al., 2014), non-destructive investigation of corrosion current density in steel reinforced concrete (Sadowski, 2013), prediction of the capacity of CCFT short columns (Ahmadi et al., 2014), prediction of the pull-off adhesion of the concrete layers in floors (Sadowski and Hola, 2013; Sadowski, 2013), modeling of shear strength of RC deep beams (Gandomi et al., 2013), structural assessment and damage identification, prediction of the scour below submerged pipeline, and scour depth downstream of sills (Azamathulla, 2012; Azamathulla et al., 2011), prediction of settlement of shallow foundations (Samui, 2008), maximum dry density and unconfined compressive strength of cement stabilized soil (Das et al., 2011), factor of safety of soil nailed slopes (Garg et al., 2014), prediction of soil liquefaction susceptibility (Samui and Sitharam, 2011), etc.

The proposed AI-based data fusion framework consists of the following main stages:

- Structural simulation;
- Information fusion in which features that are expected to characterize different properties of structures are extracted from a network of sensors; and
- Fusion of the clustered features. The data fusion is performed using the AI classifier.

Using the obtained μ and σ parameters from fitting the data to a Gaussian distribution, damage indicator features are obtained for a specified number of sensors. The defined features simultaneously fuse the information provided by array of scattered sensors. The damage indicator vectors are then used for the calibration of the classifier. Subsequently, a validation phase is performed to check the damage detection performance of the classifier.

Among different AI techniques, SVMs have been widely used in the field of damage detection

and structural identification (Worden and Lane, 2001; Satpal et al., 2016).

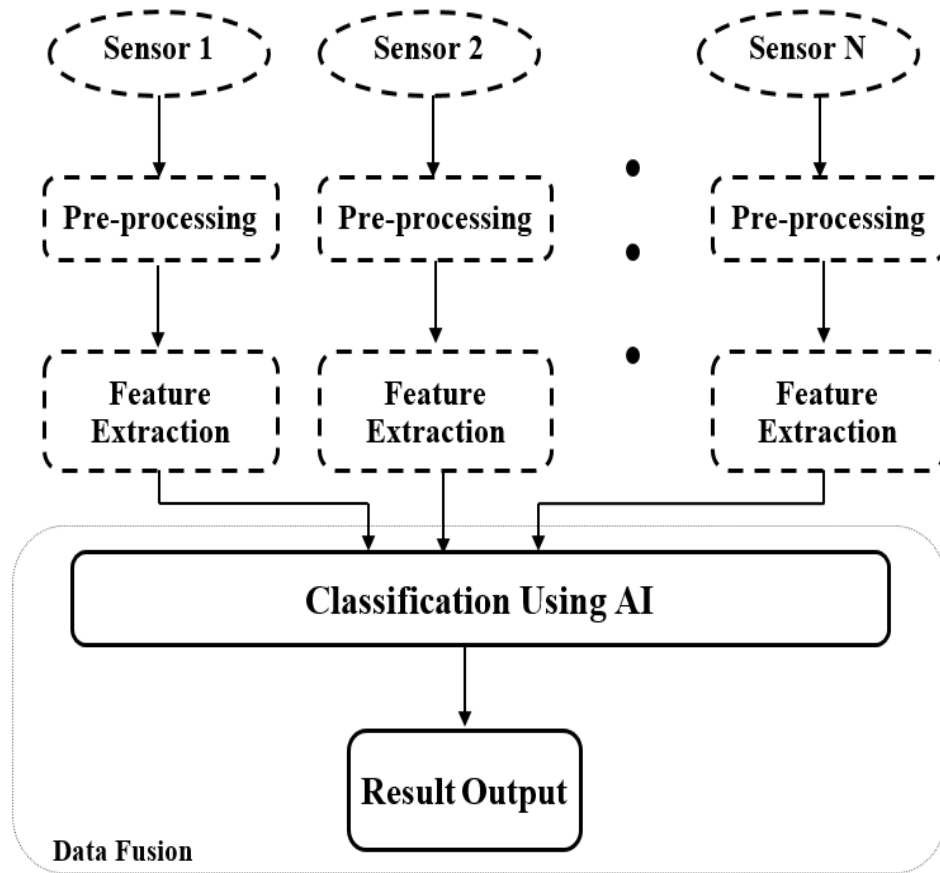


Figure 2-26: Data fusion flowchart.

Some of the main advantages of the SVM method are as follows (Burges, 1998):

- It has regularization parameters in order to avoid over fitting;
- It uses the kernel trick which makes the user able to design the kernel via engineering approach;
- The SVMs optimization techniques are based on a convex optimization to avoid local minima problems. SVM training always find a global minimum;
- They provide an alternative solution when linear decisions hyper-planes are not sufficient to separate the classes by mapping the input data into a feature space resulting in a

nonlinear classifier.

Other AI methods suffers from local minima, however the solution given by an SVM is always unique and global. Unlike ANN that they are based on empirical minimizations, the SVMs are less prone to overfitting because they use structural minimization.

A general problem for classification with SVM can be represented as follows: Suppose a given training set $S = \{(\underline{x}_i, y_i), i = 1:N\}$ where N is the number of training samples, \underline{x}_i is the feature vector that has d dimensions, and y_i is the label of the data and it is a one dimensional value. The objective of this classification problem is to find a classifier g that can classify a new example (\underline{x}_n, y_n) . In binary classification, most of the solutions are explored by finding a separating hyperplane between the classes. The SVM classifier tends to maximize the margin between two classes by determining a minimum number of support vectors (SVs). However, the main issues with using a separating hyperplane are that the solution may not be extended and generalized to classify unseen examples, and the data could be nonlinearly separable. This method was originated from a binary classification. In fact, there are many hyperplanes that can separate the data. Many of these hyperplanes do not generalize well and they may misclassify a new sample. Therefore, the idea of SVM is to select the best hyperplane that maximizes the margin between the data of different classes (Figure 2-27).

The separating hyperplane can be defined as follows:

$$\{\underline{x} \in H, g(\underline{x}) = \langle \underline{w}, \underline{x} \rangle + b = 0\} \quad \underline{w} \in H \text{ and } b \in \mathbb{R} \quad (2-13)$$

where \underline{w} is a normal vector that defines the hyperplane, b is bias, and $\langle ., . \rangle$ is the dot product.

In a two-classes d -dimensional problem, the separating conditions are given by:

$$\underline{x}_k \in C_1 \text{ if } g(\underline{x}_k) \geq 1 \quad (2-14)$$

$$\underline{x}_k \in C_2 \text{ if } g(\underline{x}_k) \leq -1 \quad (2-15)$$

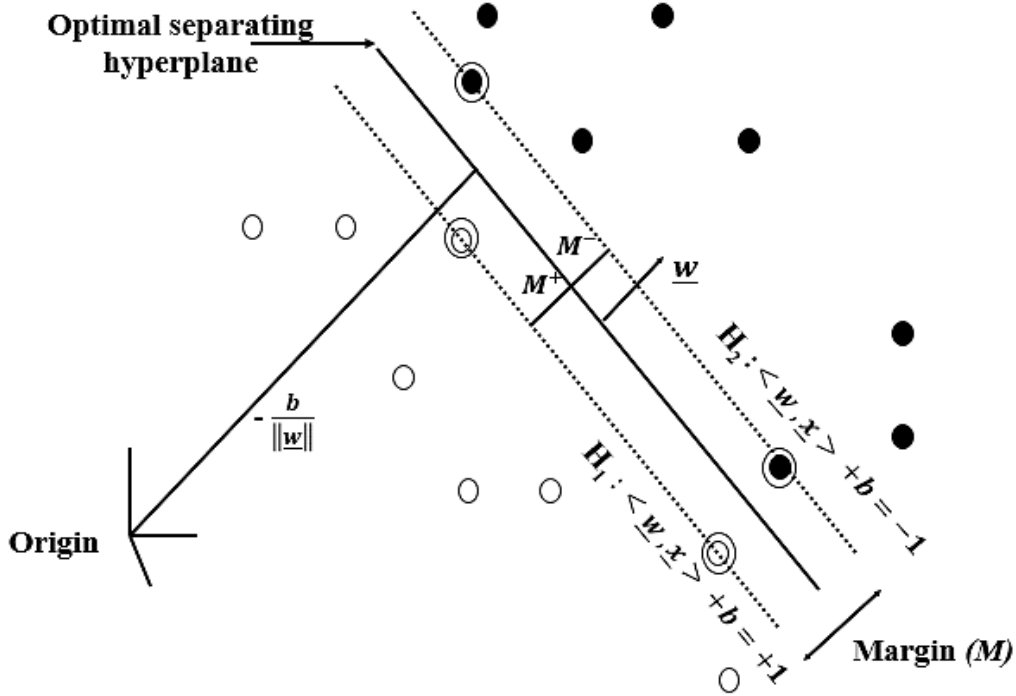


Figure 2-27: Schematic illustration of the optimal separating hyperplane and margins for SVM with samples from two classes.

Both of the preceding equations can be combined into a single equation as:

$$y_k g(\underline{x}_k) \geq 1 \quad (2-16)$$

where y_k is the class label given as: $y_k = 1$ for class C_1 and $y_k = -1$ for class C_2 . The value $\frac{b}{\|\underline{w}\|}$ in Figure 2-27 determines the distance of the hyperplane from the origin. By denoting M^+ and M^- the margin widths between the separating hyperplane and the SVs, the margin M is defined as (Rajasekaran and Amalraj, 2002; Saridakis et al., 2008):

$$M = M^+ + M^- = \frac{|\langle \underline{w}, \underline{x} \rangle + b|_{\underline{x} \in H_1}}{\|\underline{w}\|} + \frac{|\langle \underline{w}, \underline{x} \rangle + b|_{\underline{x} \in H_2}}{\|\underline{w}\|} = \frac{2}{\|\underline{w}\|} \quad (2-17)$$

Therefore, the margin width M can be maximized by minimizing $\|\underline{w}\|^2$. The problem can be formulated as follows:

$$\min_{\substack{w \in H \\ b \in R}} \frac{1}{2} \|\underline{w}\|^2 \quad \text{Subject to} \quad y_k g(\underline{x}_k) \geq 1 \quad (2-18)$$

The constraint equation could be written as:

$$y_k g(\underline{x}_k) - 1 \geq 0 \quad (2-19)$$

or:

$$-y_k (\langle \underline{w}, \underline{x}_k \rangle + b) + 1 \leq 0 \quad (2-20)$$

Now, the problem is transformed into an optimization problem with a convex quadratic optimization function. It is subject to a linear constraint equation that could be efficiently solved using Lagrangian optimization technique. The objective function to minimize becomes:

$$L(\underline{w}, b, \alpha) = \frac{1}{2} \|\underline{w}\|^2 - \sum_{k=1}^N \alpha_k [y_k (\langle \underline{w}, \underline{x}_k \rangle + b) - 1] \quad (2-21)$$

The preceding equation can be minimized by setting the derivatives of L with respect to \underline{w} and b to zeros:

$$\nabla_w L(\underline{w}, b, \alpha) = 0 \quad (2-22)$$

$$\frac{\partial L(\underline{w}, b, \alpha)}{\partial b} = 0 \quad (2-23)$$

which gives:

$$\underline{w} = \sum_{k=1}^N \alpha_k y_k \underline{x}_k \quad (2-24)$$

and:

$$\sum_{k=1}^N \alpha_k y_k = 0 \quad (2-25)$$

By replacing \underline{w} into the Lagrangian and simplifying it, we obtain the following dual optimization problem:

Maximize (over α):

$$L(\underline{w}, b, \alpha) = -\frac{1}{2} \sum_{i,j=1}^N y_i y_j \alpha_i \alpha_j \langle \underline{x}_i, \underline{x}_j \rangle + \sum_{i=1}^N \alpha_i \quad (2-26)$$

Subject to:

$$\sum_{i=1}^N \alpha_i y_i = 0 \text{ and } \alpha_i \geq 0 \text{ for } i = 1:N \quad (2-27)$$

where α_i are the Lagrangian multipliers. Finally, the optimal hyperplane is then described by the following equation:

$$g(\underline{x}) = \sum_{k=1}^N \alpha_k y_k \langle \underline{x}_k, \underline{x} \rangle + b \quad (2-28)$$

Points with $\alpha_i > 0$, are called SVs and lie on H_1 or H_2 and the classification of a new sample \underline{x}_n is given by the sign $g(\underline{x}_n)$. Up to this point, we have considered the case where the data is linearly separable. However, most of classification problems with real data are not linear. Therefore, the concept of optimal separating hyperplane is generalized to a global solution that minimizes a cost function and satisfies the following two criteria:

- Maximize the margin (as in the precedent case of linearly separable data)
- Minimize the error of misclassification

The new cost function (ψ) is now defined as:

$$\Psi(\underline{w}, \xi) = \frac{1}{2} \|\underline{w}\|^2 + C \sum_{k=1}^N \xi_k \quad (2-29)$$

where ξ_k is called the slack variable that quantifies the non-separability, and C is the regularization parameter that controls the penalty factor due to misclassification (box constraint). The same dual problem, as for the case of separable data, represents the formulation of this case. Up to this point, SVM is presented for both linearly separable and linearly non-separable cases. In order to improve the ability of the classifier to separate classes, the method described above can be generalized by introducing a nonlinear discriminant function. In this context, SVM uses the kernel method to map the data into a higher dimensional feature space. Accordingly, the data is more likely to be separable following the previously described method by merely defining a hyperplane that is fully defined by its normal vector \underline{w} and b value. If d is the dimension of the input data, then \underline{w} is defined in a higher dimensional space of dimension d' ($d' > d$). This procedure is achieved by using a map function Φ . Therefore, the inner product of the original space is replaced by the inner product of the transformed space as follows:

$$\langle \Phi(\underline{x}_i), \Phi(\underline{x}_j) \rangle \quad (2-30)$$

The only problem here is that the inner product of the transformed space is very costly to evaluate and sometimes impractical. Therefore, the kernel method provides an efficient way to tackle this problem by avoiding the computation of the inner product in the transformed space as follows:

$$K(\underline{x}_i, \underline{x}_j) = \langle \Phi(\underline{x}_i), \Phi(\underline{x}_j) \rangle \quad (2-31)$$

where K is the kernel function evaluated in the input space. The final resulting discriminant function is defined by:

$$f(\underline{x}) = \sum_{i=1}^N \alpha_i K(\underline{x}_i, \underline{x}) + b \quad (2-32)$$

The decision rule is based on the sign of $f(\underline{x})$. Typical kernel functions are:

- Polynomial: $K(\underline{x}_i, \underline{x}_j) = (\langle \underline{x}_i, \underline{x}_j \rangle + 1)^d$
- Radial basis function (RBF) (Gaussian): $K(\underline{x}_i, \underline{x}_j) = \exp\left(-\gamma \|\underline{x}_i - \underline{x}_j\|^2\right)$
- Sigmoid: $K(\underline{x}_i, \underline{x}_j) = \tanh(\eta \langle \underline{x}_i, \underline{x}_j \rangle + r)$

where d is the polynomial degree, γ , η and r are numbers that represent the kernel parameters.

$\gamma = \frac{1}{2\sigma^2}$, and σ is the width of the radial basis function. The kernel-based implementation needs

the determination of both the kernel parameter and the regularization parameter C .

For this study, the RBF kernel is used and the detection rate (DR) is used to evaluate the classifier performance as follows:

$$Detection\ rate = \frac{Number\ of\ data\ correctly\ classified}{Total\ number\ of\ data} \quad (2-33)$$

The total number of data points is 2400 (400 sensing nodes \times 6 damage states). The labels to be classified are 6 damage states (D1, ..., D6) each represented the girder condition after 1 million cycles. The data is divided into three subsets: 70 % for training, 15% for testing, and 15 % for validation. The SVM algorithm is run for different sensor configurations by adding the number of sensors from 1 (single sensor) to 400 (the entire network). The optimal parameters δ and C are found through an extensive searching algorithm. Thereafter, the sensitivity of the model to sampling error is evaluated by repeatedly randomly partitioning the data. For each sensors configuration, five tests are performed to estimate the average accuracy and evaluate the sensitivity of the model to a particular training sample.

Figure 2-28 displays the results for the testing set for different sensors configurations. The black bars on the figure represents the sensitivity analysis results.

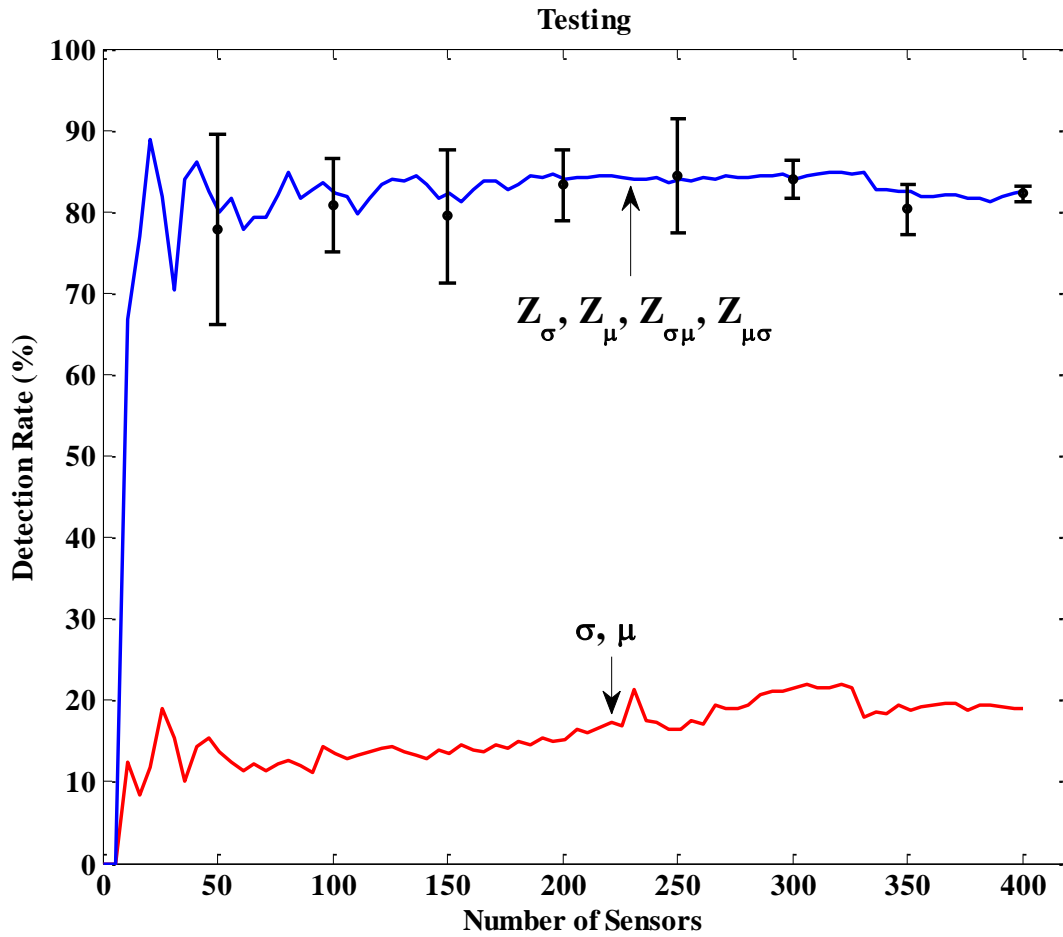


Figure 2-28: SVM performance on the testing data.

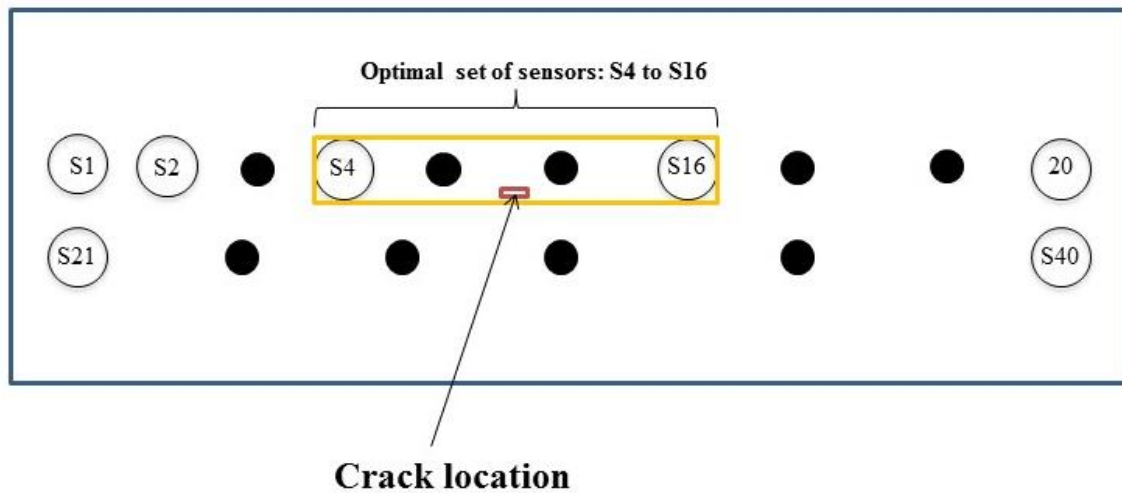
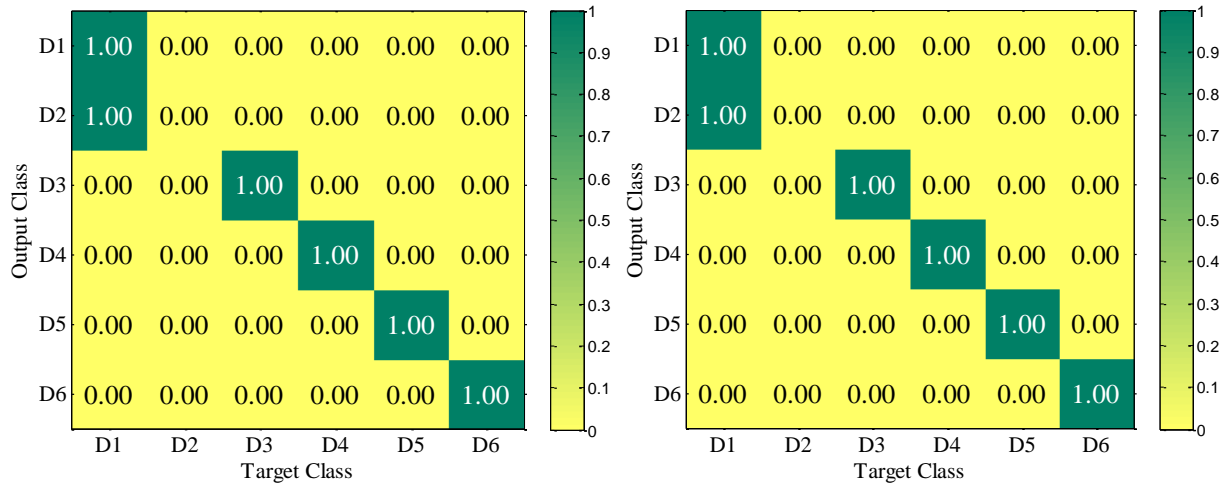


Figure 2-29: Set of sensors with the highest detection rate.

The results indicate that the new Z features have good performance for both testing and validation sets. Using only the individual sensing features μ and σ results in a very low performance (around 20% to 33%). An interesting observation from Figure 2-28 is that the curve presents the highest values for a number of sensors below 30. This indicates that the damage is located in the upper area of the web where the first 30 sensors are located. The best detection rate for the training, testing and validation is obtained using Sensing nodes 4 to 16 as shown in Figure 2-29. The optimal value of the δ and C parameters are 0.9, 100, respectively. The best performance of the classifier is:

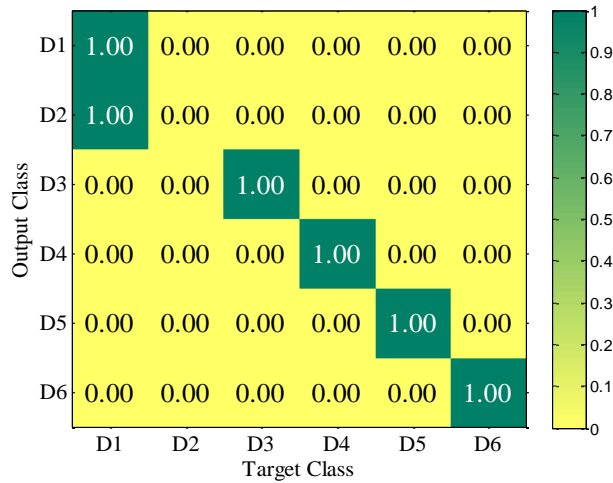
- Training = 83%
- Testing = 82%
- Validation = 85 %

Figure 2-30 displays the confusion matrixes for the best sensor configuration. A confusion matrix is a table that contains information about actual and predicted classifications. The confusion matrix can be used to describe the performance of the classifier (Fawcett, 2006).



(a) Training data

(b) Testing data



(c) Validation data

Figure 2-30: Confusion matrixes for the best sensor configuration.

Each column of the matrix represents the instances in predicted class, while each row represents the instances in an actual class. The damage states correctly classified are found along the diagonal of the matrix. In other words, if CM denotes the confusion matrix, each diagonal term CM_{ii} represents the results of classification of the i^{th} class. The off-diagonal terms $CM_{ij}(i \neq j)$ represent the classification error (MathWorks, 2016).

As seen in Figure 2-30, class 2 is misclassified as class 1 in all cases. This indicates that there is no important variation in strain amplitude between 10 mm and 20 mm crack lengths. Therefore, the classifier cannot differentiate between the two classes. However, for the other damage states, the detection performance is satisfactory.

2.4. Summary

The sensor operates by harvesting the energy from the host structure. It can record the cumulative durations of the applied strain signal at predefined threshold levels. However, the sensor output is compressed into a single histogram. This makes the interpretation of the data very challenging. In the case of a uniform PFG sensor, the output of each sensor could be characterized based by fitting the cumulative loading time histogram to a CDF.

The performance of the self-powered wireless sensor with uniform distribution was evaluated for two steel structures with complex geometry. FE models were developed to predict the strain behavior under external loadings. Thereafter, the sensor output was defined based on the strain-time history and fitted to a CDF distribution. The first investigated case is the crack propagation of a gusset plate similar to the U10W plate that caused the failure of the I-35W bridge in Minneapolis, MN, USA. The results indicate that the damage could be detected using the initial damage predictors μ and σ . For the case where the sensor is located near the crack tip, the PDF shift to the left and they expands due to damage progression. In addition, the STD of a group of sensors was found to be a good indicator of the crack propagation in gusset plates and of a good estimator of its severity. The STD of a group of sensors increases between damage states. Furthermore, a search algorithm was proposed to localize the crack. The results show that the crack can be localized using the maximum variation of the STD of all damage classes. In conclusion, using the information of a network of PFG sensors, the damage can be accurately

detected, localized and quantified.

In addition, the sensor detection capabilities were evaluated for the case of fatigue cracking in steel bridge girders. In order to evaluate the performance of the sensor, a numerical study was carried out on a typical girder. After obtaining the initial damage indicators, a data fusion model was defined based on the previously extracted features from the sensors network. The new features were inputted to an SVM classifier. The results indicate that the classification performance was increased using the data fusion model. It was observed that the SVM models could accurately classify most of the damage stages, specifically for cracks larger than 10 mm. Besides, tracking the performance of the SVM models gave an insight into the damage location.

CHAPTER 3. DAMAGE IDENTIFICATION IN STRUCTURES USING NON-UNIFORM PFG SENSORS²

3.1. Overview

The main goal of this chapter is to evaluate the performance of nonuniform class of self-powered PFG sensors for the detection damage progression. The proposed approach is evaluated on a steel plate and pavement structures. Section 3.2. describes the working principles of this class of sensors. Section 3.3.1. focuses on the detection of multi-class damage in steel plates. To this aim, an in-plane tension test is carried out on a thin steel plate with different notch sizes. Several piezoelectric transducers are attached on the plate to measure the changes of charge on the floating-gates due to damage progression. The cumulative voltage droppage for each memory gate is used to extract damage indicator features. A support vector machine classification approach is then utilized for multi-state damage detection. The obtained trends are analyzed and discussed in detail. In section 3.3.2.1, an asphalt concrete slab is studied to detect bottom-up cracking. The damage detection approach is verified numerically and experimentally. In the third section of this chapter (section 3.3.2.2), a surface sensing approach is proposed to detect bottom cracking in pavements. Different FE models are developed to analyze the response of the pavement under a dynamic moving load. The damage is defined using the element weakening method (EWM). A data fusion method integrated with a probabilistic neural network classifier is used to classify different damage states based on the response of the surface mounted PFG sensors.

² The presented results in this chapter were published in Hasni et al. (2017c,d,e,f).

3.2. Working mechanism of nonuniform PFG sensors

Figure 3-1 shows the difference of outputs between the uniform and nonuniform sensors. As previously described in Chapter 2, each floating gate has an injection rate (V_{inj}). This parameter is property of the gate that controls the injection of the electrons into the gate. The injection rate is correlated with the voltage droppage rate (V_{inj}) across the gate. The rate V_{inj} is defined as the ratio of voltage droppage during one second of injection of electrons. Figure 3-1(b) and 3-1(c) show an illustrative example of the voltage droppage calculation for gates with constant and non-constant injection rates, respectively. Note that the cumulative time at specific pre-defined strain/voltage thresholds is proportional to the voltage droppage across the memory gate.

As seen in Figures 3-1(b) and 3-1(c), Gates 1 to 3 are recording the changes of voltage on the floating gates due to electron injection for a random excitation given in Figure 3-1(a). As discussed in Chapter 2, the output of the uniform PFG sensor can be characterized by a Gaussian cumulative density function. In this case, the mean of cumulative time distribution (μ) and the standard deviation (σ) accounting for the load and frequency variability can be considered as viable tools to define the sensor output data (Hasni et al., 2017a; 2017b). These parameters are obtained by curve fitting of the sensor output distribution collected from the entire memory cells, as indicated in Figure 3-1(b). As can be observed from Figure 3-1(c), analysis of the sensor outputs becomes more challenging for the case of nonuniform sensor, and the cumulative voltage droppage cannot be fitted to a Gaussian distribution.

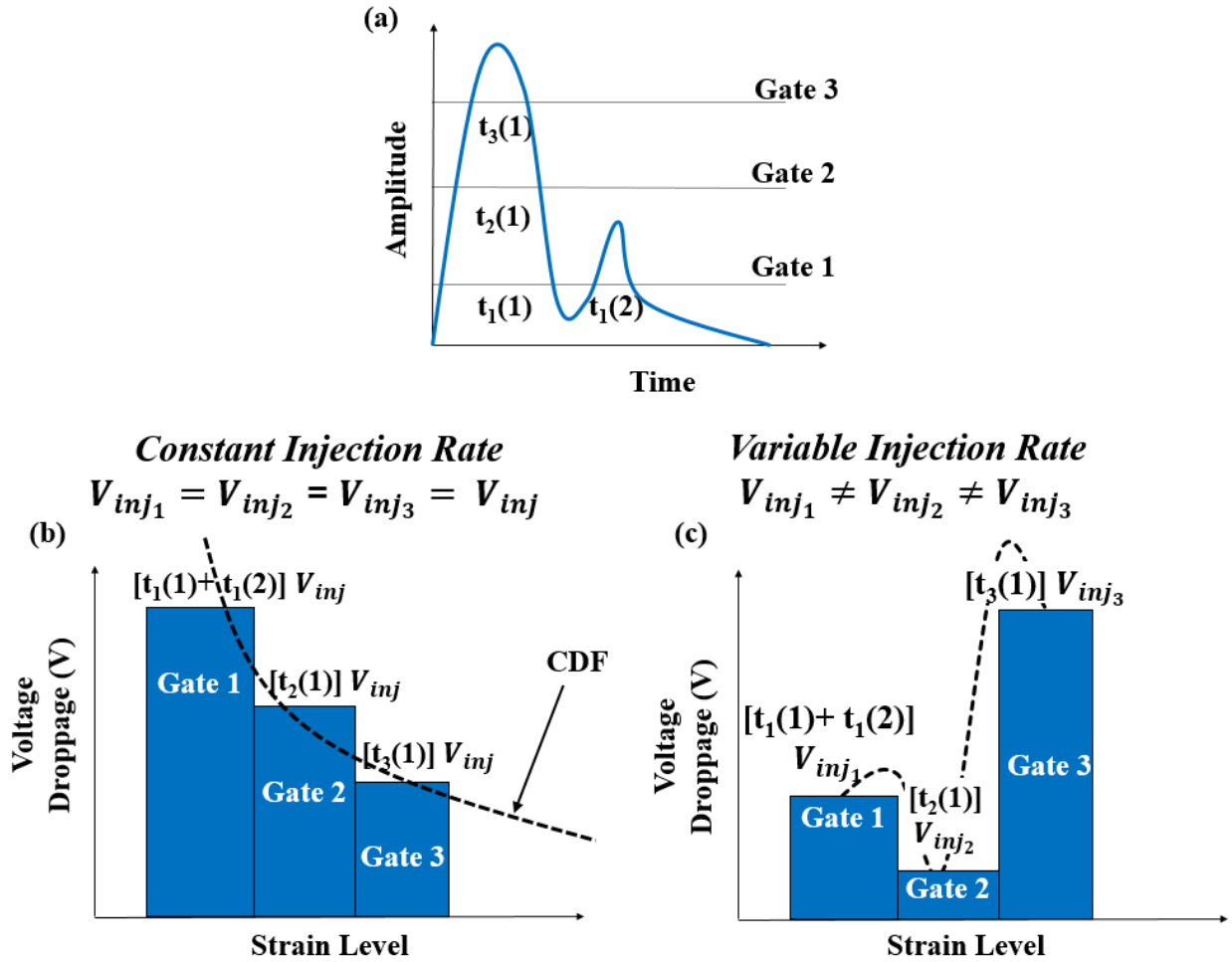


Figure 3-1: Working principle of nonuniform PFG sensor.

3.3. Evaluation of the performance of the nonuniform PFG sensor

3.3.1. Health monitoring of steel plates

The process of detecting damage progression using PFG sensors is divided into two major stages: (1) Individual sensors: This step is focused on finding a reasonable relationship between the activation and voltage droppage of the floating-gates of individual sensors and damage progression, and (2) Data fusion in a network of sensors: This stage is developed to analyze spatial measurements over the structural area. The goal is to extract features that

simultaneously fuse the information provided by multi-sensors. The fused data is then fed into an SVM classifier for multi-stage damage detection.

3.3.1.1. Detection of damage progression using individual self-powered PFG sensors

The performance of the PFG sensor is evaluated on a steel plate subjected to an in-plane tension. The load is applied using an MTS servo-hydraulic machine in a displacement controlled mode. A 16 in × 6 in × 1/32 in (406.4 mm × 152.4 mm × 0.8 mm) structural steel plate grade A36 is used. In order to satisfy the boundary conditions of uniaxial tension test, four thick steel plates 6 in × 2 in (152.4 mm × 50.8 mm) are placed in upper and bottom boundaries of the plate to restrain all the rotational and lateral translational degree of freedoms of the upper and lower edges. The upper boundary is fixed, and the lower boundary is subjected to a displacement via the MTS machine. A set of 20 PZT ceramic transducers are attached on the surface of the plate to measure the voltage induced by the loading. The type of the used PZTs is PZT-5A from Steiner & Martins, Inc. The properties of PZT-5A are listed in Table 3-1.

The PZTs output voltage is read on a NI 9220 data acquisition system (with 1 GΩ impedance) in parallel with the sensor. In addition, strain values are also measured on NI 9236 data acquisition system. The corresponding strain gage factor is 1.2 and the grid resistance is 350 Ω.

In order to attach the PZT discs to the steel plate, different adhesives are tested. Among the adhesives tested (e.g. HBM X-60 cement paste, J-B SteelStik Epoxy, and CC-33A adhesive), CC-33A epoxy is found to perform more consistently.

Figure 3-2 illustrates a schematic representation of the experimental setup. Locations of the PZTs and strain gages are shown in Figure 3-3. The tests are performed at 2 Hz loading frequency for 0.08 mm, 0.12 mm and 0.16 mm displacement amplitudes. Herein, the results for 2 Hz and 0.16 mm displacement are presented.

Table 3-1: Properties of PZT-5A.

PZT Type	Dimensions:		Elastic Modulus (<i>GPa</i>)	Capacitance (<i>nF</i>)	Electrical Permittivity ($\times 10^{-9} \frac{F}{m}$)	Piezoelectric Constant (d_{31}) ($\times 10^{-12} \frac{m}{V}$)
	Diameter (<i>mm</i>) \times Thickness (<i>mm</i>)					
PZT-5A Discs	$\phi 12 \times 0.6$		76	2.9	16.38	-190

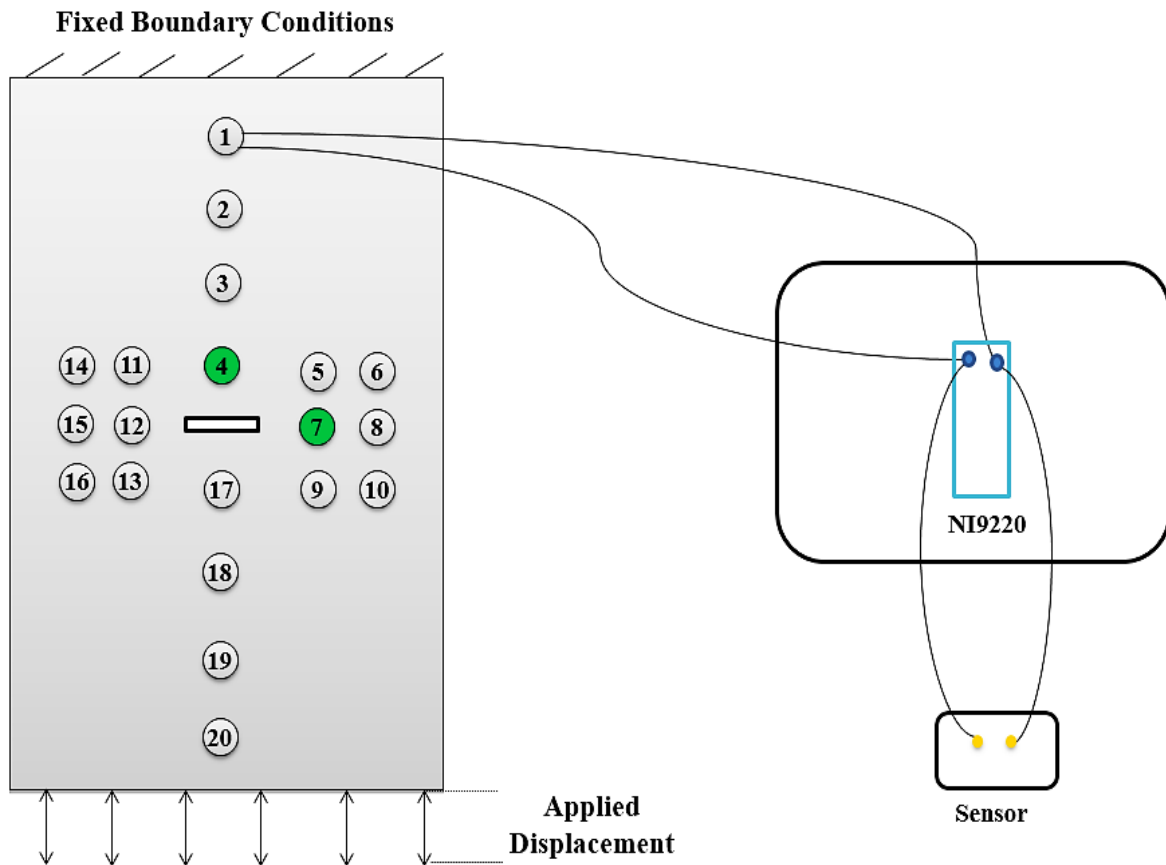


Figure 3-2: A schematic representation of test setup.

Before starting each test, a pre-load equal to 4 kN is applied to the plate to ensure that it is seated on the fixture. Thereafter, a cyclic displacement is applied to the edge of the specimen. The number of cycles is 40 for each test. Damage is introduced at the middle of the plate as shown in Figure 3-2. The damage states are defined by increasing the notch size ($2a$) as follows:

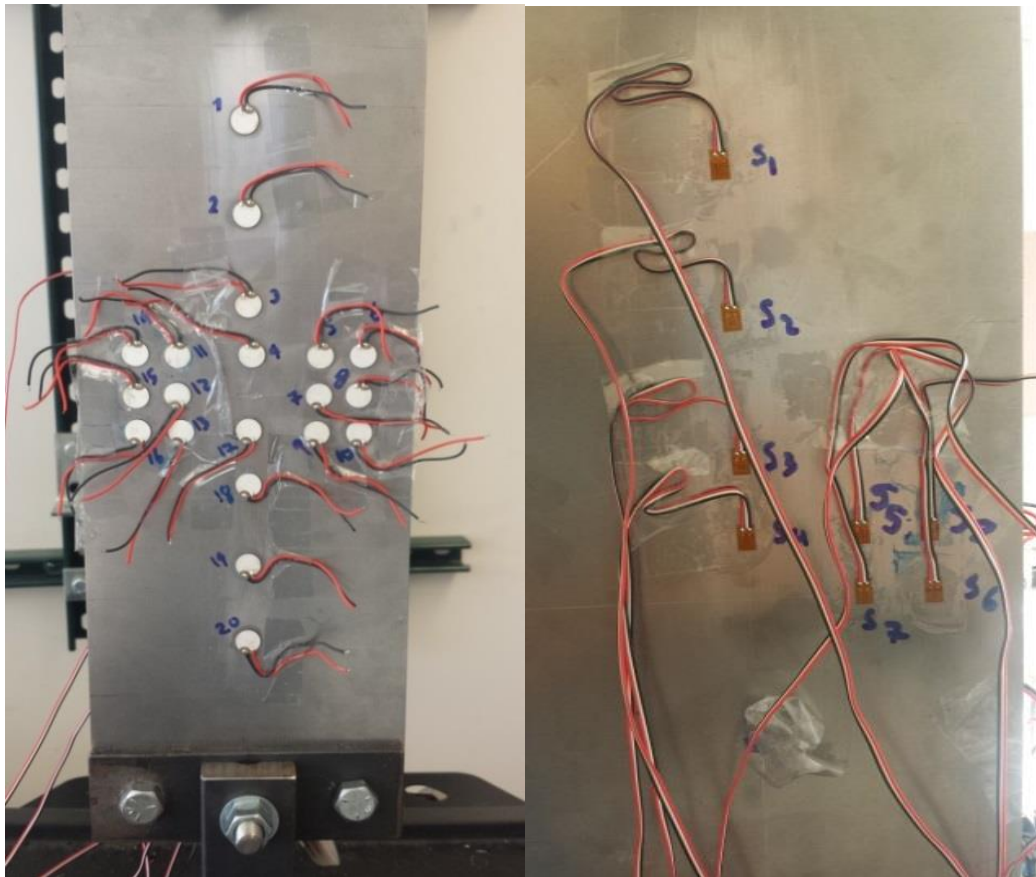


Figure 3-3: Layout of PZTs and strain gages.

- Intact: $2a = 0$ mm (Intact plate)
- Damage 1 (D1): $2a = 10$ mm
- Damage 2 (D2): $2a = 20$ mm
- Damage 3 (D3): $2a = 30$ mm

It should be noted that the notch is considered in the horizontal direction for a better control over

the crack size in such uniaxial tensile loading. However, if the notch is located at other location and at different direction, the results will be the same using the same proposed methodology in this work.

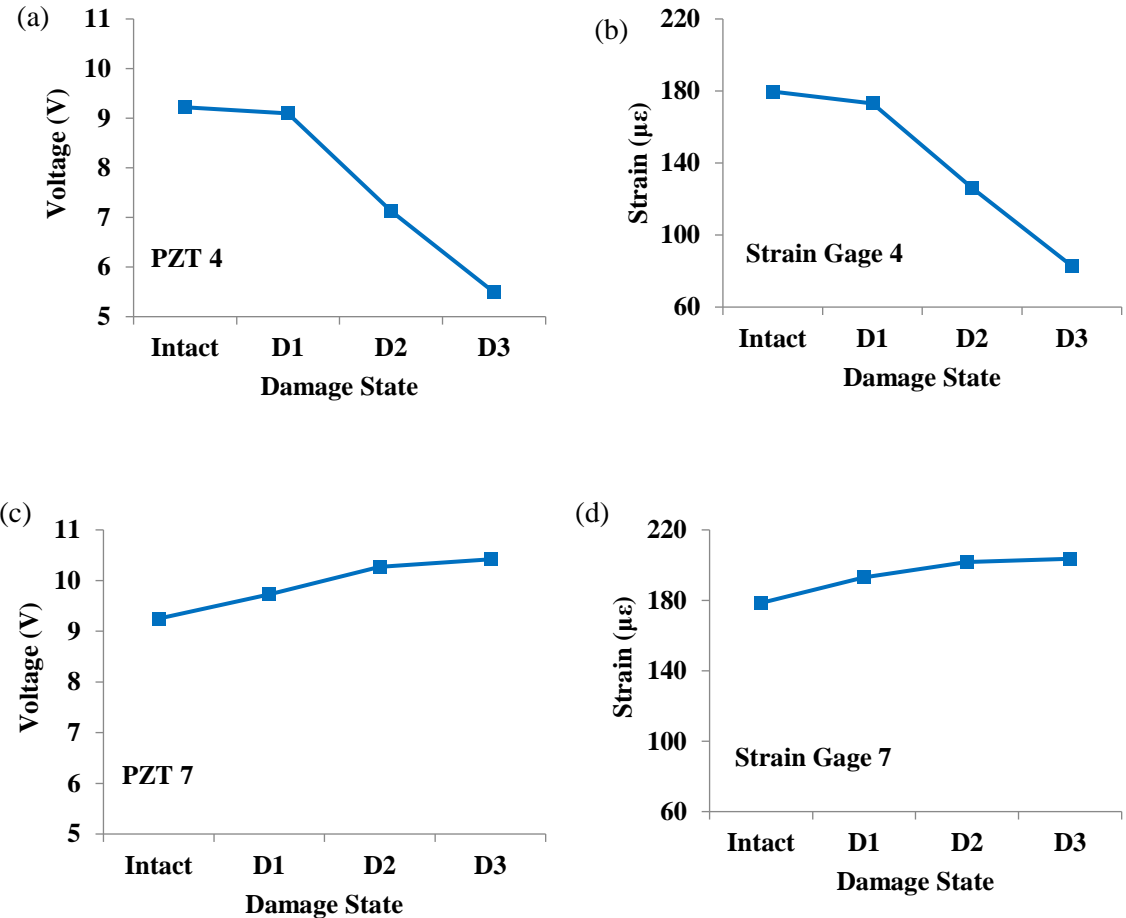


Figure 3-4: A comparison of maximum voltage and strain for 0.16 mm displacement and 2 Hz loading frequency.

On the other hand, given the small size of the sensors and the fact that that they do not rely on batteries, large number of sensors can be installed near the damage sensitive areas allowing for improved resolution and detection capabilities. In addition, preliminary results from finite element simulations can be considered as a good option for the determination of approximate

sensors locations. On this basis, denser array of sensors can be considered for regions with maximum stress and strain concentrations. In fact, the variation of the voltage droppage from the sensors is more prominent at the damage vicinity. Thus, regions of the structures that are known to be more susceptible to damage need a denser network of sensors. This is a fundamental requirement for all available commercial sensors to detect damage in structures.

Typical outputs measured by the PZTs and strain gages along (PZT 7, Gage 7) and on the top (PZT 4, Gage 4) of the notch are shown in Figure 3-4. Figure 3-5 presents the percentage variation of the strain and the voltage at locations 4 and 7 when the damage progresses. As one would expect, the voltage and strain measured by PZT 7 and Gage 7 continuously increase as the damage progresses. However, the voltage and strain have decreasing trends for the PZTs located perpendicular to the direction of the crack (PZT 4, Gage 4).

The PFG sensor used in this study to monitor the damage progression has 7 floating-gates with different injection rates.

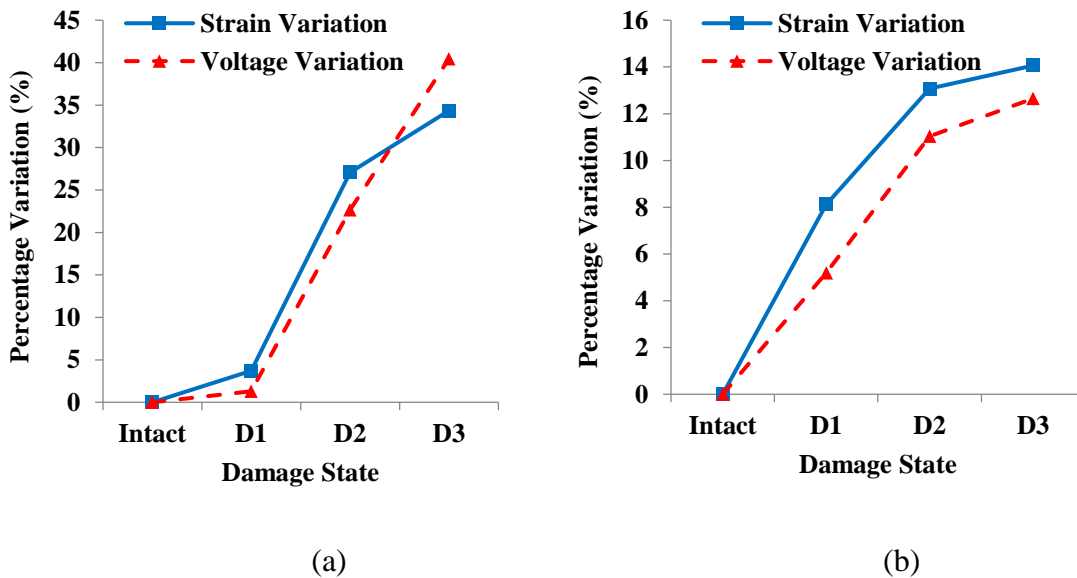


Figure 3-5: Strain and voltage variation for: (a) PZT 4 and Strain Gage 4, and (b) PZT 7 and Strain Gage 7.

The channels were programmed to trigger at different voltage thresholds. The impact-ionized hot-electron injection (IHEL) process at the floating-gate memory cell is activated only when the voltage is higher than the injection threshold. Therefore, once the voltage drops below the injection threshold of a channel, it stops recording. The higher is the generated voltage, the higher is the number of channels that are logging. In addition, the injection rate of each channel depends on the level of voltage generated by the piezoelectric transducer. The minimum voltage level that is required to trigger the injection in each of the channels is shown in Figure 3-6. The sensor voltage changes are recorded for all the PZT locations and for different damage states. In total, 560 voltage outputs are extracted from the sensors.

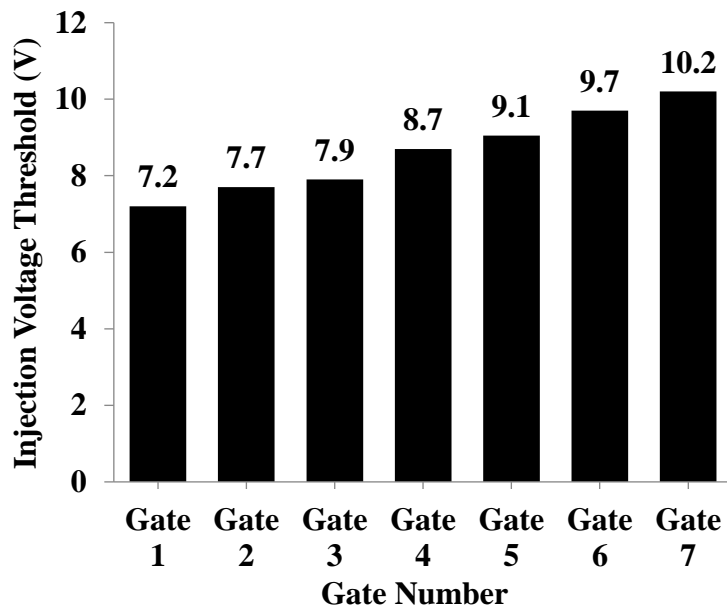


Figure 3-6: The injection thresholds for the PFG sensor.

For brevity, only results for sensing nodes located along and on the top of the notch are presented herein. Figures 3-7 and 3-8 show the voltage droppage across the floating-gates of the sensor at locations 4 and 7, respectively. As seen in these figures, the recorded droppage of the voltage highly

depends on the damage state. Each damage state corresponds to the strain sensed, and therefore the voltage amplitude generated by the PZTs. Note that, as soon as the voltage generated by a PZT exceeds a threshold corresponding to one of the gates, the procedure of electron injection initiates, and subsequently the voltage of that gate starts decreasing. Conversely, if the voltage generated by the PZT transducer is below the gate injection threshold, the injection stops, the channel shuts off, and therefore the charge on the floating-gate remains unchanged. As an example, the voltage amplitude of PZT 4 dropped from 9.22 to 5.49 V due to damage progression (see Figure 3-4(a)). At this location, the stress concentration decreases by increasing the notch size. The response of the PFG sensor indicates that gates 1 to 5 are only recording the cumulative voltage droppage for the intact and D1 modes (Figure 3-7(a)-(e)). This is because the PZT voltage values for the intact and D1 states are, respectively, 9.2 and 9.1 V which exceeded the threshold of all first 5 gates. On the other hand, the voltage is not changed at gates 6 and 7 because their activation thresholds are near 10 V. This voltage is greater than the maximum delivered voltage by PZT 4 for all damage states. As a result, the voltage at gates 6 and 7 is kept constant at its initial value (1.2 V). The damage progression process can be monitored using gates 1 to 5. In this case, as soon as the damage approaches the D2 phase, the strain decreases, and the voltage amplitude drops to 7.13 V which is below the injection thresholds of all gates. Hence, the channels shut off.

An inverse behavior can be observed from Figure 3-8 for PZT 7. This PZT is located along the notch and therefore it is experiencing higher strains as the notch size increases. As seen in Figures 3-8(a)-(e), gates 1 to 5 have experienced a drop in the charge, as the voltage generated by PZT 7 exceeded their thresholds for all damage states. Gates 6 and 7 are activated only after the voltage of PZT 7 goes beyond 9.7 V and 10.2 V, after the intact (gate 6) and D1 (gate 7) damage states (Figures 3-8(f) and 3-8(g)). Clearly, the gate activation can be considered as an indicator of damage occurrence.

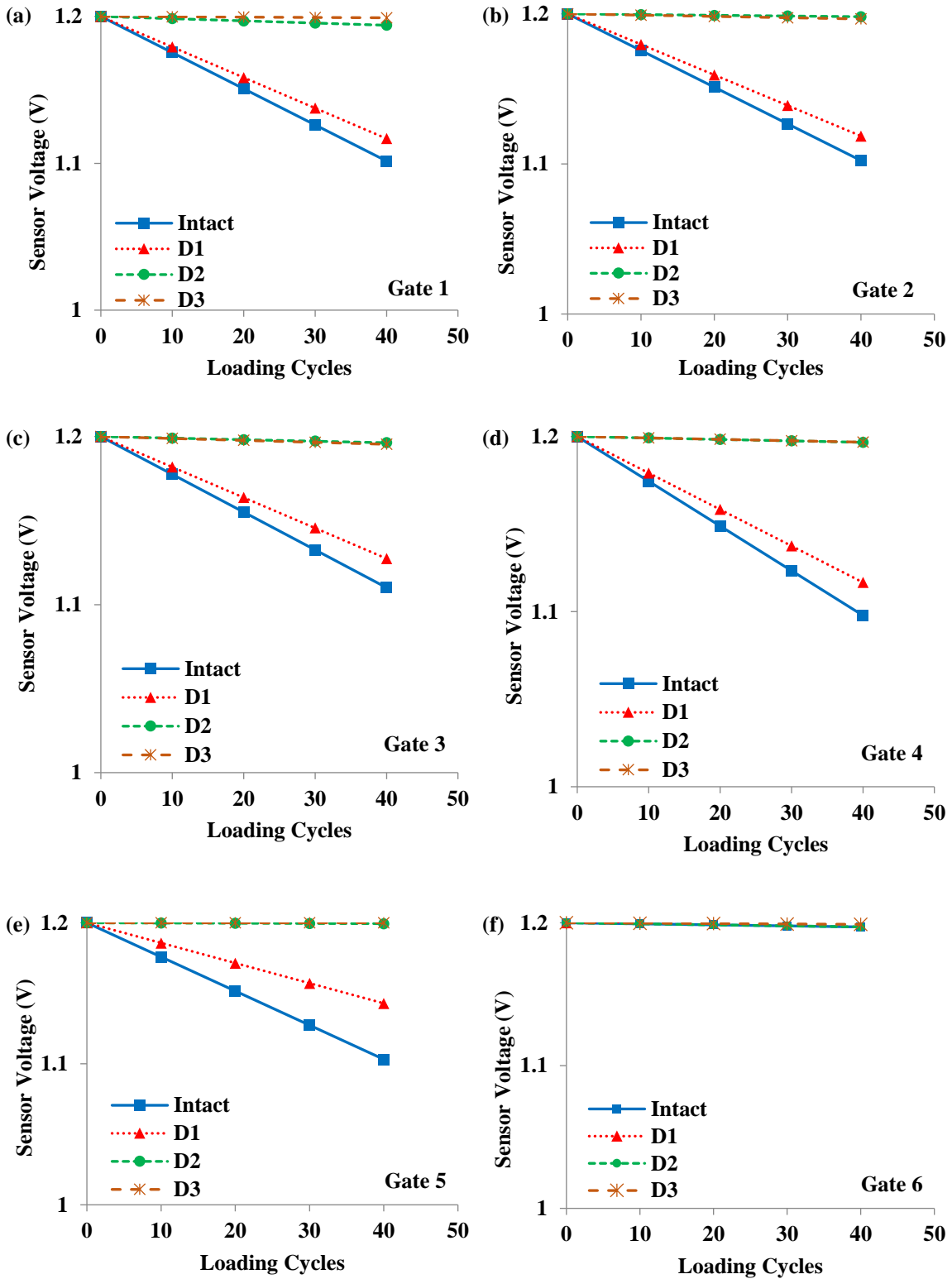
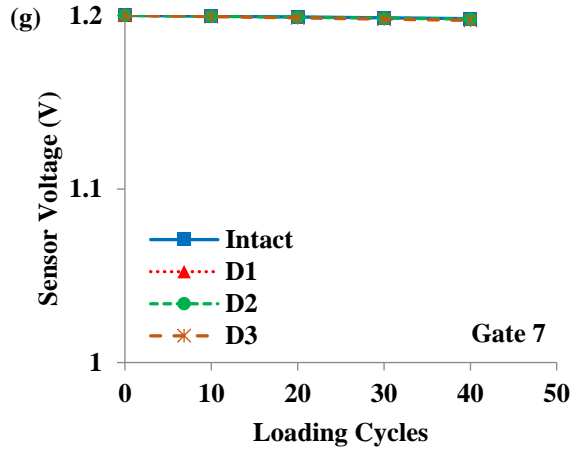


Figure 3-7: Voltage changes across the floating-gates of the PFG sensor for location 4.

Figure 3-7 (cont'd)



Another important observation from Figures 3-7 and 3-8 is that the voltage droppage rate for each gate is also a good indicator of damage progression. For instance, consider the response of gates 1, 6 and 7 generated by PZT 7 for the D2 and D3 damage states (Figures 3-8(a),(f),(g)). Since the strain amplitude is higher for D3 than D2, the injection time is also higher, and therefore the voltage on the gate dropped more for D3. In addition, the difference between the slopes of the curves is controlled by the injection rates. In fact, the maximum difference of the slopes is obtained at gate 7 and then at gate 1. However, the slopes of the two damage states have close values at gate 6.

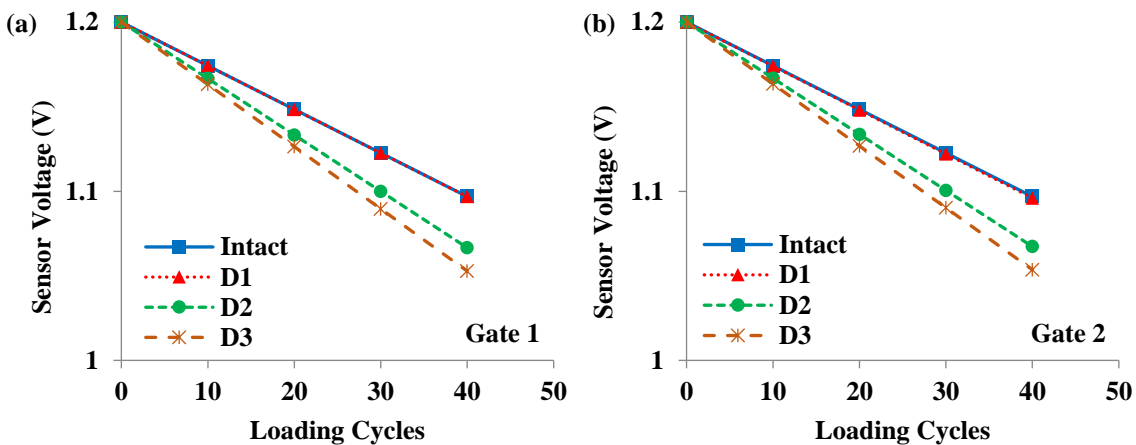
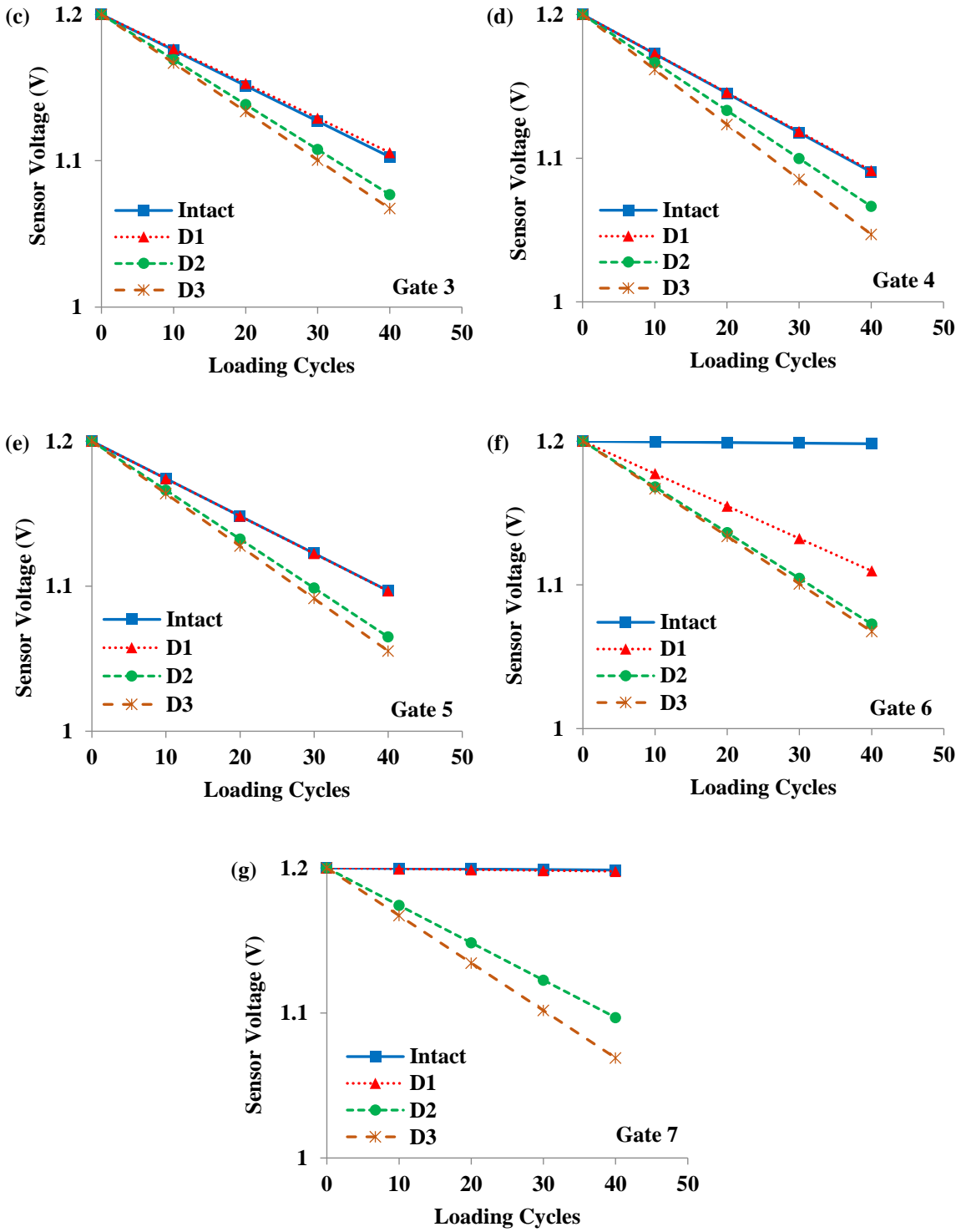


Figure 3-8: Voltage changes across the floating-gates of the PFG sensor for location 7.

Figure 3-8 (cont'd)



3.3.1.2. Data fusion in a network of PFG sensors

As discussed in the previous section, it is possible to detect the damage progression with individual PFG sensors. Although they deliver valuable quantitative information, measurements at a single location might not be sufficient for accurate damage detection (Alavi et al., 2016a). On the other hand, only a few sensors located at a specific distance from the damage zone can be used for precise damage detection (sensors close to the damage zone). For instance, PFG sensors mounted along, on the top or at the bottom of the notch are providing more useful trends for the studied plate structure, compared to other sensors. In addition, the situation becomes challenging if the damage location is unknown. Therefore, an effective sensor fusion strategy is developed to improve the damage detection performance through spatial measurements.

To this aim, features that are expected to characterize different properties of the structure are extracted from the network of PFG sensors. The classification phase is then performed through feeding of the fused features into a computational intelligence (CI)-based classifier.

In order to obtain the features, a polynomial function is fitted to the voltage droppage histograms at each sensing node. This is done for all damage states. The data has 7 dimensions that correspond to the number of the sensor gates. Thus, the following polynomial function (P) with 6 degrees and 7 coefficients is considered for the curve fitting:

$$P(x) = a_0 + a_1x + a_2x^2 + a_3x^3 + a_4x^4 + a_5x^5 + a_6x^6 \quad (3-1)$$

where a_0, \dots, a_6 are the polynomial coefficients. In order to define features that incorporate the group effect of the sensors network, different statistical functions are proposed as follows:

$$\Delta V_{Dij}^p = \frac{\Delta V_{ij}^p}{\Delta V_{avj}^p} \quad (3-2)$$

$$\Delta V_{Zij}^p = \frac{\Delta V_{ij}^p - \Delta V_{avj}^p}{\Delta V_{STDj}^p} \quad (3-3)$$

$$a_{Dij}^p = \frac{|a_{ij}|^p}{a_{avj}^p} \quad (3-4)$$

$$\alpha_{Zij}^p = \frac{|a_{ij}|^p - a_{avj}^p}{a_{STDj}^p} \quad (3-5)$$

where, ΔV_{ij}^p , ΔV_{avj}^p , ΔV_{STDj}^p are, respectively, the original drop in voltage of sensor i at gate j for damage state number p ($p = \text{Intact, D1, D2, D3}$), the average of voltage droppage of all sensors at gate j for damage state p , and the standard deviation of voltage droppage of all sensors at gate j for damage state p . $|a_{ij}|^p$, a_{avj}^p , a_{STDj}^p are, respectively, the original polynomial coefficients (in absolute value) of sensor i at gate j for damage state p , the average of the polynomial coefficients of all sensors at gate j for damage state p , and the standard deviation of all the polynomial coefficients of all sensors at gate j for damage state p .

To visualize the damage classes, a principal component analysis (PCA) is performed. This method can reduce a high-dimensional space to a lower-dimensional space that optimally describes the highest variance of the data. Figure 3-9 represents the original voltage droppage data projected onto its first two principal components. The first principal component has the highest variance, and the second principal component has the second highest variance. The resulting map shows that the classes have notable overlaps. Based on a preliminary study, the best distinction between classes is obtained using features defined by Equation (3-5) which is in fact derived from the conventional z-score function.

Thereafter, the corresponding features are later fed into the CI-based classifier. Figure 3-10

shows the featured data projected onto the first two principal components (Equation (3-5)). As seen, using these new features results in a clear distinction between damage classes.

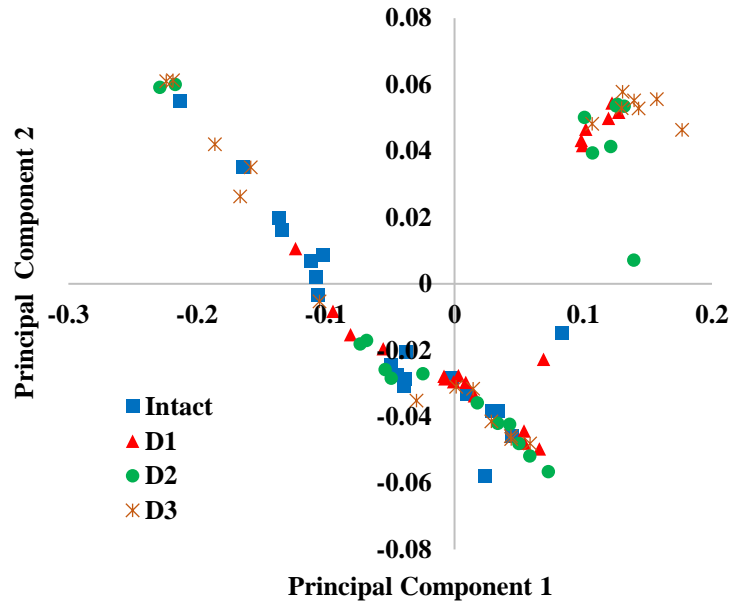


Figure 3-9: Projection of the original voltage droppage data onto the first two principal components.

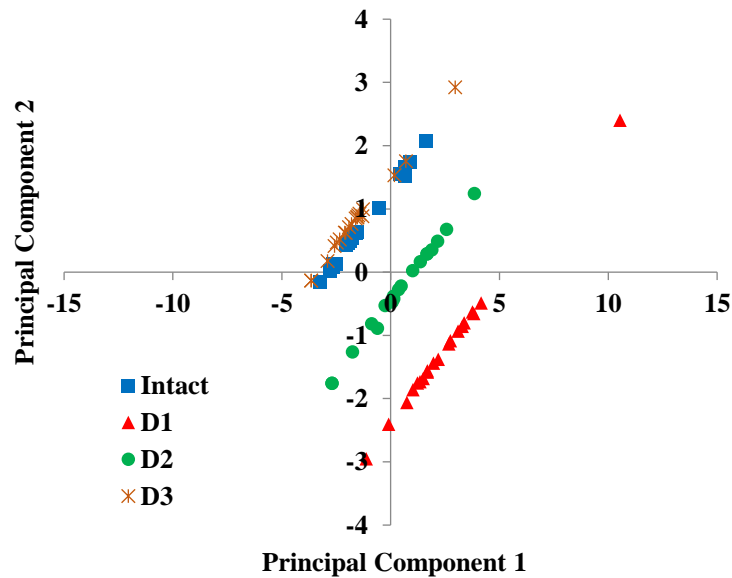


Figure 3-10: Projection of the featured data onto the first two principal components.

In this study, the SVM algorithm is implemented using different kernels, and the polynomial kernel is found to give the best performance. The performance of the developed SVM models is tested for different number of gates (1 to 7) to investigate the effect of the number of gates on the classification results. The total number of data sets for each gate is 80 (20 sensor and 4 damage states). For the SVM analysis, the available data sets are randomly divided into 3 groups as follows:

- 70% training: $56g$ -dimensional feature vector
- 15 % testing: $12g$ -dimensional feature vector
- 15% validation: $12g$ -dimensional feature vector

where g denotes the number of gates used in the analysis ($g = 1..7$). The best models are chosen based on their performance on the validation data. The generalization error of the final models is assessed using the unseen testing data. The performance of the SVM models is evaluated using the detection rate metric.

The SVM model is trained based on the experimental results of the intact and the damaged modes of the plate. In real structures, SVM models should be trained using data from similar experimental cases or based on the data provided by a calibrated FE model. More specifically, for the FE-based data interpretation, FE model updating (FEMU) method can be used. FEMU is an inverse parameter estimation problem where the unknown mechanical or geometrical parameters of an a priori structural FE model are estimated based on measurement data. In other words, FEMU is the process of correcting an FE model so that its mechanical behavior matches with experimental dynamic/static responses. By calibrating the response of the FE model, a reliable database can be developed and used for the training of the SVM and other machine learning techniques.

The polynomial degree and the regularization parameters C are important parameters in the SVM algorithm. These parameters are tuned through an optimization process. Multiple iterations are performed on both the polynomial degree and the constraint box C at the same time in order to find the optimal values. The validation set is used to optimize the kernel and the regularization parameters. Figures 3-11 and 3-12 present the variation of the detection rate accuracy as a function of the kernel parameter and the constraint box. As can be observed from these figures, the best damage detection performance is obtained for a quadratic polynomial and for $C = 22$. Figure 3-13 presents the performance of the SVM models for different number of gates.

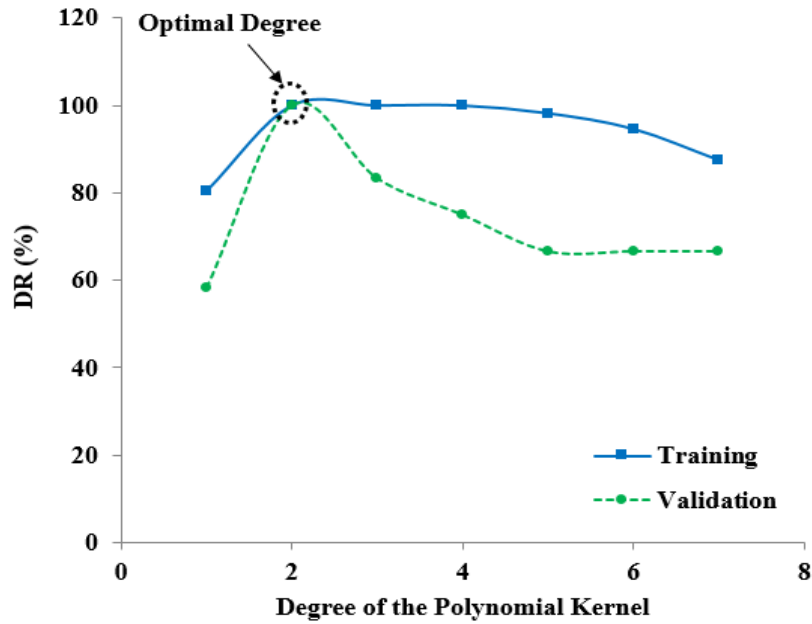


Figure 3-11: Optimization of the polynomial degree in the SVM algorithm.

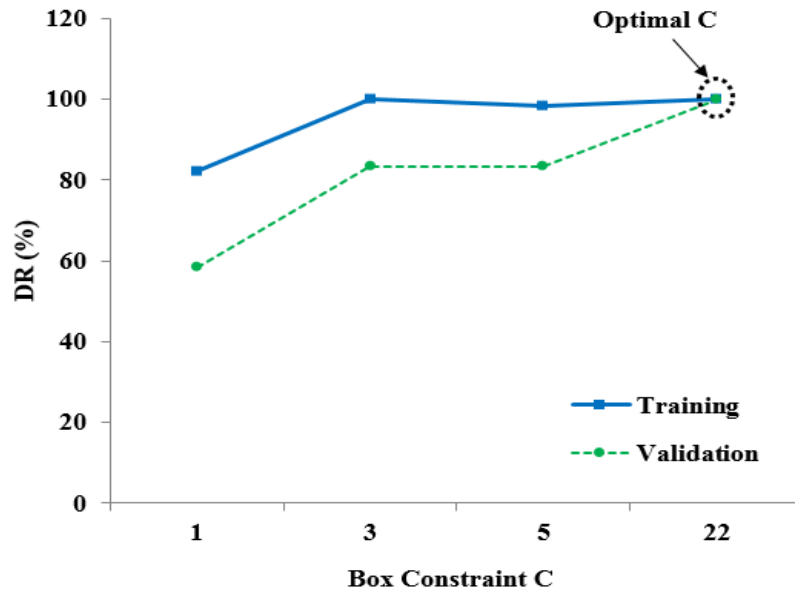


Figure 3-12: Optimization of the box constraint parameter in the SVM algorithm.

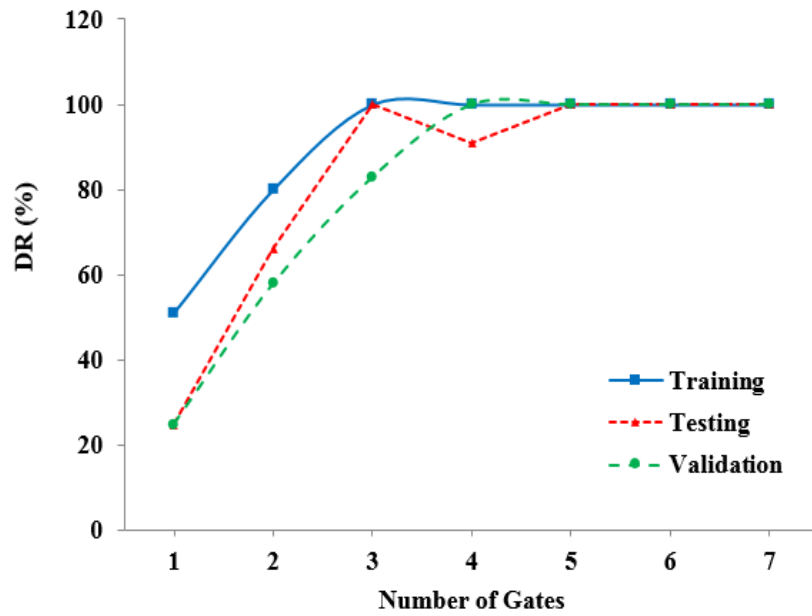


Figure 3-13: Damage detection performance of the SVM models for different number of gates.

In order to visualize the detailed classification performance, the corresponding confusion matrixes are given in Figures 3-14 to 3-16. As it is seen in the figures, the SVM models

developed with data from 3 or more gates have very good performance on the training, testing and validation data.

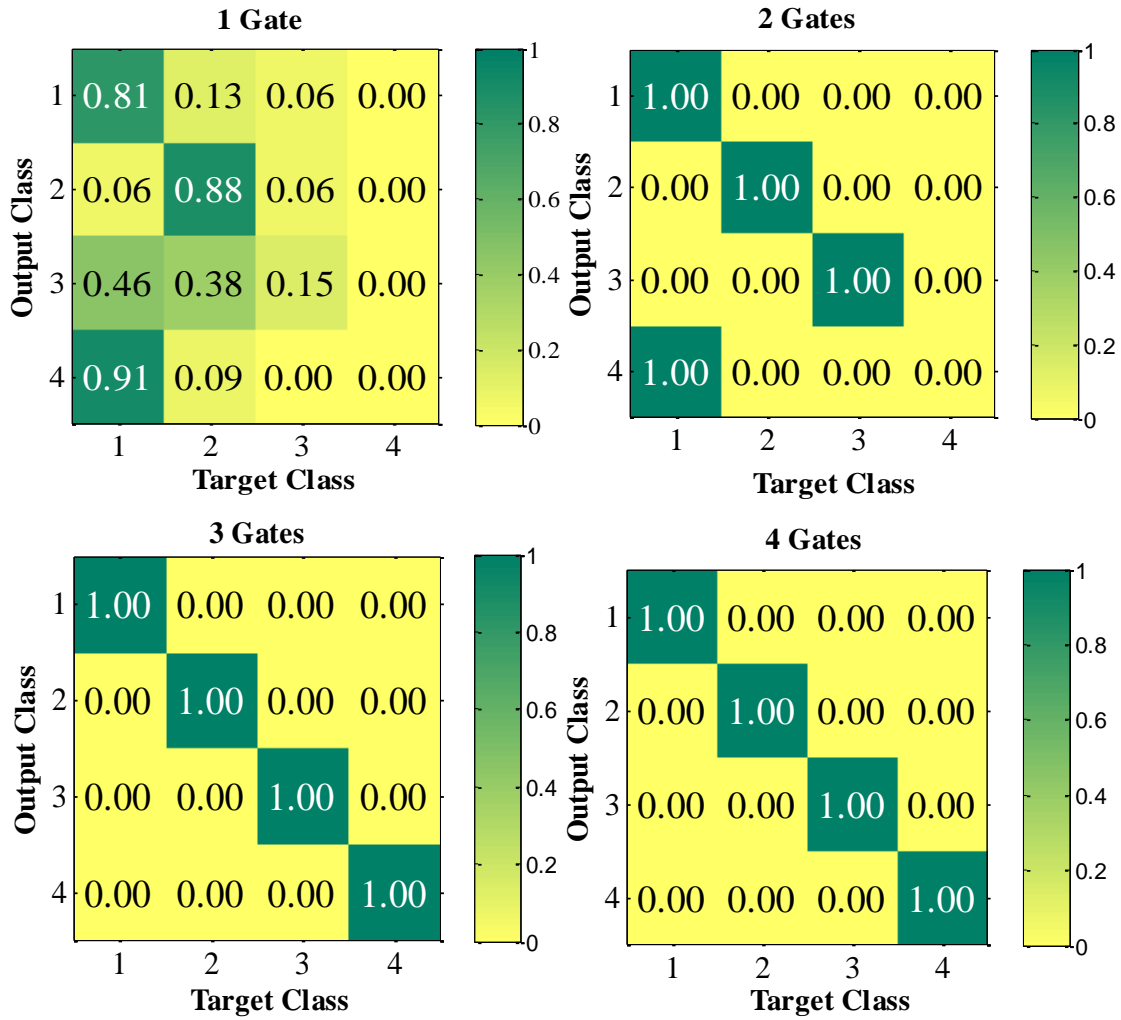
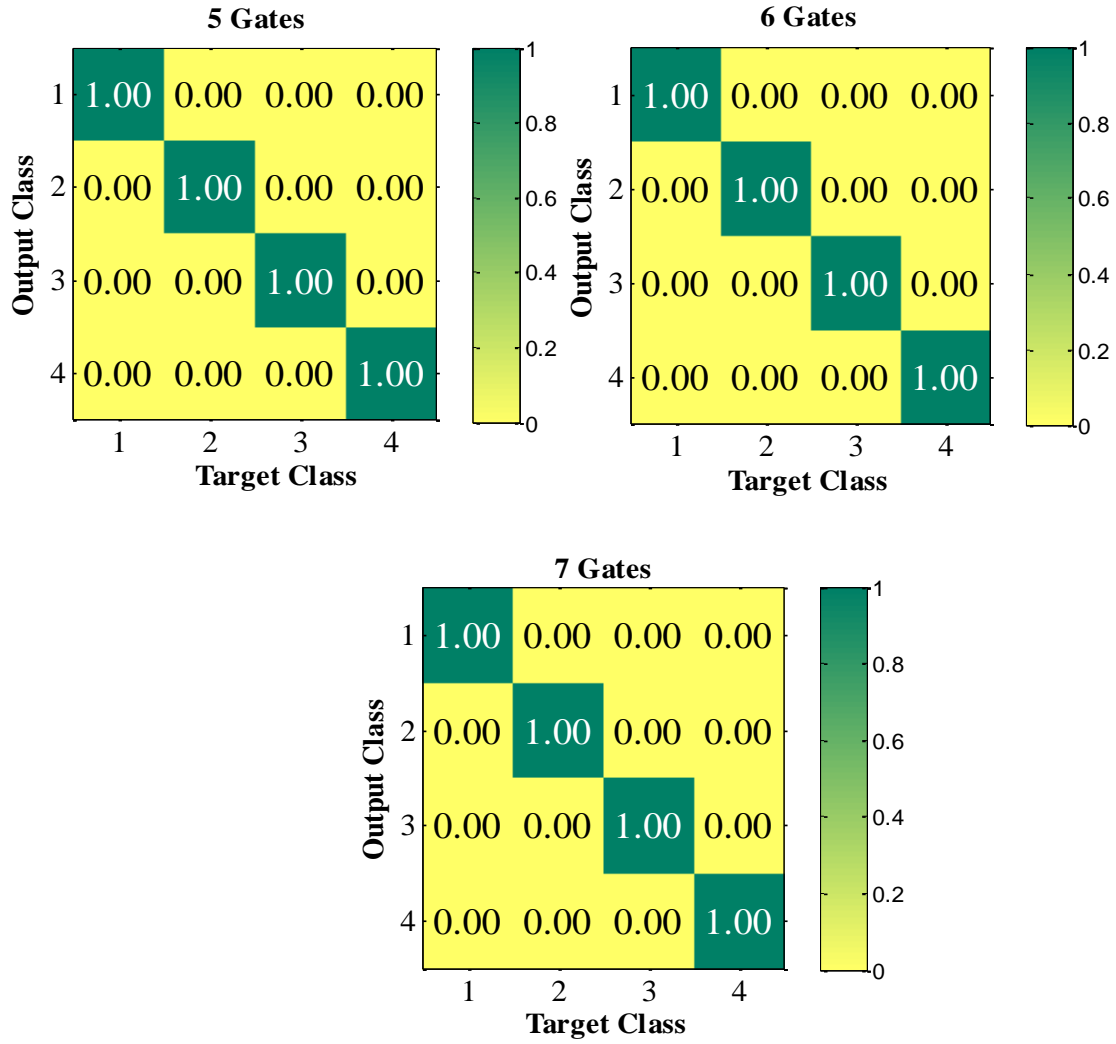


Figure 3-14: Confusion matrixes for the training data.

Figure 3-14 (cont'd)



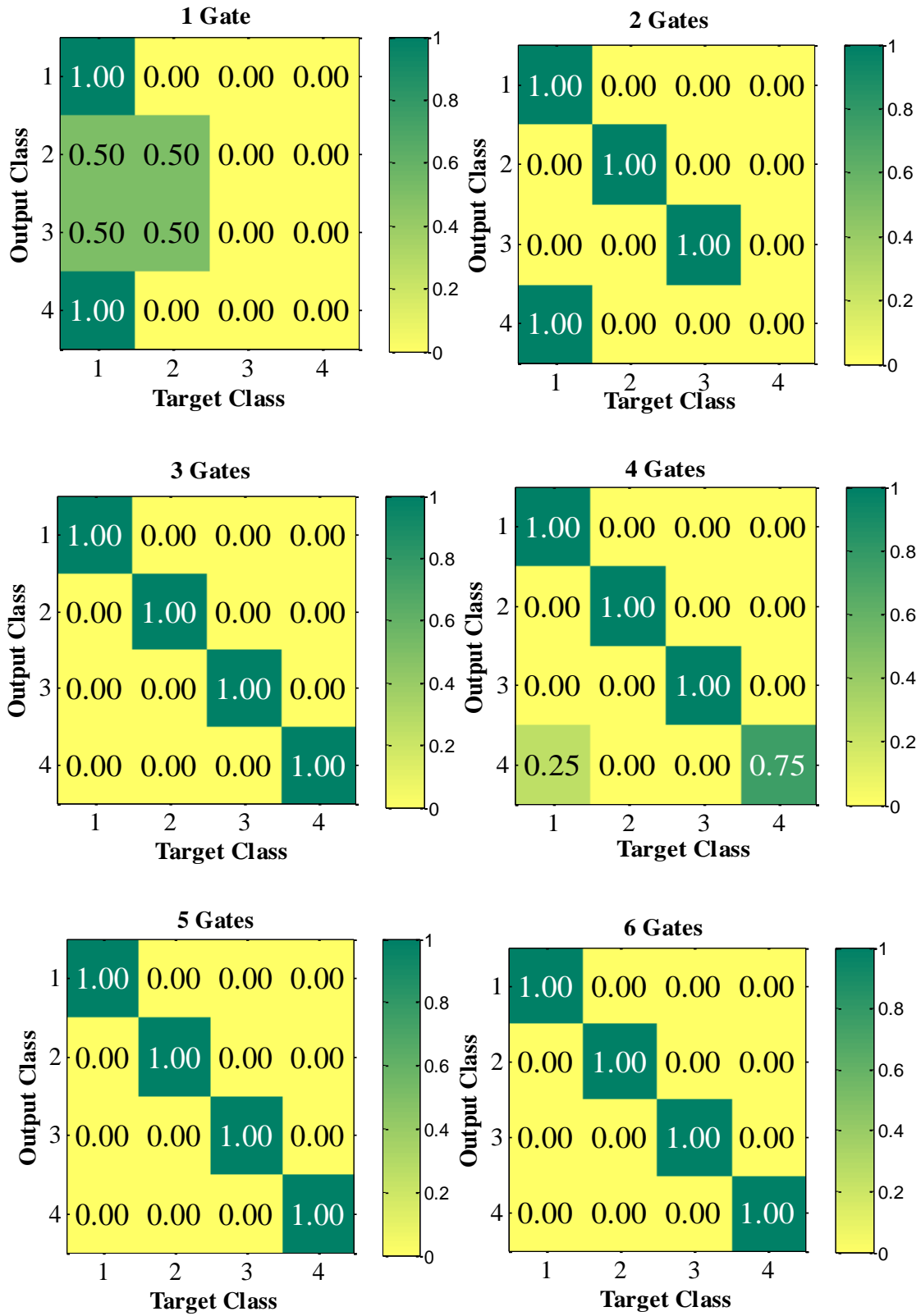
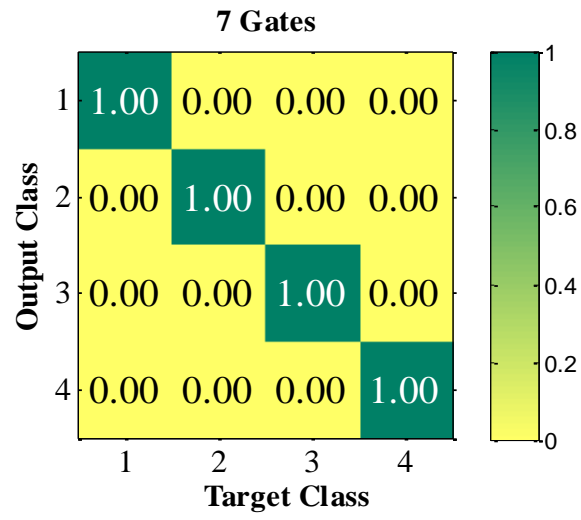


Figure 3-15: Confusion matrixes for the testing data.

Figure 3-15 (cont'd)



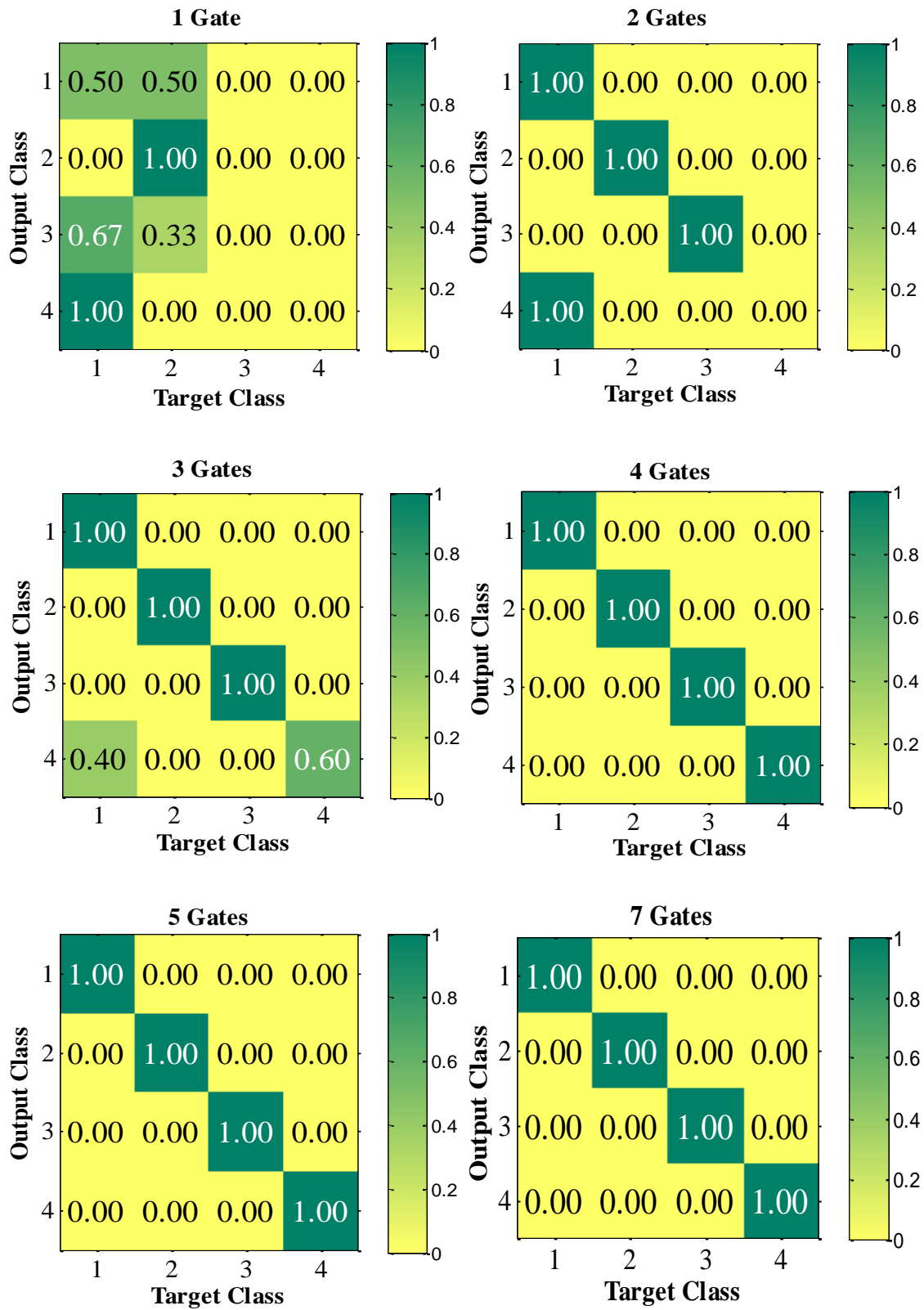
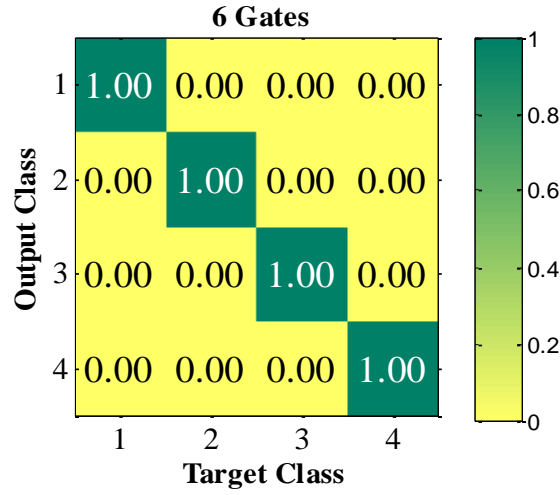


Figure 3-16: Confusion matrixes for the validation data.

Figure 3-16 (cont'd)



3.3.1.3. Uncertainty analysis

Piezoelectric sensors have major advantage comparing to conventional foil strain gages due to their superior signal to noise ratio and high frequency noise rejection (Sirohi and Chopra, 2000). However, different sources can contribute to the uncertainty in the measured signal delivered by piezoelectric sensors. The noise can be induced because the sensor is susceptible to environmental effects and operational states. In addition, the main sources that cause fluctuation of voltage in piezoelectric ceramics are the thermal noise, polarization noise and low frequency $\frac{1}{f}$ noise (Sedlak et al., 2011). The fluctuation of the electrical polarization is an additional source of voltage noise for the electrical response of piezoelectric ceramics (Sedlak et al., 2011). In order to evaluate the reliability of the proposed damage detection method, an uncertainty analysis is carried out. To this aim, the training, testing and validation sets from the original sensor signal are polluted with a white Gaussian noise, for different signal-to-noise ratios (SNRs). The SNR defines the ratio between the signal power (P_{signal}) and the noise power (P_{noise}):

$$SNR = \frac{P_{signal}}{P_{noise}} = \left(\frac{A_{signal}}{A_{noise}} \right)^2 \quad (3-6)$$

where $\frac{A_{signal}}{A_{noise}}$ is the ratio between the two amplitudes of the signal and the noise. The SVM algorithm is run for the featured data using 7 gates. Figure 3-17 depicts the best classification results for various noise levels for the training, testing and validation data.

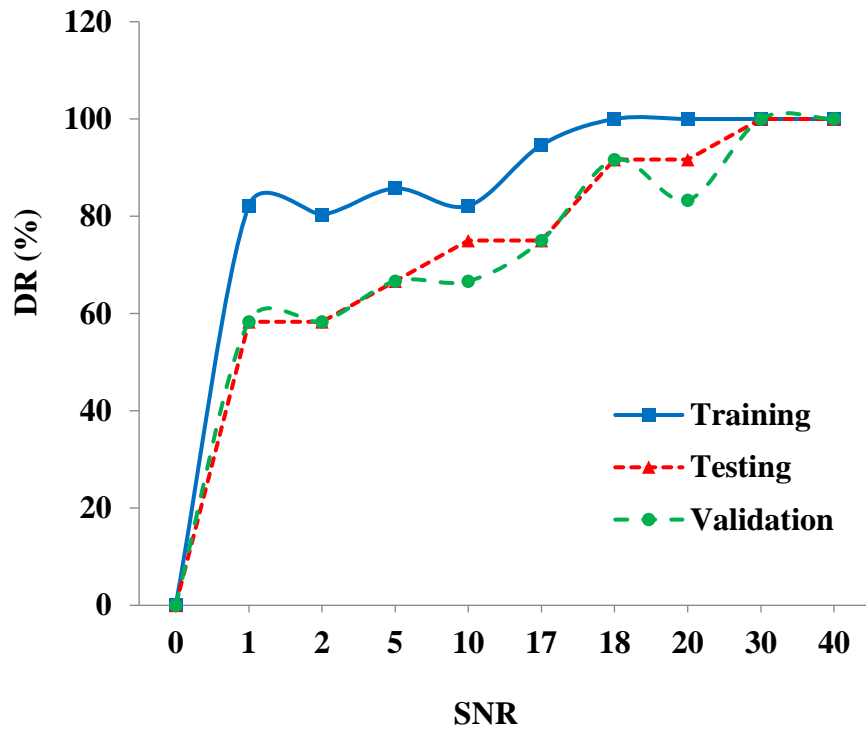


Figure 3-17: Performance of the SVM models for various noise levels.

Comparing the results shown in Figure 3-17, it can be observed that the performance of the models on testing and validation is satisfactory for SNRs above 18. In other words, the classification accuracy remains acceptable up to 23 % of voltage noise. This result indicates that the proposed approach is effective in detecting and classifying different damage states in steel plates under high noise levels.

3.3.2. Pavements health monitoring

Pavement health monitoring is an extension of the SHM concept that deals with assessing the structural state of pavement infrastructure systems. Distresses concentrated in asphalt concrete layer can lead to the failure of the pavement structure over time. The maximum tensile stresses are commonly developed at the bottom of the AC layer under repetitive loadings. As a result, cracks usually initiate at the bottom of the asphalt layer and start propagating to the surface of the pavement. This so called bottom-up fatigue cracking is one of the main failure modes in asphalt pavements. The fatigue life of pavements is mainly related to the nature and the amplitude of the applied loading.

In this context, the existing health monitoring methods can generally be categorized into two groups: the in-situ pavement sensors and external evaluation technologies (Xue et al., 2013). During the past two decades, the in-situ sensing techniques have been developed as the alternatives to the traditional monitoring methods (Potter et al., 1969; Badr and Karlaftis, 2012; Badr and Karlaftis, 2013; Karlaftis and Badr, 2015). Many types of sensors are used in this method such as deflectometer, fiber-optic sensors, moisture sensor, pressure cell, strain gauge, thermocouple, etc. (Potter et al., 1969; Badr and Karlaftis, 2012; Badr and Karlaftis, 2013; Karlaftis and Badr, 2015; Huff et al., 2005; Malekzadeh et al., 2015). The external evaluation approaches are extensively used to detect surface distresses of pavement, i.e., pavement distresses evaluation based on image analysis (Mohajeri and Manning, 1991; Koutsopoulos and Downey, 1993), or pavement deformation detection by stereo-imagery (Mills and Newton, 2001; Plati and Loizos, 2013; Plati et al., 2014; Bagherifaez et al., 2014; Behnia et al., 2014; Xu et al., 2015).

In this section, a pavement health monitoring system is proposed using the nonuniform

class of wireless sensors. In 3.3.2.1, numerical and experimental studies are focused on the detection of progression of bottom-up cracking caused by excessive strains at the bottom of an asphalt-concrete specimen under three-point bending configuration. In section 3.3.2.2, a new surface sensing approach for detection of bottom-up cracks in AC pavements using the nonuniform class of self-powered wireless sensors is proposed.

3.3.2.1. Damage growth detection in AC slabs

The performance of the sensor is numerically and experimentally investigated on an asphalt concrete specimen. The sample is loaded under three-point bending mode. The loading protocol includes applying gradually increasing compressive force to the top mid-span of the beam. A schematic illustration of the test is shown in Figure 3-18.

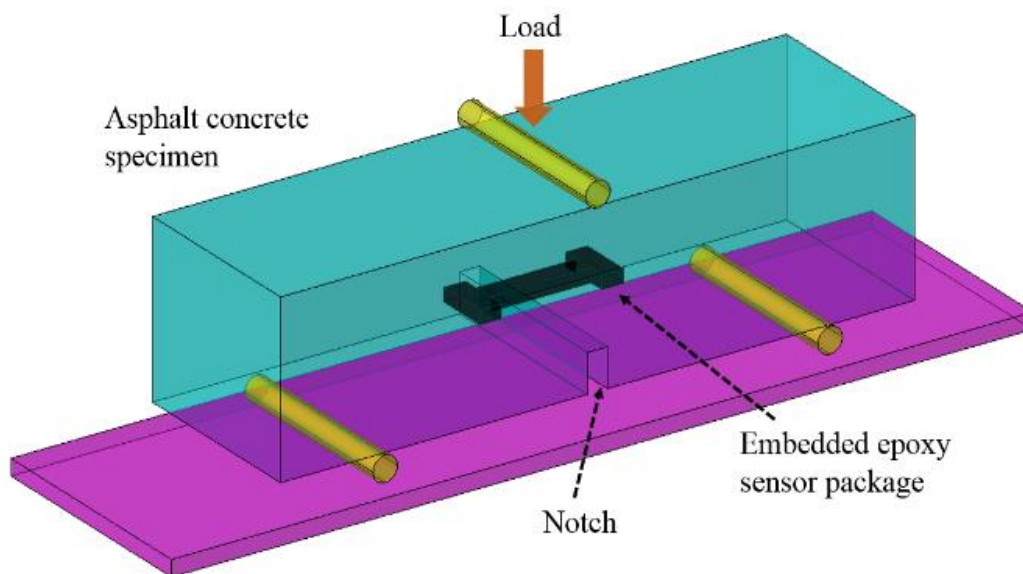


Figure 3-18: Schematic of the notched asphalt concrete specimen under three-point bending test.

The analysis carried out in this study is divided into two stages. First, an FE model is developed to obtain the structural response of the beam under different damage scenarios. The strains are

extracted at the sensing node and then a MATLAB script is developed to obtain the cumulative loading time for each gate and for each damage state. Thereafter, the percentage of strain droppage for different damage states is estimated based on the sensor output data. For the second step, the voltage droppage and the percentage of voltage droppage are directly calculated using the measured sensor data. Figure 3-19 shows a flowchart of the proposed method.

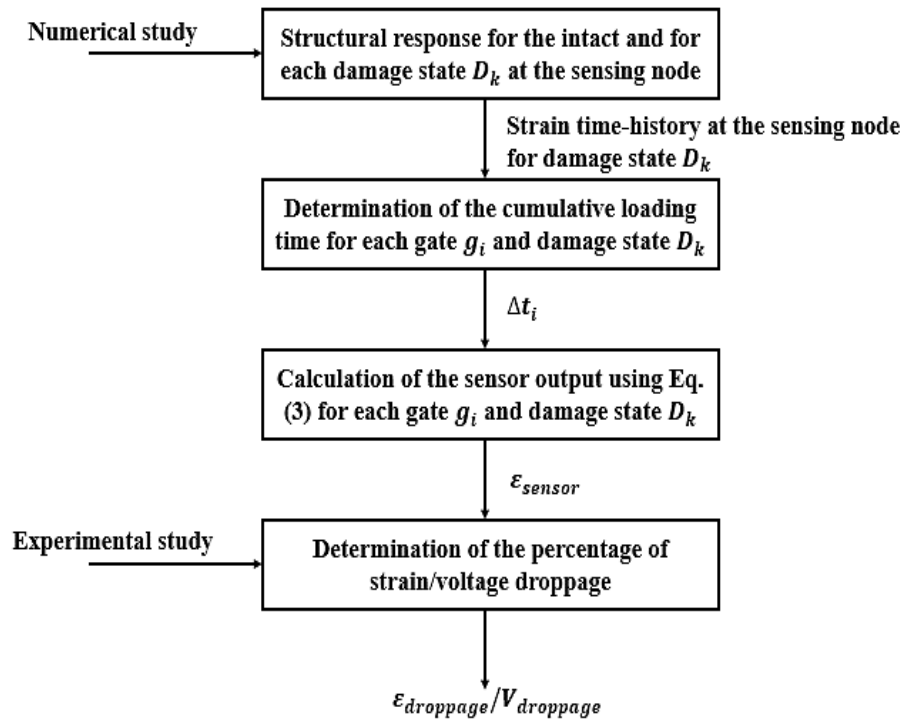


Figure 3-19: Flowchart of the proposed method.

3.3.2.1.1. FE modeling and damage detection approach

3.3.2.1.1.1. Description of the FE model

Damage is introduced by making a notch at the middle of the bottom of the asphalt concrete specimen. Damage states are defined by increasing the notch size (a) as follows:

- Intact (D0): $a = 0$ mm (Intact slab)

- Damage 1 (D1): $a = 6.35$ mm
- Damage 2 (D2): $a = 15.87$ mm
- Damage 3 (D3): $a = 19.10$ mm
- Damage 4 (D4): $a = 25.30$ mm

For the analysis, the initial strain value of each channel is set to $\varepsilon_0 = 300 \mu\varepsilon$. below which the device does not record any information. The maximum threshold is $900 \mu\varepsilon$ where all the channels are activated. Gate injection rates and strain threshold levels are displayed in Table 3-2. The selection of thresholds and injection rates is based on an existing sensor and piezoelectric transducer. In fact, each of the sensor gates has specific voltage threshold level from which the gate starts recording the data.

Table 3-2: Preselected strain levels and gate injection rates considered for the analysis.

Gate Number	Strain Threshold	Injection
	Level ($\mu\varepsilon$)	Rate ($\mu\varepsilon/s$)
1	300	9.5
2	400	17.11
3	500	9
4	600	22.5
5	700	20.4
6	800	30.4
7	900	14.2

Therefore, depending on the type of the piezoelectric transducer, the strain thresholds can be determined experimentally by gradually increasing the applied strain to the piezoelectric transducer and recording the corresponding drop in voltage for each gate.

Different 3D FE models are developed for each damage state to analyze the dynamic response of the asphalt concrete beam under a dynamic loading. ABAQUS/CAE 6.11 is used for the modeling and post-processing of the results. Dynamic implicit procedure is selected for the analysis. A displacement of 0.5 mm is applied to the upper part of the beam. The applied load has the following shape:

$$u_{applied} = \frac{A}{2} [1 - \cos(2 \pi f t)] \quad (3-7)$$

where f ($f = 2$ Hz) is the frequency and A ($A = 0.5$ mm) is the amplitude of the applied displacement.

The sample is modeled using a viscoelastic material. The expression of the stress in linear viscoelasticity can be expressed by a Boltzmann superposition integral as follows (Michalczyk, 2011):

$$\sigma(t) = \int_0^t E(t - \tau) \frac{d\varepsilon}{d\tau} d\tau \quad (3-8)$$

In the present study, a generalized Maxwell model is used for representing the linear-viscoelastic behavior of the hot mix asphalt (HMA). This model is a combination of Maxwell elements (one spring and one dashpot) connected in parallel with a spring as shown in Figure 3-20.

A single element Maxwell model is composed of one spring and one dashpot mounted in series. Therefore, the relationship between the stress-strain is expressed as follows (Michalczyk, 2011):

$$\dot{\varepsilon}(t) = \frac{\dot{\sigma}(t)}{E} + \frac{\sigma(t)}{\eta} \quad (3-9)$$

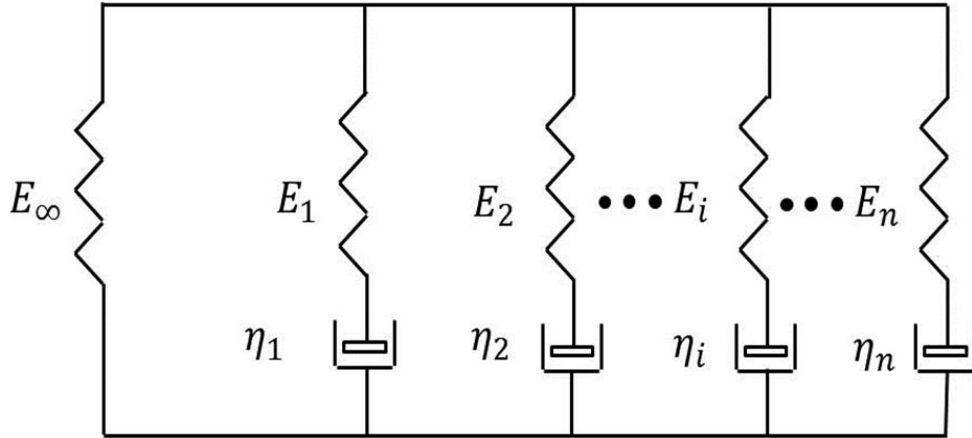


Figure 3-20: Generalized Maxwell model consisting of n Maxwell elements connected in parallel.

where E is the elastic modulus and η is the viscosity parameter.

If the material is subjected to a constant strain ε_0 , the solution of the precedent equation becomes:

$$\sigma(t) = E \varepsilon_0 \exp\left(-\frac{t}{\tau}\right) \text{ where } \tau = \frac{\eta}{E} \quad (3-10)$$

where τ represents the relaxation time. By performing a summation over the n Maxwell elements shown in Figure 3-20, the stress equation becomes:

$$\sigma(t) = E_\infty \varepsilon_0 + \sum_{i=1}^n E_i \varepsilon_0 \exp\left(-\frac{t}{\tau_i}\right) = \left(E_\infty + \sum_{i=1}^n E_i \exp\left(-\frac{t}{\tau_i}\right)\right) \varepsilon_0 \quad (3-11)$$

Therefore, the relaxation modulus:

$$E(t) = \frac{\sigma(t)}{\varepsilon_0} = E_\infty + \sum_{i=1}^n E_i \exp\left(-\frac{t}{\tau_i}\right) \quad (3-12)$$

This expression is the Prony series representation. The equilibrium modulus is E_∞ and the instantaneous modulus E_0 is the value of $E(t)$ at $t=0$, given by:

$$E_0 = E_\infty + \sum_{i=1}^n E_i \quad (3-13)$$

By replacing the equilibrium modulus E_∞ by $(E_0 - \sum_{i=1}^n E_i)$, Equation (3-12) can be rewritten as:

$$E(t) = E_0 - \sum_{i=1}^n E_i (1 - \exp\left(-\frac{t}{\tau_i}\right)) \quad (3-14)$$

Therefore, the Prony series representation is fully defined by (E_i, τ_i) . For the FE modeling, ABAQUS uses the dimensionless Prony series representation based on the shear (G) and bulk (K) moduli to define a viscoelastic behavior (Michalczyk, 2011):

$$G(t) = \frac{E(t)}{2(1+\nu)} \quad (3-15)$$

$$K(t) = \frac{E(t)}{3(1-2\nu)} \quad (3-16)$$

If we divide both expressions by the initial values G_0 and K_0 respectively, we obtain:

$$\bar{g}(t) = 1 - \sum_{i=1}^n \bar{g}_i (1 - \exp\left(-\frac{t}{\tau_i}\right)) \quad (3-17)$$

and:

$$\bar{k}(t) = 1 - \sum_{i=1}^n \bar{k}_i (1 - \exp\left(-\frac{t}{\tau_i}\right)) \quad (3-18)$$

Therefore, there are three parameters required to define a viscoelastic material property in ABAQUS: the dimensionless shear relaxation modulus \bar{g}_i , the dimensionless bulk relaxation modulus \bar{k}_i , and the relaxation time τ_i .

The relaxation modulus of the asphalt concrete material used in this study is defined by four

constants a_i ($i = 1, 2, 3, 4$) as follows:

$$\text{Log}(E(t)) = a_1 + \frac{a_2}{1+e^{-a_3-a_4 \log(t_r)}} \quad (3-19)$$

Where t_r is the reduced time, and a_i are coefficients related to the type of the AC material. The constants a_i used in this study are summarized in Table 3-3.

Table 3-3: Constant values, c_i , used in this study.

a	b	c	d
0.639	3.341	0.709	-0.691

A MATLAB code is developed to fit Equation (3-12) to the relaxation modulus given by the sigmoid function (Equation (3-19)) in order to obtain the Prony series coefficients. Figure 3-21 displays the results of the Prony representation fit to the relaxation modulus. On this basis, 33 Prony coefficients are calculated. Thereafter, the dimensionless coefficients \bar{g}_i and \bar{k}_i are obtained based on the Prony coefficients E_i . The instantaneous modulus is calculated based on the equilibrium modulus and the 33 coefficients as expressed by Equation (3-13):

$$E_0 = E_\infty + \sum_{i=1}^{33} E_i = 9548 \text{ MPa} \quad (3-20)$$

The Poisson's ratio is equal to 0.35. The viscoelastic properties used in the FE model are summarized in Table A-1. The instantaneous modulus E_0 is 24545 MPa.

The asphalt concrete beam is modeled using 9615 linear hexahedral elements of type (C3D8R). Mesh refining technique is adopted for the meshing strategy in order to capture high stresses and strains concentration around the crack tip.

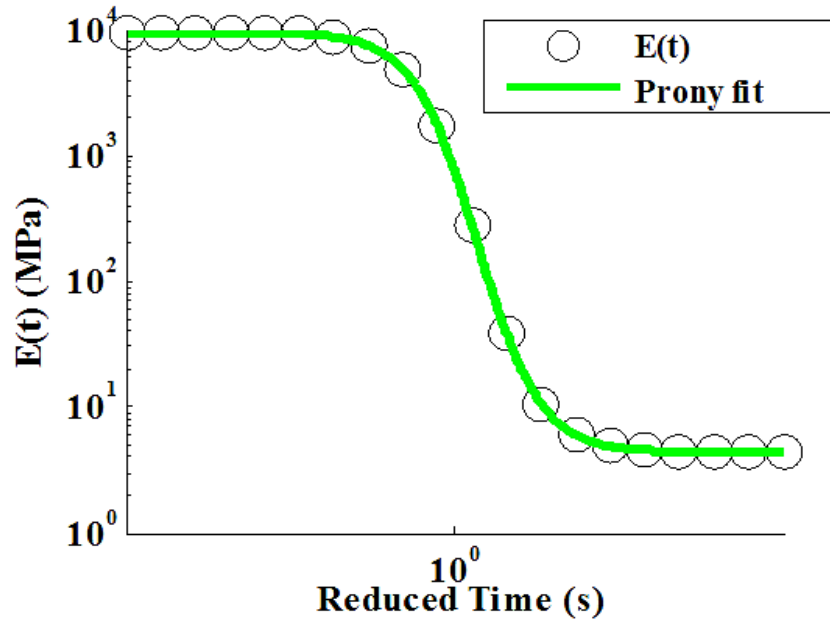


Figure 3-21: Prony series fit to the relaxation modulus of the sigmoid function.

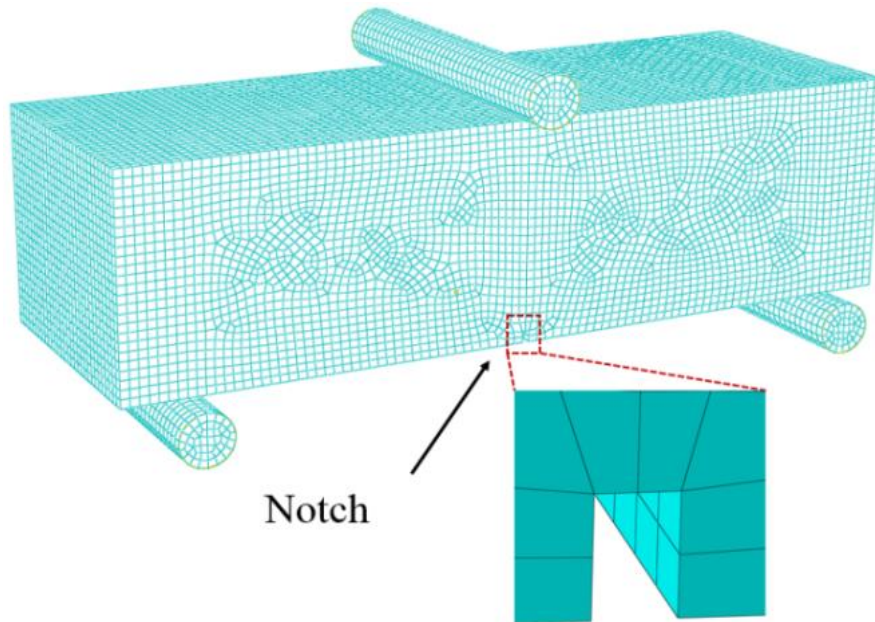


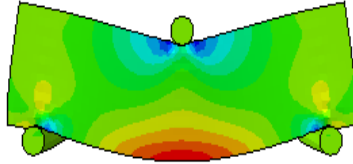
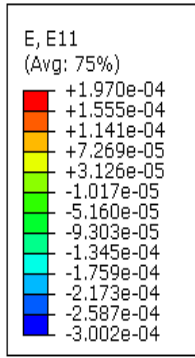
Figure 3-22: FE model mesh.

The obtained optimal element size is about 10 mm for the intact configuration. The entire length of the slab is equal to 450 mm (17.71 in), the span length is 381 mm (15 in), the thickness is 127

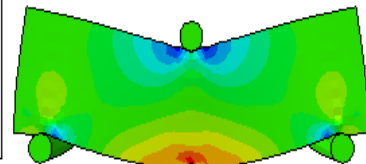
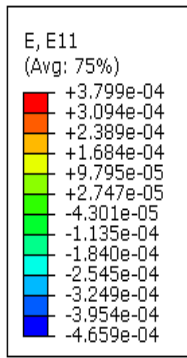
mm (5 in), and the width is 152.4 mm (6 in). The rollers have a diameter of 30 mm (1.18 in) and are setup to be free in rotation. The point of measurement is located at 30 mm from the middle bottom of the specimen. The meshed model of the beam is shown in Figure 3-22.

3.3.2.1.1.2. FE results

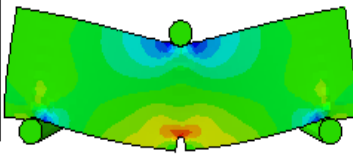
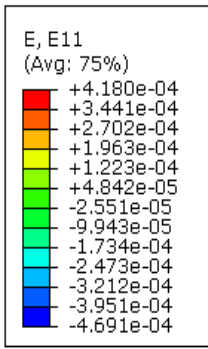
Figure 3-23 displays the results of the longitudinal strains (along the slab length) for the five damage states (D0, D1, D2, D3, D4). As one would expect, the amplitude of the strain increases as the damage progresses. This is mainly due to the stress concentration around the notch tip. Figure 3-24 displays the sensor output histogram for the damage states. It can be seen that the sensor strain shows a decreasing trend between damage states for all of the sensor channels. However, some channels do not record any change in the strain values between damage states. In particular, the outputs for {D0, D1, D2} of gate 6, and {D0, D1, D2, D3} of gate 7 are the same.



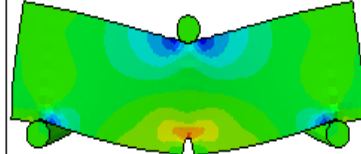
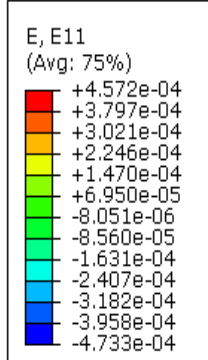
(a) D0 (Intact)



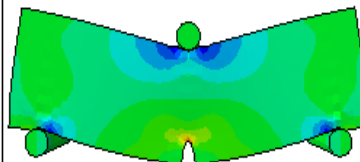
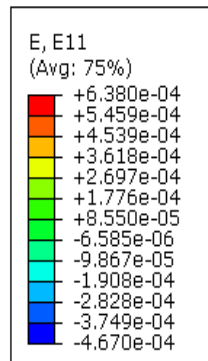
(b) D1



(c) D2



(d) D3



(e) D4

Figure 3-23: Strain distribution for different damage states.

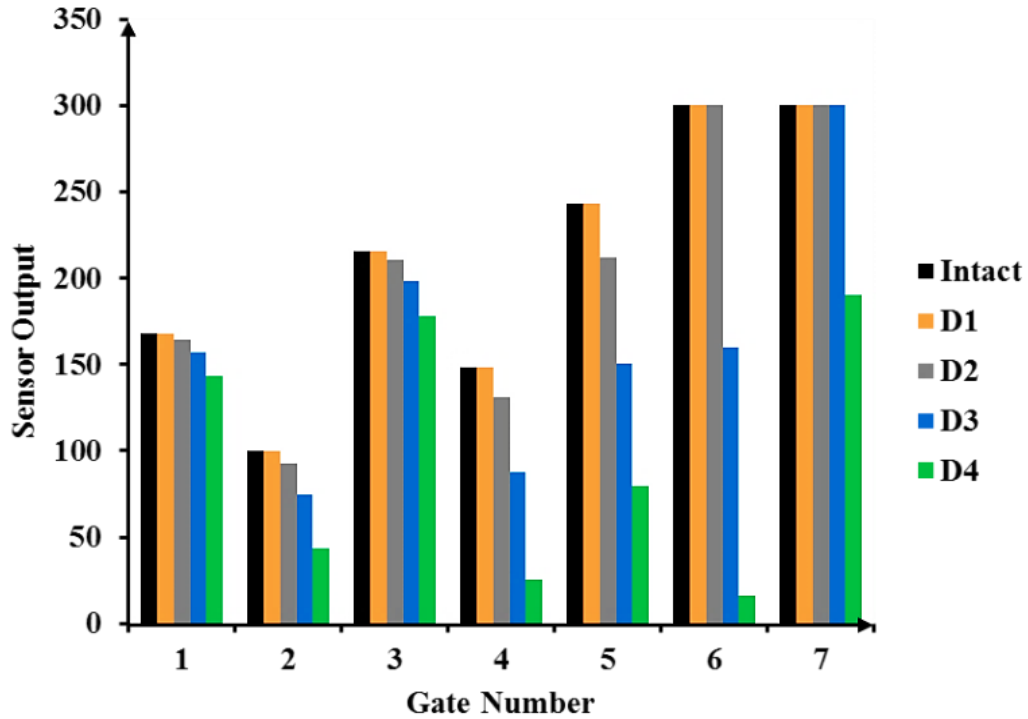
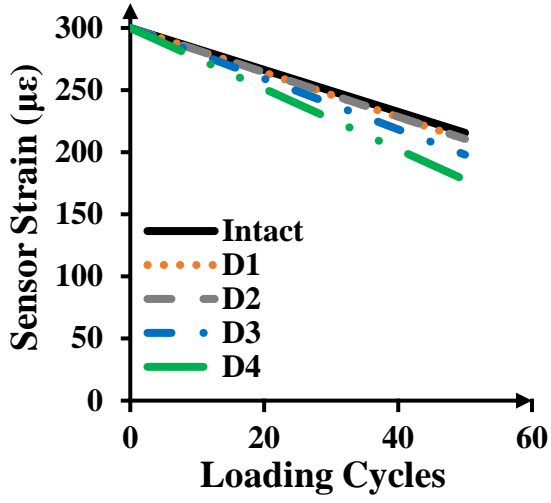


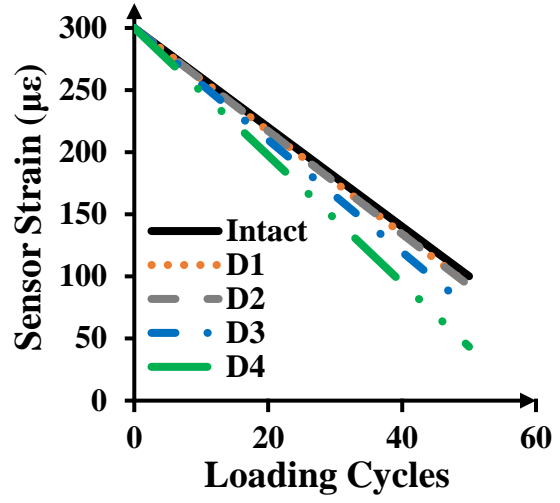
Figure 3-24: Histograms representing the output of the sensor.

3.3.2.1.1.3. Damage detection results based on FE model

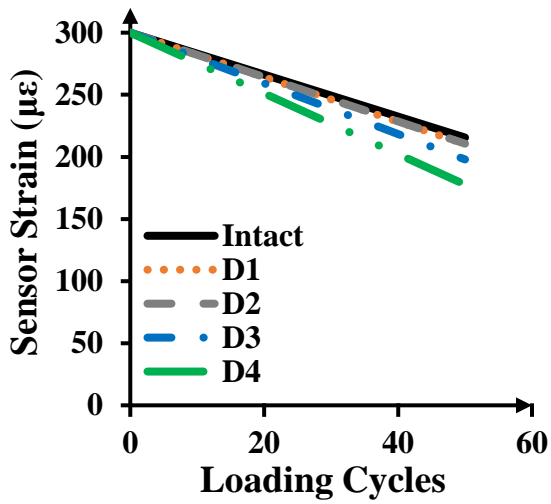
Figure 3-25 presents the variation of the sensor strain at each gate against the number of applied cycles for each damage state. Figure 3-26 displays the percentage of the sensor strain droppage after 50 cycles. As seen, the strain varies linearly with the number of cycles. Furthermore, the intact configuration has the smallest slope (in absolute value) compared to other damage states. The percentage of voltage droppage notably increases due to the damage progression. In fact, when the notch size increases, the longitudinal strain (along the slab length) increases as well. Thus, the cumulative time durations Δt_i ($i = 1..7$) measured by each gate increases.



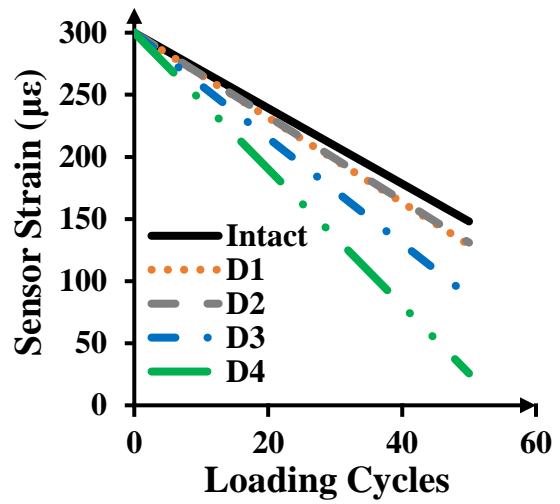
(a) Gate 1



(b) Gate 2



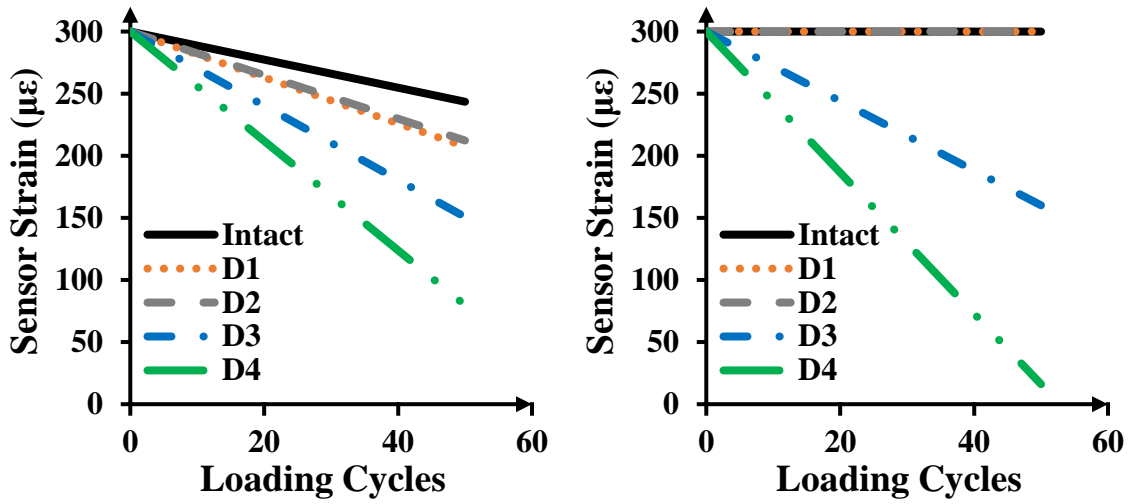
(c) Gate 3



(d) Gate 4

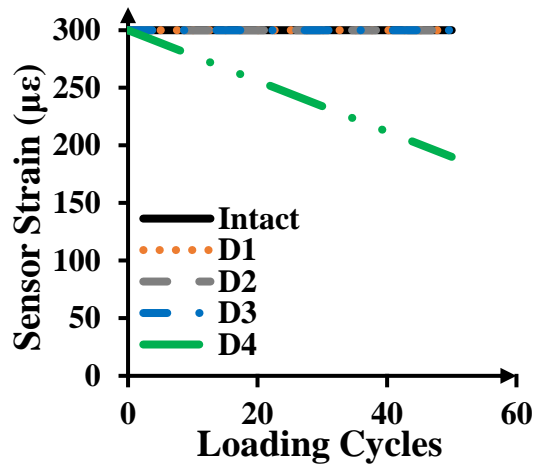
Figure 3-25: Strain changes across the floating-gates of the PFG sensor.

Figure 3-25 (cont'd)



(e) Gate 5

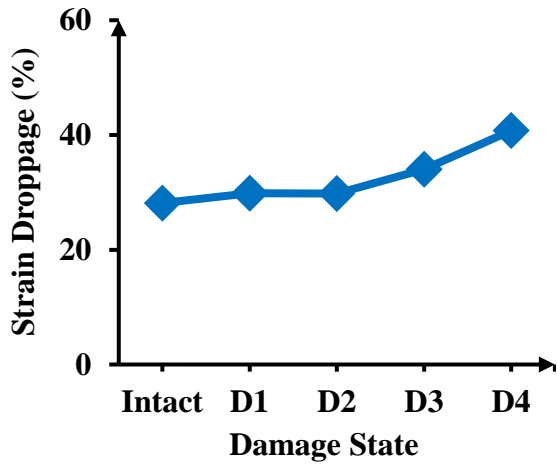
(f) Gate 6



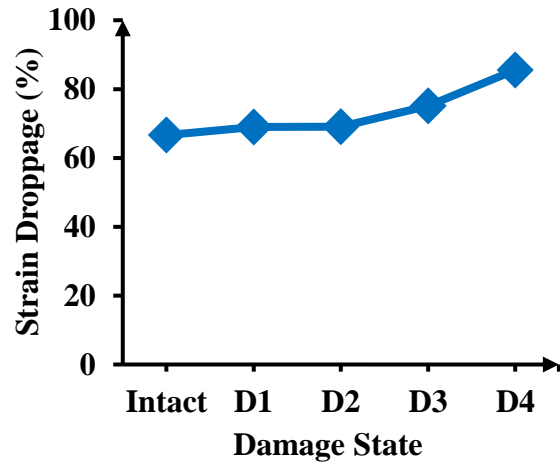
(g) Gate 7

As seen in Figure 3-25, the recorded strain droppage of the sensor highly depends on the damage state. When the strain exceeds the threshold corresponding to one of the gates, the sensor strain starts decreasing. Conversely, if the strain value is below the gate injection threshold, the sensor strain does not change. As an example, the strain amplitude for all damage states is higher than

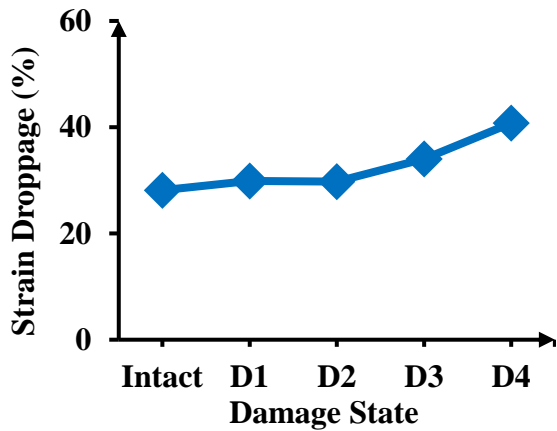
the activation threshold of the first five channels. Therefore, gates 1 to 5 are recording the cumulative strain droppage for all damage states, while gate 6 only records damage states D3 and D4.



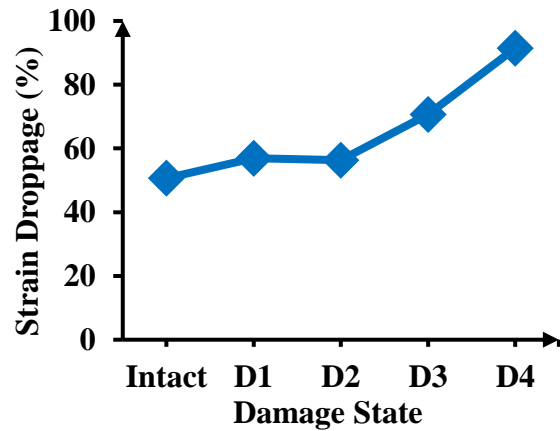
(a) Gate 1



(b) Gate 2



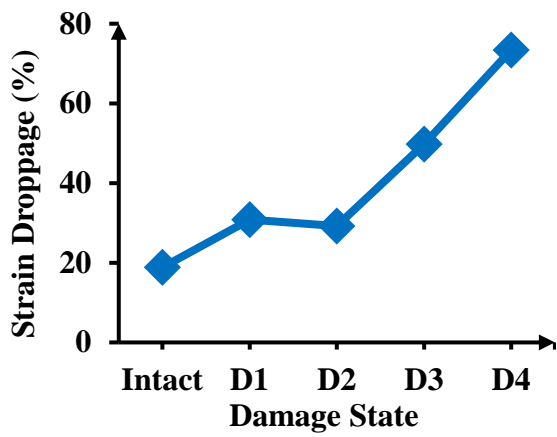
(c) Gate 3



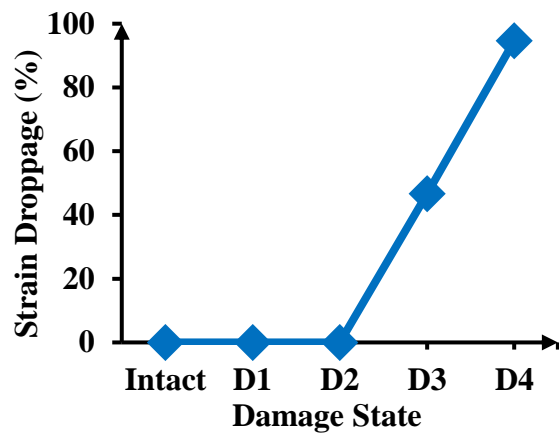
(d) Gate 4

Figure 3-26: Percentage of strain droppage for different sensor gates.

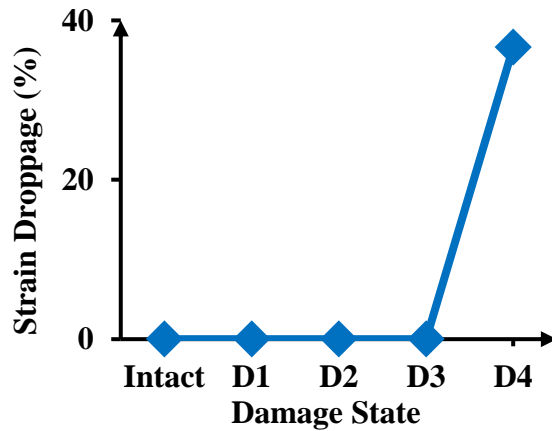
Figure 3-26 (cont'd)



(e) Gate 5



(f) Gate 6



(g) Gate 7

This is because the maximum strain values for damage states D0, D1 and D2 did not exceed the strain threshold level of gate 6 and therefore, this gate remained closed. As soon as the strain exceeded the activation value of this gate (for damage states D3 and D4), the gate starts recording.

Gate 7 merely recorded the most severe damage state, i.e. D4. As a summary, the slope representing the sensor strain versus the number of cycles is good damage indicator. In addition,

the gate number could be also used to detect severe cracks at the bottom of the pavement. In fact, gates 6 and 7 start recording only when the crack length reached high values.

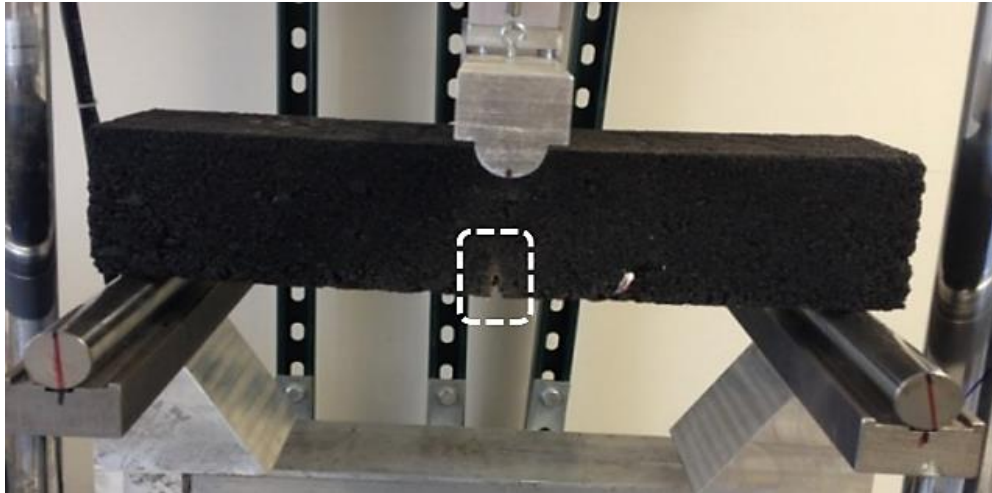
An interesting observation from Figure 3-26 is that the increasing trend of the strain droppage percentage is a good indicator of the damage severity, particularly for the activated gates.

3.3.2.1.2. Experimental investigation

3.3.2.1.2.1. Test setup

The three-point bending test setup for the experimental study is shown in Figure 3-27. The slab is built using HMA, 4E1 mixture type. The weight of the HMA is 12.5 kg and the length of the slab is equal to 450 mm (17.71 in). The loading protocol consists of applying a gradually increasing compressive force to the top mid-span of the beam using a universal mechanical testing frame. In this study, a polyvinylidene fluoride (PVDF) piezoelectric film is used to harvest the strain energy from the host structure. In order to protect the piezoelectric film and the sensor electronics from possible damage during the manufacturing of the asphalt concrete specimen, an H-shape packaging is designed (Figure 3-28). Conathane® TU-981 epoxy is used for encasing the proposed H-shape packaging system. A PVDF with a size of 7.3 cm covered by epoxy is embedded inside the asphalt layer at a distance of approximately 30 mm from the bottom of the layer. Figure 3-29 displays an image of the used PVDF and its dimensions. The PVDF dimensions and properties are summarized in Table 3-4. Before starting the test, a preload equal to 0.5 kN is applied to the sample to ensure it is seated on the fixture. A cyclic displacement loading similar to the FE study is applied to the sample. Damage is introduced by making a notch at the bottom of the asphalt layer. The damage states are defined by increasing the notch size (a) as follows:

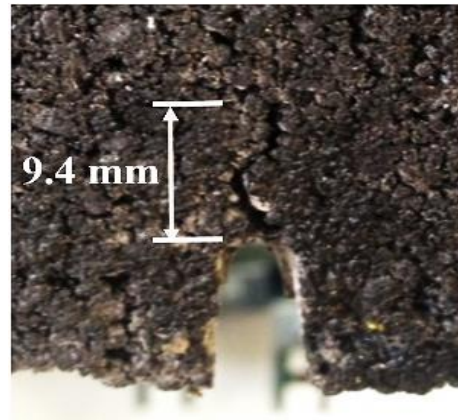
- Intact (D0): Intact plate ($a = 0$ mm)
- Damage 1 (D1): $a = 6.35$ mm (1/4 ")
- Damage 2 (D2): $a = 15.875$ mm (5/8")



(a)



(b)



(c)

Figure 3-27: (a) Three-point bending experimental setup, (b) notch at the initial stage, and (c) crack propagation phase.

After introducing the second damage phase, the displacement is increased to 2 mm to evaluate the behavior of the sample for higher amplitudes. After applying number of cyclic loadings, a crack propagation phenomenon is observed (Figure 3-27 (c)).

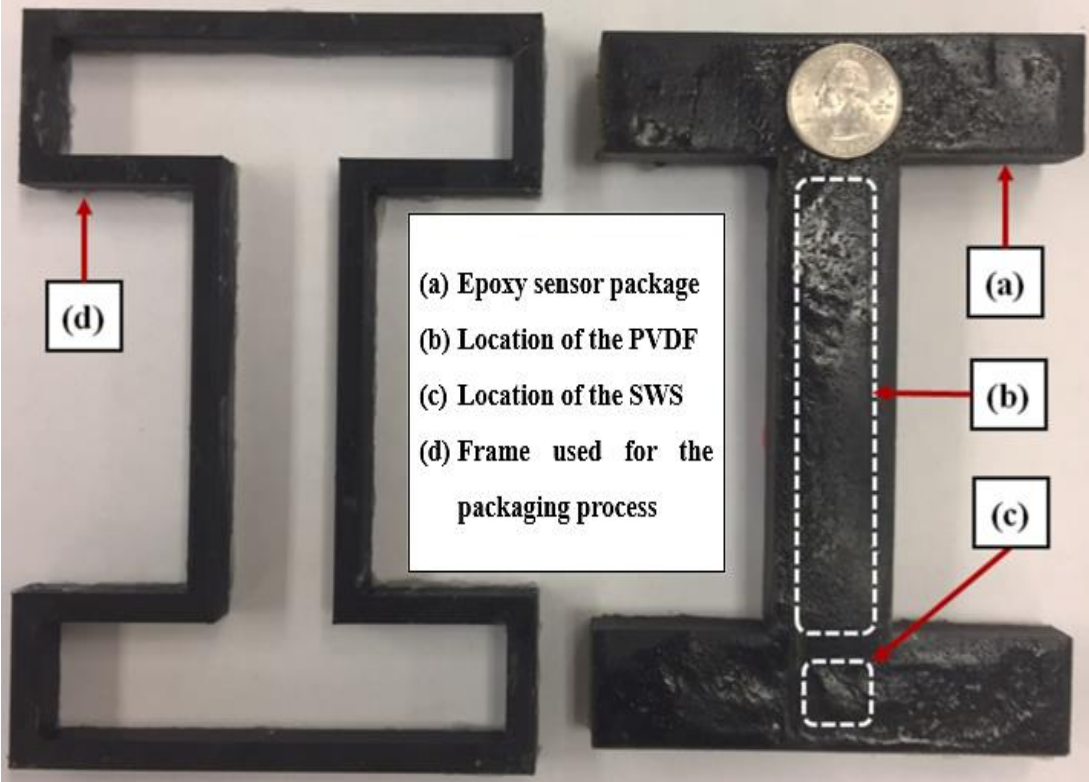


Figure 3-28: Sensor packaging design to protect the piezoelectric and electronics.

Table 3-4: PVDF dimensions and properties.

PVDF	A	B	C	D	Thickness	Capacitance
Type	(mm)	(mm)	(mm)	(mm)	(μm)	(nF)
LDT2-028K	16	12	73	62	157	2.85

The crack propagated two times with lengths of 3.2 mm and 9.4 mm. These new damage phases are considered as Damages 3 and 4. Accordingly, the total of length of crack for Damages 3 and 4 are, respectively, equal to 19.1 mm and 25.3 mm.

- Damage 3 (D3) (propagated crack): $a = 19.1$ mm
- Damage 4 (D4) (propagated crack): $a = 25.3$ mm

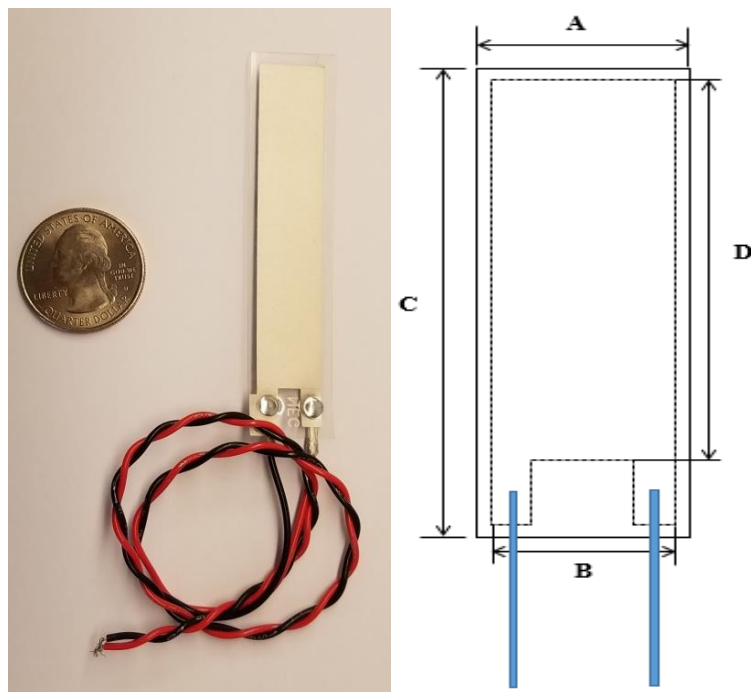


Figure 3-29: LDT2-28K PVDF Sensor.

For each of the tests, the initial voltage of the gates is set to 1.2 V. Then, the voltage is read after applying 50 cycles. The initial voltage value dropped after applying the cycling loading due to electrons injection. Therefore, after each test, the sensor is tunneled and injected to reset all gates to almost the same voltage.

Based on a series of preliminary tests, the threshold voltage of Gates 1 to 7 are summarized in Table 3-5.

Table 3-5: Voltage threshold levels of each gate.

Gate Number	Voltage (V)
1	7.6
2	8.1
3	8.5
4	8.8
5	9.0
6	9.7
7	10.2

3.3.2.1.2.2. Damage detection based on experimental results

The voltage droppage per 50 cycles with respect to different damage states for the seven gates is presented in Figure 3-30. The corresponding percentages of voltage droppage are shown in Figure 3-31. As soon as the voltage generated by the PVDF exceeds a threshold corresponding to one of the gates, the procedure of electrons injection initiates, and subsequently the voltage of that gate starts decreasing.

It can be seen that the voltage droppage rate increases when damage progresses. This is evident for all the 7 gates on-board the sensor, specifically for gates 1-6. Gate 7 is activated at a higher voltage threshold (> 10.2 V), and therefore it started injecting after the fourth damage state. Apparently, the gate activation can be considered as an indicator of damage occurrence.

The other important observation from Figure 3-31 is that the voltage droppage percentage for each gate is also a good indicator of damage progression. For instance, consider the response of

gate 1 to the voltage generated by the PVDF for D0 to D4 damage states (Figure 3-31 (a)). Since the voltage amplitude is higher for the D4 mode than that for the other modes, the injection time is higher, and therefore the voltage in the gate dropped more for this mode. The same is true for the D3-D2, D2-D1 and D1-D0 cases. These trends are similar to those observed from the FE results.

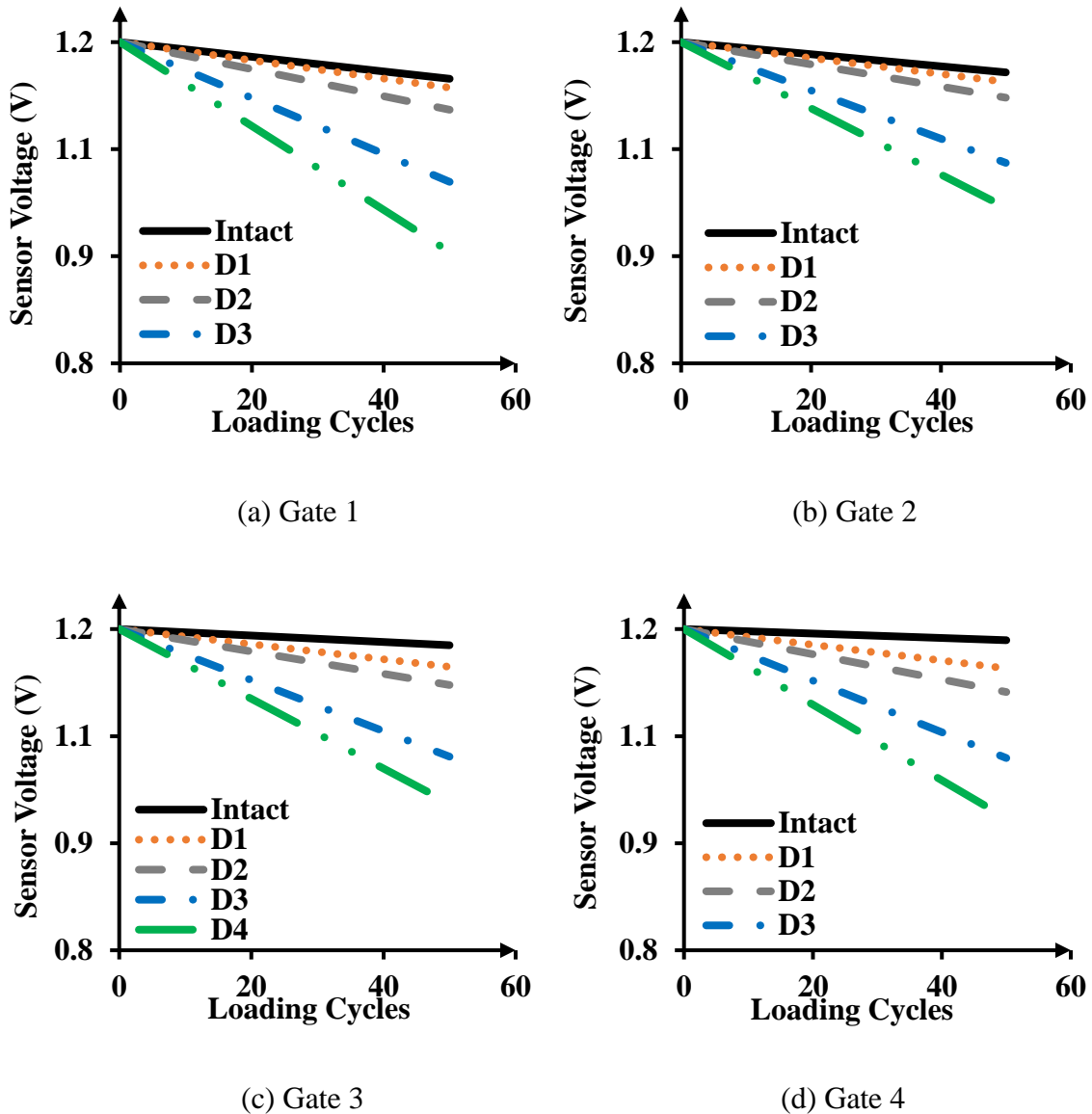
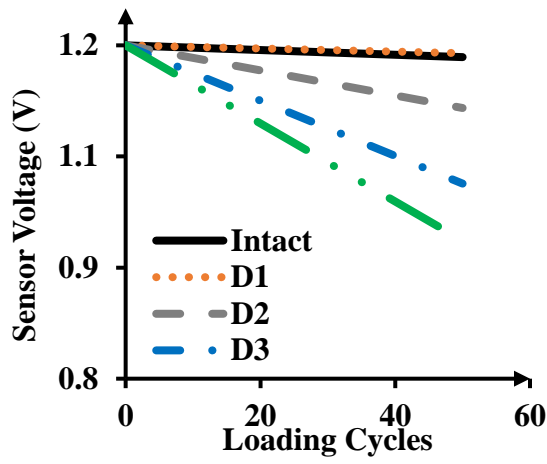
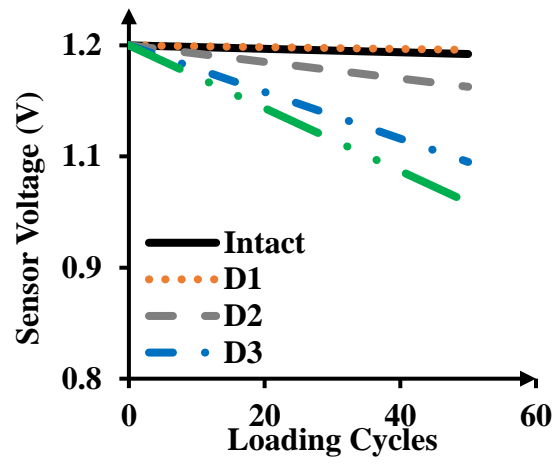


Figure 3-30: Voltage changes across the floating-gates of the sensor.

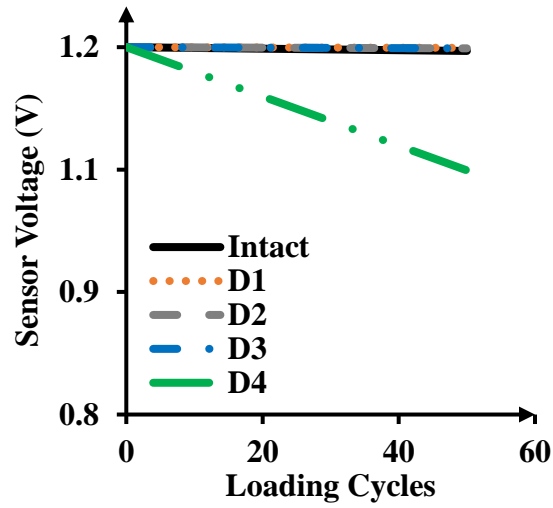
Figure 3-30 (cont'd)



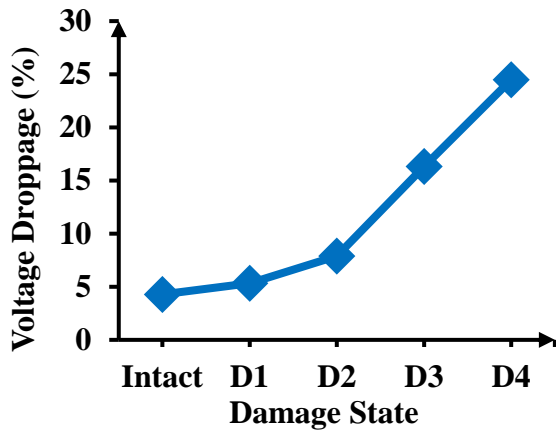
(e) Gate 5



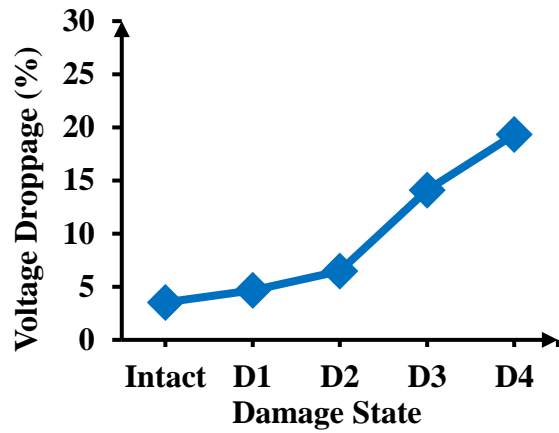
(f) Gate 6



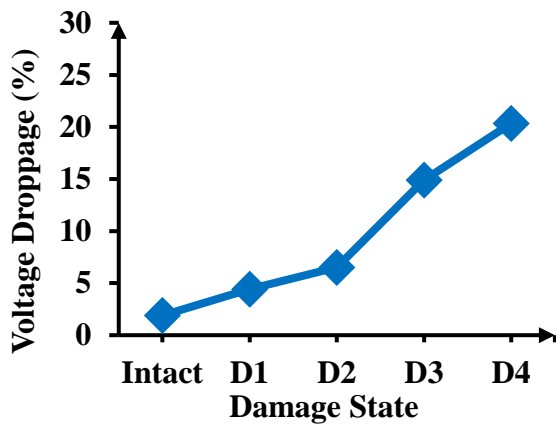
(g) Gate 7



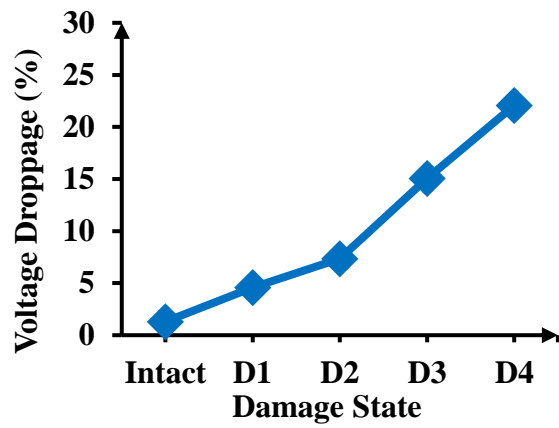
(a) Gate 1



(b) Gate 2



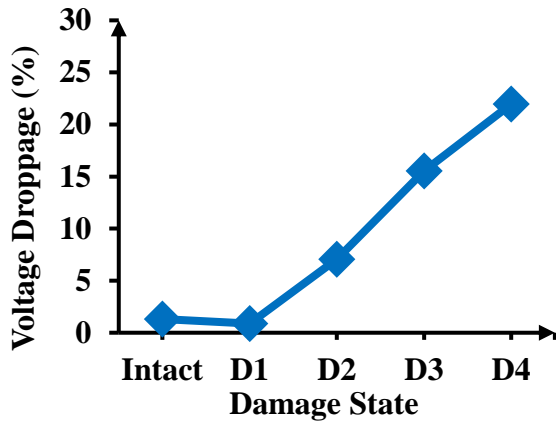
(c) Gate 3



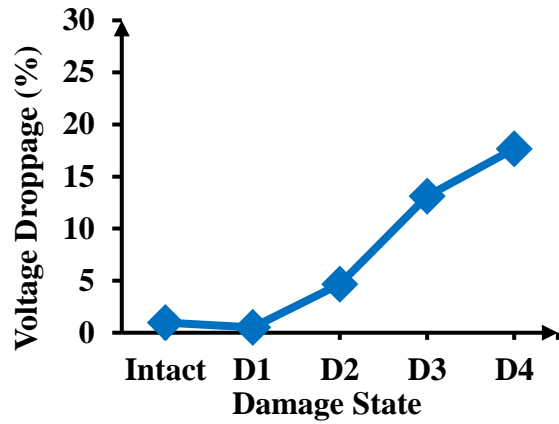
(d) Gate 4

Figure 3-31: Percentage of voltage droppage for different gates.

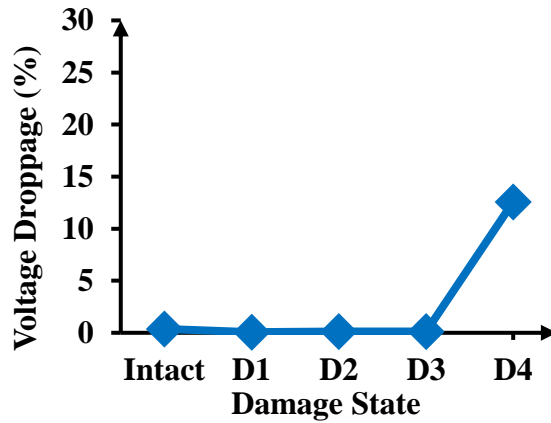
Figure 3-31 (cont'd)



(e) Gate 5



(f) Gate 6



(g) Gate 7

3.3.2.2. Surface sensing of bottom-up cracking in pavements

This section presents a self-powered surface sensing approach for detection of bottom-up cracking in AC pavements. The proposed method is based on the interpretation of compressed data stored in memory cells of a nonuniform self-powered wireless sensor. Different 3D FE models of an AC pavement are developed using ABAQUS to generate the sensor output data. A

realistic dynamic moving load is applied to the surface of the pavement via DLOAD subroutine developed in FORTRAN language. A network of sensing nodes is placed at the top of the AC layer to assess their sensitivity to the progression of bottom-up cracks. Several damage states are defined using the element weakening method. A linear-viscoelastic behavior is considered for the AC layer. In order to detect the damage progression, several damage indicators features are extracted from the data acquisition nodes. The damage detection accuracy is improved through a data fusion model that included the effect of group of sensors. The proposed fusion model is based on the integration of a Gaussian mixture model (GMM) for defining descriptive features, different feature selection algorithms, and a robust and computational intelligence approach for multi-class damage classification. Furthermore, an uncertainty analysis is carried out to verify the reliability of the proposed damage detection approach.

3.3.2.2.1. Finite element modeling of pavement structure subjected to a moving load

ABAQUS software is employed to simulate the response of the pavement under a moving load. In the FE analysis, the stress/strain response is sensitive to element type, size, and boundary conditions. In this study, 3D FE models are developed as they are more appropriate compared to 2D axisymmetric model. In fact, a 3D model allows simulating the contact stresses between the tire footprint and the pavement surface. The pavement model is meshed using two different types of elements: eight-node linear brick elements with reduced integration (C3D8R) and eight node linear infinite elements (CIN3D8). The standard finite elements are used to model the region of interest and the infinite elements are deployed in the far field region. This type of elements allows providing silent boundaries to the FE model in the dynamic analysis and reduces the number of elements at far field (ABAQUS, 2010). These elements have a special shape function to vanish the displacement field when the coordinates approach infinity. Such boundary

type can minimize the reflection of the shear and dilatational waves back into the FE mesh (Al-Qadi et al., 2010; Wang, 2011). In a dynamic analysis, the infinite elements introduce additional normal and shear tractions on the FE boundary using a viscos damping boundary. The introduced normal and shear stresses are proportional to the velocity components as follows (Wang, 2011):

$$\sigma = \rho c_p \dot{u} \quad (3-21)$$

$$\tau = \rho c_s \dot{v} \quad (3-22)$$

where ρ , σ , τ , c_p , c_s , \dot{u} and \dot{v} are the material density, normal stress along the interface between the FE/infinite elements, shear stress along the interface FE/infinite elements, longitudinal wave velocity, shear wave velocity, normal velocity and tangential velocity, respectively. The wave velocities are given by the following expressions (Wang, 2011):

$$c_p = \sqrt{\frac{(1-\nu)E}{(1-2\nu)(1+\nu)\rho}} \quad (3-23)$$

$$c_s = \sqrt{\frac{E}{2(1+\nu)\rho}} \quad (3-24)$$

where E and ν are the Young modulus and Poisson's ratio, respectively. In this study, the length of the pavement section is 7 meters in the longitudinal direction (parallel to the traffic direction) and 6 meters in the transverse direction (perpendicular to the traffic direction). The pavement thickness is 6.3 meter. The pavement is composed of three layers: AC, base and subgrade. The thickness of the AC, base and subgrade layers are 100 mm, 200 mm and 6000 mm, respectively. Large model dimensions are used to reduce the edge effect and to achieve a full passage of the tire on the pavement section. Figure 3-32 displays the pavement model as well as the meshed cross section of the AC layer. According to a study conducted by Duncan et al., the location of

the infinite elements should be at least 12 times the radius of the loading area (R) in the horizontal direction (Duncan, 1968). In this study, the infinite domain is located at approximately 16R from the initial and final locations of the load center in the longitudinal direction, and 17R in the transverse direction. The total number of elements is 393,796, from which 363,440 elements are C3D8R and 30,356 elements are CIN3D8. Figure 3-33 displays the structure of CIN3D8. A fine mesh is used around the loading path and a coarse mesh far away from the load. Different simulations are conducted to study the effect of the element dimensions on the pavement response. It is found that an element with dimensions of 20 mm × 20 mm could accurately capture the stress/strain response under the wheel footprint.

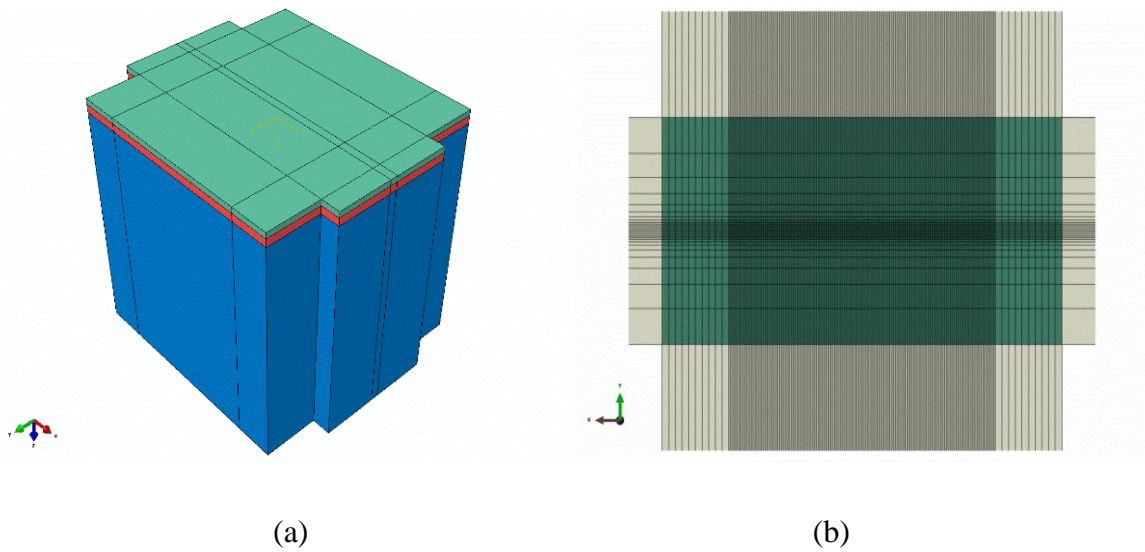


Figure 3-32: (a) The 3D FE model of the pavement structure, (b) Meshed cross section of the AC layer.

The element thickness is chosen to be 10 mm for the AC layer, 20 mm for the base, and from 20 mm to 500 mm for the subgrade. Furthermore, in a dynamic analysis, it is recommended that the maximum element size should not exceed 1/12 the minimum length of the elastic waves

propagating inside the structure (Wang, 2011).

The natural frequency of a typical flexible pavement, the vehicle loading frequency, and the stress wave velocity are around 6-14 Hz, 0.1-25 Hz and 100 m/s to 600 m/s, respectively (Wang, 2011). Accordingly, the defined element size is small enough to satisfy the minimum element size requirement.

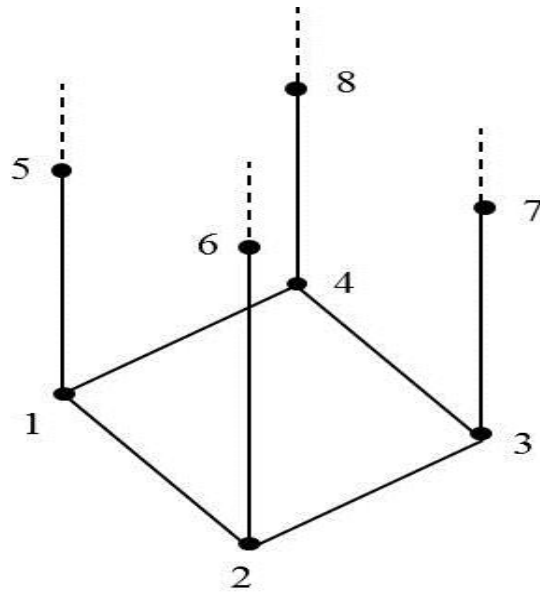


Figure 3-33: Structure of CIN3D8 element.

3.3.2.2.1.1. Dynamic analysis

For a pavement analysis, the loading can be modeled as static, quasi-static, or dynamic loading. If the loading is stationary, a static analysis is suitable for the analysis. A quasi-static approach is a sequence of static loads that are moving from one position to another at each time step. Static and quasi-static analyses do not include the effect of inertia forces. However, a dynamic analysis is more appropriate if the load is moving with a certain speed in which the loading changes in time and location. Therefore, this type of analysis is used for this study. The moving load problem can be treated as structural dynamic problem as it considers slower load

changes than wave propagation problems. The response in a wave propagation problem is rich in high frequency mode shapes. The analysis time is also in the order of the wave travel time across the structure. Therefore, a very short time step is required for this type of analysis. In structural dynamic problems, the response is dominated by low modes and the effect of high modes is insignificant (Chopra, 2001; Bathe, 1996). If the time required for the stress waves to propagate through the whole structure does not exceed a small portion of the load rise duration, the problem can be assumed to be a structural dynamic problem. As the vehicle speed is much smaller than the stress wave speed (100 m/s to 600 m/s), the problem is treated as a structural dynamic problem in this study. The equation of motion of a multi-degree of freedom system is as given below:

$$M \ddot{u} + C \dot{u} + K u = F \quad (3-25)$$

where M is the mass matrix, C is the damping matrix, K is the stiffness matrix, u is the displacement vector and F is the external force vector. The first term of the equation $M \ddot{u}$ represents the inertia forces and $(C \dot{u} + K u)$ represents the internal forces.

There are two ways to solve this type of nonlinear equations; an implicit direct integration or an explicit direct integration method. The implicit procedure is more suitable for structural dynamic problems and usually provides good numerical stability. For the method, the displacements at two consecutive times are calculated by solving a set of nonlinear equations simultaneously.

In a dynamic analysis, the selection of the time increment is very important. According to Bathe, the time increment Δt should be less than or equal to $\frac{1}{20 f_{dominant}}$ (Bathe, 1996):

$$\Delta t \leq \frac{1}{20 f_{dominant}} \quad (3-26)$$

where $f_{dominant}$ is dominant frequency of the response of the structure or of the loading. Herein, the time increment is taken 0.001 s which satisfies the time increment requirement as the highest loading frequency is usually lower than 10 Hz.

3.3.2.2.1.2. Material characterization

Each layer of the modeled pavement has unique material properties. The HMA layer has viscoelastic properties while an elastic behavior is considered for the base and subgrade layers. The HMA modulus is time (frequency) and temperature dependent. In fact, the state of the stress in the AC layer does not only depend on the current strain but on the entire strain history. Table A-1 presents the values used for the definition of the viscoelastic material property of the AC layer. The Poisson's ratio is equal to 0.35. For the AC layer, there is no need to define an additional structural damping because it behaves as a viscoelastic material. However, the base and the subgrade are elastic materials, and therefore, it is important to add an additional damping to include the effect of energy absorption when the wave propagates through the soil. Therefore, a 5 % damping ratio is defined for both the base and the subgrade layers. Table 3-6 presents the material properties of the three pavement layers.

Table 3-6: Material properties.

Layer	Modulus (MPa)	Poisson's Ratio	Density (Kg/m ³)	Damping (%)
HMA	9548	0.35	2325	-
Base	193	0.3	2000	5
Subgrade	43	0.4	1500	5

3.3.2.2.1.3. Loading

Tire-pavement interaction is a complex phenomenon due to the tire footprint, non-uniform contact area, and shear stress components (Siddharthan et al., 1998). A tire footprint consists of many small surfaces contacting the pavement separated by ribs that may not make contact with pavement and thus may not contribute to the loading. Defining a tire footprint that simulates a real tire-pavement interaction is possible using the FE modeling. Tielking and Roberts used the ILLIPAVE finite element pavement program to model non-uniform contact pressures of a tire moving on an asphalt pavement section (Tielking and Roberts, 1987). Their tire contact pressure model considered normal pressure, transverse shear pressure, and longitudinal shear pressure. Their results showed that non-uniform tire contact pressure induced greater tensile strain at the bottom of the asphalt layer compared to uniform contact pressure. However, simplifying the tire contact pressure area can affect the pavement strain response since the distribution of the stress field in the contact zone is not uniform (Tielking and Roberts, 1987; Wang and Machemehl, 2006; Yue and Svec, 1995). Tire pressure and load intensity affect contact stress distribution (Tielking and Roberts, 1987; Alkasawneh et al., 2008; Mun et al., 2006; Weissman, 1999; Perret and Dumont, 2004). In the multilayered elastic theory, the shape of the tire footprint is assumed to have a circular shape as it conserves the property of an axisymmetric problem. Wang and Machemehl showed that the assumption of a uniform circular tire-pavement pressure area can underestimate the compressive strains at the top of the subgrade and overestimate the tensile strains at the bottom of the AC layer (Wang and Machemehl, 2006). In most of the 3D FE modeling of pavements, the contact area between the tire and the pavement surface is approximated to a rectangle with two semi-circles as shown in Figure 3-34. Previous study shows that the shape of the contact area of a truck tire is closer to be rectangular than

circular (Weissman, 1999).

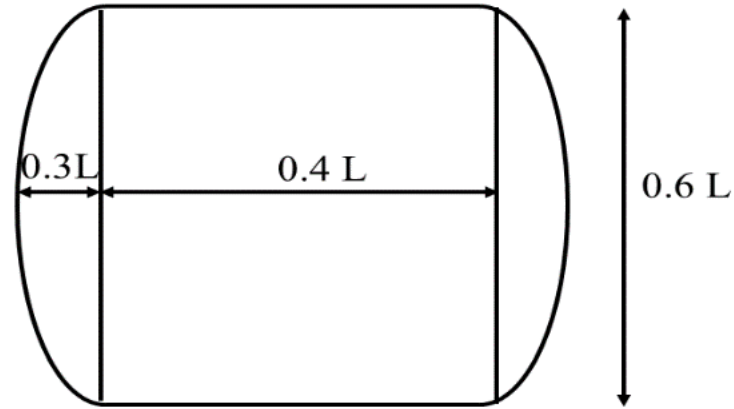


Figure 3-34: Tire contact area.

In this study, the contact area is assumed to be rectangular. The obtained contact area is transformed to a simple rectangle with the same width $0.6 L$. The area of the contact zone shown in Figure 3-34 is equal to:

$$A_c = 0.4 L \times 0.6 L + 2 \times \left(\frac{\pi (0.3 L)^2}{2} \right) = 0.5227 L^2 \quad (3-27)$$

Therefore, if a denotes the length of the equivalent rectangle, the equivalent area (Figure 3-35) is:

$$A_c = a \times 0.6 L = 0.5227 L^2 \quad (3-28)$$

which gives: $a = \frac{0.5227 L^2}{0.6 L} = 0.8712 L$

The area of the contact area used in this study is $A_c = 0.0260 \text{ m}^2$. Therefore L is given by:

$$L = \sqrt{\frac{A_c}{0.5227}} = \sqrt{\frac{0.0260}{0.5227}} = 0.2230 \text{ m} \quad (3-29)$$

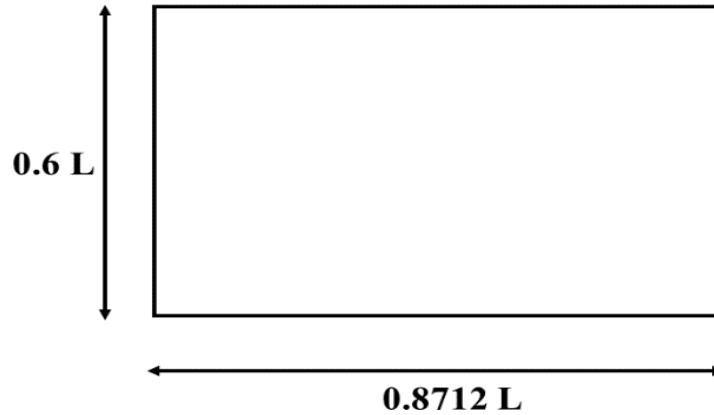


Figure 3-35: Approximated rectangular loading.

Thus, the dimensions of the rectangle are: $0.8712 L = 0.1943 \text{ m}$ and $0.6 L = 0.1338 \text{ m}$.

The loading of the pavement occurred at the center strip of the section. Figure 3-36 highlights the loaded strip. In order to simulate the movement of the load at the desired speed, a user defined DLOAD subroutine is developed using FORTRAN. In fact, regular loading functions in ABAQUS do not allow varying the location of the applied load as a function of time. In order to overcome this limitation, different approaches are proposed. The load and its amplitude can be shifted over the loading path at each step until a single wheel pass is completed (Alavi et al., 2016c; Al-Qadi and Wang, 2009). This approach is time consuming as it needs the definition of the footprint areas for each step. However, the DLOAD subroutine can be used to define the variation of the distributed load magnitude as function of the position, time, element number, and load integration point number (ABAQUS, 2010).

The script specifies the center of the rectangular loading area and its dimensions, the initial and final position of the truck, the truck speed and the tire pressure. A highway speed of 67 mph (30 m/s) is inputted to the FORTRAN code and a tire pressure of 862 kPa is applied. The location of the center of the contact area is calculated by the DLOAD subroutine in each time step as follows:

$$x = v_x \times t + x_0 \quad (3-30)$$

$$y = v_y \times t + y_0 \quad (3-31)$$

where v_x , v_y , x_0 and y_0 are the speed in x direction, the speed in the y direction, the x-coordinate of the initial location of the tire center, and the y-coordinate of the initial location of the tire center. The vehicle speed is kept constant.

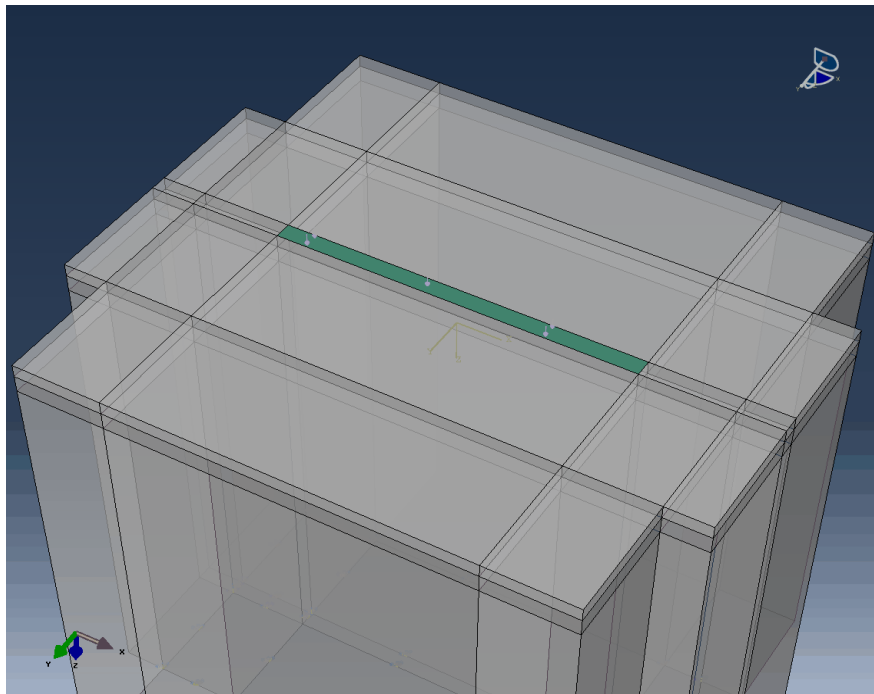


Figure 3-36: Loaded strip of the AC pavement section.

In this work, the loading is assumed to follow the x-axis, therefore, v_y is set to zero. The chosen length of the loading path is 3 m. As the selected time step of the dynamic analysis is 0.001 second, the tire progresses by:

$$\Delta x_{time-step} = v \Delta t = 30 \times 0.001 = 0.03 \text{ m} = 30 \text{ mm} \quad (3-32)$$

The size of the element around the loading path is 20 mm \times 20 mm, therefore, only one element

(in the longitudinal direction) is loaded in each time step.

3.3.2.2.1.4. Crack modeling

Many recent studies on fatigue of flexible pavements have been conducted using the FE softwares such as ABAQUS and FEP++ (Huang et al., 2010; Mun et al., 2006; Sarkar, 2016; Shafabakhsh et al., 2015; Dave and Buttlar, 2010). These programs allow the user to define various complex parameters such as the viscoelastic properties of asphalt. A limitation of using FE programs for the asphalt pavement analysis pertains to the definition of highly complex scenarios such as fatigue cracking. Fatigue cracking can begin as either bottom-up crack, top-down crack, or combination of the two. After repeated loading of the asphalt pavement, crack propagation and additional crack growth further weaken the pavement. These cracks that begin at one end can either continue growing through the thickness of the pavement or coalesce with a different crack growing in another direction. Modeling of fatigue cracking inadequately can result in overestimation of fatigue life (Mun et al., 2006). Major factors affecting fatigue cracking are asphalt properties, asphalt thickness, and tire pressure among others. Generally, top-down cracking increases in thicker asphalt, stiffer asphalt, less stiff base and/or subgrade, and under non-uniform loading (Mun et al., 2006).

ABAQUS allows the user to define certain properties by a user subroutine (ABAQUS, 2010). Detailed crack modeling is typically defined using a user subroutine in order to realize more realistic results due to limitations in the basic modeling methods. Cracks defined in ABAQUS using basic modeling for asphalt pavement yield to inaccurate results due to over simplification of the crack. Modeling crack in ABAQUS can be done using XFEM. The major limitation that deter XFEM usage in the fatigue cracking of pavements is that the method is only viable in static cases. Creating a user subroutine to accurately model fatigue cracking in asphalt has yet to be

accomplished. Song et al. have developed a user subroutine of a cohesive fracture model that successfully replicated cracking in asphalt concrete (Song et al., 2006). Dave and Buttlar have successfully modeled thermal reflective cracking using a user-defined bilinear cohesive crack model (Dave and Buttlar, 2010). A crack can also be introduced using element weakening method. Mishnaevsky Jr. has used this method to simulate the reduced properties resulting from cracking of particle reinforced composites (Mishnaevsky Jr., 2004).

In this section, the EWM is also used to introduce the damage to the pavement. Different scenarios are defined based on both the weakening state of elements defining the damage zone and the damage height. On this basis, the element elastic modulus is reduced to a certain value in order to define a damage state.

A total of 13 damage states are studied which include 4 different cases of modulus reduction, each having three varying damage zone heights. A damage having a rectangular prismatic shape of $120 \text{ mm} \times 120 \text{ mm} \times \text{damage height}$ is created at the bottom center of the HMA layer. The modulus of this volume is reduced to 30%, 50%, 70%, and 90% from the instantaneous modulus of the HMA layer. The damage zone heights are 20 mm, 40 mm and 60 mm. The defined damage states are given in Table 3-7. Figure 3-37 shows the damage location, cross section, and the measurement locations.

Table 3-7: Damage scenarios.

Damage State	Damage Height (mm)	Reduction in AC Modulus (%)
Intact	0	0
D20W30	20	30
D20W50	20	50
D20W70	20	70
D20W90	20	90
D40W30	40	30
D40W50	40	50
D40W70	40	70
D40W90	40	90
D60W30	60	30
D60W50	60	50
D60W70	60	70
D60W90	60	90

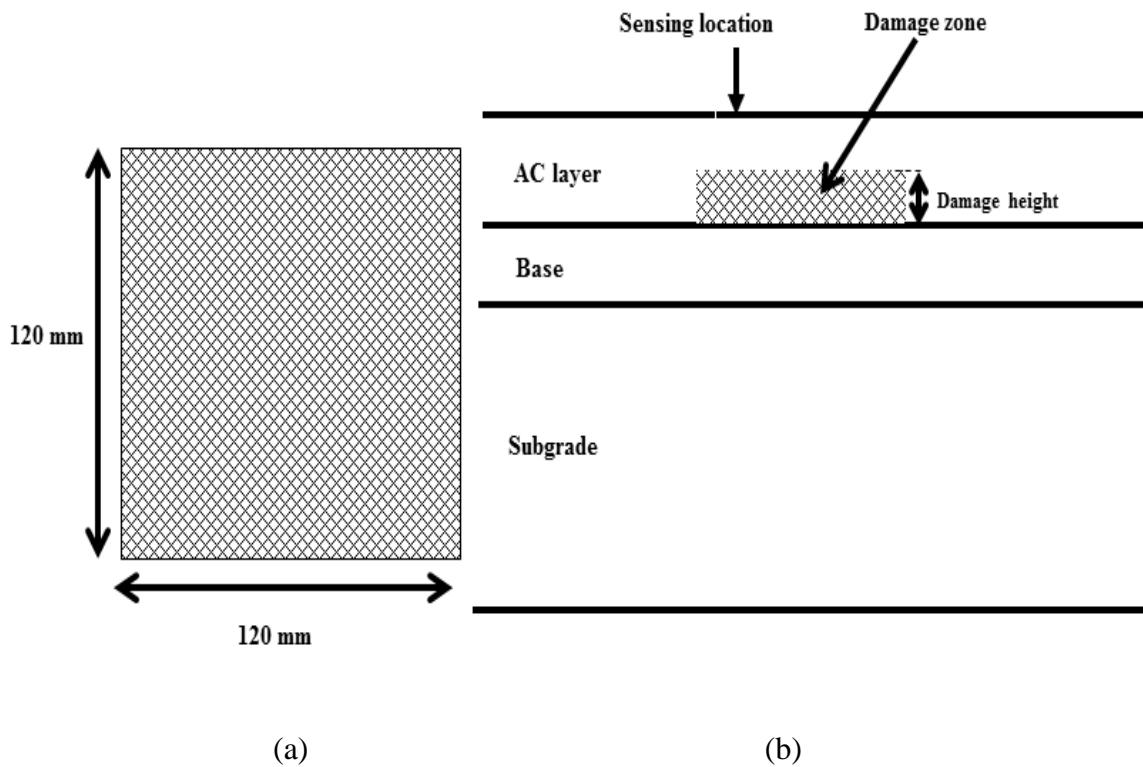


Figure 3-37: (a) Cross section of the damage (b) Crack zone and measurement location.

3.3.2.2.2. Sensors location

Figure 3-38 shows the location of the data acquisition nodes on the surface of the AC layer. A network of 32 elements is selected as the sensing nodes. The network is divided into 4 sets. Each set contains 8 sensing nodes.

In each set, the first sensor is located at $y = 0$, and the distance between two consecutive elements is 200 mm. The transversal distance between two sets is 60 mm. Therefore, the offset of the sets from the center of the pavement ($y = 0$) is considered as follows:

- Set 1: $y = 0$
- Set 2: $y = 60$ mm
- Set 3: $y = 120$ mm

- Set 4: $y = 180 \text{ mm}$

The longitudinal, transverse and principal strains ($\epsilon_1, \epsilon_2, \epsilon_3$) for each of the predefined damage cases are subsequently extracted.

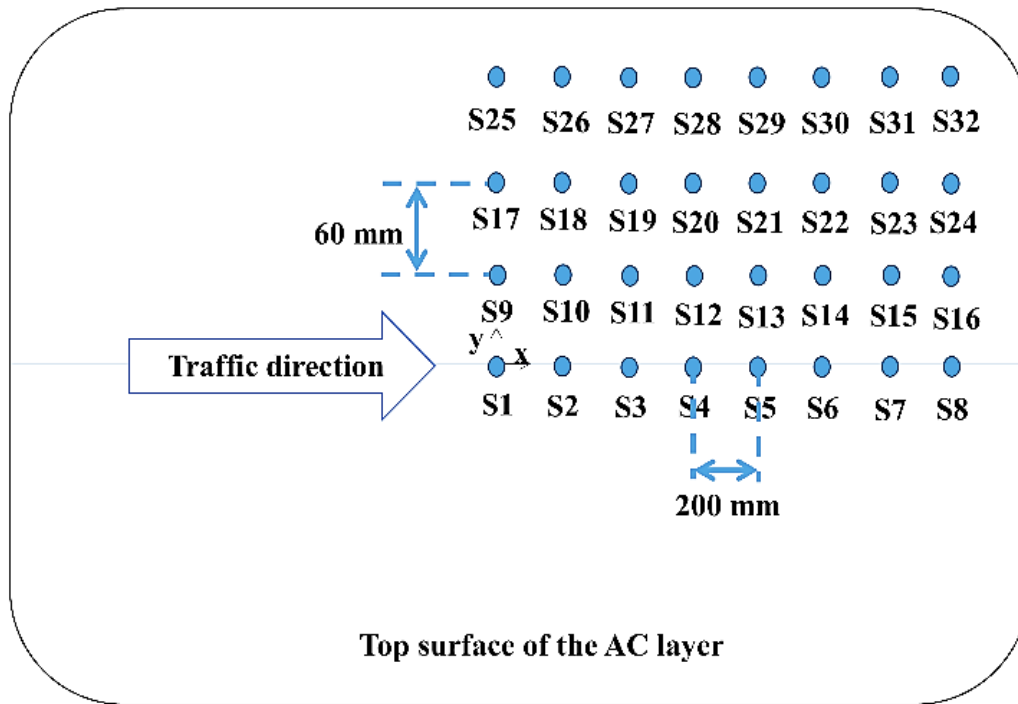


Figure 3-38: Sensors locations.

3.3.2.2.3. FE results

Figure 3-39 shows the time history of the first principal strains (in absolute value) for different sensors and for the intact, D20W90, D40W90 and D60W90 damage states. As can be seen, for sensor S1, which is located above the damage zone, the amplitude of the strain increases with damage growth. The difference of the amplitudes between the Intact and the D60W90 damage state is $111.7 \mu\epsilon$.

Figure 3-40 displays the results for sensor S2. Evidently, the difference between the maximum principle strains is being reduced comparing to sensor S1 as the sensor is located at a 200 mm

offset from S1 (along the x-axis).

Figure 3-41 displays the results for sensor S17 which is located at $x = 0$ and at $y = 120$ mm. As seen can be seen in the figure, the amplitude of the strain is changing between damage states, but it does not have an increasing trend comparing to sensors S1 and S2. However, for sensor S18, which has a 120 mm offset from the x-axis and 200 mm offset from the y-axis, the strain amplitude continuously increases as the damage progresses (Figure 3-42). Based on the results, it can be concluded that the amplitude of the strains is affected by the damage progression as well as the location of the sensor with respect to the damage.

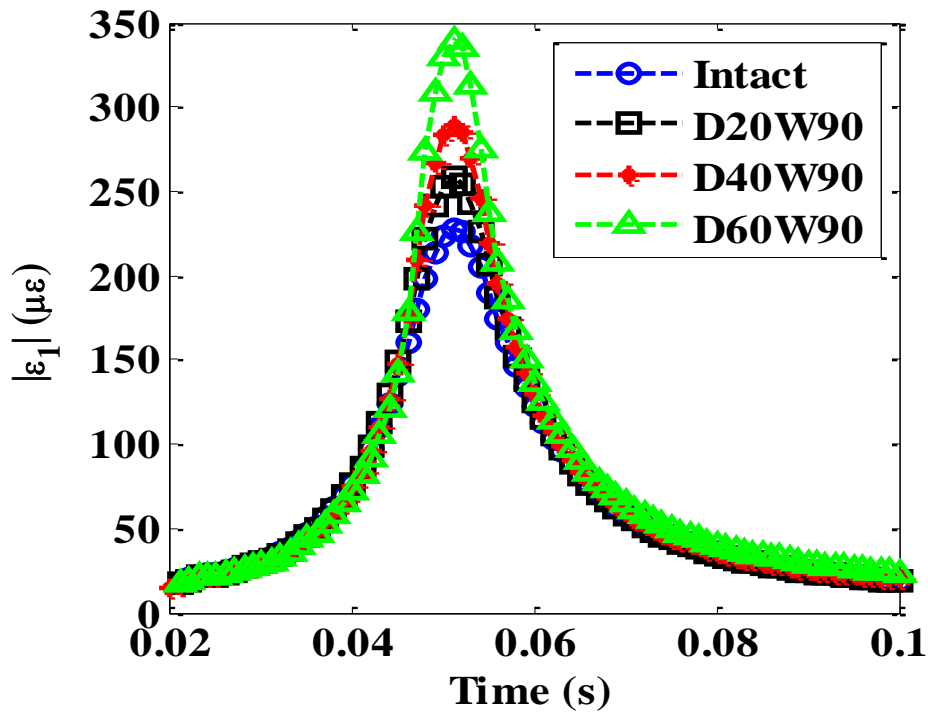


Figure 3-39: Strain history of sensor S1 for different damage states.

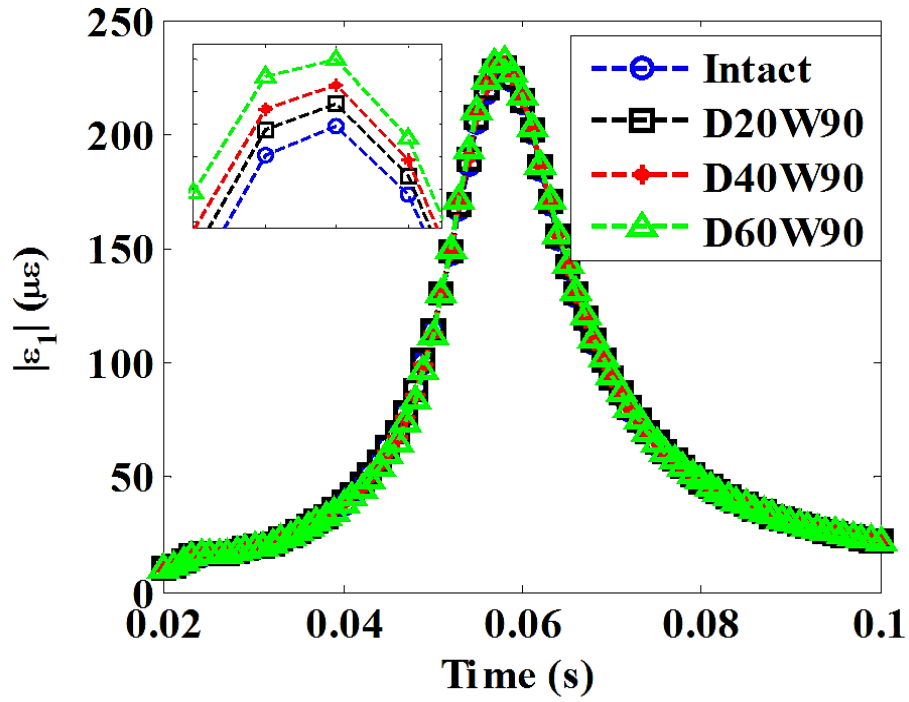


Figure 3-40: Strain history of sensor S2 for different damage states.

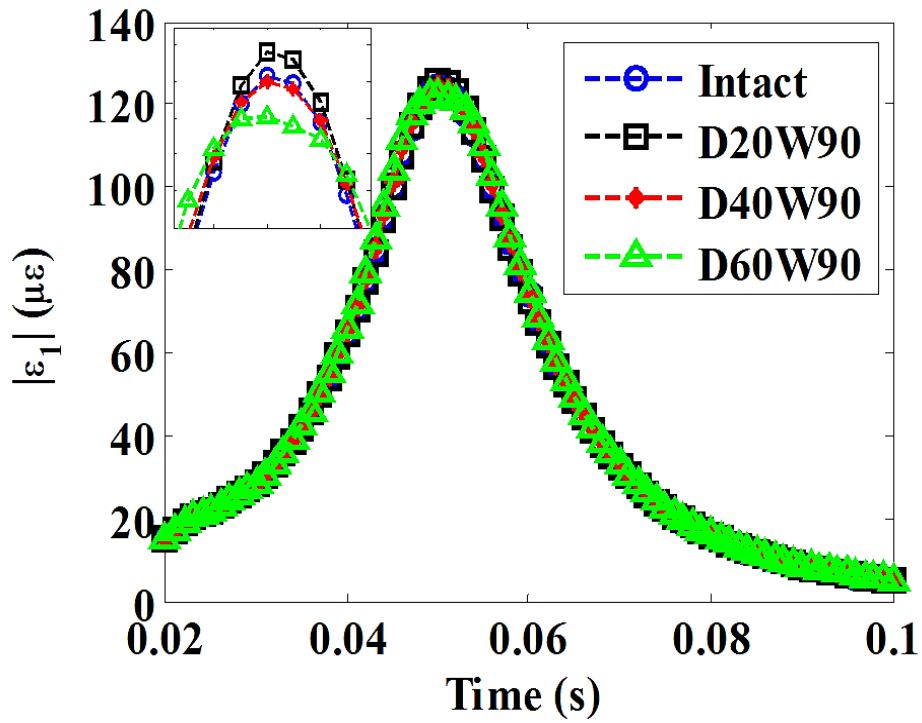


Figure 3-41: Strain history of sensor S17 for different damage states.

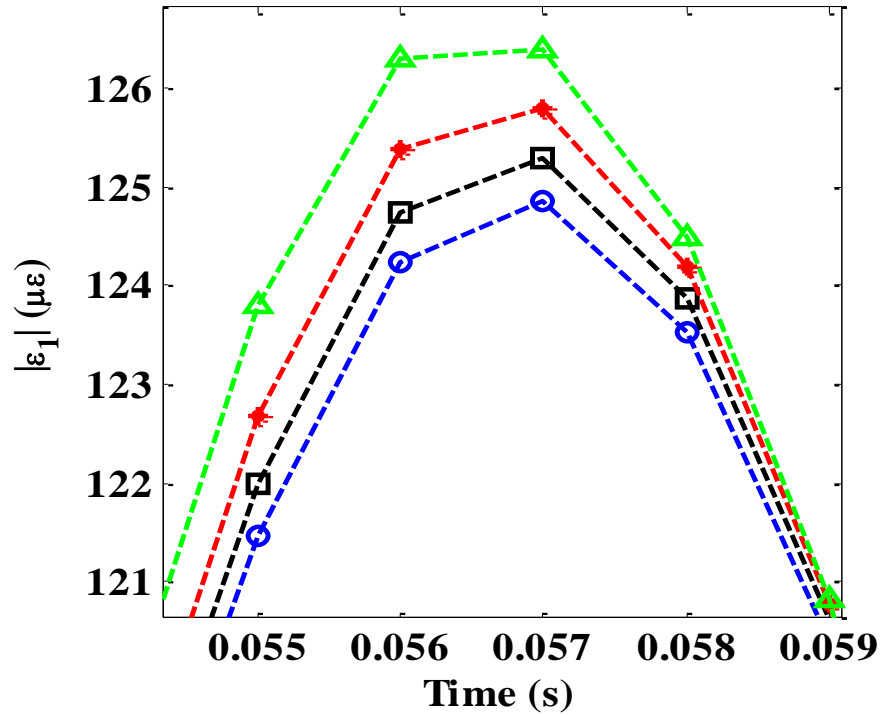
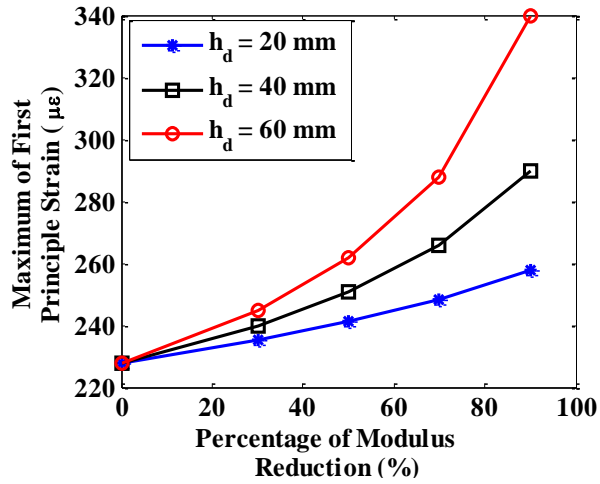
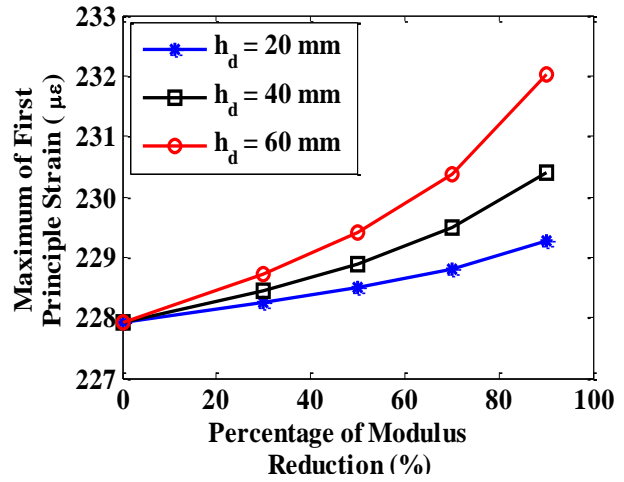


Figure 3-42: Zooming around the peak values of sensor S18.

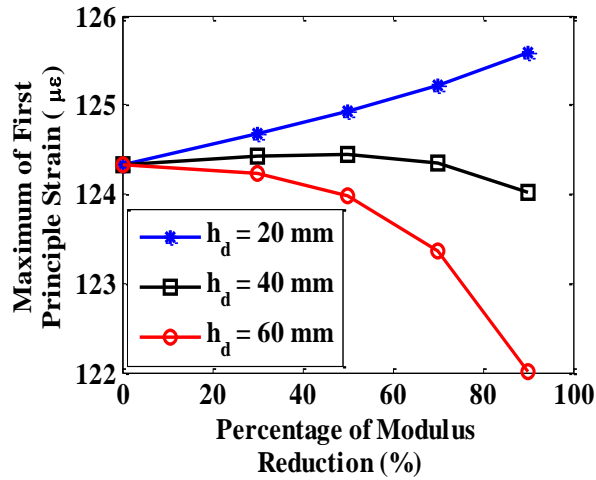
Figure 3-43 presents the variation of the maximum first principal strain (in absolute value) with respect to the percentage of modulus reduction for different damage heights (h_d). As seen in these figures, the amplitude of the strain depends on the offset of the sensor with respect to the damage zone. In fact, for a fixed reduction in the asphalt modulus, the strain amplitude increases for sensors S1 and S2 but the behavior changes when the sensor is located at a certain offset from the damage center. Furthermore, as it is illustrated by sensor S17, and for a fixed damage height, the strain increases with the percentage of modulus reduction for the case of 20 mm but it has a decreasing trend for the two other damage lengths (40 mm and 60 mm). However, when the sensors are located along the wheel path, a unique trend is observed. In this case, the amplitude of the first principal strain increases with the damage height and the percentage of modulus reduction.



(a) Sensor S1



(b) Sensor S2



(c) Sensor S17

Figure 3-43: Variation of the Maximum principal strain with the damage state.

3.3.2.2.4. Proposed damage detection approach

The damage detection approach proposed in this work is divided into three stages. The first step is focused on generating and characterizing the sensor output based on the time history of the first principal strains obtained in the previous section. Thereafter, a feature transformation method is applied to the original set of data to find a sound relationship between the damage

progression and the data of the network of sensors. Finally, a PNN classifier is integrated to classify the pre-defined damage classes.

For the analysis, the initial strain value in each memory is set to $500 \mu\epsilon$. The gate injection rates as well as the strain threshold levels are displayed in Table 3-8. The selection of the thresholds and number of gates is based on the injection rates of an existing sensor. The activation strain of the sensor is $80 \mu\epsilon$ below which the device does not record any information. The maximum threshold is $200 \mu\epsilon$.

Figure 3-44 presents the variation of the sensor strain at each gate versus the number of applied cycles for the intact pavement and for one damage scenario. For brevity, only the results pertaining to the intact and D60W90 modes are compared for sensor S1. As it is seen in Figure 3-44, the strain varies linearly as a function of the number of cycles. In addition, the slopes of the curves corresponding to the damaged pavement are higher (in absolute value) than the intact configuration. This can be explained by the fact that the amplitude of strain continuously increases at location of sensor S1 with respect to the damage progression. In addition, the cumulative time intersection increases with an increase in the strain amplitude.

In this study, a GMM is proposed to fit the cumulative droppage of the strain at the sensing nodes. GMMs are very powerful tools to adequately describe many types of data. In fact, certain models exhibit multimodalities that are poorly described by a single Gaussian distribution. In the case of different injection rates, the output histogram is expected to have different rate of strain variation between the gates resulting in multiple maxima. Therefore, a multi-modal Gaussian mixture (GM) model can be a good fit to the data. The PDF of a GM distribution is given by the following expression:

$$p(x) = \sum_{k=1}^M \frac{c_k}{\sqrt{2\pi}\sigma_k} \exp\left[-\frac{1}{2}\left(\frac{x-\mu_k}{\sigma_k}\right)^2\right] \quad (3-33)$$

where μ_k, σ_k ($k = 1..M$) are mixture component parameters and c_k are the mixture weights. The mixture weights of the PDF should satisfy the following condition:

$$\sum_{k=1}^M c_k = 1 \quad (3-34)$$

For the analysis, the strain droppage histogram is fitted by a bimodal GMM as follows:

$$\Delta\varepsilon(g) = (\sum_{i=1}^7 \Delta\varepsilon_i) \sum_{k=1}^2 \frac{\alpha_k}{\sqrt{2\pi}\sigma_k} \exp\left[-\frac{1}{2}\left(\frac{g-\mu_k}{\sigma_k}\right)^2\right] \quad (3-35)$$

where g is the gate number, (μ_k, σ_k) are the mixture components parameters, α_k is a parameter, and $\Delta\varepsilon_i$ is the cumulative droppage in strain at gate number i .

Table 3-8: Preselected strain levels and gate injection rates considered for the analysis.

Gate Number	Strain Threshold	Injection
	Level ($\mu\varepsilon$)	Rates ($\mu\varepsilon/s$)
1	80	0.001000
2	100	0.005710
3	120	0.023162
4	140	0.027822
5	160	0.006562
6	180	0.005989
7	200	0.032792

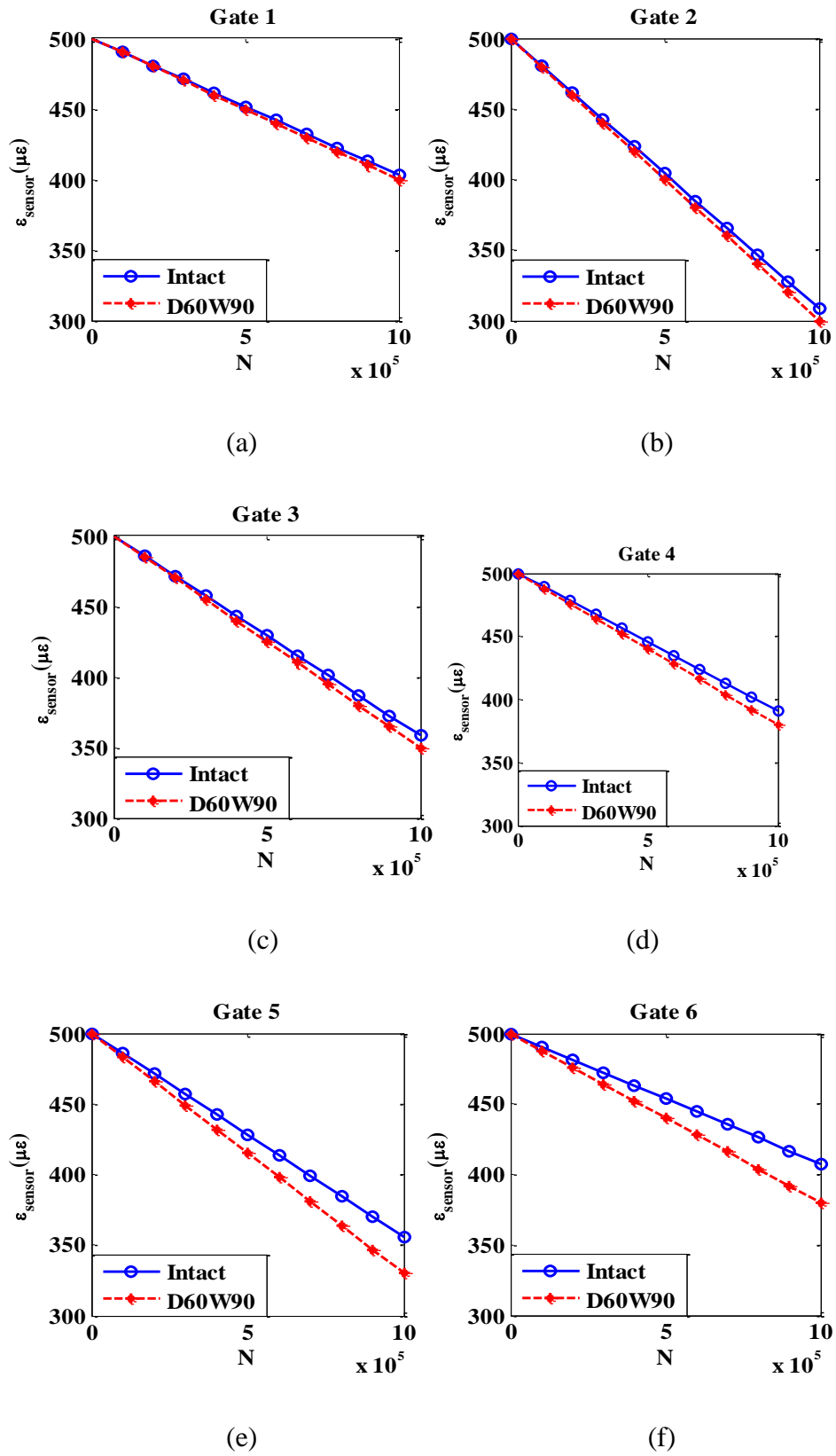
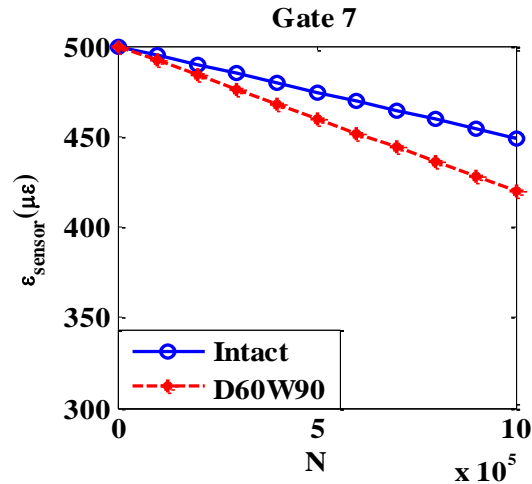


Figure 3-44: Strain change across sensor S1 gates.

Figure 3-44 (cont'd)



(g)

Equation (3-35) has 6 parameters to estimate: μ_k , σ_k , α_k , $k=1,2$. These parameters can be obtained based on the 7 values of each gate of the sensor. Figure 3-45 displays the obtained GMM fit to the data of sensor S1.

One million traffic cycles are applied to the pavement in order to get a significant droppage in the sensor output data. It is important to mention that the injection rates can be modified using an additional resistance in parallel with the internal resistance of the sensor. Therefore, for a fatigue analysis, the impedance of the sensor should be increased in order to lower the injection rates of the gates.

As seen in Figure 3-45, the output histogram presents 2 peaks corresponding to the first two maximum strain drops. It is important to mention that the maximum values do not only depend on the injection rates, but they are also related to the threshold levels, the number of cycles, and the strain rate variations. Figure 3-46 displays the results of the GMM fit for different sensors. The GMM curves are plotted for the intact configuration and for D60W90 damage state.

Based on the results, the GM distribution deviates from one damage states to another. According to the section 3.3.2.2.3, the amplitude of the strain changes with damage. As a result, the cumulative time intersection changes as well and affects the variation of the strain at the sensor level.

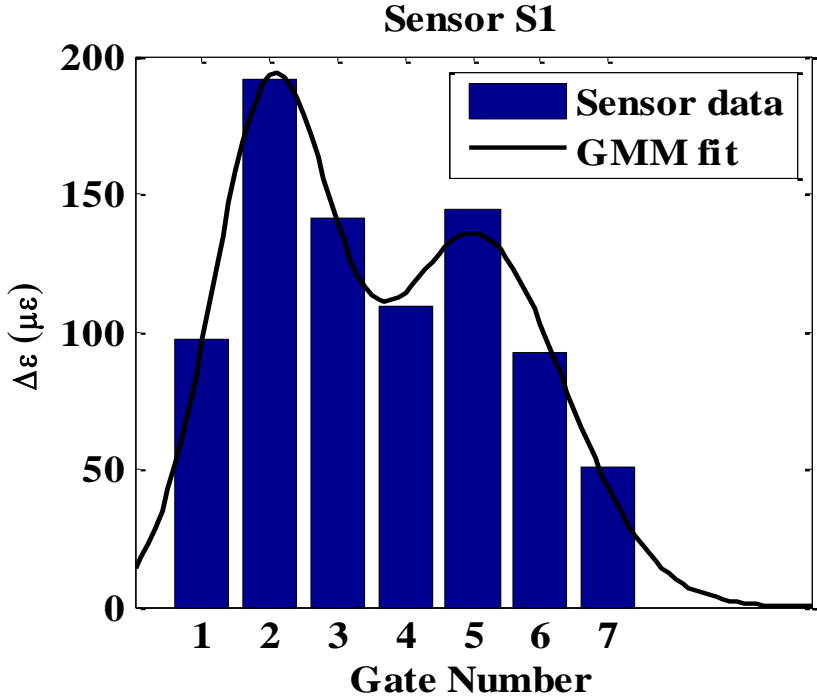


Figure 3-45: GMM fit to the sensor data.

For sensor S1, the mean (μ_1) of the first components of the GM shifts to the left (decreases) and the second mean μ_2 shifts to the right (increases). In addition, the standard deviations σ_1 and σ_2 increase with damage progression as the distribution expands. Furthermore, when the sensor is located far from the damage zone, the variation of the GMM parameters becomes less significant as indicated by sensors S2 and S3.

An interesting observation from the output of sensor S9, located at 60 mm offset from the x-axis, is that σ_2 shows a significant variation between the intact and the damaged configurations. At the

location of sensor S9, the maximum strain obtained by the FE model is below $180 \mu\epsilon$ for the intact configuration. Therefore, gates 6 and 7 are still inactive and they did not record any data.

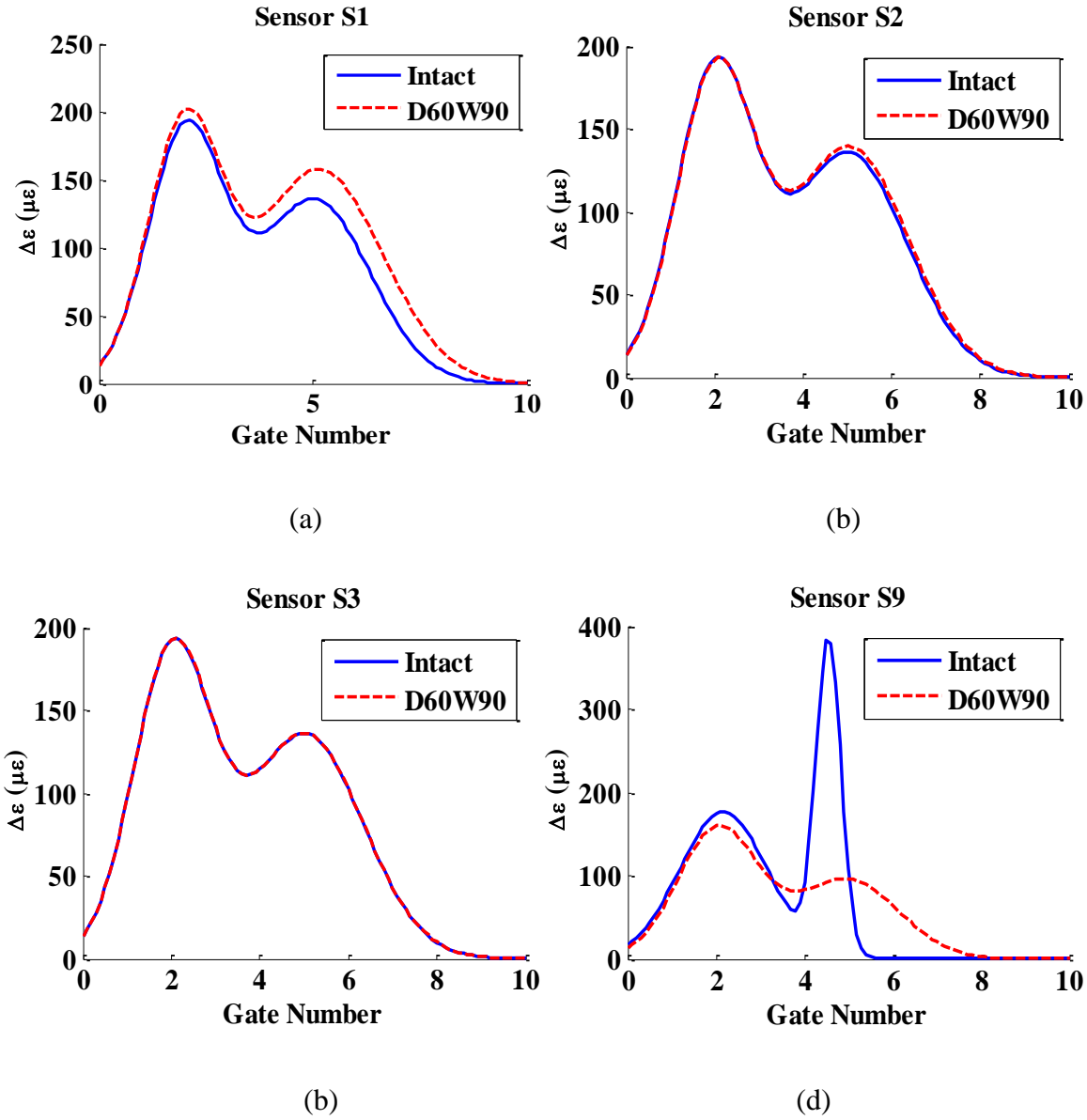
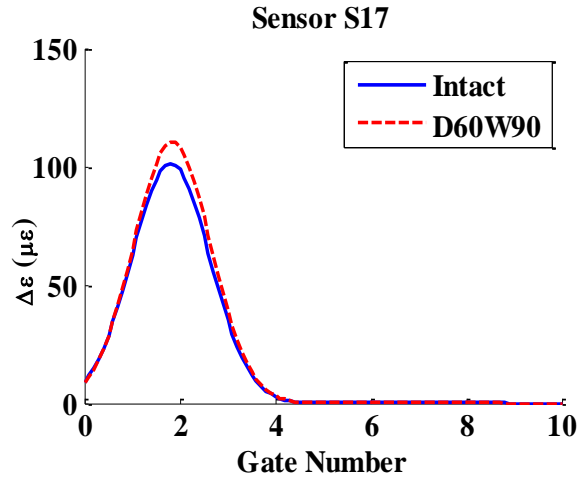


Figure 3-46: GMM distributions for different sensors.

Figure 3-46 (cont'd)



(e)

When the damage reaches the D60W90 damage state, the maximum strain increased to $210.94\mu\epsilon$ which is above the maximum threshold level of all the gates. Thus, all the gates become active. When the output of sensor S9 is fitted by the GMM, the intact configuration presents a very small σ_2 and a mean μ_2 below 6 in order to satisfy the zero strain droppage condition described before. Thereafter, when all the gates become active for the highest damage state (D60W90), the standard deviation of the second mixture component increased to 1.34 which is more than 16 times higher than σ_2 of the intact configuration. This considerably affects the width of the distribution.

For sensor S17, the amplitude of the strains is below $140\mu\epsilon$ for both of the intact and the damaged configurations. Therefore, only the first 3 gates are active. On the other hand, all the sensors located at 180 mm offset from the x-axis, the strain amplitude is lower than the minimum threshold of the sensor. Thus, all the gates of these sensors remained inactive.

Based on the results, the bimodal GM parameters change due to the damage progression in the

structure. Thus, the damage could be defined as function of these parameters as follows:

$$Damage = function(\mu_1, \sigma_1, \mu_2, \sigma_2) \quad (3-36)$$

However, the changes of the GM parameters are not always consistent. For example, for sensor S1, the first components (μ_1, σ_1) decrease and the second components (μ_2, σ_2) increase when damage progresses from the intact to D60W90 mode. For sensor S17, μ_1 and μ_2 increase, and σ_1 and σ_2 decrease. Thus, it can be concluded that μ_1, σ_1, μ_2 and σ_2 are good damage indicators but cannot be individually used for classifying damage states. To deal with this issue, a pattern recognition approach is developed to precisely detect and classify the damage phase.

3.3.2.2.5. Damage classification

3.3.2.2.5.1. Probabilistic neural network

Computational intelligence includes a set of nature-inspired approaches that can determine the model structure by automatically learning from data (Hasni et al., 2017a). CI provides alternative solutions to overcome the limitations of the traditional mathematical modeling. These limitations might be associated with the uncertainties during the process, the complexity, or the stochastic nature of the process. The CI techniques such as artificial neural network, support vector machines, fuzzy inference system, etc have been widely used for behavioral characterization and health monitoring of pavements and infrastructure systems (Szewczyk and Hajela, 1994; Wu et al., 1992; Chassiakos and Caughey, 1993; Elkordy et al., 1993; Zhao et al., 1998). Major drawbacks of the widely-used ANNs are its 'black box' nature, the proneness to overfitting, and the time-consuming iterative procedure required during training of the network to obtain the optimal learning parameters (Yan and Miyamoto, 2003). To

overcome such limitations, PNN has been proposed by Specht (Specht, 1990). One advantage of PNNs is that it does not have a separate training phase which makes the execution faster than the conventional neural networks. PNN is a supervised neural network that is closely related to the standard Bayes classification rule and Parzen non-parametric PDF estimation technique. It is commonly used for pattern classification and recognition problems (Yan and Miyamoto, 2003; Goh, 2002; Adeli and Panakka, 2009). The Bayes formula can be expressed as follows:

$$P(\omega_j | x) = \frac{p(x | \omega_j)P(\omega_j)}{p(x)} \quad (3-37)$$

where $P(\omega_j|x)$ is the posterior probability, $P(\omega_j)$ is the prior probability and $P(x|\omega_j)$ is the likelihood of ω_j with respect to x . The Bayes decision rule is based on the maximization of the posterior probability. As the evidence $p(x)$ is independent of the class label, then the decision rule can be determined by estimating the likelihood probability for each class and the priors.

The prior probability $P(\omega_j)$ highly depends on the specific task and should be decided by the physical knowledge of the problem. Thus, the only remaining unknown in the Bayes formula is the likelihood. This class conditional probability could be estimated using the non-parametric density estimation scheme using the Parzen window approach. More details about PNN can be found in (Duda et al., 2000; Mao et al., 2000).

Assuming we have N training samples, $\{\mathbf{x}_1, \dots, \mathbf{x}_N\}$, divided into c classes, each of them has d dimension, and the h is the length of side of hypercube in the Parzen window approach. The estimation of density at a point \mathbf{x} in the d dimensional space is:

$$p(\mathbf{x}) = \frac{1}{N} \sum_{n=1}^N \frac{1}{h^d} k\left(\frac{\mathbf{x} - \mathbf{x}_n}{h}\right) \quad (3-38)$$

In Equation (3-38), $k\left(\frac{x-x_n}{h}\right)$ is the kernel function that is used to count the number of patterns located inside the hypercube of volume $V = h^d$. Similarly, the value of a probability density function of class ω_j is given by:

$$P_j(\mathbf{x}) = \frac{1}{N_j} \sum_{n=1}^{N_j} \frac{1}{h^d} k\left(\frac{x-x_n^j}{h}\right) \quad (3-39)$$

When a Gaussian as kernel function is used, the final estimation becomes:

$$P_j(\mathbf{x}) = \frac{1}{N_j} \sum_{n=1}^{N_j} \frac{1}{\sigma^d} \frac{1}{(2\pi)^{\frac{d}{2}}} \exp\left(-\frac{1}{2} \frac{\|\mathbf{x}-\mathbf{x}_n^j\|^2}{\sigma^2}\right) \quad (3-40)$$

The precedent expression can be written as follows:

$$P_j(\mathbf{x}) = \frac{1}{N_j (2\pi)^{\frac{d}{2}} \sigma^d} \sum_{n=1}^{N_j} \exp\left(-\frac{\|\mathbf{x}-\mathbf{x}_n^j\|^2}{2\sigma^2}\right) \quad (3-41)$$

where N_j is the number of training patterns of class ω_j , σ is called the smoothing parameter that describes the spread of the Gaussian window function and \mathbf{x}_n^j is the n^{th} pattern belonging to class ω_j . The feature vectors \mathbf{x}_n^j represent the center of the Gaussian window. The smoothing parameter σ needs to be determined experimentally.

As mentioned before, the PNN structure is a direct implementation of the PDF estimator (Equation (3-41)) and the Bayesian decision rule. A typical PNN with 4-layers architecture is shown in Figure 3-47. The network is constructed by the following layers: input layer, pattern layer, summation layer, and output layer. The input layer consists of d input units, which corresponds to the d features. Each input unit is connected to each of the N pattern units (Alavi et al., 2016a). The number of nodes in the pattern layer is equal to the total number of

training vectors. Each pattern unit k computes the inner product of its weight vector and the normalized pattern vector \mathbf{x} as follows:

$$net_k = \mathbf{w}_k^t \mathbf{x} \quad (3-42)$$

Thereafter, each pattern unit emits a nonlinear transfer function:

$$\exp\left(\frac{net_k - 1}{\sigma^2}\right) = \exp\left(\frac{\mathbf{w}_k^t \mathbf{x} - 1}{\sigma^2}\right) \quad (3-43)$$

On the other hand, the desired Gaussian window function is:

$$k\left(\frac{\mathbf{x} - \mathbf{w}_k}{h}\right) \propto \exp\left(-\frac{(\mathbf{x} - \mathbf{w}_k)^t (\mathbf{x} - \mathbf{w}_k)}{2\sigma^2}\right) = \exp\left(\frac{2\mathbf{x}^t \mathbf{w}_k - \mathbf{x}^t \mathbf{x} - \mathbf{w}_k^t \mathbf{w}_k}{2\sigma^2}\right) \quad (3-44)$$

By taking into account the normalization of \mathbf{x} and \mathbf{w}_k , Equation (3-44) can be expressed as follows:

$$k\left(\frac{\mathbf{x} - \mathbf{w}_k}{h}\right) \propto \exp\left(\frac{\mathbf{x}^t \mathbf{w}_k - 1}{\sigma^2}\right) = \text{nonlinear transfer function} \quad (3-45)$$

The precedent equation explains the choice of the nonlinear transfer function employed by the pattern units.

Each neuron in the summation layer will sum these functions corresponding to a single population. As a result, the output of the summation layer has the same form as the Parzen window estimate of the distribution. The output of the summation layer is:

$$C_j(\mathbf{x}) = \sum_{k=1}^{N_j} \exp\left(\frac{\mathbf{x}^t \mathbf{w}_{jk} - 1}{\sigma^2}\right) \quad (3-46)$$

Thereafter, if the prior probabilities are the same, and the cost functions of making an incorrect decision are the same for all classes, the decision layer classifies according the Bayes decision

rule as follows:

$$C(x) = \underset{j=1..c}{\operatorname{argmax}} P_j(x) \quad (3-47)$$

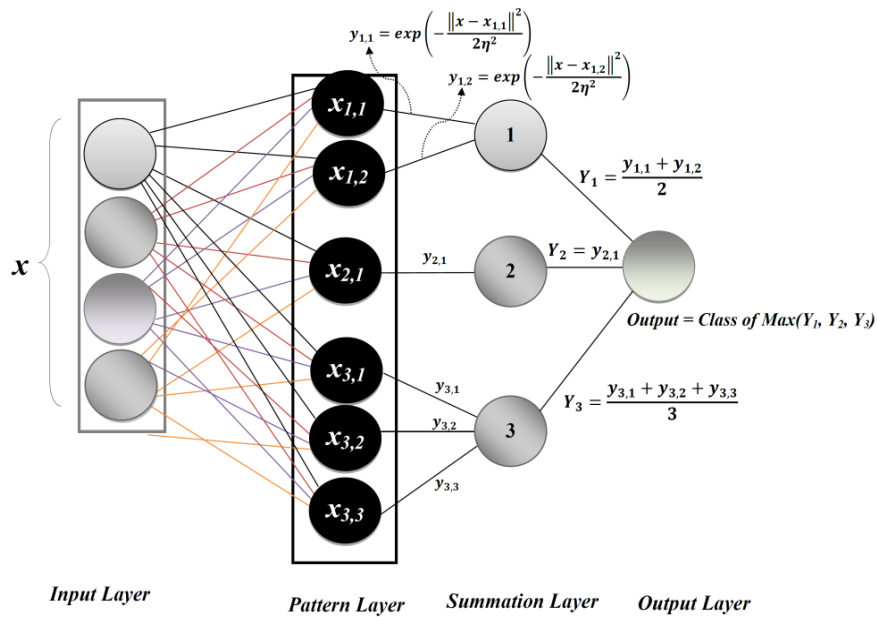


Figure 3-47: A typical architecture of PNN.

The training of PNN is fast, and it guarantees the convergence to an optimal classifier as the size of training samples increases. In addition, PNN does not have local minima problems. However, one major challenge is to find the optimal smoothing parameter σ . A very small σ can produce many empty hypercubes and may result in problems of overfitting. On the other hand, if the window width is too large, the PNN classifier may under-fit the data as it cannot present some important local variations. Therefore, the accuracy of the PNN classifier highly depends on the choice of the smoothing parameter (Alavi et al., 2016a).

As mentioned before, 32 sensors are defined on the surface of the pavement. However, only 15

sensors are considered in this analysis for the following two reasons:

- The maximum strain at the 180 mm offset set of sensors is below the minimum threshold of the sensor.
- The difference on the peak strain values for last 3 sensors of each set between any two damage states is very low.

Therefore, only sensors S1, S2, S3, S4, S5, S9, S10, S11, S12, S13, S17, S18, S19, S20, and S21 are used. In addition, the damage states are divided into 4 classes as follows:

- ω_1 : Intact structure
- ω_2 : D20W30, D20W50, D20W70, D20W90
- ω_3 : D40W30, D40W50, D40W70, D40W90
- ω_4 : D60W30, D60W50, D60W70, D60W90

Each sensor represents a pattern for the classifier, and therefore, the total number of data points is: $15 \times 13 = 195$. The performance of the developed models is measured using the DR.

3.3.2.2.5.2. Performance of the initial features

Initial feature vectors are defined based on the GMM parameters $(\mu_1, \sigma_1, \mu_2, \sigma_2)$. These parameters are used to characterize the initial input vector \underline{x} as follows:

$$\underline{x} = [x_1 \ x_2 \ x_3 \ x_4]^t \quad (3-48)$$

where:

$$\begin{cases} x_1 = \mu_1 \\ x_2 = \sigma_1^2 \\ x_3 = \mu_2 \\ x_4 = \sigma_2^2 \end{cases} \quad (3-49)$$

As indicated by Equation (3-48), the initial problem has 4 dimensions. Thus, 195 4-dimensional patterns are used for the classification. The total number of data is divided into 3 sets:

- 70 % training = 137 input vector
- 15 % validation = 29 input vector
- 15 % testing = 29 input vector

As one would expect, these 4 initial features provided very low accuracy on the validation and testing data. The maximum detection rates for the validation and testing data are 27.58% and 13.79%, respectively. Figure 3-48 displays the results of the classification in the validation set as a function of the PNN smoothing parameter (σ). Multiple iterations are performed by varying the smoothing parameter in order to find the optimal value that gives the best accuracy on the validation set. The best configuration is then applied to the unseen testing data. As seen in Figure 3-48, the best detection rate is obtained when the optimal smoothing parameter is between 1 and 10. Hence, the optimal value of σ is equal to 1.

Thereafter, PCA is performed on the initial set of patterns in order to visualize the data along its first two principal components. Figure 3-49 displays the original input data (\underline{x}) projected on the two first principal components. The obtained eigenvalues of the covariance matrix are: $\lambda_1 = 152.49$, $\lambda_2 = 1.61$, $\lambda_3 = 0.02$, $\lambda_4 = 1.57 \times 10^{-4}$. Hence, the first two components represent 99.99 % of the data. The detection accuracy using the reduced feature vector: $\underline{x}' = [x_1 \ x_2]^t$ is increased from 13.79 % to 34.48 % for the testing data. Furthermore, as seen in Figure 3-49, the defined 4 damage classes overlap intensively which results in a low detection accuracy.

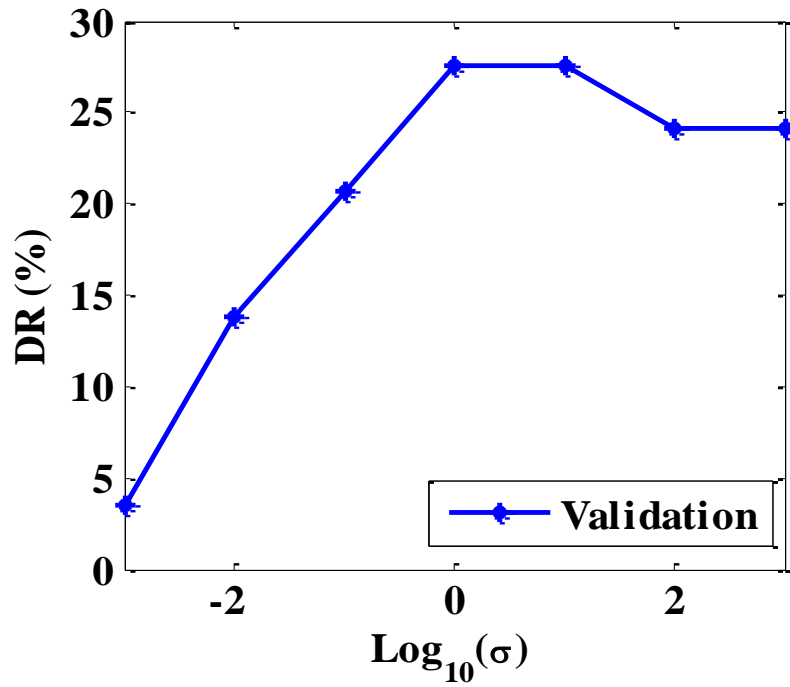


Figure 3-48: Accuracy versus smoothing parameter for the validation set.

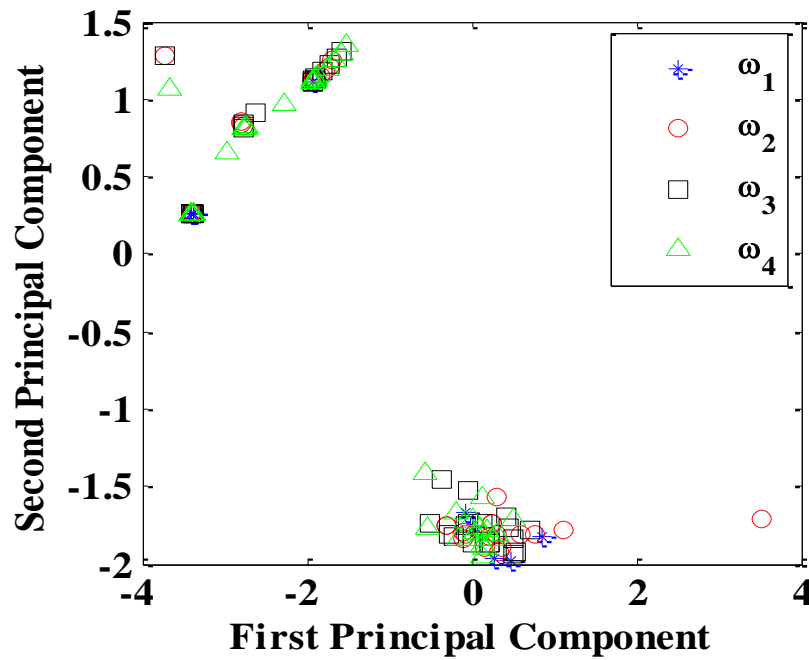


Figure 3-49: Projection of the featured data onto the first two principal components.

3.3.2.2.5.3. Sensor fusion model

Feature Transformation

According to the preliminary results, the initial input feature vector \underline{x} does not contain enough information to separate classes. Hence, a new strategy is defined to improve the damage detection performance. On its basis, it is decided to fuse both the information provided by one sensor and all the information supplied by the other sensors. Figure 3-50 summarizes the proposed method for the data fusion model. The proposed feature transformation φ could be written as follows:

$$\varphi: \mathbb{R}^4 \xrightarrow{\text{feature transformation}} \mathbb{R}^{10}$$

$$\underline{x} = [x_1 \ x_2 \ x_3 \ x_4] \xrightarrow{\varphi} \underline{y} = [y_1 \ y_2 \ y_3 \ y_4 \ y_5 \ y_6 \ y_7 \ y_8 \ y_9 \ y_{10}] \quad (3-50)$$

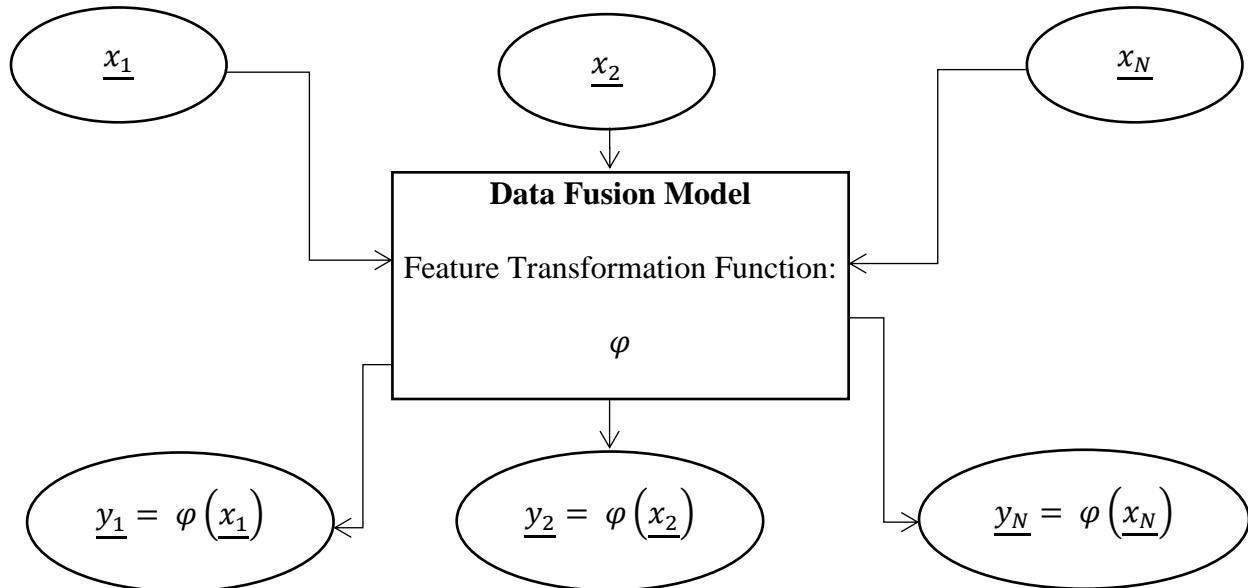


Figure 3-50: Data fusion model.

The new set of input parameters are introduced to the formulation of the damage state as follows:

$$\underline{y} = \left\{ \begin{array}{l} y_1 = \frac{x_1 - x_{1ave}}{x_{1STD}} \\ y_2 = \frac{x_2 - x_{2ave}}{x_{2STD}} \\ y_3 = \frac{x_3 - x_{3ave}}{x_{3STD}} \\ y_4 = \frac{x_4 - x_{4ave}}{x_{4STD}} \\ y_5 = \frac{x_1 - x_{1STD}}{x_{1ave}} \\ y_6 = \frac{x_2 - x_{2STD}}{x_{2ave}} \\ y_7 = \frac{x_3 - x_{3STD}}{x_{3ave}} \\ y_8 = \frac{x_4 - x_{4STD}}{x_{4ave}} \\ y_9 = \frac{(x_1 + x_3) - (x_{2ave} + x_{4ave})}{x_{1ave} + x_{3ave}} \\ y_{10} = \frac{(x_2 + x_4) - (x_{1ave} + x_{3ave})}{x_{2ave} + x_{4ave}} \end{array} \right. \quad (3-51)$$

where,

- x_i : The i^{th} feature of the initial feature vector,
- x_{iave} : The average of x_i for all patterns corresponding to a specific damage state,
- x_{iSTD} : The standard deviation of x_i for all patterns corresponding to a specific damage state.

The new defined features y_i ($i=1..10$) are derived from the conventional z-score functions. In fact, features y_1 to y_4 are the z-score functions and features y_5 to y_{10} are functions that are inspired by the form of the conventional z-score function. All the y_i ($i=1..10$) are based on the average and the standard deviation of all patterns for a specific damage state.

Feature Selection

The new features are expected to increase the ‘distance’ between classes especially

between two consecutive damage states. The word distance here refers to Euclidian distance between two features in the d-dimensional space belonging to two different classes. Furthermore, by increasing the dimensionality of the problem from 4 to 10, the accuracy is more likely to increase. However, increasing the number of features may also lead on the curse of dimensionality. Therefore, different feature selection methods are used to tackle this problem. In this study, sequential forward selection (SFS), sequential backward selection (SBS), and exhaustive search (brute-force search) algorithms are used to select the best set of features (Zongker and Jain, 1996; MathWorks, 2016; Aha and Bankert, 1996; Weston et al., 2000).

SFS

SFS sequentially adds the best feature y^+ that maximizes the objective function $J(Z_k + y^+)$. The SFS algorithm works as follows (MathWroks, 2016):

1. Start with the empty set $Z_0 = \{\emptyset\}$
 2. Select the next best feature: $y^+ = \underset{y \notin Z_k}{\operatorname{argmax}}(J(Z_k + y))$
 3. Update $Z_{k+1} = Z_k + y^+$; $k = k + 1$
- Go to 2

Table 3-9 displays the sets selected by the SFS algorithm and their performances at each step. The best accuracy on the training, validation, and testing data is obtained using feature vectors Z_8 or Z_9 selected as follows:

$$Z_8 = \{y_9, y_1, y_2, y_3, y_4, y_5, y_6, y_7\} \quad (3-52)$$

$$Z_9 = \{y_9, y_1, y_2, y_3, y_4, y_5, y_6, y_7, y_8\} \quad (3-53)$$

The detection rate accuracy using feature vectors Z_8 or Z_9 are 100%, 96.55%, and 93.10% for the

training, validation, and testing data, respectively. The optimal smoothing parameter is calculated at each iteration of the algorithm.

SBS

This method sequentially removes the worst feature y^- that least reduces the objective function $J(Z_k - y^-)$. The SBS algorithm works as follows (MathWorks):

1. Start with the full set $Z_0 = \underline{y}$,
 2. Remove the worst feature: $y^- = \underset{y \in Z_k}{\operatorname{argmax}}(J(Z_k - y))$
 3. Update $Z_{k+1} = Z_k - y^-$; $k = k + 1$.
- Go to 2

Table 3-10 displays the sets selected by the SBS algorithm at each step. The best accuracy on the training, validation, and testing data is obtained using feature vectors Z_1 , Z_2 or Z_3 , where:

$$Z_1 = \{y_2, y_3, y_4, y_5, y_6, y_7, y_8, y_9, y_{10}\} \quad (3-54)$$

$$Z_2 = \{y_3, y_4, y_5, y_6, y_7, y_8, y_9, y_{10}\} \quad (3-55)$$

$$Z_3 = \{y_3, y_4, y_5, y_6, y_7, y_8, y_9\} \quad (3-56)$$

The best detection accuracy is 100%, 96.55%, and 93.10% for the training, validation, and testing sets, respectively. Multiple iterations are performed at each step to find the optimal smoothing parameter. The optimal set extracted by the SBS algorithm is Z_3 which has 7 dimensions.

Table 3-9: Features selected by SFS and their corresponding detection rates.

Set Number	Features	Training Accuracy (%)	Validation Accuracy (%)	Testing Accuracy (%)
1	$\{y_9\}$	94.89	89.65	89.65
2	$\{y_9, y_1\}$	100	89.65	93.10
3	$\{y_9, y_1, y_2\}$	100	79.31	93.10
4	$\{y_9, y_1, y_2, y_3\}$	100	79.31	93.10
5	$\{y_9, y_1, y_2, y_3, y_4\}$	100	79.31	93.10
6	$\{y_9, y_1, y_2, y_3, y_4, y_4\}$	100	82.75	93.10
7	$\{y_9, y_1, y_2, y_3, y_4, y_4, y_5\}$	100	82.75	93.10
8	$\{y_9, y_1, y_2, y_3, y_4, y_5, y_6, y_7\}$	100	96.55	93.10
9	$\{y_9, y_1, y_2, y_3, y_4, y_5, y_6, y_7, y_8\}$	100	96.55	93.10
10	$\{y_9, y_1, y_2, y_3, y_4, y_5, y_6, y_7, y_8, y_{10}\}$	100	96.55	89.65

Table 3-10: Features selected by SBS and their corresponding detection rates.

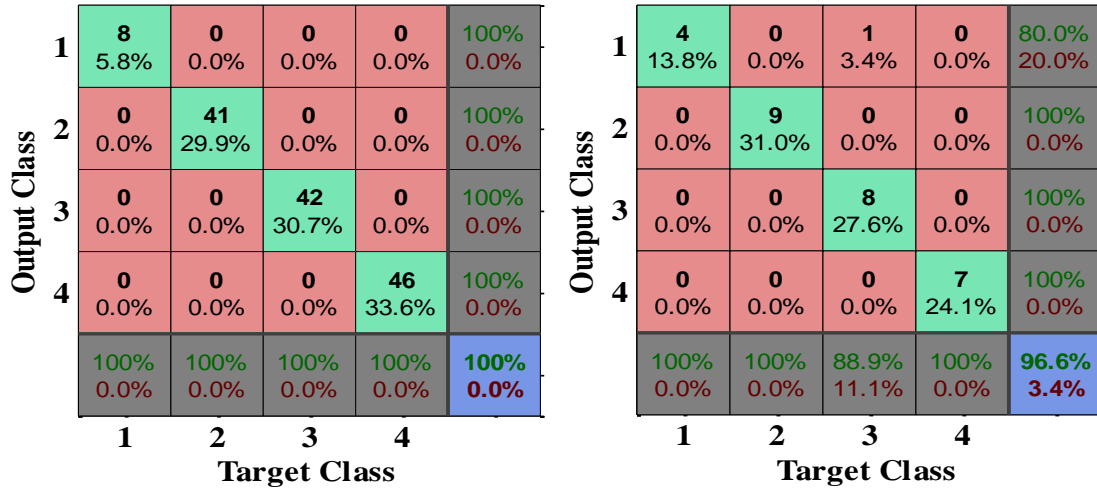
Set Number	Features	Training Accuracy (%)	Validation Accuracy (%)	Testing Accuracy (%)
1	$\{y_1, y_2, y_2, y_3, y_4, y_5, y_6, y_7, y_8, y_9, y_{10}\}$	100	96.55	89.65
2	$\{y_2, y_3, y_4, y_5, y_6, y_7, y_8, y_9, y_{10}\}$	100	96.55	93.10
3	$\{y_3, y_4, y_5, y_6, y_7, y_8, y_9, y_{10}\}$	100	96.55	93.10
4	$\{y_3, y_4, y_5, y_6, y_7, y_8, y_9\}$	100	96.55	93.10
5	$\{y_4, y_5, y_6, y_7, y_8, y_9\}$	100	96.55	89.65
6	$\{y_5, y_6, y_7, y_8, y_9\}$	100	96.55	86.20
7	$\{y_6, y_7, y_8, y_9\}$	100	96.55	86.20
8	$\{y_7, y_8, y_9\}$	100	96.55	86.20
9	$\{y_8, y_9\}$	98.54	93.10	86.20
10	$\{y_9\}$	94.89	89.65	89.65

Exhaustive search

The main limitation of SFS pertains to the fact that it is unable to remove feature that become obsolete after the addition of other features. Similarly, SBS cannot reevaluate the usefulness of a removed feature on the selected set. Both algorithms are suboptimal. Therefore, an exhaustive search algorithm is performed. It is decided to select the best 3 features that give the best classification accuracy. As the problem has 10 dimensions, the algorithm performed $C_{10}^3 = 120$ iterations to find the best set of 3 features. One the best obtained sets that gives the

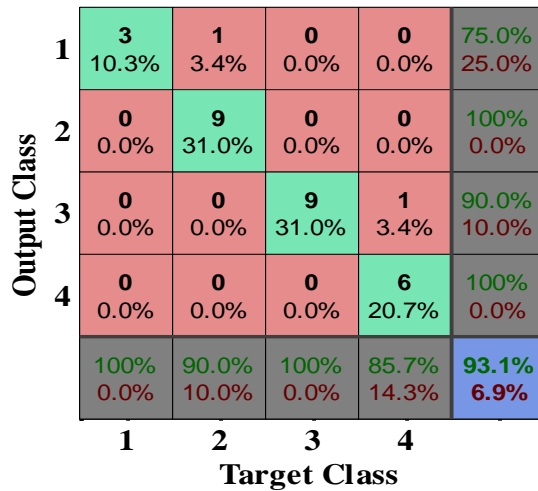
best accuracy is:

$$S_{optimal} = \{y_4, y_7, y_9\} \quad (3-57)$$



(a) Training data

(b) Validation data



(c) Testing data

Figure 3-51: Confusion matrixes for the best features selected by the exhaustive search method.

The detection rate for the training, validation, and testing data is equal to 100%, 96.55%, and 93.10%, respectively. Figure 3-51 displays the confusion matrixes. As observed from the

matrixes, only 2 patterns are misclassified in the testing set and 1 pattern in the validation set. The obtained optimal smoothing parameter is 0.01 (Figure 3-52).

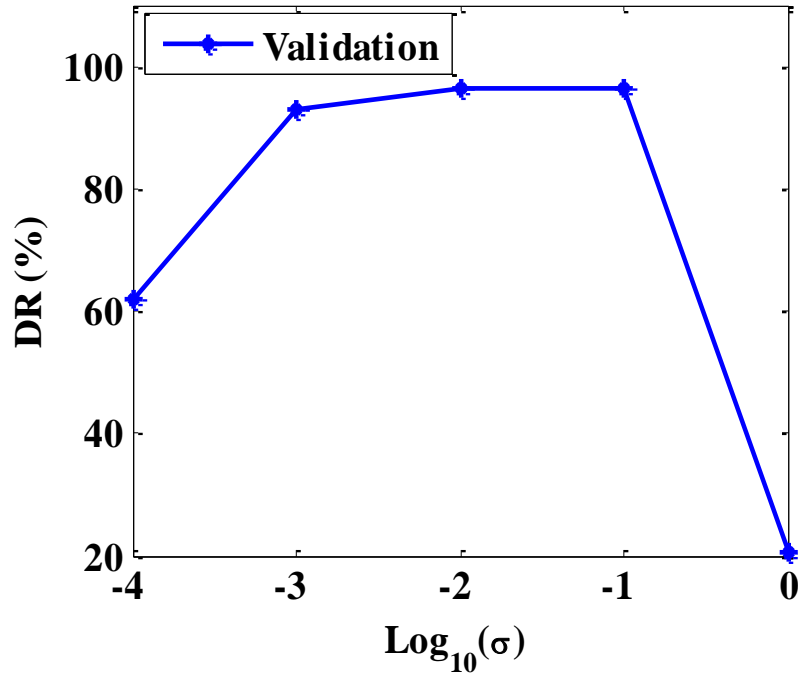


Figure 3-52: Accuracy versus smoothing parameter for the validation set using the exhaustive search method.

The new set of features based on the data fusion model has enhanced the performance of the detection rate from 13.79 % to 93.1 % on the testing set. Figure 3-53 shows the distribution of the data using the optimal set of features. As seen in this figure, the classes are more separable compared to the initial input data.

In order to evaluate the sensitivity of the model to sampling error, the PNN classifier is run for 5 different random selections of the training, validation, and testing sets. Table 3-11 presents the results. The obtained average error in classification for the unseen data is 4.83 %.

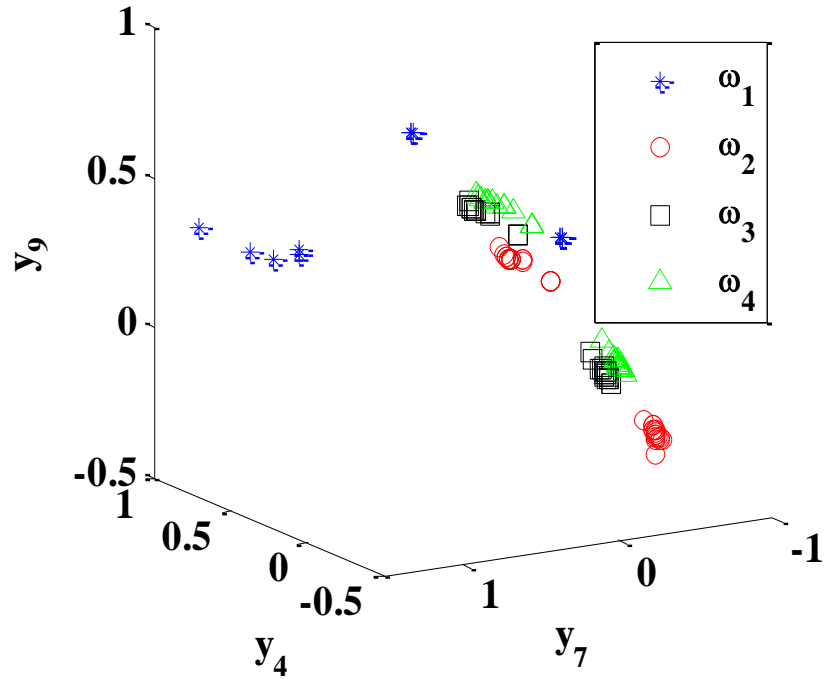


Figure 3-53: Distribution of the optimal set patterns.

Table 3-11: Model sensitivity to sampling error.

	Test 1	Test 2	Test 3	Test 4	Test 5	Average
Training	100	100	100	100	100	100
Testing	93.1	96.55	100	89.65	96.55	95.17
Validation	93.1	93.1	96.55	96.55	96.55	95.17

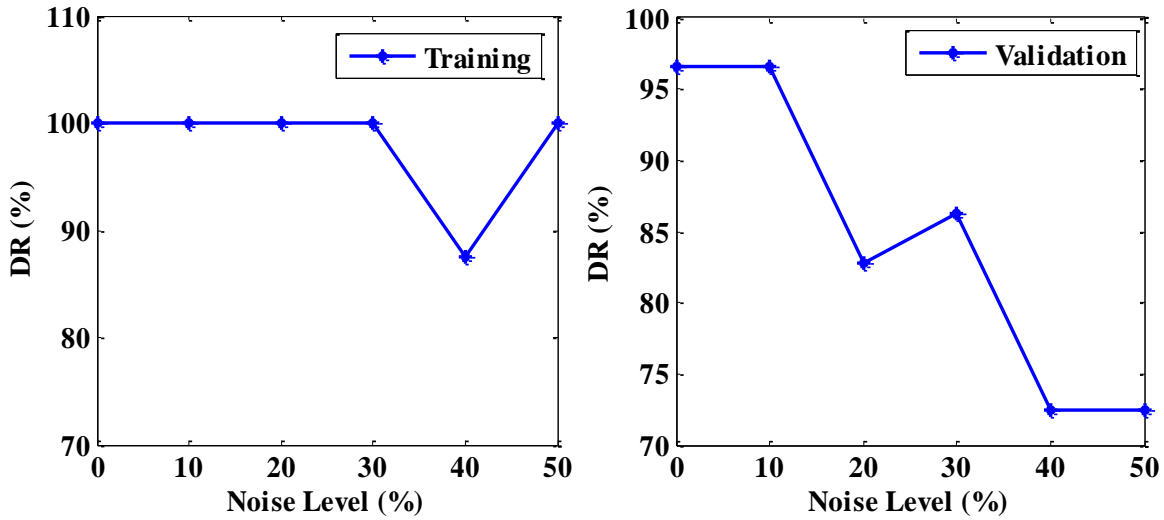
3.3.2.2.3.4. Uncertainty analysis

In this study, the sensor data is simulated using the strain history provided by the FE analysis of the pavement under different damage scenarios. However, different sources of uncertainties can contribute to an error between the FE modeling and the real structural behavior (Haukaas and Gardoni, 2011). On this basis, an uncertainty analysis can enhance the reliability

of the proposed damage detection approach. To this aim, the input data is polluted using a Gaussian noise with 5 different levels: 10%, 20%, 30%, 40%, and 50%. The best set of predictors S_{optimal} is used in the noise pollution verification phase. Thereafter, the PNN algorithm is run for all the noise levels. For each case, the optimal smoothing parameter is calculated. Table 3-12 presents the results of the uncertainty analysis. Figure 3-54 displays the detection rate accuracy as a function of the noise level using the optimal smoothing parameter. As seen in Table 3-12 and Figure 3-54, the performance of the models remains satisfactory up to a 30% noise level. The detection rates for a noise level below or equal to 30 % are above 82 % for the training, validation, and testing sets.

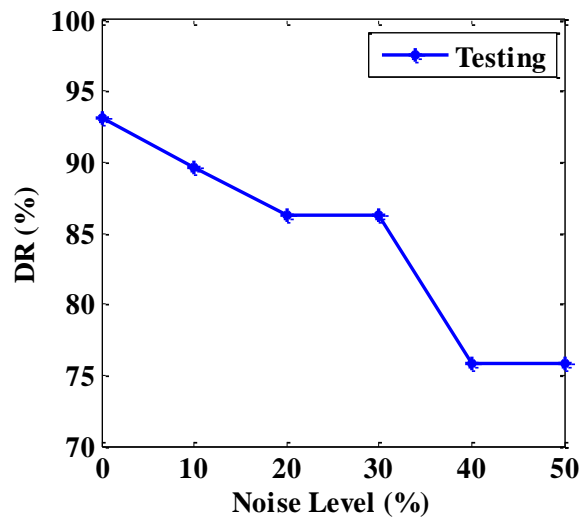
Table 3-12: The damage detection performance for various noise levels using the optimal set of features.

Noise Level	Optimal Smoothing Parameter	Damage Detection Performance (%)		
		Training	Validation	Testing
10%	1E-2	100	96.55	89.65
20%	1E-2	100	82.75	86.20
30%	1E-2	100	86.20	86.20
40%	1E-1	87.59	72.41	75.86
50%	1E-2	100	72.41	75.86



(a) Training data

(a) Validation data



(c) Testing data

Figure 3-54: Damage detection accuracy for different noise levels.

3.4. Summary

This chapter presented a novel self-sensing mechanism for detecting damage in steel and pavement structures using the nonuniform class of PFG sensors.

The first section was focused on the damage growth detection in steel plates. Before the

application of loading, piezoelectric transducers were attached to the plate to convert the strain energy to an electrical charge. Damage states were introduced at the middle of the plate by increasing the notch size. The concentration of the trapped electrons at the sensor gates was used as an indicator of damage progression. First, an attempt was made to find a reasonable relationship between the activation and voltage droppage of floating-gates of individual PFG sensors, and damage progression. The next stage was focused on processing spatial measurements using features that simultaneously fuse the information provided by a network of PFG sensors. The fused data was then fed into an SVM classifier for multi-stage damage detection. It was found that the structural damage could be monitored through the monitoring of the activation and voltage droppage of floating-gates of only few sensors at specific locations. On the other hand, the data fusion phase with SVM provides acceptable detection performance over the structural area. The best results were obtained using the featured data from 3-7 floating-gates. Based on an uncertainty analysis, the performance of the SVM models remained satisfactory even as the noise level is significantly increased.

The second part of this chapter focused on pavement health monitoring. First, a series of experiments and numerical simulations were conducted under a three-point bending configuration on the asphalt concrete specimen to analyze the sensor performance for detecting bottom-up crack in AC pavements. An H-shaped epoxy packaging was used to protect the PVDF film and the sensor electronics. Damage classes were defined based on the notch length defined at the bottom of the specimen. Based on the results, the strain amplitude changed with increasing the notch size. Consequently, the measured voltage from the piezoelectric transducer increased as well. The other important observation was that the slope (in absolute value) of the curves representing the sensor strain/voltage versus the number of applied cycles increased as damage

progresses. More, the gate number and activation threshold can be considered as good indicators of damage occurrence, and the slope representing the percentage of voltage/strain droppage was found to be a good indicator of damage severity.

Most of the available sensing technologies for pavements rely on embedding the sensor inside the AC layer. In section 3.3.2.2., an innovative approach for detecting bottom-up cracking in pavement using the surface data was proposed. This technique allows for the sensors to be placed on the surface of the structures, which is a significant improvement over existing method that can help in reducing the cost of sensor installation and replacement, and can be applied for existing pavements. The FE results show that the strain amplitude changes as a function of the damage state. In addition, the locations of sensors with respect to the damage control the change in the strain amplitude. The sensor output was calculated based on the FE strain history. Based on the results, it was found that the damage could be detected through the strain droppage of the sensor gates. However, only the sensors at a specific location with respect to the damage location were sensitive to the damage progression. To tackle this problem, two different stages were considered for the performance verification of the proposed approach. At the first stage, the sensor histogram was fitted to a bi-modal GM model in order to define initial damage indicators. The results show that the bi-modal GM parameters are good damage indicators only at specific locations. Thus, a data fusion model was proposed by defining new descriptive features from the GMM parameters. These new predictors contained the information supplied by all the sensors at each specific sensing location. Thereafter, different feature extraction methods (SFS, SBS, Brute force) were used to check the curse of dimensionality and to select the optimal set of sensors that give the best accuracy. A PNN classification scheme was used to classify the predefined damage stages. The results showed that the optimal set of features provided satisfactory detection rate

accuracy (100% on the training data, 96.6% on the validation data, and 93.1% on the testing data). Finally, an uncertainty analysis was carried out to evaluate the performance of the proposed surface sensing approach under different noise levels and to take into account the errors of the numerical modeling. A Gaussian noise with different levels was applied to the data. The detection performance remained satisfactory up to 30% noise level.

CHAPTER 4. LOCAL-GLOBAL DAMAGE IDENTIFICATION

APPROACH USING HYBRID NETWORK OF STRAIN AND

ACCELERATION PFG SENSORS ³

4.1. Overview

This chapter presents a novel approach to detect damage in steel frames using hybrid network of piezoelectric strain and vibration PFG sensors. A numerical study is conducted on a steel frame with bolted connections to verify the accuracy of the proposed method. The damage is introduced to the structure by loosening the bolts and by cracking structural members. The frame is subjected to a cyclic loading and the bolts are pre-tensioned before applying the external loads. Two types of piezoelectric transducers are used to transfer the mechanical energy into and electrical energy that can be used to empower the sensor and assess the health state of the structure. Circular PZTs are used as strain sensors, and bimorph PZT cantilever plates as vibration sensors. The strain and acceleration time histories are obtained from the FE models, and an analytical model is developed to obtain the voltage delivered by the PZTs. Thereafter, the sensor output histograms are calculated using the cumulative time durations of the voltage at a specific threshold level. Each sensor distribution is fitted to a GMM to define initial damage indicator features. Moreover, a sensor fusion model is proposed to improve the accuracy of the damage detection system.

³ The results presented in this chapter were published in Hasni et al. (2018b).

4.2. Sensing mechanism

The sensing mechanism consists of two main components: a piezoelectric transducer unit and a sensor unit (Figure 4-1).

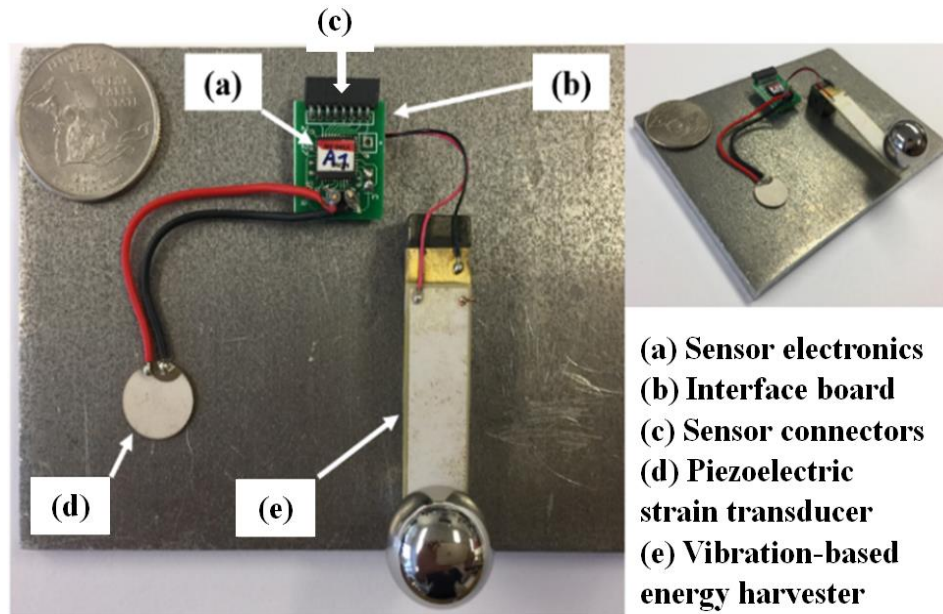


Figure 4-1: Sensing mechanism.

Vibration-based piezoelectric harvester converts ambient acceleration into electrical power. As mentioned in the previous chapters, the strain transducer is used to convert the strain energy into an electrical power. Many techniques and mechanisms have been presented to increase the efficiency of energy conversion. A post-buckling cell is developed as a triggering mechanism to optimally convert ambient displacement/strain into electrical power. The piezoelectric harvester is attached to a bilaterally constrained beam in the post-buckling system and, thus, electrical power can be generated by the release of the strain energy stored in the beam through its buckling mode transitions (Chen et al., 2012; Jiao et al., 2012; Jiao et al., 2016). Connecting to the power reservoir on the interface board, the electrical energy is used to empower the wireless

sensor.

The damage detection mechanism presented in this study can be divided into the following phases:

- FE model of steel frames under different damage scenarios;
- Extraction of strain and acceleration data from the FE model under cyclic loads;
- Estimation of the voltage output generated by the PZT harvesters from the accelerations and strains;
- Generation of the sensor output histograms for each sensor;
- Extraction of the features from the sensor distribution in order to define preliminary damage indicators; and
- Fusion of data from a network of the wireless sensors to identify a parameter that has a unique relationship with the damage progression in the structure.

4.3. Numerical simulation of steel frames with bolted connections

4.3.1. Finite element description of the model

The steel frame under consideration is modeled using ABAQUS Version 6.12. Figure 4-2 presents the meshed steel frame with bolts in details. It can be seen that the frame is fixed on a shaking table. More details about the dimensions, material properties, and loading conditions are listed in Table 4-1. In Table 4-1, l , w , h , and t denote the length, width, height, and thickness, respectively. A cyclic loading is imposed to the shaking table as follows:

$$u_{table} = A \cos(2 \pi f t) \quad (4-1)$$

where A and f represent the amplitude and frequency of the input displacement, respectively. In

this study, the displacement amplitude is 10 mm and the frequency is 10 Hz. Different three-dimensional FE models are developed to analyze the dynamic response of the frame under different damage scenarios.

The damage is defined based on two different mechanisms: Bolt/torque loosening, and cracking of the frame columns. The numerical modeling of bolted connections is formulated in terms of the following five aspects:

- Contact between the bolts and frame (C_{bf});
- Contact between the nuts and bolt-shank (C_{nb});
- Contact between the nuts and frame (C_{nf});
- Contact between the beams and columns (C_{bc});
- Friction between the bolt-shank and the nut (F_{cs}); and
- Bolts pre-tension (P_b).

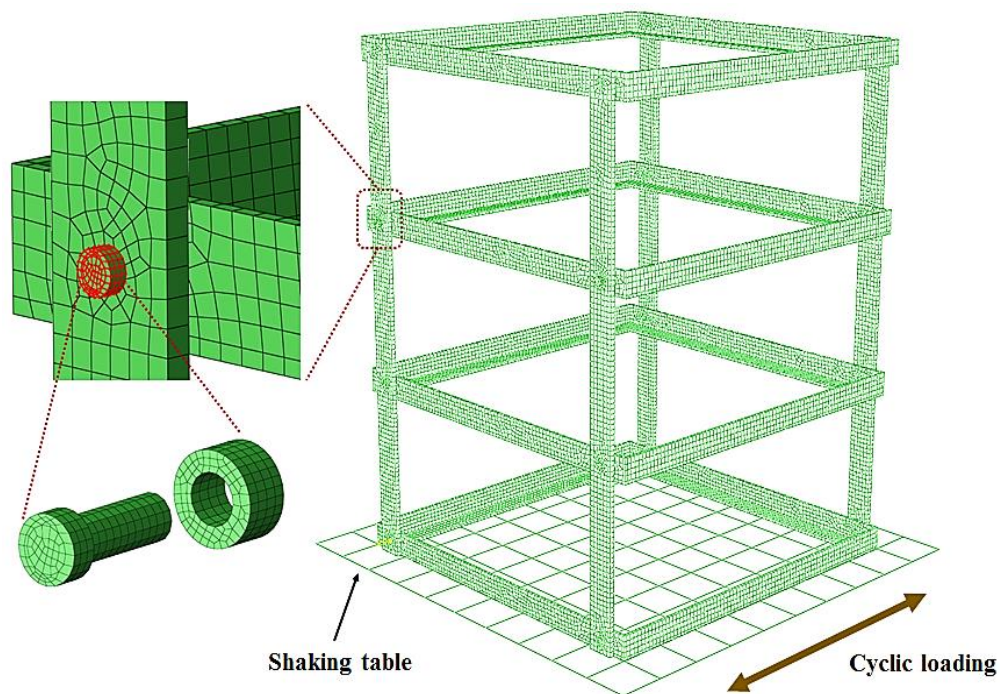


Figure 4-2: Mesh details of the steel frame.

In order to effectively take into account the Rayleigh damping in the FE model, material nonlinearity is addressed using a direct integration method. The damping ratio ξ is defined as a function of the system natural frequencies as:

$$\xi(\omega) = \frac{\alpha}{2\omega} + \frac{\beta\omega}{2} \quad (4-2)$$

where α and β refer to the Rayleigh damping coefficients, and ω is a natural frequency of the system. For two natural frequencies ω_1 and ω_2 , the damping coefficients in Equation (4-2) can be written as:

$$\lambda^t = \Omega^{-1}\xi^t \quad (4-3)$$

where

$$\begin{cases} \lambda = (\alpha & \beta) \\ \Omega = \begin{bmatrix} \frac{1}{2\omega_1} & \frac{\omega_1}{2} \\ \frac{1}{2\omega_2} & \frac{\omega_2}{2} \end{bmatrix} \\ \xi = (\xi_1 & \xi_2) \end{cases} \quad (4-4)$$

The first three modes are selected to calculate the damping ratio because they participate by more than 95 % of the effective mass. An iterative procedure is followed to obtain the optimal Rayleigh coefficients (Spears and Jensen, 2012). The obtained coefficients are: $\alpha = 0.0406$ and $\beta = 0.0032$.

Bolt pretension is defined by applying a torque T to the bolts. The applied torque is converted into axial compressive load P as:

$$P = \frac{T}{KD} \quad (4-5)$$

where D is the nominal diameter of the bolts, and K is the nut factor related to friction. The preload can be expressed as a function of the percentage of the bolt yield strength as follows:

$$P = n \sigma_{sy} A_b \quad (4-6)$$

Table 4-1: Geometry, material properties and loading conditions of the steel frame.

Geometry (mm)							Material Property			Cyclic Loading	
Overall			Beam (L-section)		Column		Density (g/cm ³)	Young's Modulus (GPa)	Poisson's Ratio	f (Hz)	A (mm)
l	w	h	w	t	w	t					
800	800	1100	50	6	55	10	7.6	200	0.3	10	10

where n , σ_{sy} and A_b represent the percentage bolt's yield strength, bolt yield strength, and cross-section area, respectively. Five levels of bolts pretension are considered: $n = 0\%$, 10% , 25% , 50% , and 75% . Substituting Equation (4-6) into Equation (4-5), we obtain:

$$T = n \sigma_{sy} A_b K D \quad (4-7)$$

Table 4-2 displays the parameters and bolts pretensions results. Grade 8 bolts are used for the connections. The analysis procedure is divided into three different steps:

- Initial step: Defining boundary conditions. In this step, all the degree of freedoms (DOFs) of the shaking table are fixed;
- Step 1: Defining contacts and bolt preload. During this step, the bolt is restrained against displacements and rotations to prevent numerical singularities that can occur due to rigid body motion;
- Step 2: Fixing the bolt length and applying external load.

Bolt pre-tension force could be directly defined by splitting the bolt-shank into two parts and apply the desired force to the pre-tension surface. The fastener axis should be selected to define the direction of the pre-tensioning. Furthermore, the element size for the frame (beams and columns) should be smaller than the element size of the bolt-head and nut. Figure 4-3 displays the results of the numerical simulations of the bolt.

The FE model consists of a total of 15696 C3D8R elements and 34108 nodes. The approximate element size is 10 mm. The computational time took 3 hours and 42 minutes for the intact configuration. As mentioned before, the damage is introduced by loosening/removing the bolts and by introducing a crack to the columns of the frame. The two front bolts of the second floor are chosen to define the first class of damage as follows:

- Healthy: $n = 75\%$ (see Table 4-2). This case represents the healthy structure (no bolt loosening/removing, and no cracks);
- D1bo: One bolt is removed from the second floor;
- D2bo: Two front bolts were removed from the second floor;
- T10: $n = 10\%$ (see Table 4-2);
- T25: $n = 25\%$ (see Table 4-2); and
- T50: $n = 50\%$ (see Table 4-2).

Table 4-2: Parameters and bolts pretension values.

Parameters		Bolts Pretension			
		n (%)	$n \sigma_{sy}$ (MPa)	Preload P (N)	Torque T (N·mm)
Nominal Diameter D (mm)	6	0	0	0	0
		10	89.63	2534	3041.11
		25	224.08	6336	7602.77
Nut Factor K	0.2	50	448.16	12671	15205.54
		75	672.23	19007	22808.31
Yield Strength (MPa)	896				

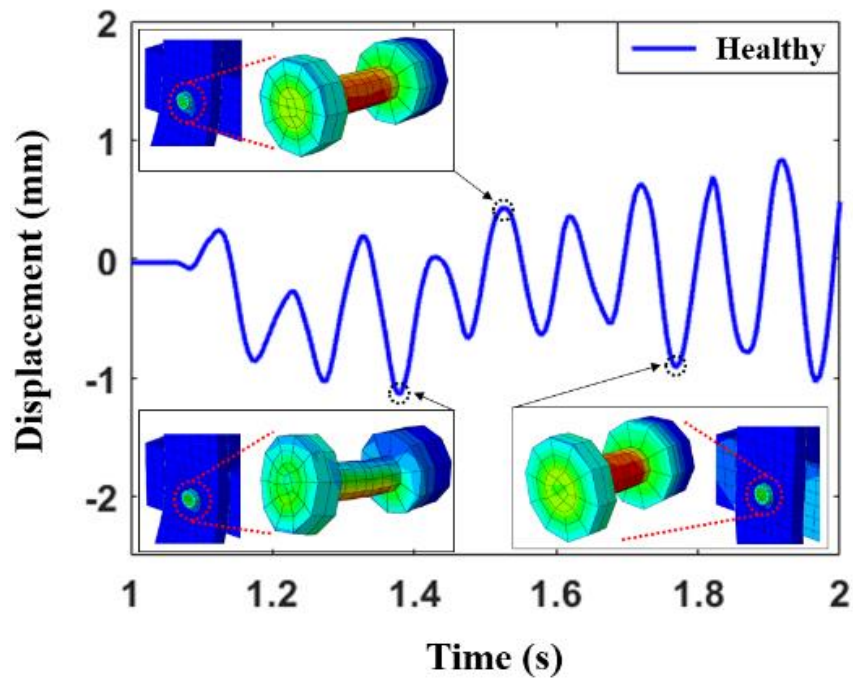


Figure 4-3: Bolt displacement response of the steel frame.

The second type of damage is defined by introducing a crack to the middle of the two front columns of the frame. The crack length is 30 mm. This damage state is referred as ‘CR’.

4.3.2. FE results

4.3.2.1. Bolt loosening effect on the mechanical response of the frame

The sensing locations are defined by selecting the middle node from the beams of each floor, as indicated in Figure 4-4. Figure 4-5 displays the results of the numerical analysis for the Healthy, D1bo, and D2bo damage states for each floor level. It is seen that the acceleration amplitude is considerably changed between damage states. The first floor is insufficient in sensing any changes as it is directly attached to the shaking table, and the bolts connecting the first floor to the columns are completely fastened (100 % of the full torque).

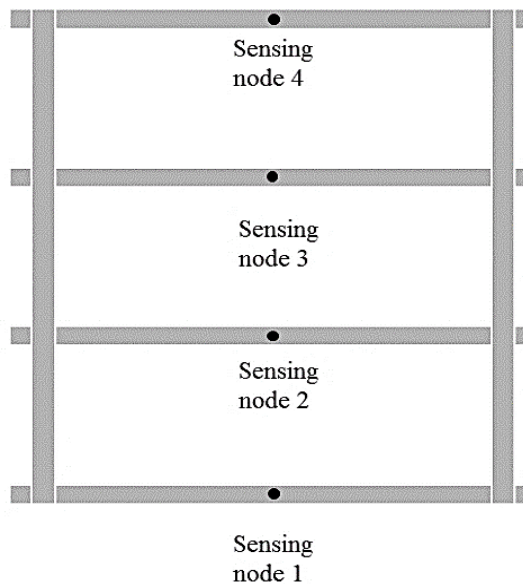


Figure 4-4: Sensing locations.

For the second floor, the maximum peak acceleration is recorded at the healthy state. Removing

one bolt results in decreasing the peak acceleration. Same conclusion is obtained when taking into account the minimum peak acceleration, i.e., removing both bolts, as seen in Figure 4-5(b). Conversely, at sensing nodes 3 and 4, the peak acceleration keeps increasing when introducing damage to the structure (removing the bolts).

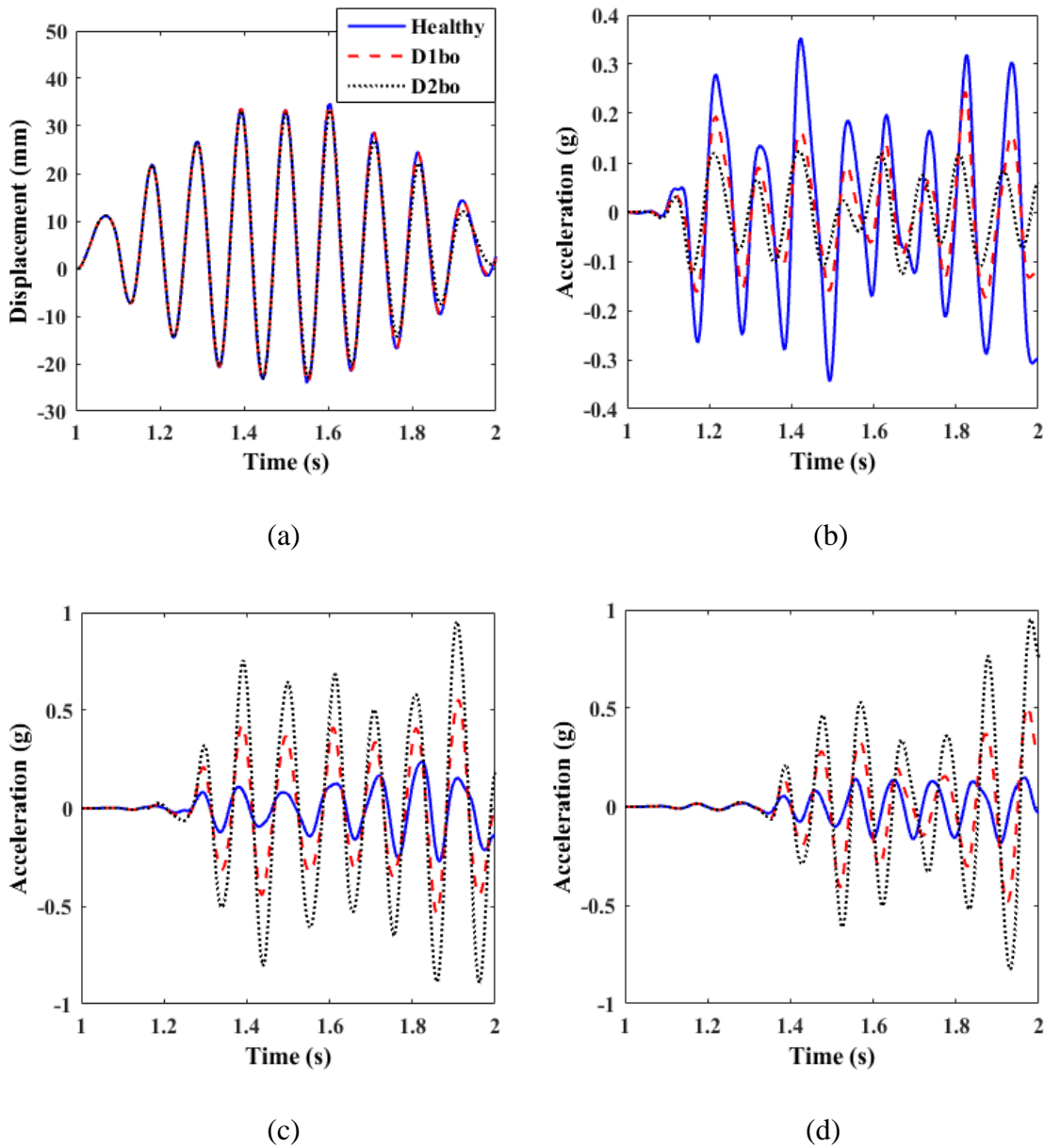


Figure 4-5: (a) 1st floor displacement vs. time, (b) 2nd floor acceleration vs. time, (c) 3rd floor acceleration vs. time, and (d) 4th floor acceleration vs. time.

Table 4-3 presents the peak acceleration for the three studied damage states in each floor. The variation percentages of the acceleration between the Healthy and D2bo damage states are, 64.96 % for the second floor, 303.74 % for the third floor, and 546.16 % for the fourth floor. Figure 4-6 displays the variation percentages of the peak acceleration for all floor levels. As indicated by the figure, the highest floor level is the best indicator of damage occurrence in the structure caused by removing the bolts. For damage states T10, T25, and T50, the acceleration response of the frame is first extracted at the sensing locations shown in Figure 4-4. The results indicate that at these locations, the variation of the peak acceleration is very small. Therefore, a closer node located at about 56 mm from the center of the connection bolt-beam is used. Figure 4-7 displays the results of loosening both bolts for damage states T10, T25, and T50. Table 4-4 shows the maximum detected difference in the acceleration due to torque loosening.

Figure 4-8 displays the variation percentage of the acceleration between damage states. A pretensioning force of 50 % of the yield strength can result in decreasing the acceleration by about 27 % near the bolt area. In addition, below 50 % of the full torque, the acceleration is changed by nearly 23 % between damage states.

Table 4-3: Variation of the peak acceleration between damage states.

Peak Acceleration (g)			
Floor Number	Healthy	D1bo	D2bo
Floor 2	0.35205	0.24304	0.12336
Floor 3	0.2365	0.55178	0.95484
Floor 4	0.14701	0.50842	0.94989

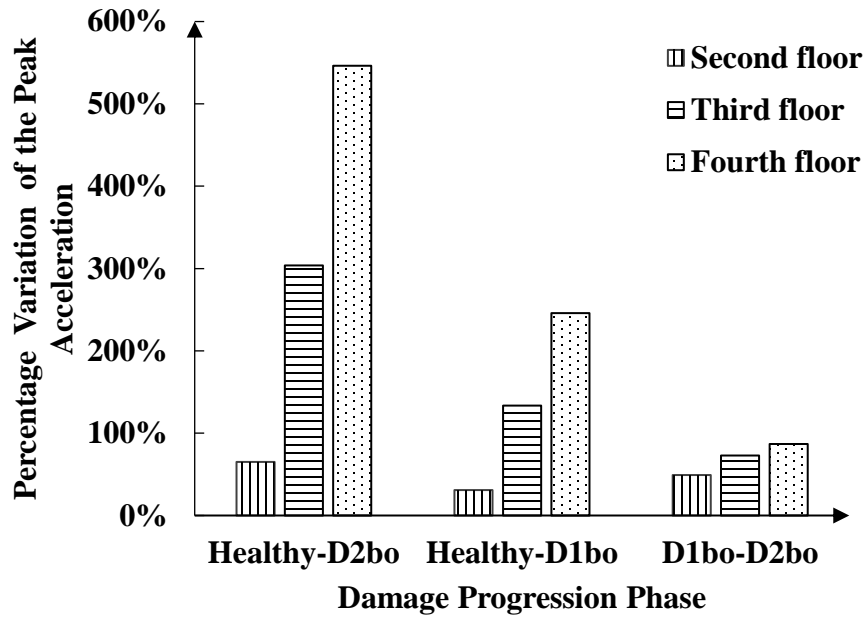


Figure 4-6: Percentage variations of the peak acceleration between damage states.

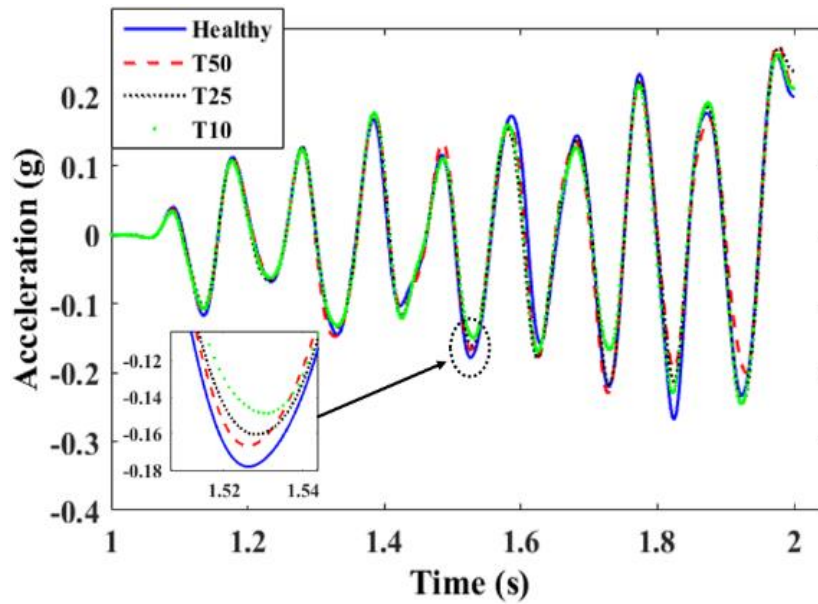


Figure 4-7: Variation of the acceleration at a node located close to the bolt connection of the second floor as a function time for different torque levels.

Table 4-4: Peak acceleration for different torque levels.

Damage Growth	Difference in Peak Acceleration (g)
Healthy– T50	0.0726
T50 – T25	0.0455
T25 – T10	0.0505

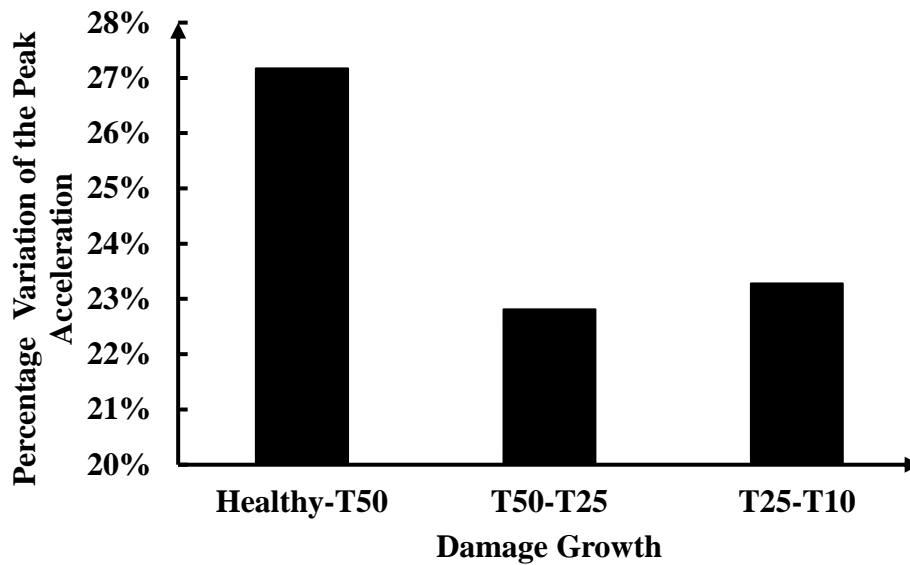


Figure 4-8: Percentage variation of the acceleration vs damage growth.

The strain time history is also extracted from the FE results. Figure 4-9 displays the strain time history for all the 4 floors and for the healthy, D1bo, and D2bo damage states. As seen in the figures, the maximum strain shows a variation between damage states, especially for the 3rd and 4th floors. The strain amplitude is increased when removing the bolts from the structure. Comparing with the variation on the third and fourth floors, the variation caused by the strain changes between damage states on the second floor is relatively trivial. Besides, the maximum

percentage of strain variation is detected at the fourth floor between the intact and the D2bo damage state (160 %).

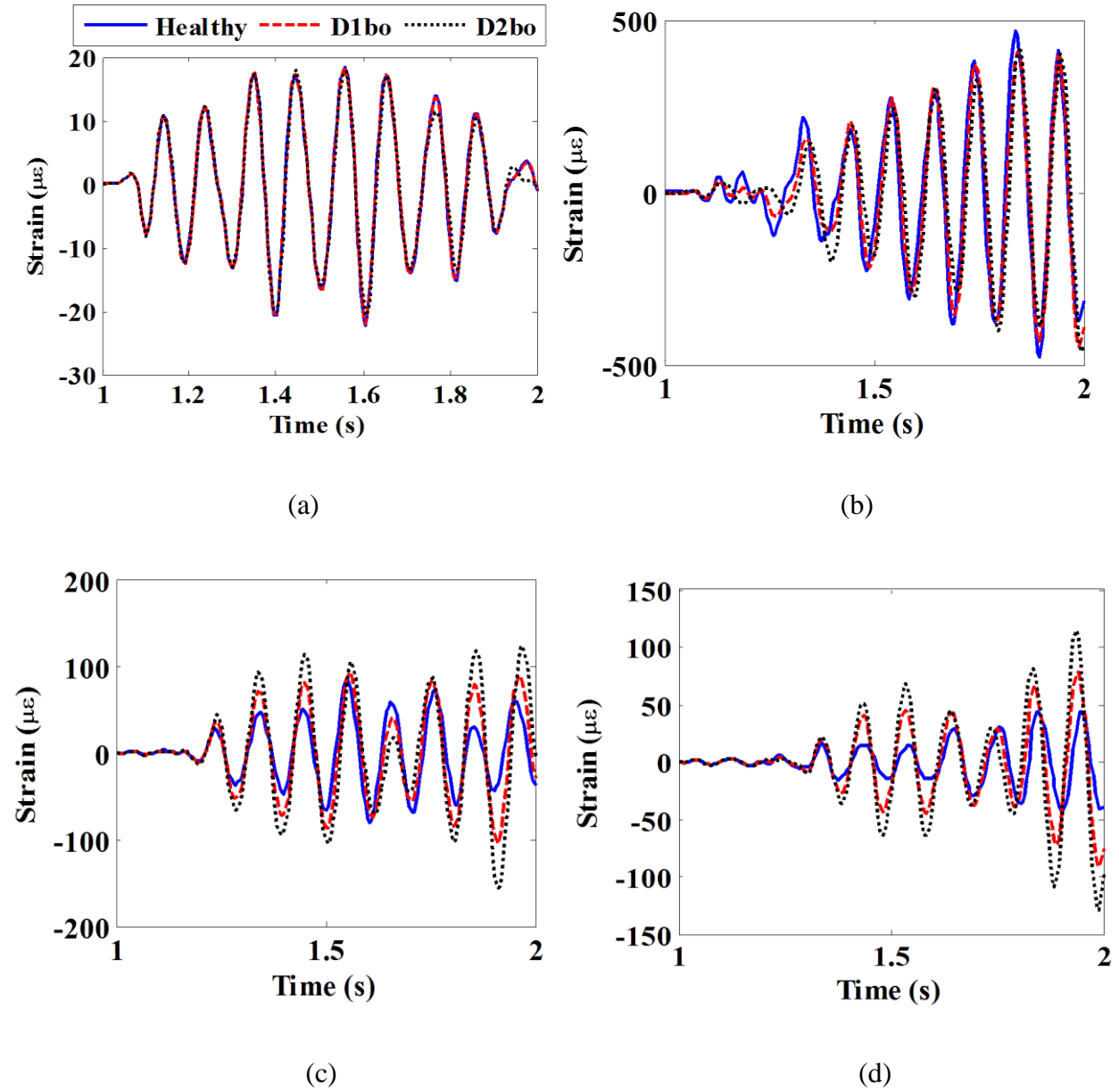


Figure 4-9: Variation of the strain between damage states, (a) first floor, (b) second floor, (c) third floor and (d) fourth floor.

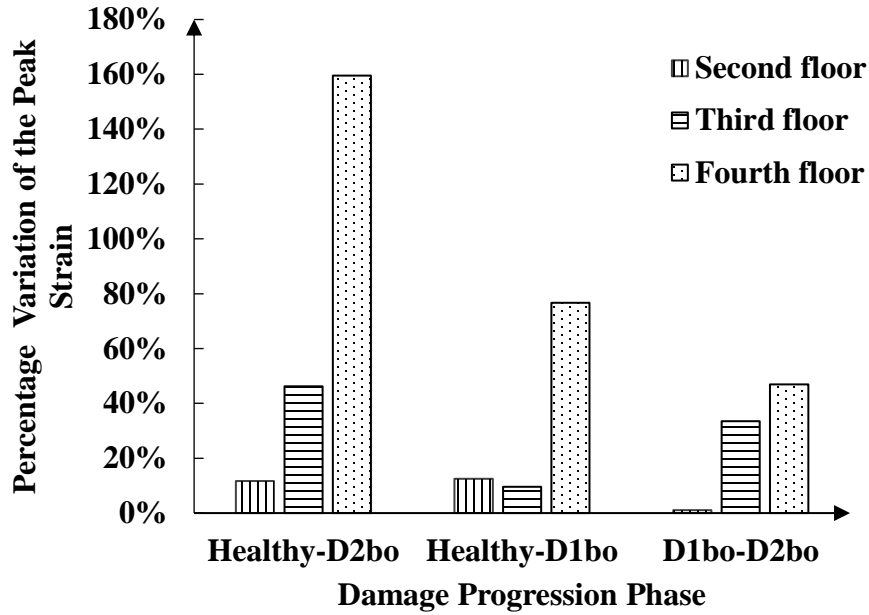


Figure 4-10: Percentage variation of the peak strain between damage states.

Moreover, 546 % variation is sensed by the acceleration on the fourth floor between the healthy and D2bo damage states. Figure 4-10 displays the percentage variation of the maximum strain between damage states. For damage classes T10, T25, and T50, an insignificant variation of the strain is observed. Therefore, it is concluded that loosening of bolts is more sensitive to the acceleration than the strain.

4.3.2.2. Crack effect on the frame response

The objective of this section is to determine whether if the strain or the acceleration is more sensitive to damage of type cracks. The crack is introduced to the structure at both front columns as indicated in

Figure 4-11. The strain is measured at the same sensing locations given in Figure 4-4. The analysis is first run for the CR damage state without loosening or removing the bolts. Thereafter, the results are compared between the acceleration and the strain to study the effect of

cracking on the frame behavior.

Figure 4-12 displays the relative changes of strain and acceleration between the healthy and the cracked frame (CR), and between the Healthy and D1bo damage states. Each bin of the presented histograms is calculated based on the local maxima of the time history curves of the strain and the acceleration. According to Figure 4-12(a), the maximum percentage variation of the strain is 111 % (peak number 3) when introducing a crack to the columns. However, removing one of the bolts leads to a maximum variation of 80.2 % in the strain (peak number 2). Therefore, cracking results in more important variation to the strain amplitude comparing with removing one bolt from the frame. On the other hand, the variation of the peak accelerations (Figure 4-12 (b)) caused by removing bolts is always higher than that due to cracking (61.8 % at peak number 6 vs. 49.2 % at peak number 4).

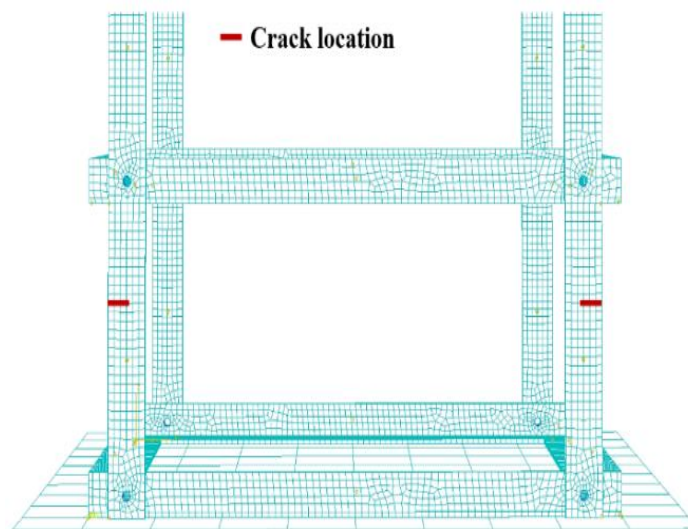


Figure 4-11: Crack location.

Finally, it can be concluded that the acceleration is more sensitive to bolt loosening/removing, while the strain is more sensitive to cracking. Therefore, the rest of the study mainly focuses on using acceleration to detect bolt loosening damages, and using strain to detect damage of type

cracks based on PFG sensor data. Accordingly, two types of piezoelectric transducers, i.e., vibration-based energy harvester and strain transducer, are used to harvest the vibration and strain energy from the frame. The former generates the electrical charge based on the acceleration sensed at the location shown in Figure 4-4. However, the latter generates the electrical energy based on the strain amplitude.

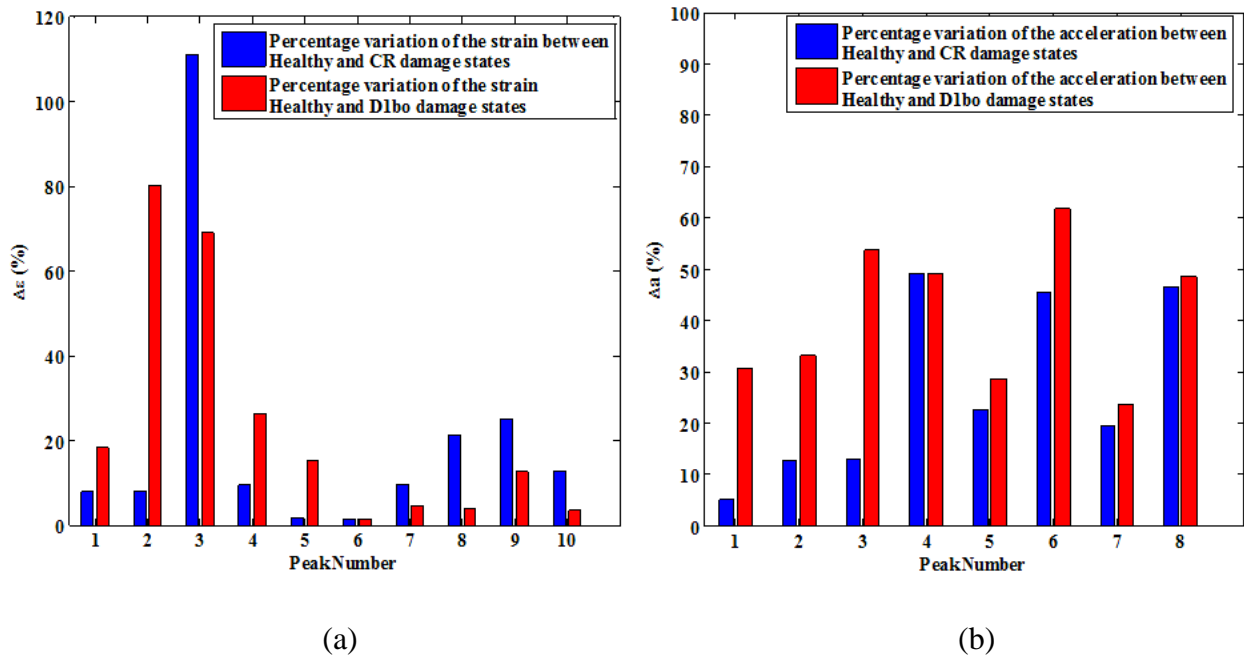


Figure 4-12: Variation of (a) strain and (b) acceleration behavior due to cracking and bolt loosening.

4.4. Energy harvesting from the frame structure

This section focuses on estimating the energy than can be harvested from the strain and acceleration signals. A circular PZT strain transducer and a bimorph cantilever PZT beam are, respectively, considered to convert the strain and acceleration energy into electrical signals. This outputted electrical energy from the PZT is used to empower the wireless sensor and detect damage progression in the structure. Referring to section 4.3.2., the FE results showed that the

strain is more sensitive to local damage (i.e. cracking) and the acceleration is more sensitive to global damage (i.e., loosening/removing of bolts). Hence, for remaining part of this chapter, the strain transducers are used to detect damage of type cracks while the cantilever PZT beams are used to detect bolt loosening related damages.

A schematic description of the cantilever piezoelectric beam used in this study is shown in Figure 4-13.

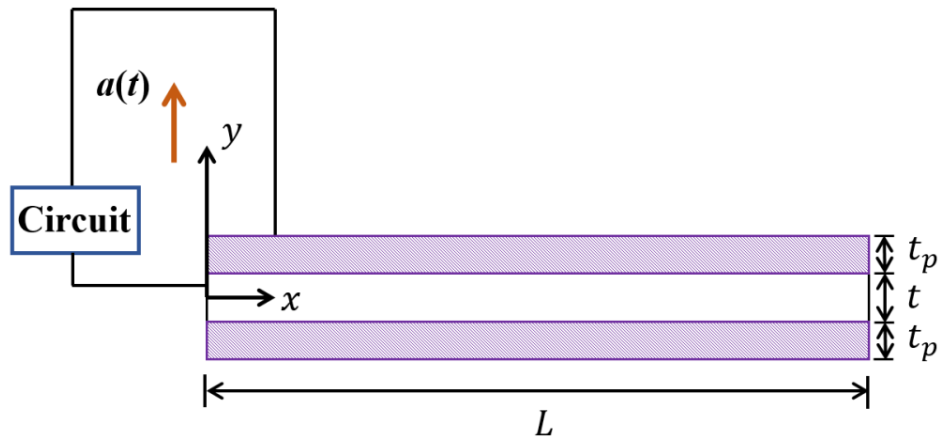


Figure 4-13: Schematic description of the cantilever piezoelectric beam.

The coupled electro-mechanical system of equations is given by (Sodano et al., 2004):

$$(M_s + M_p + M_t) \ddot{r}(t) + C \dot{r}(t) + (K_s + K_p) r(t) - \Theta v(t) = -M_e a(t) \quad (4-8)$$

$$\Theta^T r(t) + C_p v(t) = q(t) \quad (4-9)$$

where:

$$\begin{cases} M_s = \int \rho_s \underline{\phi}^T(x) \underline{\phi}(x) dV_s \\ M_p = \int \rho_p \underline{\phi}^T(x) \underline{\phi}(x) dV_p \\ M_t = \underline{\phi}^T(L) \underline{\phi}(L) M_{tip} \\ M_e = \int \rho_s \underline{\phi}(x) dV_s + \int \rho_p \underline{\phi}(x) dV_p + M_{tip} \underline{\phi}(L) \end{cases} \quad (4-10)$$

$$\begin{cases} K_s = \int y^2 \underline{\phi}^T(x)'' c_s \underline{\phi}(x)'' dV_s \\ K_p = \int y^2 \underline{\phi}^T(x)'' c_p \underline{\phi}(x)'' dV_p \end{cases} \quad (4-11)$$

$$\Theta = - \int y \underline{\phi}^T(x)'' e^T \psi(y) dV_p \quad (4-12)$$

$$C_p = \int \psi^T(y) \varepsilon^S \psi(y) dV_p \quad (4-13)$$

M_s , M_p , M_t , and M_p are the mass matrices of the system. K_s and K_p are the stiffness matrices, and Θ and C_p represent the electromechanical coupling matrix and the capacitance matrix, respectively. The subscripts s and p stand for the substrate and the PZT layers respectively. The terms e and ε , are the PZT coupling coefficient and the dielectric constant, respectively. The matrix C designates the amount of the mechanical damping added to the model. The voltage and charge outputs are noted as $v(t)$ and $q(t)$, respectively, and $a(t)$ represents the input acceleration. The obtained electro-mechanical system of equation is based on three major assumptions:

- The first assumption states that the displacement $u(x, t)$ of the beam is assumed to be written as a summation of the beam modes and the temporal coordinates as follows (Rayleigh-Ritz procedure):

$$u(x, t) = \sum_{k=1}^n \phi_i(x) r_i(t) = \underline{\phi}(x) \underline{r}(t) \quad (4-14)$$

where ϕ_i is the assumed mode shape of the structure that satisfies the boundary conditions, and r_i is the temporal coordinate of the displacement. The assumed shape function in this study has the following form (Elvin et al., 2006):

$$\phi(x) = 1 - \cos\left(\frac{\pi x}{2L}\right) \quad (4-15)$$

- The second assumption is based on the Euler-Bernoulli beam theory. Accordingly, the strain (S) can be written as follows:

$$S = -y \frac{\partial^2 u(x,t)}{\partial x^2} \quad (4-16)$$

- The electrical potential is assumed to be constant through the thickness of PZT layers. The electrical potential is given by the following equation:

$$\underline{E}(y, t) = \psi(y)v(t) = \begin{cases} -\frac{v}{t_p} & \text{if } \frac{t}{2} < y < \frac{t}{2} + t_p \\ 0 & \text{if } -\frac{t}{2} < y < \frac{t}{2} \\ \frac{v}{t_p} & \text{if } -\frac{t}{2} - t_p < y < -\frac{t}{2} \end{cases} \quad (4-17)$$

In order to incorporate the energy dissipation into the governing equation of the system, resistive element between the PZT electrodes can be expressed as:

$$v(t) = -R \frac{dq}{dt} \quad (4-18)$$

Thereafter, by deriving over time Equation (4-9), the final system can be expressed as a function of voltage and the temporal coordinate of the displacement as:

$$(M_s + M_p + M_t) \ddot{r}(t) + C \dot{r}(t) + (K_s + K_p) r(t) - \Theta v(t) = -M_e a(t) \quad (4-19)$$

$$\Theta^T \dot{r}(t) + C_p \dot{v}(t) = -\frac{v(t)}{R} \quad (4-20)$$

Giving the acceleration time history, the coupled system of equations could be easily solved for $r(t)$ and $v(t)$. As mentioned before, the obtained acceleration from the numerical simulation is used as an input acceleration $a(t)$ for the cantilever beam. In fact, the PZT beams are attached to the frame at the sensing locations shown in Figure 4-4.

Table 4-5 shows the properties of the considered commercial piezoelectric ceramic bimorph by Steiner & Martins, Inc, (# SMBA4510T05M). A MATLAB code is developed to solve the electro-mechanical system of equations. A tip mass of 8.5 g is attached to the end of the cantilever beam to shift-back the resonant frequency to the low-frequency range and increase the voltage output of piezo. Multiple iterations are performed to find the optimal tip mass that gives above the minimum voltage threshold of the sensor.

The sensor resistance ($R= 50 \text{ m}\Omega$) is used as a source of energy dissipation in Equation (4-18). The capacitance of the strain transducer might be expressed as (Sirohi and Chopra, 2000):

$$C_p = \frac{\epsilon A_p}{t_p} \quad (4-21)$$

where A_p and t_p are the cross-section area and thickness of the piezo, respectively.

The strain transducer has a diameter of 10 mm and thickness of 0.25 mm. Note that only the voltage outputs corresponding to the Healthy, D1bo, and D2bo damage states are displayed in Figure 4-14. The strain transducer results are displayed in Figure 4-15.

Table 4-5: Properties of the bimorph PZT beam.

Property	Value
Elastic Modulus of PZT c_p (GPa)	72
Elastic Modulus of Substrate c_s (GPa)	11
Density of PZT ρ_p ($\frac{Kg}{m^3}$)	7800
Density of Substrate ρ_s ($\frac{Kg}{m^3}$)	8900
Electrical Permittivity ϵ ($\frac{F}{m}$)	3500 ϵ_0
Piezoelectric Constant d_{31} ($\times 10^{-12} \frac{m}{V}$)	-270
Beam Length L (mm)	40
Beam Width b (mm)	10
PZT Thickness t_p (mm)	0.1
Substrate Thickness t (mm)	0.2

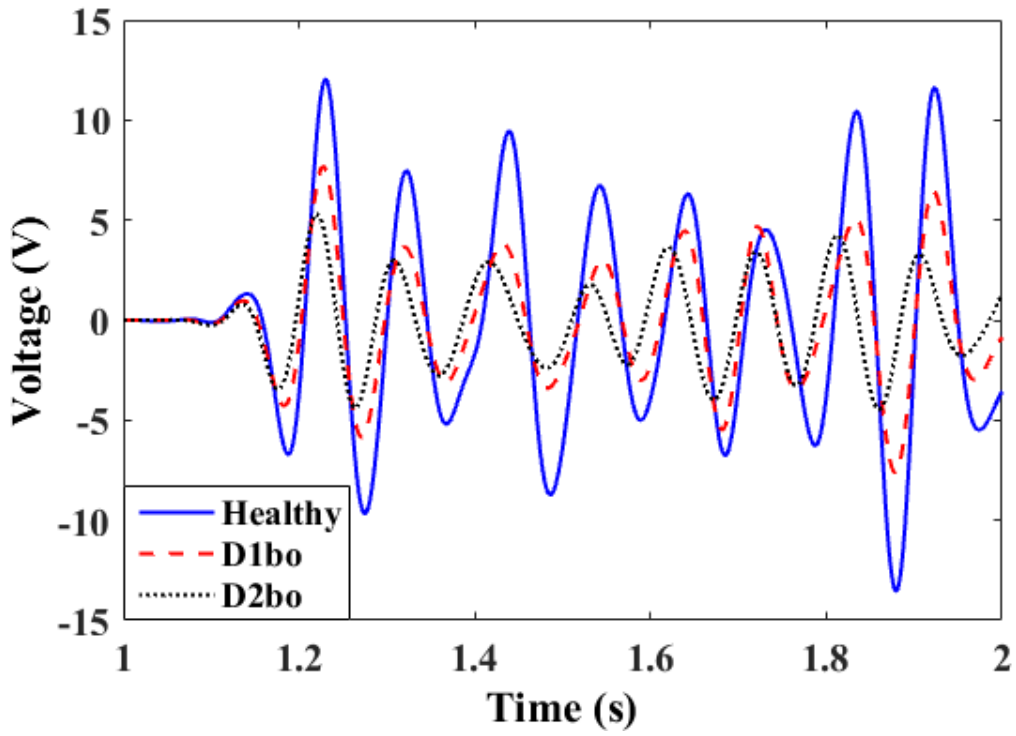


Figure 4-14: Voltage outputted by the bimorph PZT beam on the second floor.

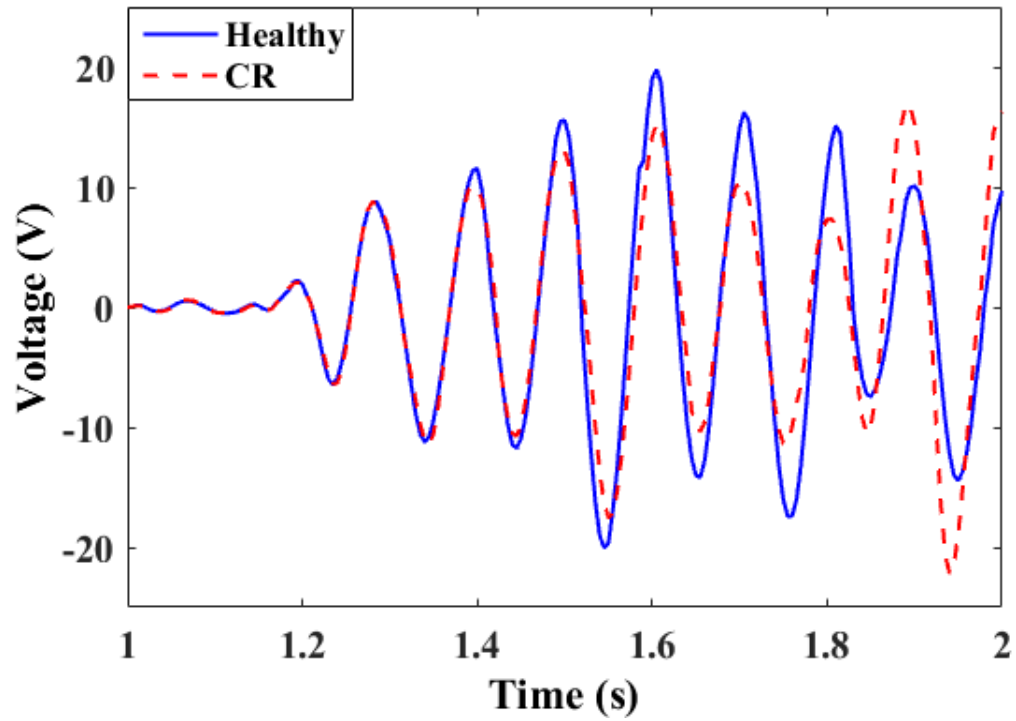


Figure 4-15: Voltage outputted by the strain transducer disc on the third floor.

4.5. Damage detection results

4.5.1. Bolt loosening detection results

After obtaining the voltage time history at the sensing locations from the accelerations and strains, the voltage droppage at the sensor gates is calculated. The sensor voltage thresholds of each gate are presented in Table 4-6. The minimum voltage required to activate the sensor is 7.60 V, and hence, voltages smaller than that cannot be recorded.

The sensor output histograms for the Healthy, D1bo, and D2bo damage states at each floor level are displayed in Figure 4-16. As seen in the figure, the recorded voltage droppage highly depends on the damage state. Each damage state corresponds to the sensed acceleration and therefore, is correlated to the voltage amplitude generated by the PZT beams. When the outputted voltage amplitude from the PZTs exceeds the threshold level of a specific gate j , the procedure of electrons injection initiates. Subsequently, the voltage droppage increases at all gates from 1 to j . In other words, if the voltage is higher than the threshold of gate j and lower than the threshold of gate $j+1$, only gates 1 to j start recording the droppage of voltage.

Referring to Figure 4-14, the maximum voltage for healthy state is 12 V which is above the maximum voltage threshold of the sensor. As a result, all channels (gates) of the sensor for the undamaged structure are recording the drop of voltage. Thereafter, when removing one bolt from the structure, the maximum voltage obtained by the cantilever piezo beam drops to 7.66 V, which can only activate the first channel of the sensor. Hence, the second histogram of Figure 4-16(a) presents only one bin at channel 1.

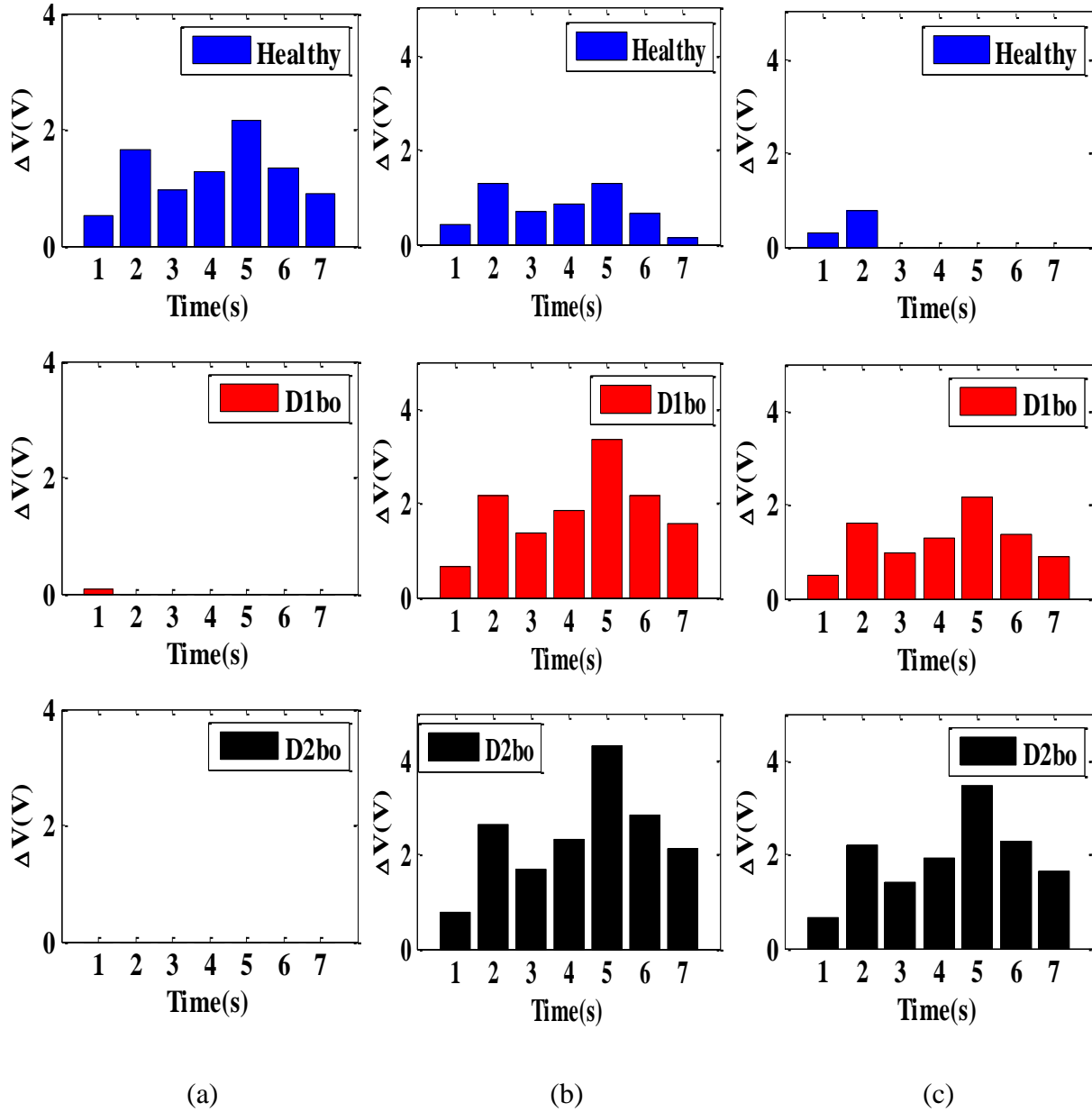


Figure 4-16: Sensor output histogram for different damage states for: (a) Second floor, (b) Third floor, (c) Fourth floor.

In addition, the maximum voltage obtained after removing both bolts from the second floor is 5.32 V, which is below the sensor minimum voltage threshold. Therefore, all the sensor gates remain closed and do not recorded the voltage droppage. For the third floor, the sensor is recording for all damage states as the minimum outputted voltage was 10.48 V.

By comparing Figure 4-16(a) to Figure 4-16(c), an inverse behavior can be observed. According to the numerical results, the acceleration on the fourth floor is increased with the damage progression. As a result, the generated voltage amplitude is enlarged. The maximum obtained voltage is 8.87 V for the intact structure, which is increased to above 10.45 V after removing the bolts. Therefore, gates 3 to 7 start recording for the D1bo and D2bo damage states. Although the output of the sensor changes with damage progression, there is a considerable loss of information.

Table 4-6: Voltage threshold levels of each gate.

Gate Number	Voltage Threshold (V)
1	7.60
2	8.20
3	8.92
4	9.21
5	9.69
6	10
7	10.45

In fact, the sensor output histograms took different shapes depending on the damage states as well as the floor number, which makes the data interpretation more complicated in the case of a network of sensors. It is worth to mention that the injection rates and the number of cycles also affect the shape of these histograms. Therefore, it is of importance to extract valuable and

reliable information from the sensor distribution. In this work, a GMM is used to fit the cumulative droppage of voltage at the sensing nodes. Figure 4-17 displays the obtained GMM fit to the data at the sensor located on the third floor for the healthy structure. The results of the GMM fitting to the data at all sensors locations and for all damage states are displayed in Figure 4-18. As it is seen in Figure 4-18, the GMM parameters deviate between damages states. At the second floor (Figure 4-18(a)), the sensor histogram has only 1 active gate for the D1bo damage state. Therefore, the sensor output is fitted to a unimodal Gaussian distribution. Moreover, the histograms are fitted to bimodal distribution, as the entire channels of the sensors located on the third floor are active for all damage classes (Figure 4-18(b)). In Figure 4-18(c), the D1bo and D2bo damage states are fitted to a bimodal Gaussian distribution. However, the healthy state is fitted to a unimodal distribution. Depending on the number of active gates, the GMM fit changes between sensors locations and damage states, and hence, the GMM parameters vary as well. On the second floor, and for the D2bo damage class, the sensor does not record any information as the voltage amplitude is below the activation threshold the sensor.

As seen in Figure 4-18, the shape of the GMM plots change with damage progression in the structure. This indicates that the damage progression due to bolt loosening can be monitored by the GMM parameters even far from the damage zone. An interesting observation from Figure 4-18(a) is that all the parameters of the distribution are decreased with damage growth. However, on the third floor (Figure 4-18(b)), the first set of GMM parameters (μ_1, σ_1) decreases and the second set (μ_2, σ_2) increases with damage evolution. On the fourth floor, all the damage predictors increase with respect to damage progression.

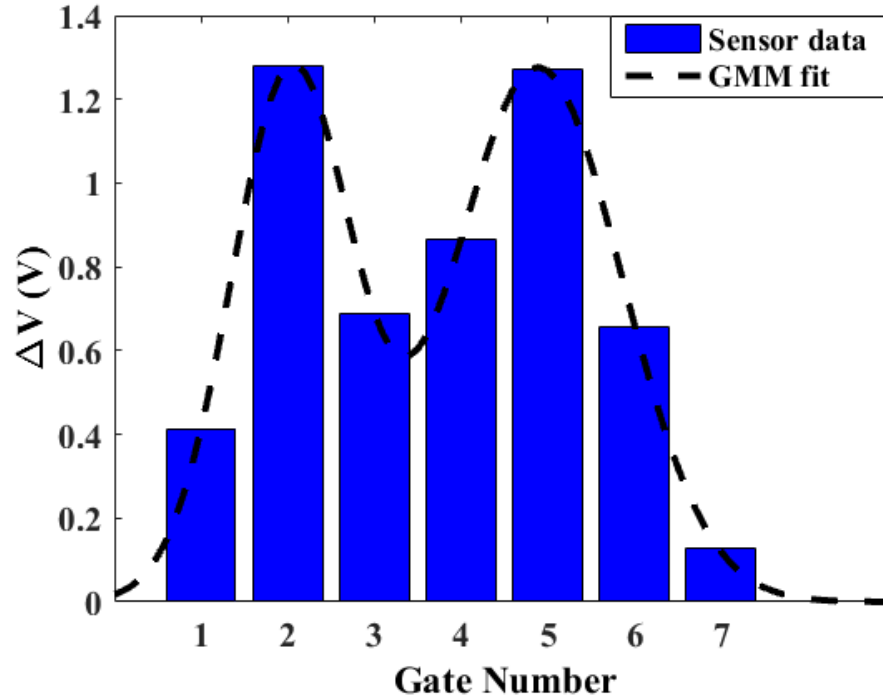
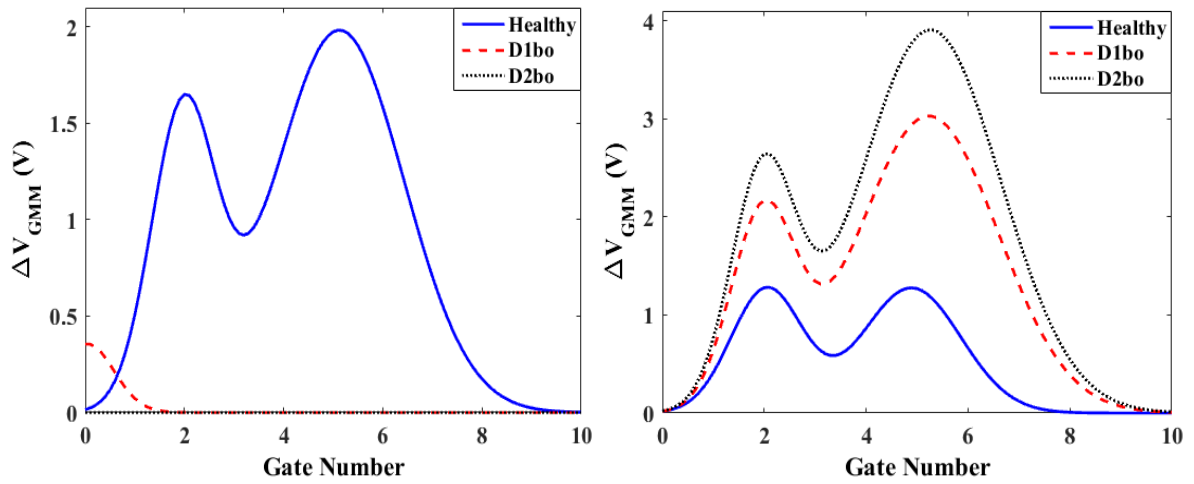


Figure 4-17: The GMM fit to the sensor data on the third floor for the intact structure.

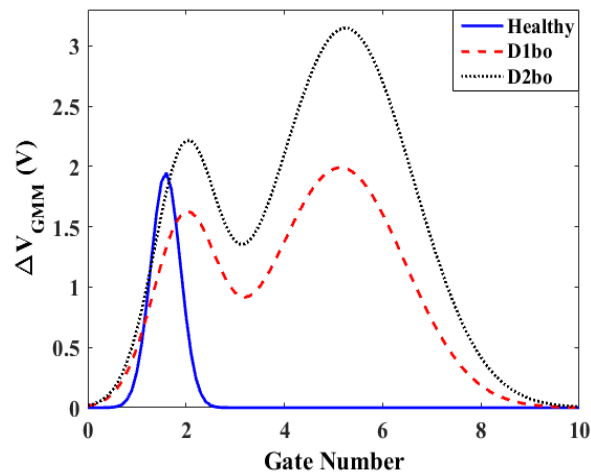
The results of this phase show that the GMM parameters seem to be good indicators of structural damage occurrence. However, after preliminary analyses, it is found that these damage indicators tend not to have sound relationship with the progression of damage. In fact, the variations of these parameters highly depend on the relative locations between the sensors and damage. Moreover, only sensor 2 located on the second floor (the location of the loosened bolts) has the most prominent variation of the GMM parameters, especially between the D1bo and D2bo damage states. The rest of sensors do not have good resolution in detecting the damage transition between the D1bo and D2bo damage classes. Although the sensors provide valuable information about the damage, the measurement at a single location could not be sufficient to accurately detect and classify damage states. To overcome this limitation, it is tried to fuse the data from multi-sensors based on the ‘group effect of sensors’ concept. The proposed sensor fusion model aims to improve the detection accuracy of the proposed approach by obtaining a reasonable trend

describing the transition from one damage state to another.



(a)

(b)



(c)

Figure 4-18: GMM fit to the sensor data at all sensing locations and for the Healthy, D1bo and D2bo damage states at (a) second floor, (b) third floor, and (c) fourth floor.

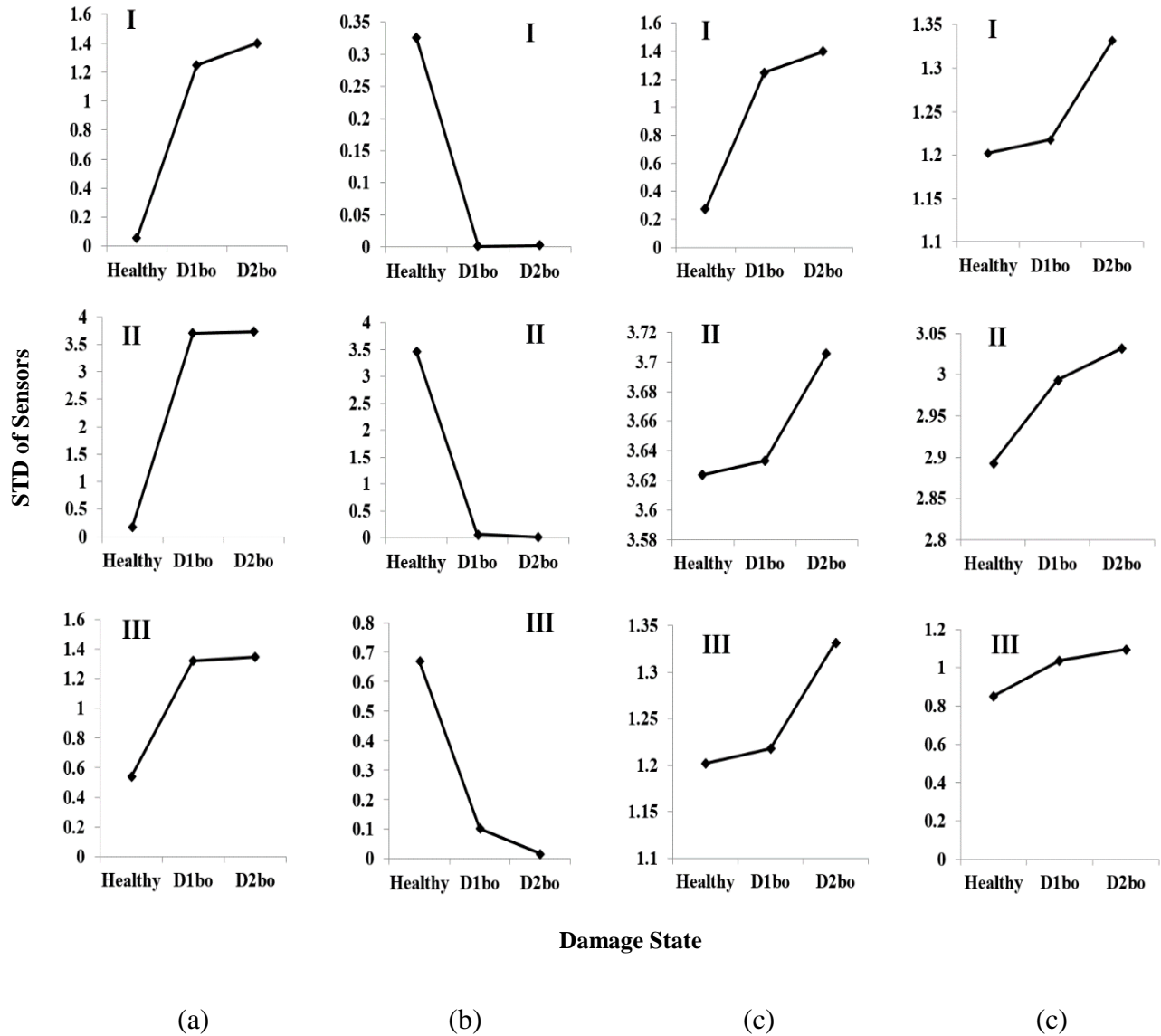


Figure 4-19: STDs of sensor groups: I (μ_1), II (μ_2), and III (σ_2^2) with respect to the scenarios of (a) sensing nodes 2 and 3 (G1) (b) sensing nodes 3 and 4 (G2), (c) sensing nodes 2 and 4 (G3), and (d) sensing nodes 2, 3 and 4 (G4).

Based on a preliminary analysis, the average, range, minimum, maximum, skewness, and kurtosis of the GMM parameters do not have sound relationships with the damage progression. Only the standard deviation (STD) gives a unique relationship with damage progression. The

results of the data fusion model for the bolt loosening scenarios are displayed in Figure 4-19.

As seen in Figure 4-19, the STD of the group of sensors has a unique trend between damage states. The STD of σ_1^2 is not presented because it does not have a specific trend with damage progression. An interesting observation from Figure 4-19(b) is that the STD decreases from one damage state to the other. For this scenario, sensor 2 (the location of damage) is not included in the analysis. However, by including sensor 2, the STD is increased between damage states. Hence, the sign of the slope of STD is changed only after including the sensor located on the damaged floor. This means that the damage due to bolt loosening can be localized based on the sign of the STD curves.

4.5.2. Crack detection results

Figure 4-20 displays the sensor output histograms based on the voltage harvested from the strain transducers. The results are compared between the healthy and the cracked structure. Figure 4-21 presents the GMM fit to the sensor data. According to Figure 4-21, the GMM parameters are changed when the frame is cracked. In Figure 4-21(a), the first mean and variance of the distribution are increased with crack propagation, however the second mean and variance are decreased, and the distribution is reduced to unimodal Gaussian model. For the third floor, the GMM parameters μ_1, μ_2, σ_1^2 are increased and σ_2^2 is decreased. This means that the GMM distributions are shifted to the right, the first GMM component is expanded, and the second component is shrunk with damage occurrence. In Figure 4-21(c), the first mixture component is slightly expanded and shifted to the left, and the second is shrunk and shifted to the left for CR damage state.

The GMM parameters change is primarily due to the cracking of the frame columns. However, they do not have a sound relationship with damage progression. The same sensor fusion model

presented in section 4.5.1 is used. Only the standard deviations of two means μ_1 and μ_2 for different set of sensors are presented because they have a unique trend with damage. Figure 4-22 displays the results of the data fusion model applied to μ_1 and μ_2 for each set of sensors. For all of the plots, the STDs of the considered group of sensors are increased with damage. Hence the STD of μ_1 and μ_2 can accurately detect cracking in steel frames based on the data provided by the sensor.

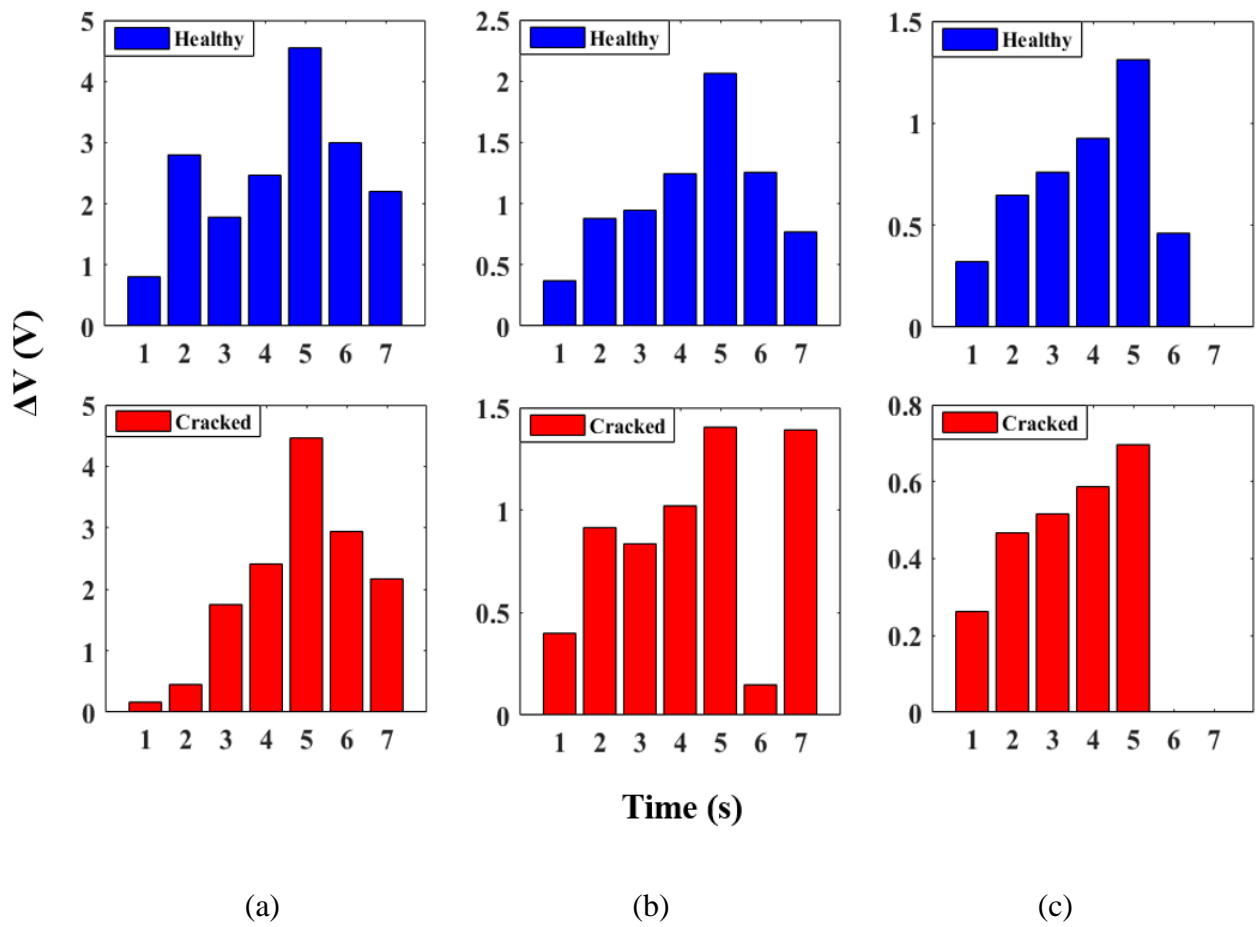
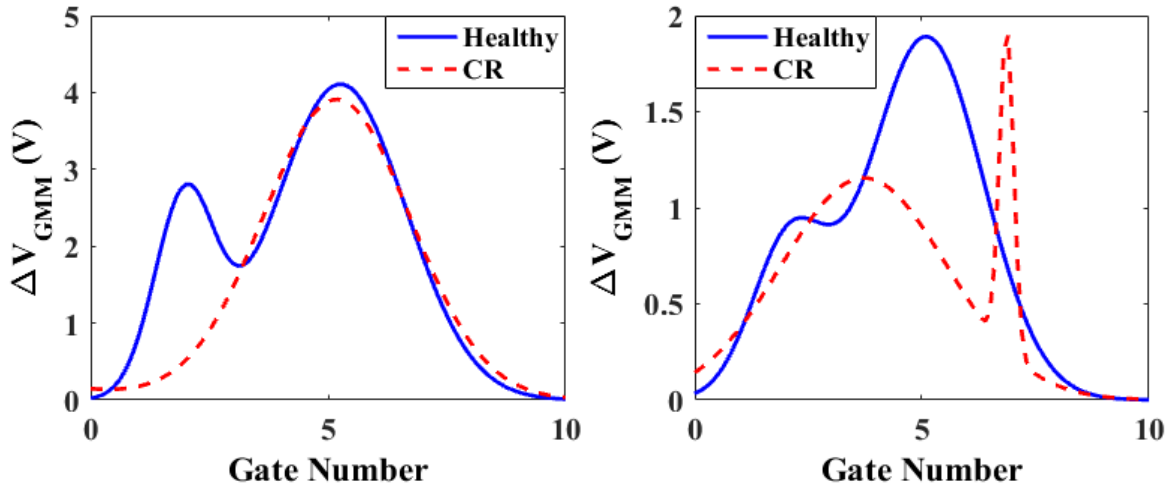
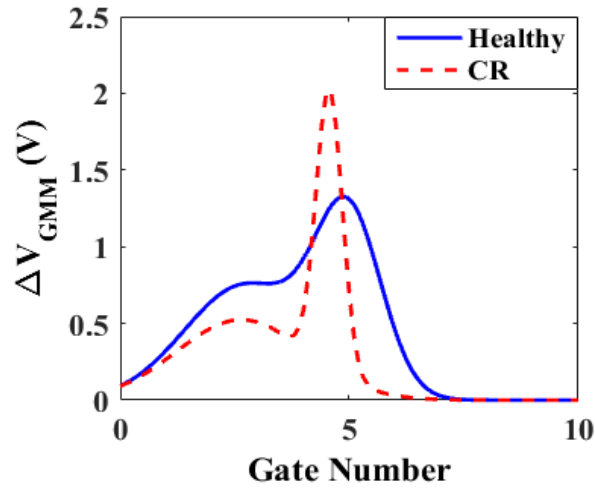


Figure 4-20: Sensor output histogram of different damage states for: (a) Second floor, (b) Third floor, and (c) Fourth floor.



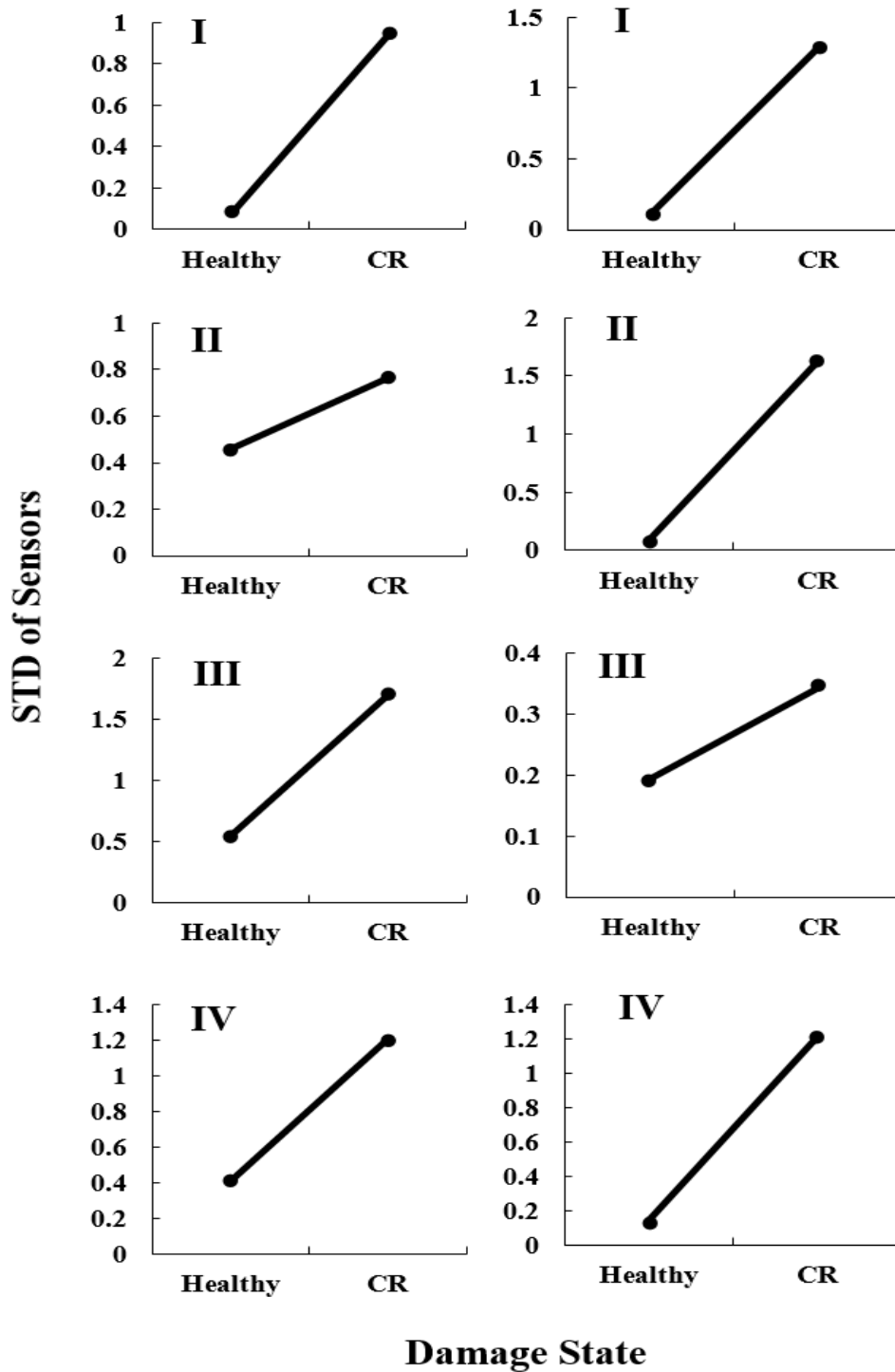
(a)

(b)



(c)

Figure 4-21: GMM fit to the sensor data at all sensing locations and for the Healthy and CR damage states at (a) second floor, (b) third floor, and (c) fourth floor.



(a)

(b)

Figure 4-22: STDS of sensor groups: I (1), II (G2), III (G3), and IV (G4) for (a) μ_1 and (b) μ_2 .

4.6. Summary

This chapter presented a procedure of detecting local-global damage in steel frames based on the interpretation of the data of the PFG sensor. The damage identification mechanism was composed by a hybrid network of vibration- and strain-based sensors. Numerical simulations were performed to obtain the mechanical response of the bolted frame under different damage scenarios. Damages were defined based on loosening/removing the bolts and by introducing a crack to the structure. Seven damage classes were considered in the analysis and four sensing locations were used to extract the data. The numerical results indicate that acceleration response of the frame is more sensitive to loosening the bolts. However, damages of type cracks are better sensed by the strain as they are local events rather than global.

Circular PZT strain transducers and cantilever bimorph PZT beams were used to harvest the mechanical energy. A theoretical model was developed to estimate the electrical charge output from both types of PZT transducers. Thereafter, the sensor output histograms were calculated from the voltage generated by the PZTs and fitted to a bimodal Gaussian distribution. The results showed that the parameters of the Gaussian mixture model are good predictors of damage occurrence in the structure. A sensor fusion model was developed to find a sound relationship between the Gaussian mixture distribution parameters and damage progression. The results indicate that standard deviation of μ_1 , σ_1^2 , and σ_2^2 of all the sensors combination used in the model is good predictor of bolt loosening from the structure and the damage can also be localized based on the sign of the slope of the STD curves. Moreover, The STD of μ_1 and μ_2 is good indicator of crack occurrence in the steel frame. As a summary, the PFG sensor is capable in detecting and localizing the change in boundary in steel frames and in sensing cracking of its structural members using a hybrid network of self-powered wireless PFG sensors.

CHAPTER 5. FIELD DEPLOYMENT OF THE SELF-POWERED PFG SENSOR: THE MACKINAC BRIDGE CASE STUDY

5.1. Overview

The Mackinac Bridge in Michigan, one of the longest suspensions in the world, is taken as a case study for evaluating the performance of the PFG sensing mechanism under real operating conditions. In this chapter, we also verify the benefits of battery-powered wireless transmission in acquiring data without the need for taking the structure out of service. First, an experimental study is developed to correlate the strain to the sensor threshold voltage levels according to traffic loading experienced by the bridge. The effect of temperature variation in wireless communication system is also investigated in this study. The preparation and the installation processes are presented in detail. The data acquired from the sensing system is used to evaluate the health status of the bridge. Results indicate that the sensor can operate under real field conditions and the data outputted is useful for monitoring the Bridge status over time. Moreover, the operational life of the wireless transmission can last for more than 20 years.

5.2. Experimental study of strain-sensors

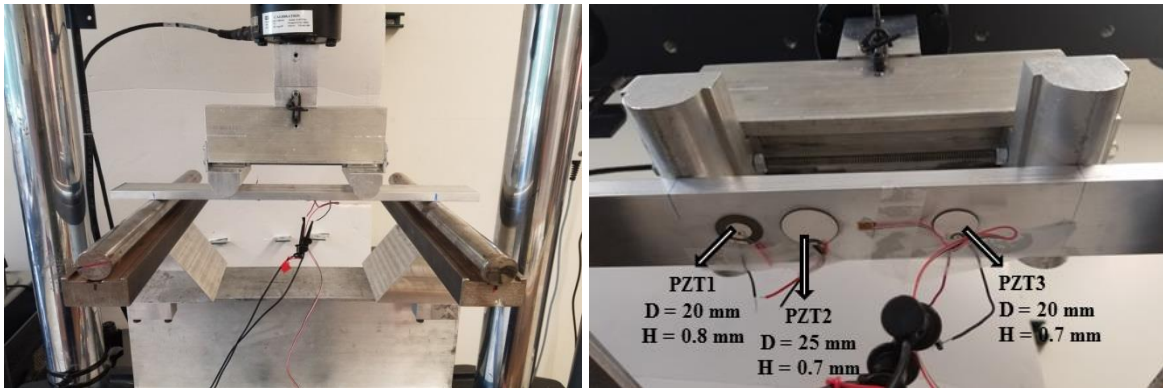
5.2.1. Preliminary testing of the transducers

The objective of this section is to identify the type/dimensions of the piezoelectric transducers that will be used to harvest the micro-strain energy from the Mackinac Bridge. In fact, and as stated before, each gate of the sensor has a specific voltage threshold level from which it starts recording. Therefore, depending on the type of the piezo, the strain amplitude can be correlated to the voltage thresholds at the sensor level. To this aim, three different piezoelectric ceramic discs are chosen for the testing, and a strain gage is placed at the middle of the specimen to measure the strain. The experimental setup is shown in Figure 5-1. All used PZTs are from STEMINC Inc company. The material properties are given in Table A-2. As shown in Figure 5-1, a four-point bending test is performed. The transducers are attached to the bottom of the aluminum beam. The specimen dimensions are 457.2 mm × 50.8 mm × 12.7 mm (18 in × 2 in × ½ in). In a four-point bending test, the strain is assumed to be constant between the load application points. The strain amplitude is given as:

$$\varepsilon_{surf} = \frac{3 F A}{E b h^2} \quad (5-1)$$

where F, A, b, h and E are the applied force, the coordinate of the first inner clamp with respect to the first outer clamp, the width, the thickness, and elastic modulus of the beam, respectively.

The outputted voltage from PZTs are read on the NI 9220 and the strain from NI 9236. The CC-33A epoxy is used to attach both transducers and strain gages. Figure 5-2 illustrates a schematic representation of the experimental setup. As seen in the figure, each PZT is connected to the NI9220 in parallel with the sensor that has 50 MΩ impedance.



(a)

(b)

Figure 5-1: Piezo discs mounted on the aluminum beam.

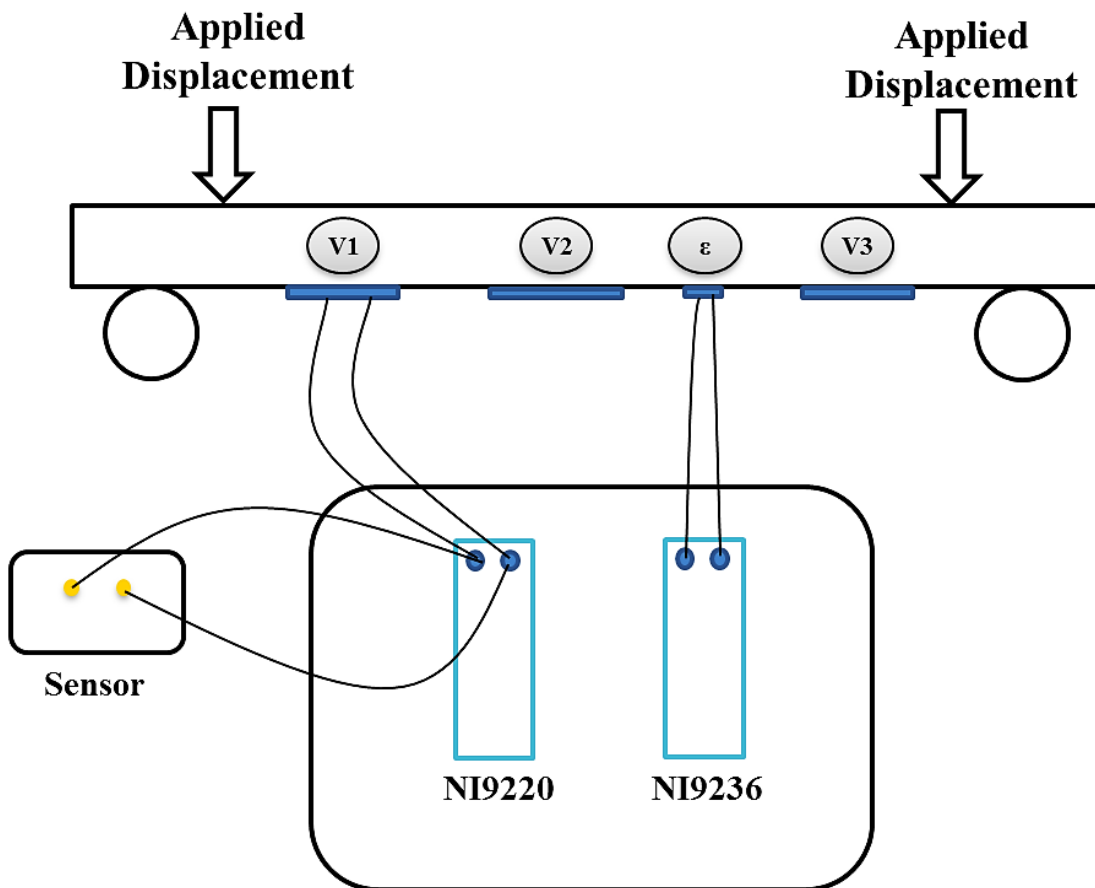


Figure 5-2: Test setup.

The load is applied using an MTS servo-hydraulic machine in a displacement-controlled mode. For each test, a cyclic displacement is applied. The number of cycles is initially set to 50 and gradually increased until the first gate of the sensor starts recording the voltage droppage. The procedure of increasing the number of cycles is repeated until all the gates record the voltage variations due to electrons injection. The load input frequency is set to 2 Hz. Figure 5-3 and Tables 5-1 to 5-3 present the results of the testing for each PZT. The binary values ‘0’ and ‘1’ denote the activation status of the sensor. As shown in Figure 5-3, PZTs 1 and 3 have almost the same voltage output. However, PZT 2 delivers higher voltage for the same strain value. In fact, PZTs 1 and 3 cover the range strains from 75 $\mu\epsilon$ to 220 $\mu\epsilon$ and PZT1 records from 50 $\mu\epsilon$ to 100 $\mu\epsilon$. Therefore, combining PZT1 and PZT2 (or PZT3), the sensors start recording from 50 $\mu\epsilon$ up to 220+ $\mu\epsilon$.

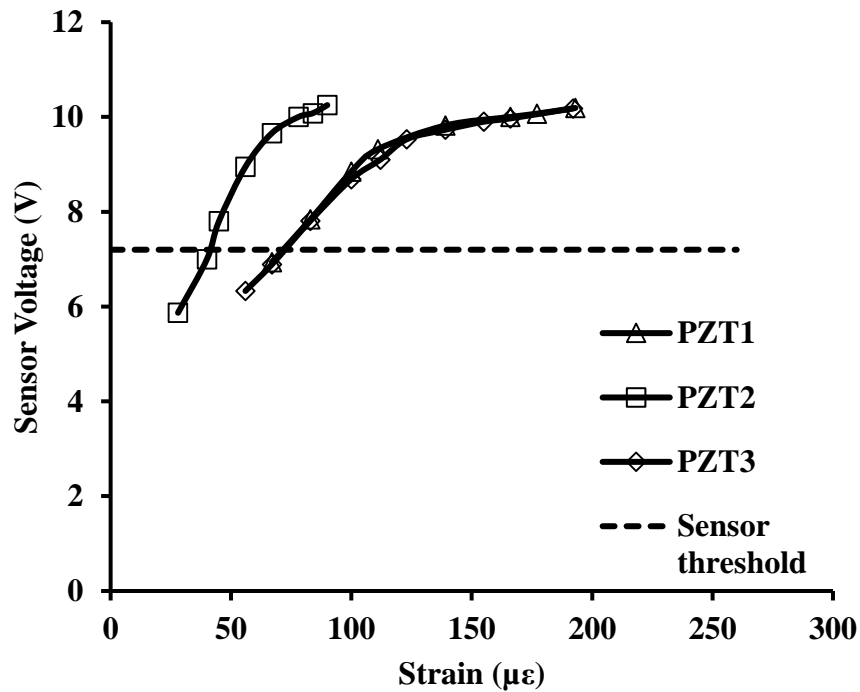


Figure 5-3: Sensor voltage vs strain.

Table 5-1: Sensor voltage for PZT1.

PZT1		
Strain ($\mu\epsilon$)	Sensor Voltage (V)	Activation
67	6.94	0
83	7.84	1
100	8.85	1
111	9.32	1
139	9.82	1
166	10	1
177	10.07	1
193	10.19	1

Table 5-2: Sensor voltage for PZT2.

PZT2		
Strain ($\mu\epsilon$)	Sensor Voltage (V)	Activation
28	5.87	0
40	7	0
45	7.8	1
56	8.95	1
67	9.66	1

Table 5-2 (cont'd)

78	10	1
84	10.08	1
90	10.25	1

Table 5-3: Sensor voltage for PZT3.

PZT3		
Strain ($\mu\epsilon$)	Sensor Voltage (V)	Activation
56	6.33	0
67	6.89	0
83	7.81	1
100	8.69	1
112	9.1	1
123	9.53	1
139	9.73	1
155	9.9	1
166	9.97	1
192	10.18	1

5.2.2. Analysis at low frequencies

Bridge vibration frequencies are usually lower than 1Hz. Therefore, the sensor is tested at low frequencies. Figures below show the results for 0.4 Hz and 0.5 Hz. The corresponding values are presented in Tables 5-4 and 5-5. As seen in Figure 5-4, the voltage slightly increases with increasing the input frequency. For both frequencies, the strain threshold to activate the first gate of the sensor is around $70 \mu\epsilon$.

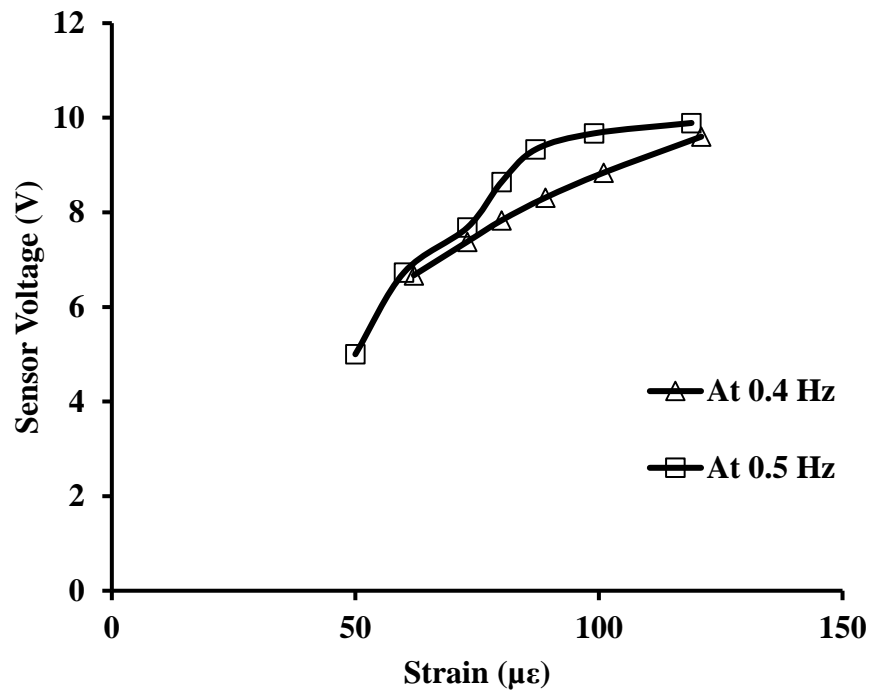


Figure 5-4: Sensor voltage vs strain for 0.4 and 0.5 Hz.

Table 5-4: Sensor voltage for PZT2 at 0.4 Hz.

Frequency = 0.4 Hz		
Strain ($\mu\epsilon$)	Sensor Voltage (V)	Activation
62	6.67	0
73	7.38	1
80	7.83	1
89	8.31	1
101	8.84	1
121	9.6	1

Table 5-5: Sensor voltage for PZT2 at 0.5 Hz.

Frequency = 0.5 Hz		
Strain ($\mu\epsilon$)	Sensor Voltage (V)	Activation
50	5	0
60	6.73	0
73	7.68	1
80	8.64	1
87	9.33	1
99	9.67	1
119	9.89	1

5.2.3. Analysis at low temperatures

The effect of low temperature on the transducer response is studied. It is known that piezoelectric materials are highly sensitive to temperature. After preliminary tests, it was found that the output sensor voltage dramatically decreases with decreasing the temperature. Therefore, a rubberized coating ‘Flex Seal’ is used to protect the piezo from harsh environmental conditions. This product can be also used to seal against water, air, moisture, and helps to prevent corrosion related damage. The same previously performed 4-point bending test in the precedent sections is also used to compare the output of the protected transducers, before and after the decreasing the temperature.

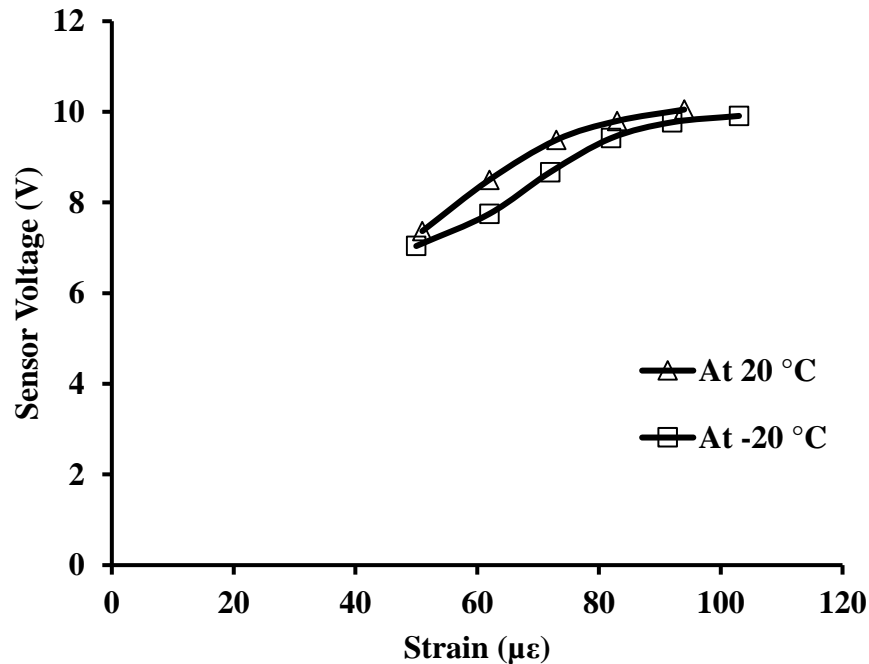


Figure 5-5: Sensor voltage vs strain at 20 °C and -20 °C.

Figure 5-5 and Tables 5-6 and 5-7 display the results at 0.5 Hz input frequency and at +20 °C

and -20 °C. The tests are performed for all used PZTs (PZT1, PZT2 and PZT3); however, only results pertaining to PZT2 are presented for reason of brevity.

Table 5-6: Sensor voltage for PZT2 at 20 °C.

Before cooling (20 °C)		
Strain ($\mu\epsilon$)	Sensor Voltage (V)	Activation
51	7.37	1
62	8.5	1
73	9.38	1
83	9.8	1
94	10.05	1

Table 5-7: Sensor voltage for PZT2 at -20 °C.

After cooling (-20 °C)		
Strain ($\mu\epsilon$)	Sensor Voltage (V)	Activation
50	7.04	0
62	7.75	1
72	8.67	1
82	9.42	1
92	9.77	1
103	9.91	1

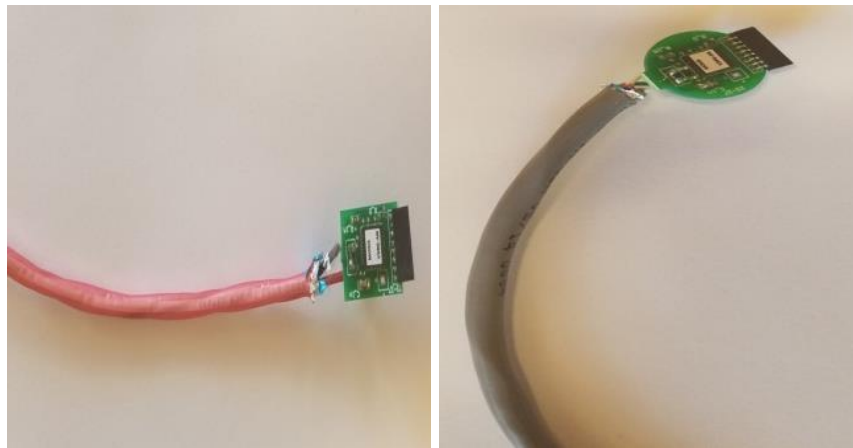
5.2.4. Wiring effect on the sensor response

In this section, the effect of the wires connecting the sensors to the transducers is studied. Two types of material are used to protect the sensor wires as shown in Figure 5-6. It should be noted that the wiring might affect the capacitance and the electrical resistance of the piezoelectric transducer. The shape of the sensor on Figures 5-6(a) and 5-6(b) is meant only to differentiate between the wires and not the sensors. Both wires are sourced from General Cable, manufacturer part numbers C8101.41.03 and C0744A.41.10, and have 100% shield coverage along the length of the cable. The wire in Figure 5-6(a) contains two 18 AWG stranded copper conductors with 0.0160" of Fluorinated Ethylene-Propylene jacket insulation rated for -40 °C to 150 °C, the nominal capacitance per foot between conductors is 51.0 pF and from conductor to shield is 95.0 pF. Figure 5-6(b) has eight conductors of 24 AWG stranded copper and 0.0320" of poly-vinyl chloride jacket insulation rated for -20 °C to 80 °C, with 30.0 pF capacitance between conductors and 55.0 to the shield. The red cable was originally chosen for its robust weather rating, and ability to isolate the connections to the sensors without worry of crosstalk. The higher capacitance of the thicker conductor could increase the required driving capabilities of the piezo and potentially reduce the sensor sensitivity to external stimuli. For this reason, the lower capacitance grey wire is also considered.

The tests are performed at low input frequencies and at room temperature. The number of cycles is incrementally increased to find the strain and voltage thresholds. Tables 5-8 to 5-9 show the testing results for PZTs 2 and 3. Results of PZT1 are not presented because they are almost same as PZT3.

According to the results, the strain and voltage threshold levels for both cabling types are very close for PZTs 2 and 3. The maximum obtained difference is 6 micro-strain and 0.18 V, which

means that both cables give similar outputs.



(a)

(b)

Figure 5-6: Sensor wiring, (a) 1st model, (b) 2nd model.

Table 5-8: Sensor voltage threshold vs strain threshold for sensor 1 (1st model).

Sensor 1, PZT2		
Channel	Strain Threshold ($\mu\epsilon$)	Voltage Threshold (V)
Ch1	43	7.71
Ch2	49	8.42
Ch3	51	8.81
Ch4	60	9.45
Ch5	65	9.74
Ch6	84	10.11
Ch7	123	10.45+

Table 5-8 (cont'd)

Sensor 1, PZT3		
Ch1	77	7.69
Ch2	85	8.2
Ch3	96	8.92
Ch4	102	9.21
Ch5	124	9.69
Ch6	152	10
Ch7	242	10.45

Table 5-9: Sensor voltage threshold vs strain threshold for sensor 2 (2nd model).

Sensor 2, PZT2		
Channel	Strain Threshold ($\mu\epsilon$)	Voltage Threshold (V)
Ch1	43	7.81
Ch2	48	8.56
Ch3	52	8.87
Ch4	56	9.39
Ch5	62	9.66
Ch6	79	10.06
Ch7	141	10.45+

Table 5-9 (cont'd)

Sensor 2, PZT3		
Ch1	74	7.64
Ch2	84	8.36
Ch3	90	8.74
Ch4	103	9.32
Ch5	120	9.69
Ch6	153	10.03
Ch7	267	10.45

5.3. Preliminary testing of the sensor: Mackinac Bridge

The Mackinac Bridge is the gateway to north connecting the upper and the lower peninsulas of Michigan, USA. This suspension Bridge is considered as one of the greatest engineering structures in the world. The total length of the structure is 26,372 ft (3,038 m), the width is 68.6 ft (20.9 m), and the maximum height, located at the central tower is 552 ft (168 m). Figure 5-7 displays an image of the Mackinac Bridge. The installation procedure is divided into two major steps. In the first step, a preliminary prototype is designed and installed in the bridge to study the effect of the environmental conditions on the sensor boxes and on the piezoelectric transducers. In addition, the results of this phase are also used to select the right dimensions of the piezoelectric transducers that will be used for the final sensing system. Figure 5-8 displays the PFG sensor board details, and Figure 5-9 shows the used preliminary sensors box. Each box contains 3 sensors connected to 3 transducers. Each of the sensor boards utilizes a Texas

Instruments (TI) CC1310 Radio Frequency (RF) microcontroller (MCU) as the main commercial off-the-shelf component to enable wireless communications (Aono et al., 2018). In addition to enabling wireless communication in the 915 MHz, Industrial, Scientific, and Medical radio band (ISM band), the MCU has firmware-programmable general-purpose input/output pins (GPIO) that are utilized for interfacing with the three sensors in each box (Aono et al., 2018). Commands are sent to the sensors by simply raising certain pins high (e.g. to cycle through the sensor's channels, a GPIO needs to give a rising edge to a pre-determined pin, there is no SPI or communication protocol implemented on this version of the sensor). By sending wireless commands encoded per TI specifications, the MCU will negotiate with the sensors to retrieve their data and reply with its own wireless packet containing all of the sensor data at that time instance, as well as the responding box ID. By leveraging the expertise of commercial vendors, we can achieve wireless communication with sensitivities below -110 dBm and average active current consumption of 12 mA; furthermore, the wireless technology can be swapped out as project requirements change. In this version, we opted for the 915 MHz RF MCU to enable long-range communications, estimates using data from TI suggest that a 10 dBm transmission power could yield a range of approximately 1 km using the low efficiency PCB antenna (Aono et al., 2018). Each sensor board also has a sleep timer that will force all components into an ultra-low power mode consuming less than 50 nA from the batteries. This sleep timer is implemented with a TI TPL5111 that has been hardwired to go to sleep for five minutes (300 s) before waking up the MCU and related subsystems (Aono et al., 2018). Upon wakeup, there will be up to six seconds spent to search for nearby wireless nodes (225 μ A average current), if there is no pending command the system will go back to sleep (Aono et al., 2018). Otherwise the MCU will collect the sensor data and reply in less than 15 seconds with average current consumption

around 2.5 mA (Aono et al., 2018).

$$\text{Average Current (Command)} = \frac{I_{on}t_{on} + I_{search}t_{search} + I_{off}t_{off}}{t_{on} + t_{search} + t_{off}} = \frac{2.5m \cdot 13.5 + 225\mu \cdot 6 + 50n \cdot 300}{10 + 6 + 300} < 110\mu A \quad (5-2)$$

$$\text{Average Current (No Command)} = \frac{I_{search}t_{search} + I_{off}t_{off}}{t_{search} + t_{off}} = \frac{225\mu \cdot 6 + 50n \cdot 300}{6 + 300} < 5\mu A \quad (5-3)$$

Assuming commands are sent only 1% of the time (this is in the range of two or three per day), a first-order estimate that includes an 85% derating factor, but that neglects battery self-discharge, temperature degradation, etc., will show that a single ½ AA Lithium-Thionyl Chloride (Li-SOCI2) battery with 900 mAh would last (Aono et al., 2018):

$$\text{Battery Life} = 900 \frac{\text{mAh}}{0.99 \cdot 5\mu + 0.01 \cdot 110\mu} \cdot 0.85 \cdot \left(\frac{1 \text{ year}}{8760 \text{ hour}} \right) \approx 20 \text{ years} \quad (5-4)$$

The failure mode for this preliminary test deployment was in the attempt to pass three wires through a single cable gland, this created a small void in the weatherproof seal that did not present itself during short-term laboratory submersion tests. After being exposed to the elements for months, enough moisture worked its way through the opening to wreak havoc on the internals of the box. The PCB had weatherproofing protection independent of the box in the form of a conformal coating of silicone on all conductive surfaces. Figure 5-9 demonstrates that there was little direct impact to the PCB top surface. The majority of the damage came from the moisture pooling on the bottom of the box and causing a short between the batteries that were mounted under the PCB. This ultimately caused the batteries to fail and leak the brown/orange substance in the figure.



Figure 5-7: Photo of the Mackinac Bridge (Mackinac Bridge Authority, 2018).

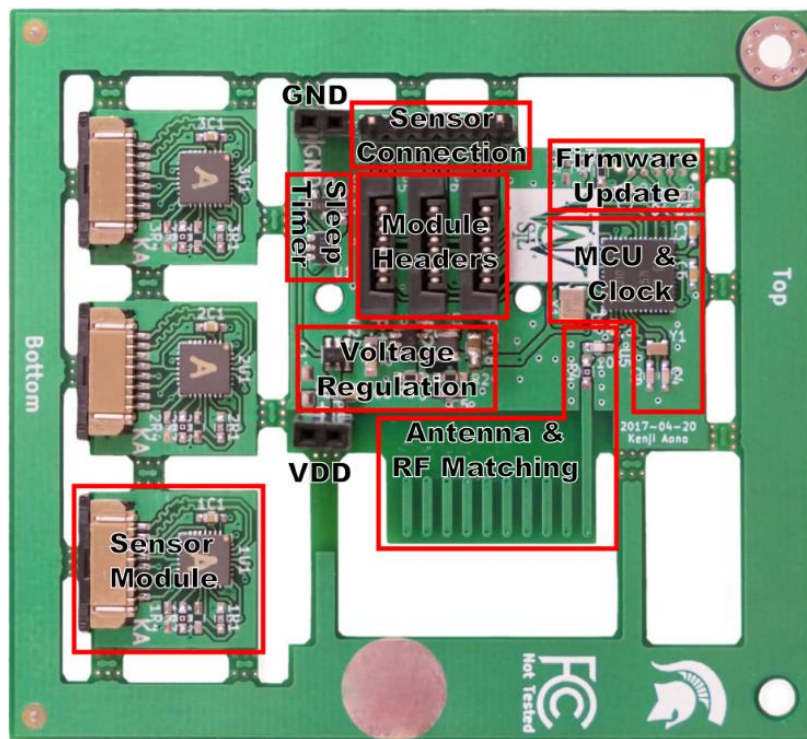


Figure 5-8: PFG board (Aono et al., 2018).

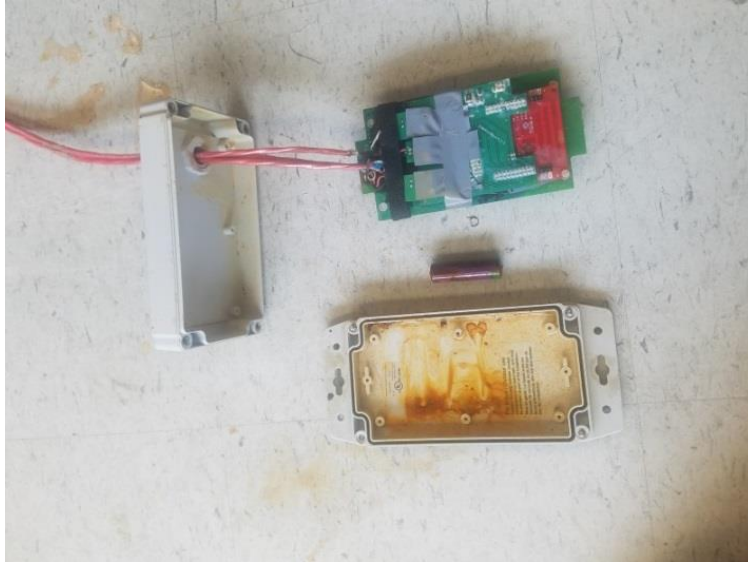
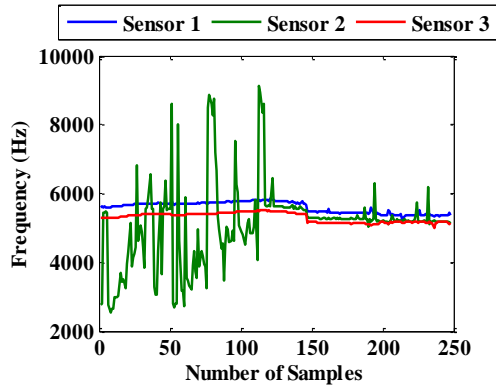


Figure 5-9: Preliminary sensor box.

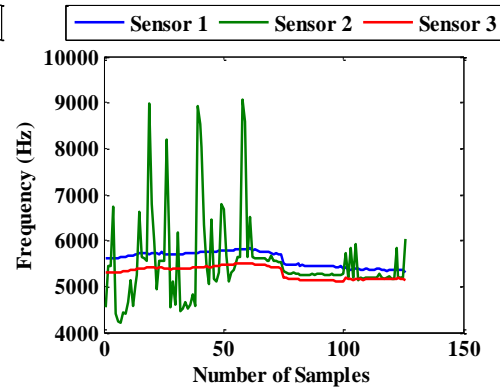
In order to extract the data from the installed boxes, a TI Launchpad from commercial retail is used. The launchpad uses the same 915 MHz ISM band RF for communication. The reader is connected to a computer through a USB cable to send signals to the box. The firmware on the reader will continuously sample all sensors in a round robin fashion and log any responses to a database. Although there is a five-minute latency designed into the sensor boxes for purposes of extending battery life, the actual data transmission takes on the order of tens of milliseconds and is capable of being done from a moving vehicle (verified at Mackinac Bridge speed limit of 45 mph or 72 km/h).

Figures 5-10 and 5-11 display the output results of the sensors for November (installation time) and September readings. Table 5-10 presents the average readings for each channel, and Figure 5-12 shows the variation of the sensors output over time. In Figure 5-12, the averaged readings of each channel are plotted against the reading period.

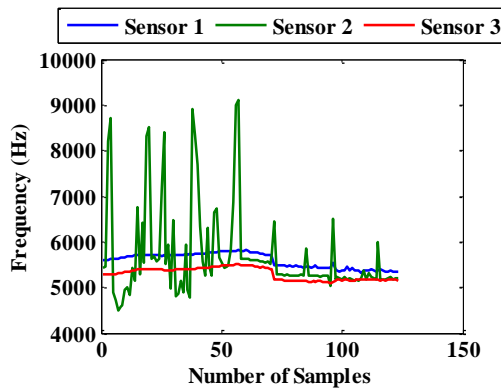
A Gaussian mixture model is used to fit the sensor data. Figure 5-13 presents the results of the GMM fitting to the sensor data.



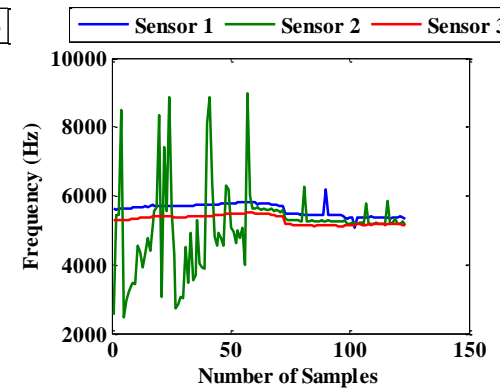
(a) Ch1



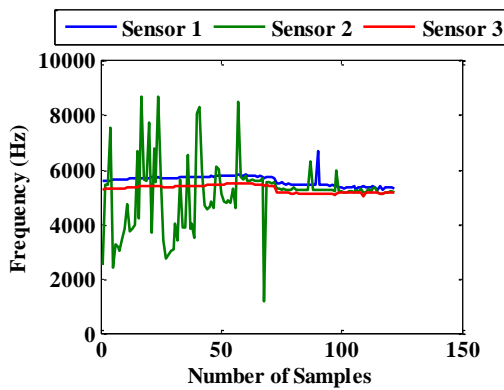
(b) Ch2



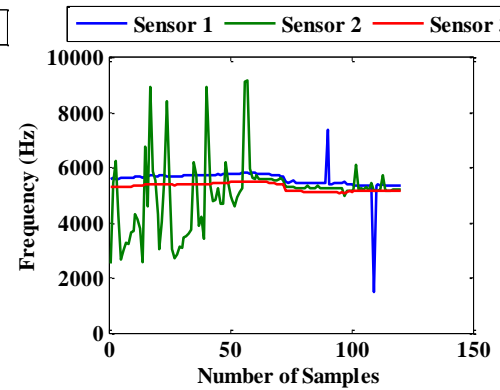
(c) Ch3



(d) Ch4



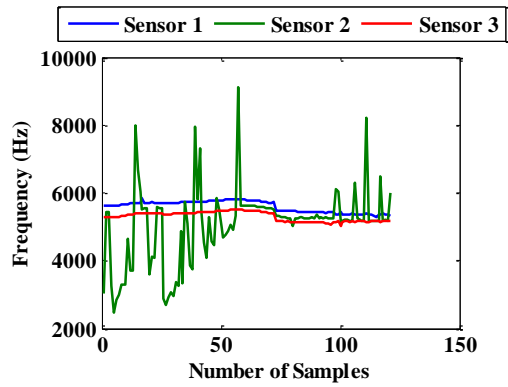
(e) Ch5



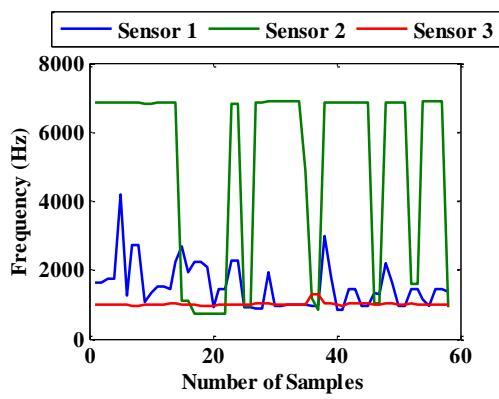
(f) Ch6

Figure 5-10: September Readings.

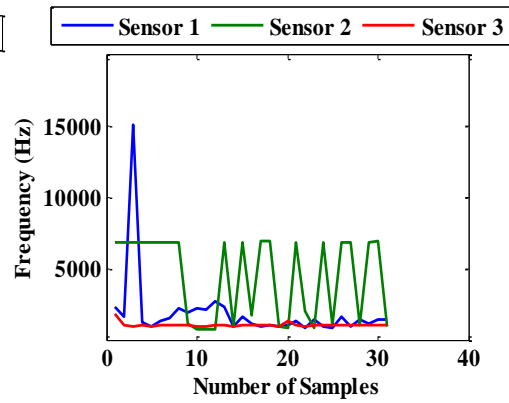
Figure 5-10 (cont'd)



(g) Ch7



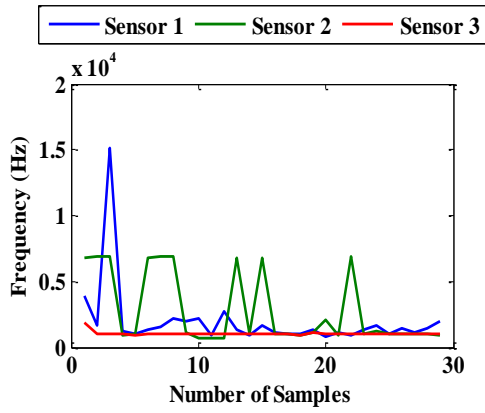
(a) Ch1



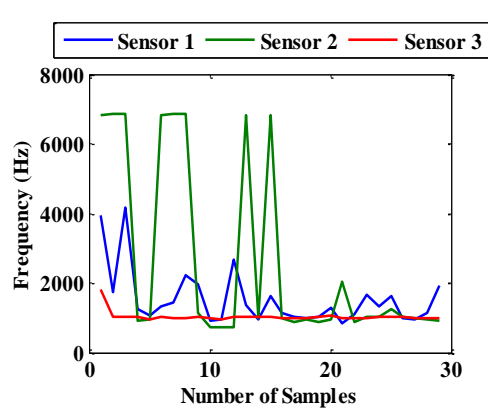
(b) Ch2

Figure 5-11: November Readings.

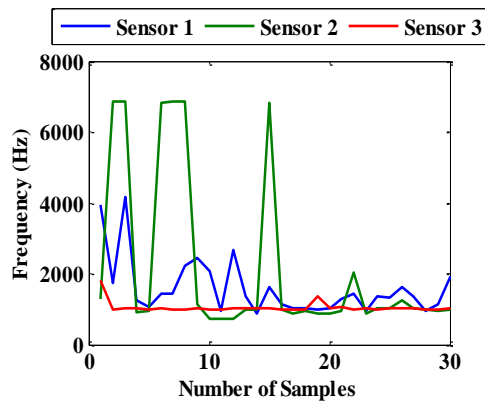
Figure 5-11 (cont'd)



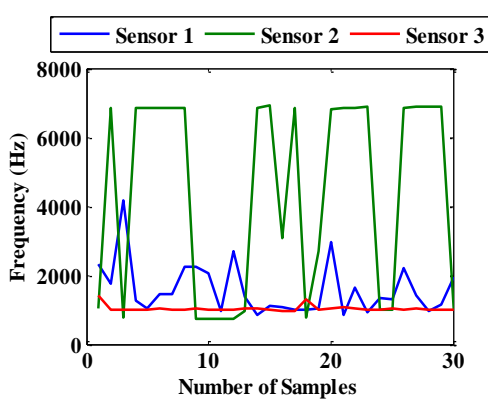
(c) Ch3



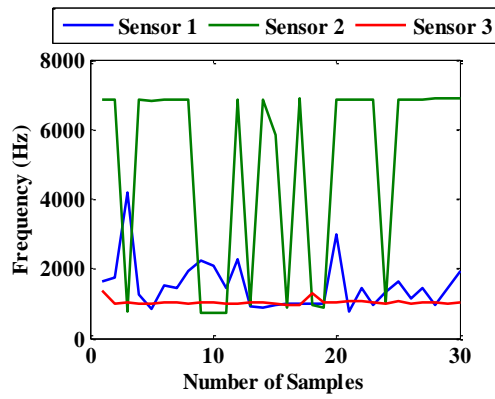
(d) Ch4



(e) Ch5



(f) Ch6

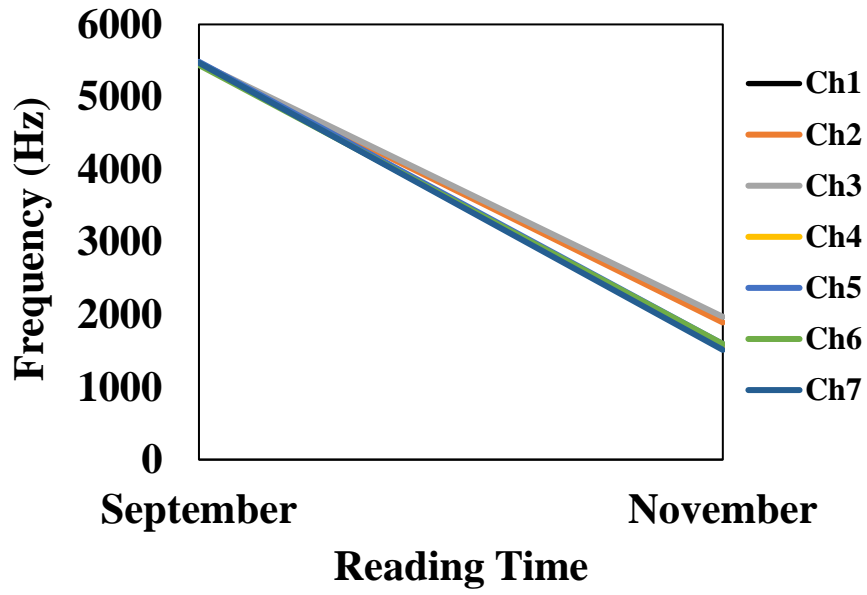


(g) Ch7

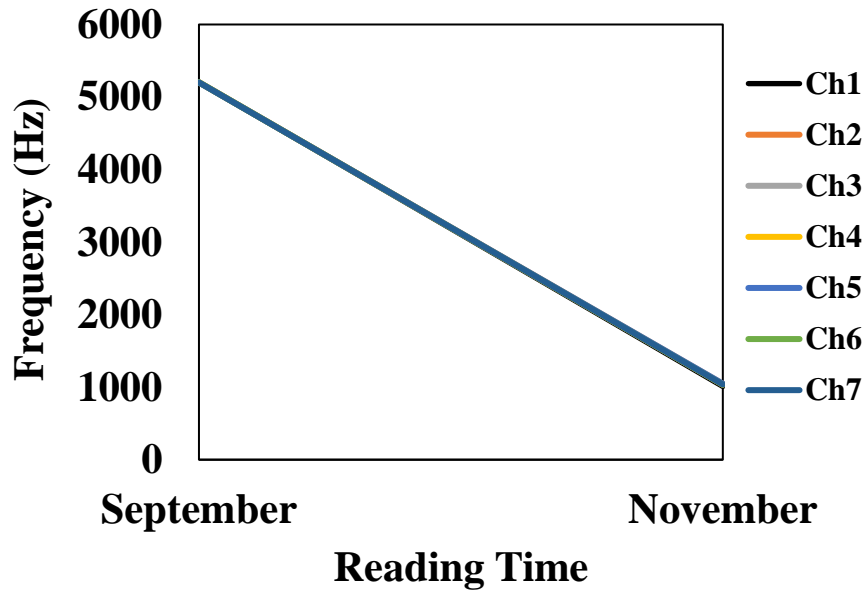
As seen from the figures, the sensors outputs are fitted to a bi-modal Gaussian model that has four parameters representing the means and the standard deviations of the distribution components. According to chapters 3 and 4, these parameters will be used to assess the health status of the bridge over time.

Table 5-10: Average readings values.

	September			November		
	Sensor 1	Sensor 2	Sensor 3	Sensor 1	Sensor 2	Sensor 3
Ch1	5472.511	5315.14	5200.709	1528.788	-	1009.389
Ch2	5465.402	5342.908	5202.56	1890.772	-	1045.498
Ch3	5471.044	5351	5204.524	1968.606	-	1033.826
Ch4	5476.541	5334.718	5203.892	1539.786	-	1034.031
Ch5	5484.831	5258.539	5200.626	1593.481	-	1048.181
Ch6	5440.522	5324.939	5202.664	1594.032	-	1034.053
Ch7	5470.905	5422.212	5201.321	1513.435	-	1036.512



(a)



(b)

Figure 5-12: Readings of: (a) Sensors 1, (b) Sensor 3.

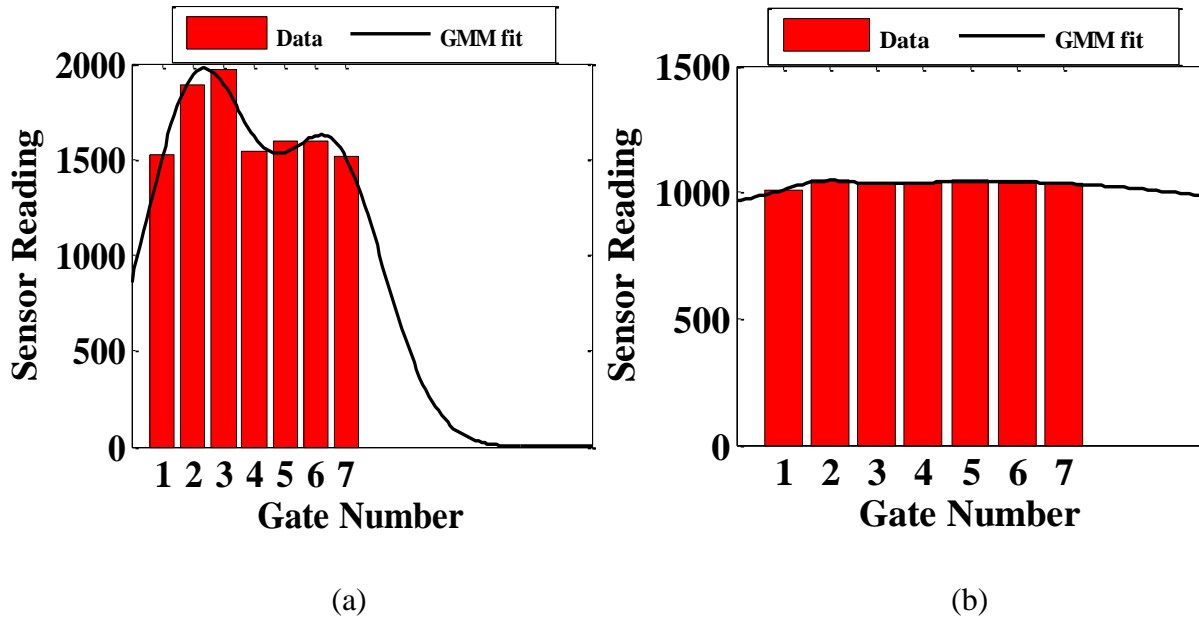


Figure 5-13: GMM fit to: (a) Sensor 1, (b) Sensor 3 data.

5.4. Final sensing system deployed in the Mackinac Bridge

Taking into account the lessons learned from the preliminary deployment, a new box is developed, as shown in Figure 5-14. To combat the issue of moisture, a single cable with six conductors (General Cables, C3029.41.86 with 24 AWG conductors, a fluoropolymer jacket rated for -40°C to 150°C , 13.0 pF per foot between conductors and 23.0 pF to the shield.) is passed through a smaller cable gland. The battery connection is also moved off the floor of the box via a socket, and all components and connections have received a layer of conformal coating. The weatherproofing of this box is confirmed in one-week submersion test in the lab, with occasional agitation to the setup.

Beyond the mechanical changes for improving the weatherproofing, the major changes include the addition of the sleep timer, a more power efficient power converter between the batteries and MCU, and an embedded PCB antenna to reduce cost and save size.

Four sensing boxes are installed in different locations. Figure 5-15 shows a picture of the

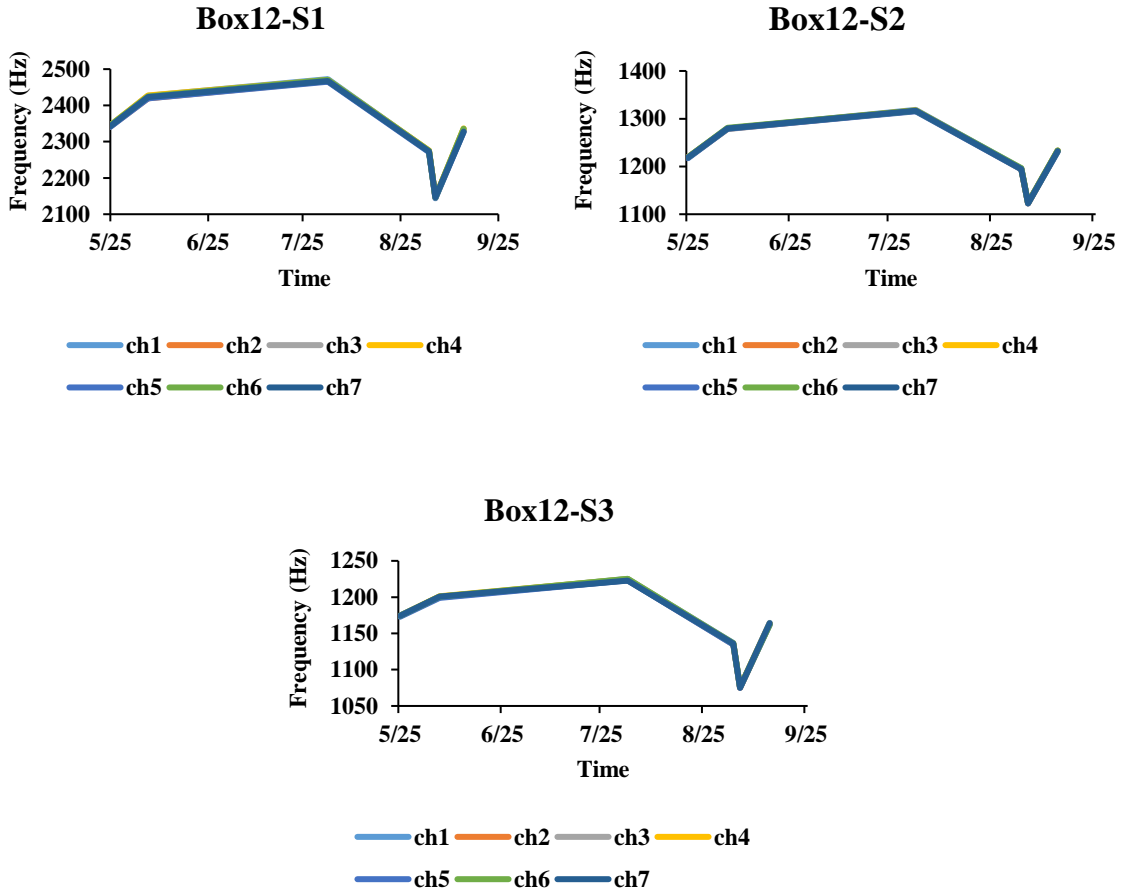
installation. Some of the sensors are placed near the damage sensitive areas to detect possible cracking events. The same procedure of the previously installed boxes is followed to install the new boxes. After gluing the strain transducers to the structure and connecting each piezo to the corresponding box, the data is read, and the initial values of each gate are recorded. Thereafter, five readings are effectuated as follows: June 6, Aug 2, Sep 3 (1 day before the Labor Day walk), Sep 5 (The day after the Labor Day walk), and Sep 14.



Figure 5-14: New box.



Figure 5-15: Sensor installation.



(a) Box 12

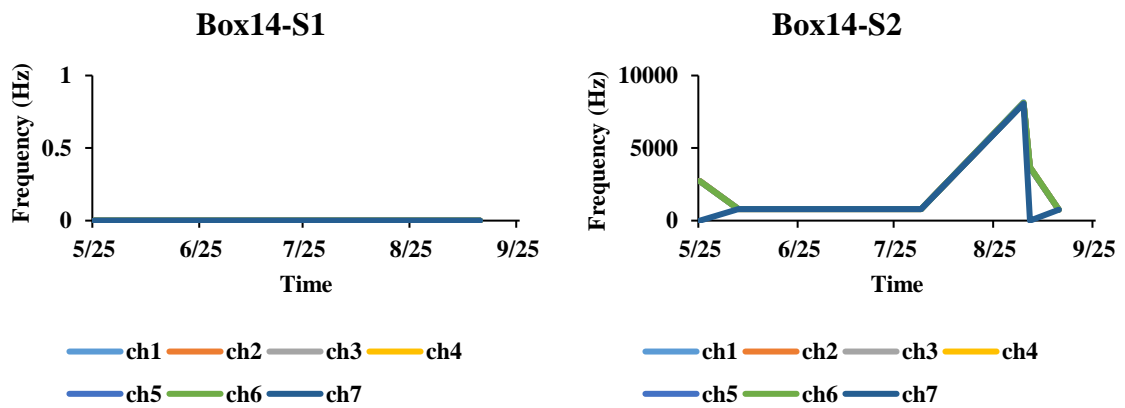
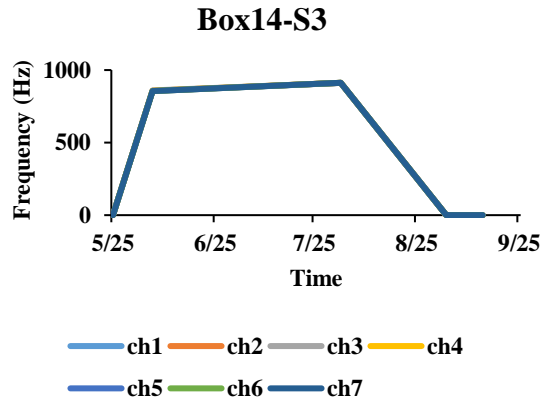
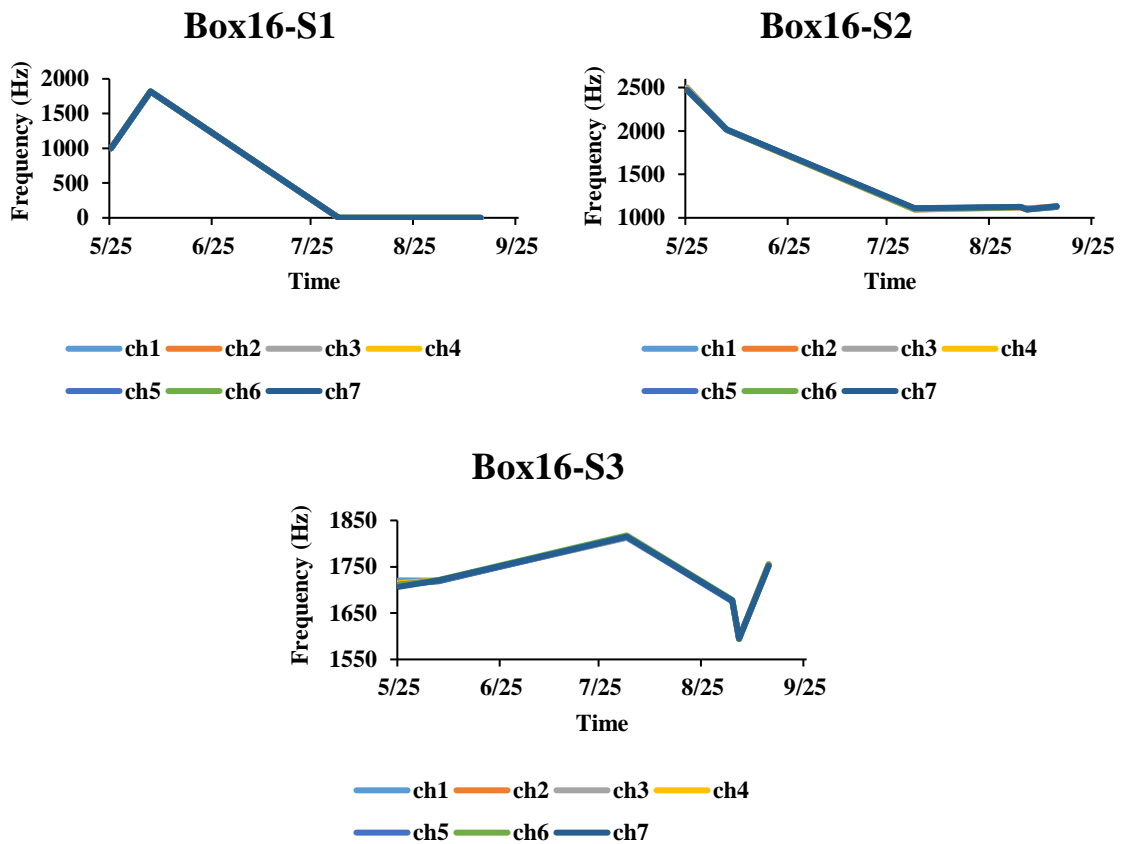


Figure 5-16: Readings.

Figure 5-16 (cont'd)

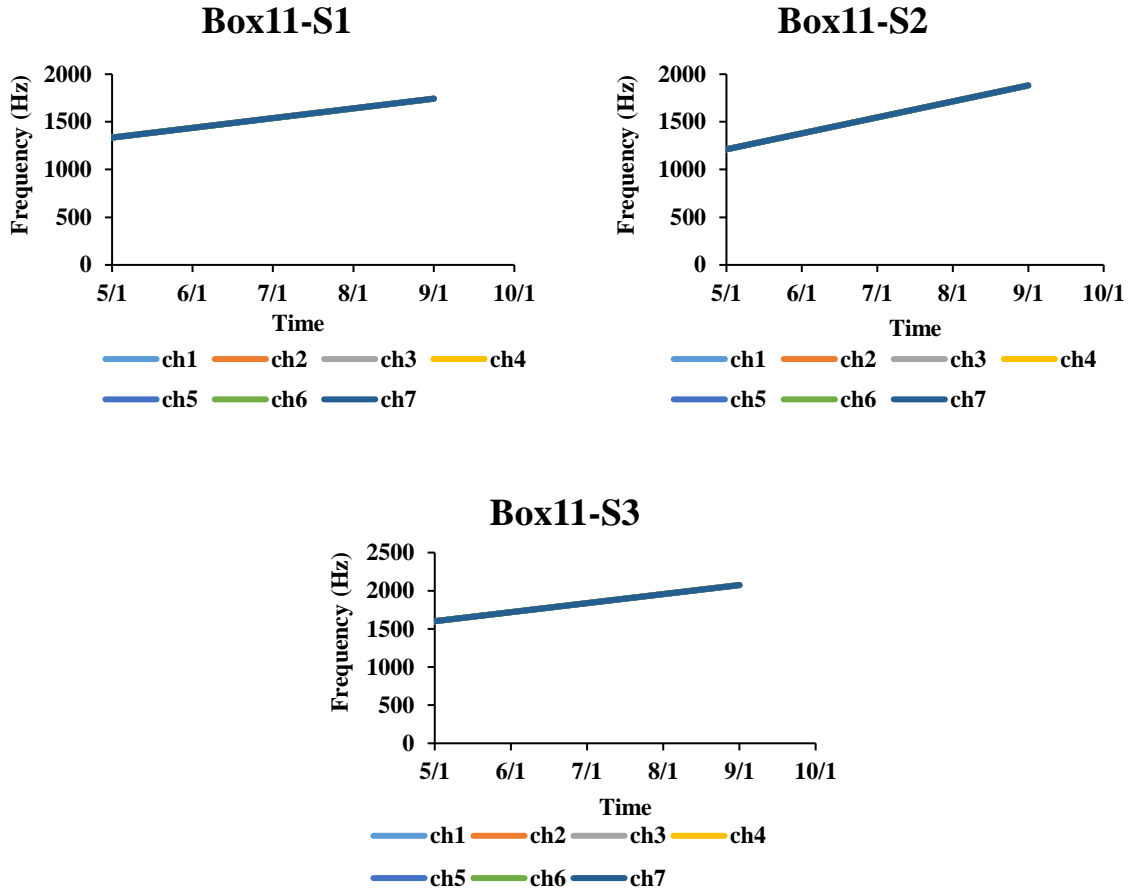


(b) Box 14 (no sensor installed in S1 slot)



(c) Box 16

Figure 5-16 (cont'd)



(d) Box 11

The sensors utilized in this system have a limitation in their robustness against temperature since a simple PTAT current generates the biases for the internal analog-to-digital converter (ADC) that translates the stored charge on the floating-gates into a form that the MCU can understand (Ueno, 2010). So long as this limitation is characterized, the effects can be calibrated out of the readings (as we have done in Figure 5-16). The temperature characteristics of the ADC are measured in a thermal chamber and are presented in Figure 5-17. When collecting the data from the wireless sensor systems, the ambient temperature at the Mackinac Bridge were also recorded and used in conjunction with the calibration curve of Figure 5-17 to normalize all outputs to their

equivalent frequency at 20 °C. In interpreting the data presented, it is also imperative to note that the ADC output is not monotonic, rather it follows a distribution demonstrated in Figure 5-18. In the initialized state, the buffered output voltage from the floating gate is near the supply rail at 1.8 V and subsequently has a low frequency output. As excitations get cumulatively logged onto the sensor, the negative charge buildup on the floating gate will cause a drop in buffered voltage. This drop in the voltage is reflected by an increase in frequency output from the ADC. This is the primary range of operation for our sensor, and the output duty cycle is approximately 3%, until the voltages begin to creep below the saturation region of the CMOS transistors, there is then an inversion in the trajectory of frequency. That is, as more excitations are logged, the frequency no longer increases, but will begin to decrease. We can still discern the floating gate voltage since the duty cycle of the ADC output indicates whether it is operating below the saturation region or not. After the inversion, further charge buildup will increase the duty cycle until it saturates at 100% near 0 V.

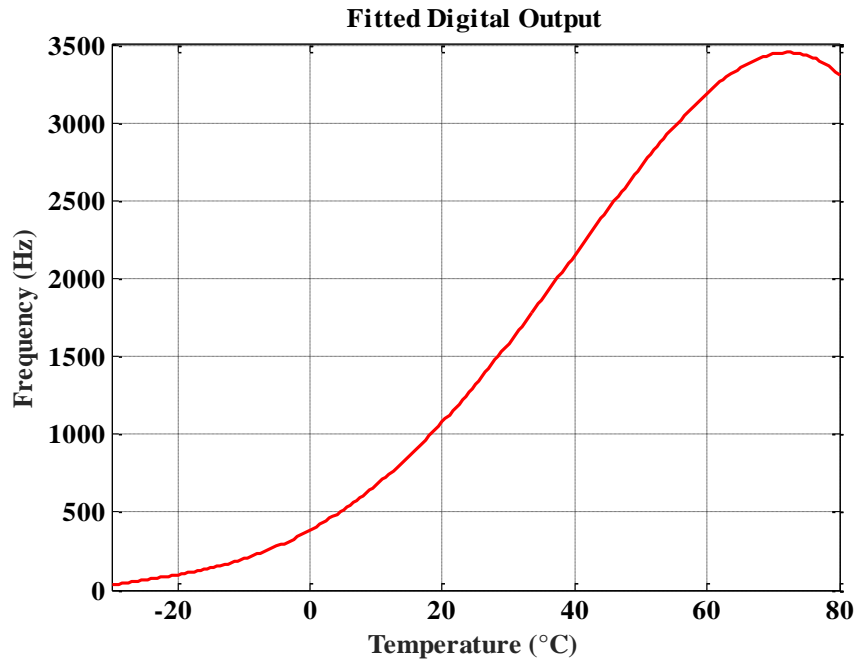


Figure 5-17: Analog-to-digital converter output as a function of temperature (nominally ~1 kHz at 20 °C) (Aono et al., 2018).

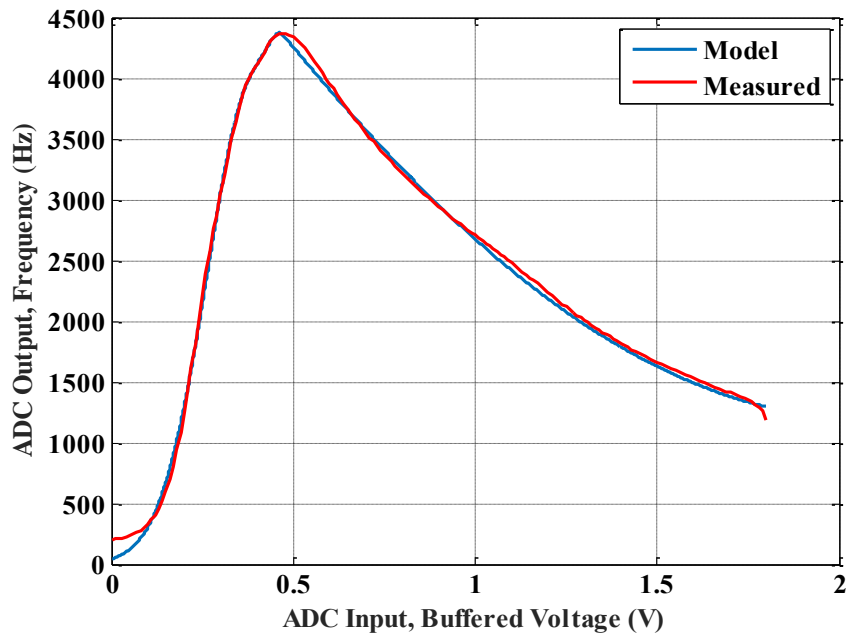


Figure 5-18: Results showing ADC output as function of voltage (i.e. floating gate charge) (Aono et al., 2018).

5.5. Summary

This chapter presented a deployment study of the PFG sensor in real-life structure. The sensing system incorporated piezoelectric harvesters, sensors unit, and a wireless reader for the communication of the data to a central computer. The network of sensors was deployed in the Mackinac Bridge in Michigan. The results showed the ability of the system in capturing data and transmit it via wireless communication device. The effect of temperature was also studied, and the measurement validated the expected trends from the sensor. Detection and logging of a major event (the Labor Day walk) that stressed the bridge was demonstrated using the proposed system.

CHAPTER 6. CONCLUSIONS

6.1. Research contributions

The research presented in this dissertation has led to the development of a robust damage quantification approach in civil infrastructures using an ultra-low power sensing technology.

In this work, the performances of the uniform and nonuniform sensors were evaluated on several structures. Identification of damage on steel and pavement structures were studied. The analysis was based on the integration of finite element methods and artificial intelligence approaches. New damage indicators were proposed for both type of sensors. In addition, an innovative surface sensing approach for detection of bottom-up cracking in pavements was developed. Data fusion models were proposed to increase the damage detection capabilities of sensors especially for multi-stage damage growth. The results show that the damage could be detected, localized, and quantified using the developed data interpretation system in this research. More, this research proposed a novel local-global damage detection system using a hybrid network of heterogeneous PFG sensors (strain and acceleration sensors).

The most important contribution of this work is that the technology was deployed in real life structure. A calibration process was performed, and a network of sensors were installed in the Mackinac Bridge in Michigan. On the other hand, this work has led to the development of a damage sensing mechanism that can be deployed in the next generation of smart cities.

6.2. Conducted work

The presented work is established through the integration of FE, AI, and statistical approaches to interpret the sensor data and identify damage in civil infrastructures. The

performance of the proposed models was investigated experimentally, numerically, and theoretically. Two types of sensors were investigated: uniform and nonuniform PFG sensors. Different damage characterization strategies were proposed for each type. For the first class of sensors, a gusset plate similar to the U10W plate of the I-35W Bridge, Minneapolis, MN, USA, was studied. An FE model that incorporated the geometrical complexities was developed to obtain the response of the plate under loading. Using the damage predictors, μ and σ , damage localization and quantification algorithms were proposed. For the second case study, a fatigue analysis of a steel bridge girder was studied. In this case, a network of strain sensors was placed around the connection stiffener to web to detect crack propagation caused by the out-of-plane displacement at the connection. The damage detection process was divided into three phases: First, the data was collected from the FE simulations, and features were extracted to define individual damage indicators (PDF parameters μ and σ). Thereafter, a data fusion model was defined based on the previously extracted features and the ‘sensors group effect’ concept. Finally, the new features were inputted to SVM classifiers to identify damage states.

The following conclusions can be inferred from the studied cases:

- The mean μ and the standard deviation σ of the distributions are good indicators of damage occurrence in the structure.
- The PDF parameters for sensors located around the damage zone are more sensitive to crack propagation.
- PDFs shift to the left and they expand with damage evolution for sensors located near the stress concentration zone generated by the crack.
- In general, for structures with high geometrical and loading complexities, the initial damage indicators (μ and σ) do not have a sound relationship with damage progression in structures.

- For the studied gusset plate, the STD of μ and σ of a group of sensors increases with damage progression. Moreover, this function gives an idea about the damage severity.
- Cracks in gusset plates could be localized using the proposed algorithm.
- A new equation is proposed to predict the crack length based on the data provided by the sensors. The results indicated that the proposed equation is accurate in predicting different crack lengths in gusset plates.
- The proposed sensor fusion model for the bridge case has increased the damage detection accuracy by improving the individual sensor resolution using the concept of ‘group effect of sensors’.
- SVM models can accurately classify most of the damage stages for steel bridge girders, specifically for cracks larger than 10 mm.
- Tracking the performance of the SVM models gives an insight into the damage location.

For the case of nonuniform PFG sensors, three structures were studied: Steel plate, AC beam, and an AC pavement. The data of nonuniform sensor is fully controlled by the injection rates. Therefore, a new data interpretation system was developed for this class of sensors. For the plate, piezoelectric transducers were mounted on the specimen for both empowering the sensor and monitoring the damage progression. The changes of charge on the floating-gates of the sensor due to electron injection were considered as initial damage indicator parameters. Data fusion model and an SVM classification scheme were developed to classify the predefined damage states. Moreover, an uncertainty analysis was performed to through the contamination of the initial input data with different noise levels.

For the AC beam, different 3D FE models were developed using ABAQUS to generate the sensor output data for different damage states. Thereafter, laboratory tests were carried out to

validate the performance of the proposed damage detection approach. PVDF piezoelectric film was used to harvest the strain energy from the host structure and empower the sensor. In order to protect the embedded sensor, an H-shape packaging system was designed and tested.

For the third case study, a new surface sensing approach was developed to detect bottom-up cracking in pavements. The following conclusions can be inferred from the studied cases:

- Structural damage can be monitored through the monitoring of the activation and voltage droppage of the floating-gates of only few sensors at specific locations.
- The data fusion model with SVM provides acceptable detection performance over the structural area. The best results were obtained using featured data from 3 to 7 floating-gates.
- The detection rate accuracy of crack growth in steel plates remains satisfactory under high noise level.
- The percentage of voltage/strain droppage can be considered as good predictor of damage progression, and the gate number and activation are good indicators of damage severity.
- The bi-modal GM parameters are good damage indicators.
- The proposed optimal set of predictors provided satisfactory detection rate accuracy (100% on the training data, 96.6% on the validation data and 93.1% on the testing data).

The presented local-global damage detection system in steel frames was based on the interpretation of the data of the strain and acceleration sensors. The damage identification mechanism was composed by a hybrid network of vibration- and strain-based sensors. The following conclusion could be inferred:

- The standard deviation of μ_1 , σ_1^2 , and σ_2^2 of a group of sensors is a good predictor of bolt loosening/removing.

- The damage could be localized based on the sign of the STD curves.
- Crack in steel frames could be monitored through the STD of μ_1 and μ_2 .

In Chapter 5, a network of PFG sensors was prepared for field testing. A series of experimental tests were performed to obtain the gates threshold levels for different piezoelectric transducers. The effect of temperature on the harvester response was studied. Finally, the prototype was deployed in the Mackinac Bridge in Michigan for testing. The following conclusions could be deduced:

- Rubber coating helps in protecting the piezoelectric transducers from harsh environmental conditions.
- The self-powered sensing mechanism is able to operate under low/high temperature conditions and the outputted data is robust.
- The PFG-based sensing system is able to capture data and transmit it wirelessly.

6.3. Future research

Although the work presented in this thesis provided a robust damage progression quantification in civil infrastructures, there are still some challenges to be investigated in future research:

- More comprehensive approach may need to be further developed for optimal sensor placement (OSP) using robust optimization algorithms.
- Corrosion related damage should be investigated in depth in future study.
- Future research may also focus on detecting damage for the case where the target classes are unknown. To this aim, unsupervised learning algorithms such as self-organizing map (SOM) seem to be the most efficient tool.

- Verification of the hybrid network of sensors in identifying local-global damage in real-life structure.
- Development of a FEMU system using the sensor data to identify damage in large scale structures and to develop a reliable data base for training AI models.

APPENDIX

Appendix A

Table A-1: Prony series coefficients.

\bar{g}_i	\bar{k}_i	τ_i
6.6622E-05	6.6622E-05	1.00E-13
0.00012834	0.00012834	6.49E-13
0.00024903	0.00024903	4.22E-12
0.00048324	0.00048324	2.74E-11
0.00093704	0.00093704	1.78E-10
0.00181707	0.00181707	1.15E-09
0.00351793	0.00351793	7.50E-09
0.00680272	0.00680272	4.87E-08
0.01309445	0.01309445	3.16E-07
0.02504117	0.02504117	2.05E-06
0.04711772	0.04711772	1.33E-05
0.08602016	0.08602016	8.66E-05
0.14652054	0.14652054	0.000562
0.21559013	0.21559013	0.003652
0.23267158	0.23267158	0.023714
0.1499758	0.1499758	0.153993
0.0529047	0.0529047	1
0.01273171	0.01273171	6.493816
0.00289254	0.00289254	42.16965
0.00077742	0.00077742	273.842
0.00025633	0.00025633	1778.279
0.0001018	0.0001018	11547.82
4.4828E-05	4.4828E-05	74989.42
2.1436E-05	2.1436E-05	486967.5
1.0515E-05	1.0515E-05	3162278
5.3281E-06	5.3281E-06	20535250
2.6994E-06	2.6994E-06	1.33E+08
1.3899E-06	1.3899E-06	8.66E+08
7.0905E-07	7.0905E-07	5.62E+09
3.7066E-07	3.7066E-07	3.65E+10
1.8002E-07	1.8002E-07	2.37E+11
1.1627E-07	1.1627E-07	1.54E+12
2.2759E-08	2.2759E-08	1E+13

Table A-2: Piezoelectric properties.

Property	Unit	Symbol	Value
Electromechanical		Kp	0.58
Coupling	----	Kt	0.45
Coefficient		K31	0.34
Frequency		Np	2200
Constant	Hz-m	Nt	2070
		N31	1680
Piezoelectric	$\times 10^{-12}$ m/v	d33	320
Constant		d31	-140
	$\times 10^{-3}$ Vm/N	g33	25
		g31	-11.0
Elastic		Y33	7.3
Constant	$\times 10^{10}$ N/m ²	Y11	8.6
Mechanical			
Quality Factor	-----	Qm	1800
Dielectric	@1KHz	eT33/e 0	1400
Constant			
Dissipation Factor	% @1KHz	tan δ	0.4
Curie	°C	Tc	320
Temperature			
Density	g/cm ³	r	7.9

BIBLIOGRAPHY

BIBLIOGRAPHY

- ABAQUS. (2010). ABAQUS/CAE User's Manual, Version 6.10, Dassault Systèmes.
- Adeli, H., & Panakkat, A. (2009). A probabilistic neural network for earthquake magnitude prediction. *Neural networks*, 22(7), 1018-1024.
- Aha, D. W., & Bankert, R. L. (1996). A comparative evaluation of sequential feature selection algorithms. In *Learning from Data* (pp. 199-206). Springer New York.
- Ahmadi, M., Naderpour, H., & Kheyroddin, A. (2014). Utilization of artificial neural networks to prediction of the capacity of CCFT short columns subject to short term axial load. *Archives of Civil and Mechanical Engineering*, 14(3), 510-517.
- Alavi, A. H., Hasni, H., Lajnef, N., & Chatti, K. (2016c). Continuous health monitoring of pavement systems using smart sensing technology. *Construction and Building Materials*, 114, 719-736.
- Alavi, A. H., Hasni, H., Lajnef, N., & Chatti, K. (2016d). Damage growth detection in steel plates: Numerical and experimental studies. *Engineering Structures*, 128, 124-138.
- Alavi, A. H., Hasni, H., Lajnef, N., Chatti, K., & Faridazar, F. (2016a). An intelligent structural damage detection approach based on self-powered wireless sensor data. *Automation in Construction*, 62, 24-44.
- Alavi, A. H., Hasni, H., Lajnef, N., Chatti, K., & Faridazar, F. (2016b). Damage detection using self-powered wireless sensor data: an evolutionary approach. *Measurement*, 82, 254-283.
- Alippi, C., & Galperti, C. (2008). An adaptive system for optimal solar energy harvesting in wireless sensor network nodes. *IEEE Transactions on Circuits and Systems I: Regular Papers*, 55(6), 1742-1750.
- Alkasawneh, W., Pan, E., & Green, R. (2008). The effect of loading configuration and footprint geometry on flexible pavement response based on linear elastic theory. *Road materials and pavement design*, 9(2), 159-179.
- Al-Qadi, I. L., & Wang, H. (2009). Pavement damage due to different tire and loading configurations on secondary roads (No. NEXTRANS Project No. 008IY01). NEXTRANS.
- Al-Qadi, I., Wang, H., & Tutumluer, E. (2010). Dynamic analysis of thin asphalt pavements by using cross-anisotropic stress-dependent properties for granular layer. *Transportation Research Record: Journal of the Transportation Research Board*, (2154), 156-163.
- Aono, K., Hasni, H., Pochettino, O., Lajnef, N., & Chakrabarty, S. (2018). Quasi-self-powered Infrastructural Internet of Things: The Mackinac Bridge Case Study. In *GLSVLSI '18: 2018 Great Lakes Symposium on VLSI*, May 23–25, 2018, Chicago, IL, USA. ACM, New York,

NY, USA, 6 pages. <https://doi.org/10.1145/3194554.3194622>.

- Azamathulla, H. M. (2012). Gene expression programming for prediction of scour depth downstream of sills. *Journal of Hydrology*, 460, 156-159.
- Azamathulla, H. M., Guven, A., & Demir, Y. K. (2011). Linear genetic programming to scour below submerged pipeline. *Ocean Engineering*, 38(8), 995-1000.
- Badr, A., & Karlaftis, A. G. (2012). Duration model estimation for pavement rehabilitation and service life. *Advances and Applications in Statistics*, 31(1).
- Badr, A., & Karlaftis, A. G. (2013). Using the asphalt pavement dynamic stiffness modulus in assessing falling weight deflectometer test results. In *Advanced Materials Research* (Vol. 685, pp. 233-239). Trans Tech Publications.
- Bagherifaez, M., Behnia, A., Majeed, A. A., & Hwa Kian, C. (2014). Acoustic emission monitoring of multicell reinforced concrete box girders subjected to torsion. *The Scientific World Journal*, 2014.
- Bathe, K. J. (1996). *Finite element procedures*, Englewood Cliffs, NJ: Prentice Hall.
- Behnia, A., Chai, H. K., Yorikawa, M., Momoki, S., Terazawa, M., & Shiotani, T. (2014). Integrated non-destructive assessment of concrete structures under flexure by acoustic emission and travel time tomography. *Construction and Building Materials*, 67, 202-215.
- Borchani, W., Aono, K., Lajnef, N., & Chakrabartty, S. (2016). Monitoring of Postoperative Bone Healing Using Smart Trauma-Fixation Device With Integrated Self-Powered Piezo-Floating-Gate Sensors. *IEEE Transactions on Biomedical Engineering*, 63(7), 1463-1472.
- Burges, C. J. (1998). A tutorial on support vector machines for pattern recognition. *Data mining and knowledge discovery*, 2(2), 121-167.
- Chakrabartty, S., Feng, T., & Aono, K. (2013, April). Gen-2 RFID compatible, zero down-time, programmable mechanical strain-monitors and mechanical impact detectors. In *SPIE Smart Structures and Materials+ Nondestructive Evaluation and Health Monitoring* (pp. 86921A-86921A). International Society for Optics and Photonics.
- Chakrabartty, S., Lajnef, N., Elvin, N., Elvin, A., & Gore, A. (2011). Self-powered sensor, US Patent Number: US 8,056,420 B2.
- Chang, P. C., Flatau, A., & Liu, S. C. (2003). Review paper: health monitoring of civil infrastructure. *Structural health monitoring*, 2(3), 257-267.
- Chassiakos, A. G., & Caughey, T. K. (1993). Identification of nonlinear dynamic systems using neural networks. *Journal of Applied Mechanics*, 60, 123.
- Chen, A., Davalos, J. F., Jiao, P., & McGraw, B. (2012). Buckling behavior of sinusoidal web for composite wood I-Joist with elastically restrained loaded edges under

- compression. *Journal of Engineering Mechanics*, 139(8), 1065-1072.
- Chen, S., Dong, X., Kim, J. Y., Wu, S., & Wang, Y. (2016). Design and performance validation of a compact wireless ultrasonic device for localized damage detection. *Advances in Structural Engineering*, 19(2), 270-282.
- Cho, S., Giles, R. K., & Spencer, B. F. (2015). System identification of a historic swing truss bridge using a wireless sensor network employing orientation correction. *Structural Control and Health Monitoring*, 22(2), 255-272.
- Chopra, A. K. (2001). *Dynamics of Structures*, 2nd ed., Prentice Hall, Upper Saddle River, NJ.
- Das, S. K., Samui, P., & Sabat, A. K. (2011). Application of artificial intelligence to maximum dry density and unconfined compressive strength of cement stabilized soil. *Geotechnical and Geological Engineering*, 29(3), 329-342.
- Dave, E. V., & Buttlar, W. G. (2010). Thermal reflective cracking of asphalt concrete overlays. *International Journal of Pavement Engineering*, 11(6), 477-488.
- Dexter, R. J., & Ocel, J. M. (2013). *Manual for repair and retrofit of fatigue cracks in steel bridges* (No. FHWA-IF-13-020).
- Duda, R. O., Hart, P. E., & Stork, D. G. (2000). *Pattern Classification and Scene Analysis Part 1: Pattern Classification*. Wiley, Chichester.
- Duncan, J. M., Monismith, C. L., & Wilson, E. L. (1968). Finite element analyses of pavements. *Highway Research Record*, (228).
- El Haddad, M. H., Dowling, N. E., Topper, T. H., & Smith, K. N. (1980). J integral applications for short fatigue cracks at notches. *International Journal of Fracture*, 16(1), 15-30.
- Elewa, M. A. (2004). *Influence of Secondary Components on the Serviceability of Steel Girder Highway Bridges*. Michigan State University East Lansing, MI.
- Elkordy, M. F., Chang, K. C., & Lee, G. C. (1993). Neural networks trained by analytically simulated damage states. *Journal of Computing in Civil Engineering*, 7(2), 130-145.
- Elvin, N. G., Lajnef, N., & Elvin, A. A. (2006). Feasibility of structural monitoring with vibration powered sensors. *Smart materials and structures*, 15(4), 977.
- Elvin, N., Elvin, A., & Choi, D. H. (2003). A self-powered damage detection sensor. *The Journal of Strain Analysis for Engineering Design*, 38(2), 115-124.
- Farrar, C. R., & Worden, K. (2007). An introduction to structural health monitoring. *Philosophical Transactions of the Royal Society of London A: Mathematical, Physical and Engineering Sciences*, 365(1851), 303-315.
- Fawcett, T. (2006). An introduction to ROC analysis. *Pattern recognition letters*, 27(8), 861-874.

- Fisher, J. W. (1984). Fatigue and fracture in steel bridges. Case studies.
- Fisher, J. W., & Mertz, D. R. (1985). Hundreds of bridges-thousands of cracks. *Civil Engineering*, (4).
- Fukuda, Y., Feng, M. Q., & Shinozuka, M. (2010). Cost-effective vision-based system for monitoring dynamic response of civil engineering structures. *Structural Control and Health Monitoring*, 17(8), 918-936.
- Gandomi, A. H., Yun, G. J., & Alavi, A. H. (2013). An evolutionary approach for modeling of shear strength of RC deep beams. *Materials and structures*, 46(12), 2109-2119.
- Garg, A., Tai, K., & Gupta, A. K. (2014). A modified multi-gene genetic programming approach for modelling true stress of dynamic strain aging regime of austenitic stainless steel 304. *Meccanica*, 49(5), 1193-1209.
- Goh, A. T. (2002). Probabilistic neural network for evaluating seismic liquefaction potential. *Canadian Geotechnical Journal*, 39(1), 219-232.
- Hall, D. L., Llinas J. Introduction to multisensor data fusion, *Handbook of multisensor data fusion*, 1st ed., Boca Raton: CRC press pp.1-15, 2001.
- Hasni, H., Alavi, A. H., Chatti, K., & Lajnef, N. (2017e). A self-powered surface sensing approach for detection of bottom-up cracking in asphalt concrete pavements: Theoretical/numerical modeling. *Construction and Building Materials*, 144, 728-746.
- Hasni, H., Alavi, A. H., Chatti, K., & Lajnef, N. (2017f). Continuous Health Monitoring of Asphalt Concrete Pavements Using Surface-Mounted Battery-Free Wireless Sensors.
- Hasni, H., Alavi, A. H., Jiao, P., & Lajnef, N. (2017a). Detection of fatigue cracking in steel bridge girders: a support vector machine approach. *Archives of Civil and Mechanical Engineering*, 17(3), 609-622.
- Hasni, H., Alavi, A. H., Jiao, P., & Lajnef, N. (2017b, April). A new method for detection of fatigue cracking in steel bridge girders using self-powered wireless sensors. In *SPIE Smart Structures and Materials+ Nondestructive Evaluation and Health Monitoring* (pp. 101680Q-101680Q). International Society for Optics and Photonics.
- Hasni, H., Alavi, A. H., Jiao, P., Lajnef, N., Chatti, K., Aono, K., & Chakrabartty, S. (2017d). A new approach for damage detection in asphalt concrete pavements using battery-free wireless sensors with non-constant injection rates. *Measurement*, 110, 217-229.
- Hasni, H., Alavi, A. H., Lajnef, N., Abdelbarr, M., Masri, S. F., & Chakrabartty, S. (2017c). Self-powered piezo-floating-gate sensors for health monitoring of steel plates. *Engineering Structures*, 148, 584-601.
- Hasni, H., Jiao, P., Alavi, A. H., Lajnef, N., & Masri, S. F. (2018b). Structural health monitoring of steel frames using a network of self-powered strain and acceleration sensors: A numerical

- study. *Automation in Construction*, 85, 344-357.
- Hasni, H., Jiao, P., Lajnef, N., & Alavi, A. H. (2018a). Damage localization and quantification in gusset plates: A battery-free sensing approach. *Structural Control and Health Monitoring*, e2158.
- Haukaas, T., & Gardoni, P. (2011). Model uncertainty in finite-element analysis: Bayesian finite elements. *Journal of Engineering Mechanics*, 137(8), 519-526.
- Huang, C. W., Abu Al-Rub, R. K., Masad, E. A., & Little, D. N. (2010). Three-dimensional simulations of asphalt pavement permanent deformation using a nonlinear viscoelastic and viscoplastic model. *Journal of Materials in Civil Engineering*, 23(1), 56-68.
- Huang, C., Lajnef, N., & Chakrabartty, S. (2010). Calibration and characterization of self-powered floating-gate usage monitor with single electron per second operational limit. *IEEE Transactions on Circuits and Systems I: Regular Papers*, 57(3), 556-567.
- Huff, R., Berthelot, C., & Daku, B. (2005). Continuous primary dynamic pavement response system using piezoelectric axle sensors. *Canadian journal of civil engineering*, 32(1), 260-269.
- Jiao, P., Borchani, W., Hasni, H., Alavi, A. H., & Lajnef, N. (2016). Post-buckling response of non-uniform cross-section bilaterally constrained beams. *Mechanics Research Communications*, 78, 42-50.
- Jiao, P., McGraw, B., Chen, A., Davalos, J. F., & Ray, I. (2012). Flexural-torsional buckling of cantilever composite wood I-beams with sinusoidal web geometry. In *Earth and Space 2012: Engineering, Science, Construction, and Operations in Challenging Environments* (pp. 684-693).
- Juntunen, D. Study of Michigan's Link Plate and Pin Assembly. Michigan Department of Transportation (MDOT). Research Report No.
- Karlaftis, A. G., & Badr, A. (2015). Predicting asphalt pavement crack initiation following rehabilitation treatments. *Transportation Research Part C: Emerging Technologies*, 55, 510-517.
- Koutsopoulos, H. N., & Downey, A. B. (1993). Primitive-based classification of pavement cracking images. *Journal of Transportation Engineering*, 119(3), 402-418.
- Krajewski, S., & Nowacki, J. (2014). Dual-phase steels microstructure and properties consideration based on artificial intelligence techniques. *Archives of Civil and Mechanical Engineering*, 14(2), 278-286.
- Kurata, N., Spencer, B. F., & Ruiz-Sandoval, M. (2004, August). Building risk monitoring using wireless sensor network. In *Proc. 13th World Conference on Earthquake Engineering* (No. 1406).

- Lajnef, N., Chatti, K., Chakrabartty, S., Rhimi, M., & Sarkar, P. (2013). Smart pavement monitoring system (No. FHWA-HRT-12-072).
- Lajnef, N., Rhimi, M., Chatti, K., Mhamdi, L., & Faridazar, F. (2011). Toward an integrated smart sensing system and data interpretation techniques for pavement fatigue monitoring. *Computer Aided Civil and Infrastructure Engineering*, 26(7), 513-523.
- Lee, J. J., Lee, J. W., Yi, J. H., Yun, C. B., & Jung, H. Y. (2005). Neural networks-based damage detection for bridges considering errors in baseline finite element models. *Journal of Sound and Vibration*, 280(3), 555-578.
- Li, J., & Hao, H. (2016). Health monitoring of joint conditions in steel truss bridges with relative displacement sensors. *Measurement*, 88, 360-371.
- Liao, M. (2009). A Computational Study of the I-35W Bridge Failure (Doctoral dissertation, Thesis (MS) University of Minnesota Major: Civil engineering.).
- Loh, K. J., Hou, T. C., Lynch, J. P., & Kotov, N. A. (2009). Carbon nanotube sensing skins for spatial strain and impact damage identification. *Journal of Nondestructive Evaluation*, 28(1), 9-25.
- Lynch, J. P., & Loh, K. J. (2006). A summary review of wireless sensors and sensor networks for structural health monitoring. *Shock and Vibration Digest*, 38(2), 91-130.
- Lynch, J. P., Law, K. H., Kiremidjian, A. S., Kenny, T. W., Carryer, E., & Partridge, A. (2001, Mackinac Bridge Authority. (2018). Retrieved from <http://www.mackinacbridge.org/fares-traffic/bridge-cam/>.
- Maia, N. M., Almeida, R. A., Urgueira, A. P., & Sampaio, R. P. (2011). Damage detection and quantification using transmissibility. *Mechanical Systems and Signal Processing*, 25(7), 2475-2483.
- Malekzadeh, M., Atia, G., & Catbas, F. N. (2015, April). A hybrid data interpretation framework for automated performance monitoring of infrastructure. In *Structures Congress 2015* (pp. 426-434).
- Mao, K. Z., Tan, K. C., & Ser, W. (2000). Probabilistic neural-network structure determination for pattern classification. *IEEE Transactions on neural networks*, 11(4), 1009-1016.
- MathWorks, MATLAB the language of technical computing, Version R2016a, MathWorks Inc., Natick, MA, USA, 2016.
- Michalczyk, R. (2011). Implementation of generalized viscoelastic material model in ABAQUS code. *Logistyka*.
- Mills, J. P., Newton, I., & Peirson, G. C. (2001). Pavement deformation monitoring in a rolling load facility. *The Photogrammetric Record*, 17(97), 07-24.

- Mishnaevsky, L. L. (2004). Three-dimensional numerical testing of microstructures of particle reinforced composites. *Acta Materialia*, 52(14), 4177-4188.
- Mohajeri, M. J. H., & Manning, P. J. (1991). Aria (trademark): An operating system of pavement distress diagnosis by image processing. *Transportation research record*, (1311).
- Mun, S., Guddati, M. N., & Kim, Y. R. (2006). Viscoelastic continuum damage finite element modeling of asphalt pavements for fatigue cracking evaluation. *KSCE Journal of Civil Engineering*, 10(2), 97-104.
- Perret, J., & Dumont, A. G. (2004). Strain and stress distributions in flexible pavements under moving loads. *Road Materials and Pavement Design*, 5(sup1), 203-225.
- Plati, C., & Loizos, A. (2013). Estimation of in-situ density and moisture content in HMA pavements based on GPR trace reflection amplitude using different frequencies. *Journal of Applied Geophysics*, 97, 3-10.
- Plati, C., Georgiou, P., & Loizos, A. (2014). Use of infrared thermography for assessing HMA paving and compaction. *Transportation Research Part C: Emerging Technologies*, 46, 192-208.
- Potter, J. F., Mayhew, H. C., & Mayo, A. P. (1969). Instrumentation of the Full-scale Experiment on A1 Trunk Road at Conington, Huntingdonshire. Rrl Reports, Road Research Lab/UK/.
- Pugno, N., Ciavarella, M., Cornetti, P., & Carpinteri, A. (2006). A generalized Paris' law for fatigue crack growth. *Journal of the Mechanics and Physics of Solids*, 54(7), 1333-1349.
- Raghavan, A., Kessler, S. S., Dunn, C. T., Barber, D., Wicks, S., & Wardle, B. L. (2009, September). Structural health monitoring using carbon nanotube (CNT) enhanced composites. In *Proceedings of the 7th International Workshop on Structural Health Monitoring*, Stanford University.
- Rajasekaran, S., & Amalraj, R. (2002). Predictions of design parameters in civil engineering problems using SLNN with a single hidden RBF neuron. *Computers & structures*, 80(31), 2495-2505.
- Roeder, A., Zhang, H., Sanchez, L., Yang, Y., Farrar, C., & Mascareñas, D. (2017). Identification of Full-Field Dynamic Loads on Structures Using Computer Vision and Unsupervised Machine Learning. In *Shock & Vibration, Aircraft/Aerospace, Energy Harvesting, Acoustics & Optics*, Volume 9 (pp. 41-48). Springer, Cham.
- Saafi, M. (2009). Wireless and embedded carbon nanotube networks for damage detection in concrete structures. *Nanotechnology*, 20(39), 395502.
- Sadowski, Ł. (2013). Non-destructive evaluation of the pull-off adhesion of concrete floor layers using RBF neural network. *Journal of Civil Engineering and Management*, 19(4), 550-560.

- Sadowski, L. (2013). Non-destructive investigation of corrosion current density in steel reinforced concrete by artificial neural networks. *Archives of Civil and Mechanical Engineering*, 13(1), 104-111.
- Sadowski, L., & Hoła, J. (2013). Neural prediction of the pull-off adhesion of the concrete layers in floors on the basis of nondestructive tests. *Procedia Engineering*, 57, 986-995.
- Samui, P. (2008). Support vector machine applied to settlement of shallow foundations on cohesionless soils. *Computers and Geotechnics*, 35(3), 419-427.
- Samui, P., & Sitharam, T. G. (2011). Machine learning modelling for predicting soil liquefaction susceptibility. *Natural Hazards and Earth System Sciences*, 11(1), 1-9.
- Saridakis, K. M., Chasalevris, A. C., Papadopoulos, C. A., & Dentsoras, A. J. (2008). Applying neural networks, genetic algorithms and fuzzy logic for the identification of cracks in shafts by using coupled response measurements. *Computers & Structures*, 86(11), 1318-1338.
- Sarkar, A. (2016). Numerical comparison of flexible pavement dynamic response under different axles. *International Journal of Pavement Engineering*, 17(5), 377-387.
- Satpal, S. B., Guha, A., & Banerjee, S. (2016). Damage identification in aluminum beams using support vector machine: Numerical and experimental studies. *Structural Control and Health Monitoring*, 23(3), 446-457.
- Schreurs, P.J.G. (2012). Fracture mechanics, Technical Report, Eindhoven University of Technology, Netherland.
- Sedlak, P., Majzner, J., & Šikula, J. (2011). Noise in Piezoelectric Ceramics at the Low Temperatures. *Radioengineering*, 20(1), 200-203.
- September). The design of a wireless sensing unit for structural health monitoring. In *Proceedings of the 3rd International Workshop on Structural Health Monitoring* (pp. 12-14).
- Shafabakhsh, G., Naderpour, H., & Motamedi, M. (2015). Dynamic analysis and determination of maximum tensile strain of bottom asphalt concrete for different vehicle velocities. *Engineering Journal (Eng. J.)*, 19(4), 107-116.
- Shahidi, S. G., Gulgec, N. S., & Pakzad, S. N. (2016). Compressive Sensing Strategies for Multiple Damage Detection and Localization. In *Dynamics of Civil Structures, Volume 2* (pp. 17-22). Springer International Publishing.
- Siddharthan, R. V., Yao, J., & Sebaaly, P. E. (1998). Pavement strain from moving dynamic 3D load distribution. *Journal of Transportation Engineering*, 124(6), 557-566.
- Simulia, D. (2011). ABAQUS 6.11 analysis user's manual. Abaqus, 6, 22-2.
- Sirohi, J., & Chopra, I. (2000). Fundamental understanding of piezoelectric strain

- sensors. *Journal of Intelligent Material Systems and Structures*, 11(4), 246-257.
- Sodano, H. A., Park, G., & Inman, D. J. (2004). Estimation of electric charge output for piezoelectric energy harvesting. *Strain*, 40(2), 49-58.
- Song, S. H., Paulino, G. H., & Buttlar, W. G. (2006). A bilinear cohesive zone model tailored for fracture of asphalt concrete considering viscoelastic bulk material. *Engineering Fracture Mechanics*, 73(18), 2829-2848.
- Spears, R. E., & Jensen, S. R. (2012). Approach for selection of Rayleigh damping parameters used for time history analysis. *Journal of pressure vessel technology*, 134(6), 061801.
- Specht, D. F. (1990). Probabilistic neural networks. *Neural networks*, 3(1), 109-118.
- Stallings, J., Cousins, T., & Tedesco, J. (1997). Fatigue of diaphragm-girder connections. *Transportation Research Record: Journal of the Transportation Research Board*, (1594), 34-41.
- Szewczyk, Z. P., & Hajela, P. (1994). Damage detection in structures based on feature-sensitive neural networks. *Journal of computing in civil engineering*, 8(2), 163-178.
- Tielking, J. T., & Roberts, F. L. (1987). Tire contact pressure and its effect on pavement strain. *Journal of Transportation Engineering*, 113(1), 56-71.
- Ueno, K. (2010). CMOS Voltage and Current Reference Circuits consisting of Subthreshold MOSFETs—Micropower Circuit Components for Power-Aware LSI Applications—. In *Solid state circuits technologies*. InTech.
- Wang, F., & Machemehl, R. (2006). Mechanistic-empirical study of effects of truck tire pressure on pavement: Measured tire-pavement contact stress data. *Transportation Research Record: Journal of the Transportation Research Board*, (1947), 136-145.
- Wang, H. (2011). Analysis of tire-pavement interaction and pavement responses using a decoupled modeling approach (Doctoral dissertation, University of Illinois at Urbana-Champaign).
- Weissman, S. (1999). Influence of tire-pavement contact stress distribution on development of distress mechanisms in pavements. *Transportation Research Record: Journal of the Transportation Research Board*, (1655), 161-167.
- Weston, J., Mukherjee, S., Chapelle, O., Pontil, M., Poggio, T., & Vapnik, V. (2000, January). Feature selection for SVMs. In *Proceedings of the 13th International Conference on Neural Information Processing Systems* (pp. 647-653). MIT Press.
- Worden, K., & Lane, A. J. (2001). Damage identification using support vector machines. *Smart Materials and Structures*, 10(3), 540.
- Wu, X., Ghaboussi, J., & Garrett, J. H. (1992). Use of neural networks in detection of structural

- damage. *Computers & structures*, 42(4), 649-659.
- Xu, D., Banerjee, S., Wang, Y., Huang, S., & Cheng, X. (2015). Temperature and loading effects of embedded smart piezoelectric sensor for health monitoring of concrete structures. *Construction and Building Materials*, 76, 187-193.
- Xue, W., Wang, L., Wang, D., & Druta, C. (2013). Pavement health monitoring system based on an embedded sensing network. *Journal of Materials in Civil Engineering*, 26(10), 04014072.
- Yan, B., & Miyamoto, A. (2003, August). Application of probabilistic neural network and static test data to the classification of bridge damage patterns. In *Smart Structures and Materials* (pp. 606-617). International Society for Optics and Photonics.
- Yang, Y., Dorn, C., Mancini, T., Talken, Z., Theiler, J., Kenyon, G., ... & Mascarenas, D. (2017). Reference-free detection of minute, non-visible, damage using full-field, high-resolution mode shapes output-only identified from digital videos of structures. *Structural Health Monitoring*, 1475921717704385.
- Yen, B. C., & Lang, J. H. (2006). A variable-capacitance vibration-to-electric energy harvester. *IEEE Transactions on Circuits and Systems I: Regular Papers*, 53(2), 288-295.
- Yeum, C. M., & Dyke, S. J. (2015). Vision-based automated crack detection for bridge inspection. *Computer-Aided Civil and Infrastructure Engineering*, 30(10), 759-770.
- Yue, Z. Q., & Svec, O. J. (1995). Effects of tire-pavement contact pressure distributions on the response of asphalt concrete pavements. *Canadian Journal of Civil Engineering*, 22(5), 849-860.
- Zha, J. W., Zhang, B., Li, R. K., & Dang, Z. M. (2016). High-performance strain sensors based on functionalized graphene nanoplates for damage monitoring. *Composites Science and Technology*, 123, 32-38.
- Zhao, J., Ivan, J. N., & DeWolf, J. T. (1998). Structural damage detection using artificial neural networks. *Journal of Infrastructure Systems*, 4(3), 93-101.
- Zhao, Y., & Roddis, W. K. (2004). *Fatigue Prone Steel Bridge Details: Investigation and Recommended Repairs* (No. K-TRAN: KU-99-2). Kansas Department of Transportation.
- Zongker, D., & Jain, A. (1996, August). Algorithms for feature selection: An evaluation. In *Pattern Recognition, 1996., Proceedings of the 13th International Conference on* (Vol. 2, pp. 18-22). IEEE.
- Zou, Y., Tong, L. P. S. G., & Steven, G. P. (2000). Vibration-based model-dependent damage (delamination) identification and health monitoring for composite structures—a review. *Journal of Sound and vibration*, 230(2), 357-378.